

Engineered binding sites for indoxyl sulfate and p-cresol sulfate

by

Shuhui Li

A thesis submitted in partial fulfillment of the requirements for the degree of

Doctor of Philosophy

in

Chemical Engineering

Department of Chemical and Materials Engineering

University of Alberta

© Shuhui Li, 2023

Abstract

The removal of uremic toxins is of great importance in preventing the progression of chronic kidney disease. The investigation of the interaction of uremic toxins with serum and dialysis materials will contribute to the advancement of techniques in uremic toxins removal. This study investigates the host-guest system of uremic toxins with human serum albumin and polymer-coated particles. First, the driving force of uremic toxins binding with human serum albumin is investigated and determined. Second, a series of novel polymer-coated magnetic nanoparticles are created and tested for toxin removal ability and hemocompatibility.

Although the removal of uremic toxins has been researched for decades and well progress has been achieved on water-soluble small molecules removal. Protein-bound uremic toxins are retained in the blood causing detrimental complications. Herein, through an in-depth thermodynamic investigation using isothermal titration calorimetry, the driving force for protein-bound uremic toxins binding to human serum albumin was identified unveiling the contribution of hydrophobic interaction and electrostatic interaction to the binding behavior. Furthermore, STD NMR provided solid evidence that identified the binding site of indoxyl sulfate and p-cresol sulfate on human serum albumin, that IS binds to Sudlow's site I and site II whereas PCS only partially binds to site II. The human serum albumin secondary and tertiary conformation shifting upon addition of uremic toxins is reflected through the tryptophan fluorescence changing and the spatial formation determined by fluorescence spectrometry and circular dichroism, respectively.

Secondly, the novel poly(β -Cyclodextrin-*co*-2-(methacryloyloxy)ethyl phosphorylcholine) coated magnetic nanoparticle is created to remove uremic toxins. Instead of investigating the two iconic protein-bound uremic toxins, indoxyl sulfate and p-cresol sulfate, a profile of uremic toxins

has been researched. Native β -cyclodextrin was decorated with the alkane group and copolymerized with 2-(methacryloyloxy)ethyl phosphorylcholine (MPC) through the route of atomic transfer radiation polymerization on the surface of initiator fixed magnetic nanoparticle. The study shows that surface chemistry and incubation time have an impact on the adsorbed toxinome profile, even with "low-fouling" polymers. The findings suggest a dynamic interaction between toxins and surfaces that is not solely driven by solution concentration, which could help in the design of adsorbent films for clearing uremic toxins.

Following the previous work, we investigated the biocompatibility of β -cyclodextrin-co-2-(methacryloyloxy)ethyl phosphorylcholine grafted magnetic nanoparticles (p(PM β CD-co-MPC) MNP). The impact of bare magnetic nanoparticles and coated particles on the structure of human serum albumin, α -Lactalbumin, and Lysozyme proteins was studied using circular dichroism and fluorescence spectroscopy. The study also examined the stability of plasma and uremic plasma in the presence of particles using a plasma clotting assay. Immunoblotting was utilized to study the adsorption of plasma proteins to different types of MNPs using UTX-treated and non-UTX-treated plasma. The results indicate that p(PM β CD-co-MPC) coated MNPs have better biocompatibility than bare MNPs, and that particle D (PM β CD: MPC=1:3) exhibited the strongest inhibition of clotting formation in the UTX-treated group. The findings provide important insights into the biocompatibility of p(PM β CD-co-MPC) MNPs and their potential application in biomaterials.

In conclusion, this study presents valuable insights into the host-guest system of uremic toxins with human serum albumin and p(PM β CD-co-MPC) MNPs. The investigation of the driving force for protein-bound uremic toxins binding with human serum albumin and the identification of their binding sites are significant contributions to the field. Additionally, the creation and testing of novel polymer-coated magnetic nanoparticles for toxin removal and

hemocompatibility showed intriguing results. The study highlights the importance of surface chemistry and incubation time in the adsorption of uremic toxins and the biocompatibility of the coated nanoparticles. The findings provide a foundation for the design of adsorbent films and potential biomaterials for clearing uremic toxins.

Preface

In this thesis, Chapter 1 section 1.5 has been published as “Yuhao Ma, Shuhui Li, Marcello Tonelli, Larry D. Unsworth, “Adsorption-based strategies for removing uremic toxins from blood” *Microporous and Mesoporous Materials*, May 2021.” Published by Elsevier Ltd. All right reserved. I was responsible for partial table making, and data gathering. Yuhao Ma was the first author who responsible for literature review and manuscript composition. Larry. D. Unsworth was the supervising author and was involved with editing the manuscript.

Chapter 2 of the thesis has been published as “Shuhui Li, Marcello Tonelli, Larry D. Unsworth, “Indoxyl and p-cresol sulfate binding with human serum albumin” *Colloids and Surfaces A: Physicochemical and Engineering Aspects*, February 2022” Published by Elsevier Ltd. All right reserved. I was responsible for all data gathering and manuscript composition. Larry D. Unsworth was the supervising author and was involved with editing the manuscript.

Chapter 3 of the thesis was written in paper format and submitted. The author of the paper includes Shuhui Li, Mehdi Ghaffari Sharaf, Lun Zhang, David Wishart, Marcello Tonelli, Larry D. Unsworth. I was responsible for sample synthesis, TGA, FTIR, GPC, HPLC sample preparation, analysis and manuscript composition. Mehdi Ghaffari Sharaf was responsible for bare MNP synthesis and was involved in study design. Lun Zhang was responsible for the LC/MS experiment and raw data analysis. David Wishart, Marcello Tonelli, and Larry D. Unsworth were the supervising authors and were involved in the study design and manuscript composition.

Chapter 4 of the thesis was written in paper format and submitted. The author of the paper includes Shuhui Li, Mehdi Ghaffari Sharaf, Elyn M. Rowe, Katherine Serrano, Dana V. Devine, Larry D. Unsworth. I was responsible for sample synthesis, plasma clotting assay experiment,

circular dichroism experiment, data analysis, and manuscript composition. Mehdi Ghaffari Sharaf was responsible for immune blotting experiment, fluorescence spectroscopy experiment, and BCA assay, data analysis and manuscript composition. Elyn Rowe will be responsible for the platelet activation, data analysis and manuscript composition. Katherine Serrano and Dana V. Devine are the supervising authors. Larry D. Unsworth was the supervising authors and was involved in the study design and manuscript composition.

Chapter 5 of the thesis is undergoing writing and data collection. The author of the paper includes Shuhui Li, Mehdi Ghaffari Sharaf, Elyn M. Rowe, Katherine Serrano, Dana V. Devine, Larry D. Unsworth. I was responsible for sample preparation, plasma clotting assay experiment, data analysis, and manuscript composition. Mehdi Ghaffari Sharaf was responsible for immune blotting experiment, and BCA assay, data analysis and manuscript composition. Elyn Rowe will be responsible for the blood related experiments, including platelet activation, Whole blood hemocompatibility and impact on platelet function, and data analysis and manuscript composition. Katherine Serrano and Dana V. Devine are the supervising authors. Larry D. Unsworth was the supervising authors and was involved in the study design and manuscript composition.

Acknowledgements

I would like to take this opportunity to express my heartfelt gratitude to my supervisor, Dr. Larry D. Unsworth, for his unwavering patience and meticulous guidance throughout my Ph.D. journey. His valuable insights and expertise have been invaluable to the completion of this thesis.

Furthermore, I am deeply grateful to my parents, Xianhua Zeng and Zhong Li, for their unconditional support. Their unwavering encouragement and sacrifices have been the bedrock of the completion of my Ph.D. 谢谢妈妈爸爸的支持和关爱!

I would also like to extend my sincere appreciation to my esteemed colleagues, Dr. Mehdi Ghaffari Sharaf and Dr. Shammy Raj, for their academic and spiritual support. Their unwavering encouragement and friendship have been instrumental in keeping me motivated during challenging times.

Finally, I would like to acknowledge the financial support of Alberta Innovates - Strategic Research Project, Alberta Innovates – Alliance, and Natural Sciences and Engineering Research Council of Canada, without which this thesis would not have been possible.

Table of Contents

Abstract	ii
Preface.....	v
Acknowledgements	vii
Table of Contents	viii
List of Tables.....	xiii
List of Figures	xv
Chapter 1	1
1.1 Chronic Kidney Disease.....	2
1.1.1 Treatment of CKD.....	2
1.2 Uremic Toxins.....	3
1.2.1 Classification of Uremic Toxins.....	4
1.2.2 The Association of Uremic Toxins with Disease	5
1.2.3. Protein-Bound Uremic Toxins	5
1.3. Human Serum Albumin	6
1.3.1. Structure of Human serum albumin	6
1.3.2. Binding site on HSA.....	7
1.3.3. A close look to Sudlow’s site I and Sudlow’s site II.....	8
1.4 Driving Forces Responsible for Ligands-HSA binding	9
1.4.1. Hydrophobic Interactions	9
1.4.2. Electrostatic Interaction.....	11
1.4.3. Current Methodology for Assessing Binding Mechanisms	12
1.4.4. Mechanism of ITC.....	13
1.5. Overview of Polymer Adsorbents in Uremic Toxins Removal	15
1.5.1. Pure Polymer and Polymer Coated Adsorbent.....	16
1.5.2. Molecular imprinted polymer (MIP).....	18
1.5.3. Mixed matrix membrane (MMM).....	19
1.6 Cyclodextrin (CD).....	23
1.6.1 Cyclodextrin Polymers	24
1.6.1.1 Crosslinked Cyclodextrin Polymers	25
1.6.1.2 Linear-linked Cyclodextrin Polymers.....	25
1.6.1.3 Cyclodextrin Star Polymers	26
1.6.1.4 Cyclodextrin polyrotaxanes	27
1.6.2 β -Cyclodextrin.....	28
1.7 Magnetic Nanoparticle Technology	29
1.8 Research Proposal	30
1.8.1 Rationale.....	30
1.8.2. Objectives.....	31
1.8.3 Scope of Dissertation.....	32

1.9 References	33
Chapter 2	45
2.1 Introduction	46
2.2 Experimental	48
2.2.1 Materials and methods.....	48
2.2.2 Fluorescence	48
2.2.3 Circular dichroism.....	48
2.2.4 Isothermal titration calorimetry	49
2.2.5 Saturation transfer difference (STD) NMR.....	50
2.3 Results and discussion.....	50
2.3.1 Binding of IS and PCS to HSA	50
2.3.2 Fluorescence	55
2.3.2.1 Effect of IS and PCS on fluorescence.....	55
2.3.2.2 Fluorescence quenching mechanism	56
2.3.2.3 Binding Parameters.....	58
2.3.3 Effect of PBUT on I structure	58
2.3.4 Analysis of STD-NMR experiments	59
2.3.5 Identification of IS or PCS binding site on I.....	62
2.4 Conclusion.....	64
2.5 References	65
Chapter 3	71
Dynamic adsorption profile for uremic toxins to beta-cyclodextrin, 2-(methacryloyloxy)ethyl phosphorylcholine modified magnetic nanoparticles.....	71
3.1 Introduction	72
3.2 Experimental	76
3.2.1 Materials.....	76
3.2.2 Molecular Characterization	77
3.2.3 Toxin solution.....	78
3.2.4 LC/MS quantification of adsorbed toxin profile	78
3.3 Results and discussion.....	79
3.3.1 Synthesis.....	79
3.3.1.1 Synthesis of Fe ₃ O ₄ nanoparticles (MNP).....	79
3.3.2 Surface polymer synthesis.....	79
3.3.2.1 ATRP initiator fixation on MNP	79
3.3.3 Thermogravimetric analysis of bare and coated MNPs.....	80
3.3.4 Chemical composition and charge of coatings	82
3.3.5 Coating morphology analysis	83
3.3.6 Profile of adsorbed uremic toxins for all particle systems.....	85
3.4 Conclusion.....	93
3.5 References	95
Chapter 4	101

Hemocompatibility of β -cyclodextrin modified (methacryloyloxy)ethyl phosphorylcholine coated magnetic nanoparticles.....	101
4.1 Introduction.....	102
4.2 Materials and Methods.....	104
4.2.1 Materials.....	104
4.2.2 Methods.....	105
4.2.2.1 Polymer synthesis and fixation.....	105
4.2.2.2 Polymer Characterization.....	106
4.2.2.3 Circular Dichroism.....	107
4.2.2.4 Fluorescence spectroscopy.....	107
4.2.2.5 SDS-PAGE and immunoblot.....	108
4.2.2.6 Fibrin clot formation in plasma.....	109
4.2.2.7 Whole blood hemocompatibility testing.....	109
4.3 Results and discussions.....	111
4.3.1 Properties and characterization of the modified MNPs.....	111
4.3.2 Circular Dichroism.....	113
4.3.3 Changes in intrinsic fluorescence of HSA upon adsorption.....	117
4.3.4 Total adsorbed protein.....	119
4.3.5 Plasma clotting in the presence of polymer-coated nanoparticles.....	120
4.3.6 Quantification of protein adsorption.....	122
4.3.6.1 Immune response-related proteins.....	125
4.3.6.2 Coagulation-related proteins.....	128
4.4 Conclusion.....	136
4.5 References.....	138
Chapter 5.....	147
Effect of uremic toxins on hemocompatibility of β -cyclodextrin, 2-(methacryloyloxy)ethyl phosphorylcholine grafted magnetic nanoparticles.....	147
5.1 Introduction.....	148
5.2 Materials and Methods.....	151
5.2.1 Materials.....	151
5.2.2 Methods.....	152
5.2.2.1 Toxin solution preparation and lyophilization.....	152
5.2.2.2 Polymer coated particle preparation.....	152
5.2.2.3 Polymer Characterization.....	153
5.2.2.4 Plasma Calcification.....	154
5.2.2.5 SDS-PAGE and Immunoblot.....	154
5.3 Result and Discussion.....	156
5.3.1 Properties and characterization of the modified MNPs.....	156
5.3.2 Plasma clotting in the presence of polymer coated nanoparticles.....	159
5.3.3 Total adsorbed protein.....	161
5.3.4 Immunoblot analysis.....	164

5.3.4.1 Immune response-related bands.....	164
5.3.4.2 Coagulation related bands.....	168
5.4 Conclusion.....	173
5.5 References.....	175
Chapter 6.....	183
Concluding remarks and perspectives.....	183
6.1 Major contributions.....	184
6.2 Future work.....	185
Bibliography.....	186
Appendix A.....	226
A Detailed Protocol of Making Metabolite Solution.....	226
1. Metabolite solution preparation.....	227
1.1 Materials.....	227
1.2 Procedure of preparing metabolite solution for non-plasma included experiment.....	229
1.2.1 Metabolite solution preparation.....	231
1.2.2 Aliquot the stock solution.....	232
1.2.3 Lyophilization.....	232
1.3 Experiment.....	233
1.4 Procedure of preparing metabolite solution for plasma included experiment.....	233
1.4.1 Supplies preparation.....	233
1.4.2 Stock solution preparation.....	233
1.4.3 Metabolite solution preparation.....	235
1.4.4 Aliquot the stock solution.....	236
1.4.5 Lyophilization.....	236
1.4.6 Experiment.....	237
Appendix B.....	238
A Detailed Protocol of Fluorescence Spectroscopy Experiment.....	238
1. Materials.....	239
2. Procedure to conduct fluorescence experiments.....	239
2.1 Sample preparation.....	239
2.2 Experiment.....	239
2.3 Data analysis.....	240
Appendix C.....	242
A Detailed Protocol of Isothermal Titration Calorimetry Experiment.....	242
1. Materials.....	243
2. Procedure to conduct experiment on isothermal titration calorimetry.....	243
3. Data analysis.....	245
Appendix D.....	246
A Detailed Protocol of Circular Dichroism Experiment.....	246
1. Materials.....	247
2. Procedure to conduct fluorescence experiments.....	247

2.1 Sample preparation.....	247
2.2 Experiment	247
3. Data analysis	248

List of Tables

Table 1.1 Summary of <i>in vitro</i> research using adsorbent for removal of uremic toxins.....	20
Table 2.1 Thermodynamic parameters for the interaction of IS or PCS with HSA obtained from ITC at 298 K and pH 7.20.....	51
Table 2.2 Stern–Volmer quenching constant KSV and association constant Ka for IS and PCS binding with I at 298, 303, and 310 K.....	56
Table 2.3 Representative results for the effect of IS or PCS on the secondary structure of I, as determined using CD spectra between 190 to 260 nm. Results are an average of three repeated scans.	59
Table 3.1 Composition of uremic toxin solutions developed based on literature analysis of the blood of patients with kidney dysfunction.	74
Table 3.3 Average percent weight loss from particles within specific temperature regimes as determined using TGA.	81
Table 3.4 Quantitative LC/MS evaluation of adsorbed toxinome from Particles A through E, for 1 and 4 hr incubation times, respectively. Note that all values represent μM concentrations of eluted toxins, <LOD indicating a response below the level of detection for that species. Note that the experimental repeats yielded standard deviations less than the expected 20% inherent to targeted mass spectroscopy, however, an error of 20% in these values were used for all analysis.	86
Table 3.5 Heat map highlighted selectivity of binding as determined by taking the experimentally adsorbed mol% and dividing by the mol% for each compound in the original solution. Data greater than unity (red) indicates an increased adsorption relative to the compound’s initial concentration, less than 0.2 (light blue) and less than 0.1 (dark blue) highlights adsorbed amounts much less than initial concentrations, and - shows compounds where calculations could not be done due to values being lower than the detectable level.	88
Table 3.6 Percent change in mol% from 1 to 4 hr incubation time. Red indicates an increase in mol% of compound, blue a decrease, and white a nominal change.....	92
Table 4.1 The representative synthesis scheme for A to E particle series.....	106
Table 4.5 Relative intensities of immunoblot of plasma proteins adsorbed to different types of MNPs.....	123
Table 5.1 Composition of uremic toxin solutions based on literature values for the analysis of the blood of patients with kidney dysfunction.	150
Table 5.2 Summary of TGA, GPC and molecular weight results for polymers cleaved from MNPs.....	157
Table 5.3 Summary of clot formation kinetics and plateau onset for MNP in platelet poor plasma without uremic toxins and after 1 and 4 hr incubation with uremic toxin laden plasma (n=3, all SDs are less than 3 seconds). The ratio in the bracket represents the mole ratio of PM β CD: MPC.	160

Table 5.4 Relative intensities of immunoblot of UTX-treated and non-UTX-treated plasma proteins adsorbed to different types of MNPs.....	170
Table A.1 The metabolite solution formula includes the toxins, stock solution concentration, and volume/amount taken from the stock solution in order to make 250 mL metabolite solution. ...	229
Table A.2 The metabolite solution formula includes the toxins, stock solution concentration and volume/amount taken from the stock solution in order to make 250 mL metabolite solution for plasma included experiment.....	234

List of Figures

Figure 1.1 Schematically illustration of (A) Hemodialysis [8], (B) Peritoneal dialysis [9].....	3
Figure 1.2 Chemical structure of categories of PBUTs.....	6
Figure 1.3 Illustration of domains, subdomains, and Sudlow’s sites on HSA [31].	7
Figure 1.4 Illustration of (A) Sudlow’s site I bind with warfarin and (B) Sudlow’s site II bind with ibuprofen. Ligands are represented in grey [20].	8
Figure 1.5 Scheme of an isothermal titration calorimetry and the typical data set (Copyright 2012 by D.G. Lambright) [41].	14
Figure 1.6 Three adsorbent strategies used for removal UTX [43].....	16
Figure 1.7 Representative chemical structure of p-cresol, polyamide, polyacrylonitrile, and polysulfone.	18
Figure 1.8 Chemistry structure of α -, β -, and γ -CD.	24
Figure 1.9 Illustration of types of cyclodextrin polymers.	24
Figure 1.10 Structural illustration of β CD. (A) The primary hydroxyl groups composed primary face, the secondary hydroxyl groups composed secondary face [104]. (B) Illustration of C2, C3, C6 on each glucose unit.	28
Figure 2.1 ITC thermogram (upper panel) and fitting (lower panel) of HAS with single ligand. ITC thermogram (upper panel) and fitting (lower panel) of HAS with single ligands. The solid line represents the best nonlinear least-squares fit to the independent binding site model, where fit quality is represented as R^2 . The initial concentration is $2 \times 10^{-3} \text{ mol L}^{-1}$ for ibuprofen or warfarin and $1 \times 10^{-4} \text{ mol L}^{-1}$ for HSA. $T=298 \text{ K}$, $\text{pH}=7.20$. (A) Left panel: Corrected heat data for the titration of ibuprofen with HSA, with an $R^2=0.88$. (B) Right panel: Corrected heat data for the titration of warfarin with HSA, with an $R^2=0.84$. (C) Left panel: Corrected heat data for the titration of PCS with HSA, with an $R^2=0.99$. (D) Right panel: Corrected heat data for the titration of IS with HSA, with an $R^2=0.99$	53
Figure 2.2 ITC thermogram (upper panel) and fitting (lower panel) of I with double ligands. The solid line represents the best nonlinear least-squares fit to the competitive binding model. The initial concentration is $2 \times 10^{-3} \text{ mol L}^{-1}$ for IS/PCS/ibuprofen/warfarin, and $1 \times 10^{-4} \text{ mol L}^{-1}$ for I. $T=298 \text{ K}$, $\text{pH}=7.20$. (A) Corrected heat data for the titration of ibuprofen with I and IS mixture, with an $R^2=0.91$ (B) Corrected heat data for the titration of warfarin with I and IS mixture, with an $R^2=0.99$ (C) Corrected heat data for the titration of ibuprofen with I and PCS mixture, with an $R^2=0.82$ (D) Corrected heat data for the titration of IS with I and PCS mixture, with an $R^2=0.95$	55
Figure 2.3 Fluorescence emission spectra results for I ($2 \times 10^{-6} \text{ mol L}^{-1}$, $\text{pH}=7.20$) and IS or PCS. (A) I emission in the presence of different concentrations of IS (a-f: 0-1 mM) at 298 K. (B) I emission in the presence of different concentrations of PCS (a’-f’: 0-4 mM) at 298 K. (C)(D): IS (g-l: 1-0.2 mM) and PCS (g’-l’: 4-0.8 mM) in PBS; I(F): Stern–Volmer plots for I quenching by IS or PCS with temperature.....	57

Figure 2.4 The plots of $\log((F_0 - F)/F)$ vs. $\log(1/([Q] - (F_0 - F)[P]/F_0))$ for IS/PCS-I system at three different temperatures and pH 7.2.....	58
Figure 2.5 Circular dichroism spectrum of I in the absence and presence of IS (A) or PCS (B), where the $[I] = 1.0 \times 10^{-5}$ mol L ⁻¹ , $[IS]$ (a-e) or $[PCS]$ (a'-e') was 0.32 to 0 mM.	59
Figure 2.6 Detection of IS and PCS bind with I. $[I] = 30$ mM, $[IS] = [PCS] = 1.5$ mM. (A). Upper panel: STD spectrum of IS with I. Lower panel: NMR spectrum of off-resonance IS and I mixture solution. (B) Upper panel: STD spectrum of PCS with I. Lower panel: NMR spectrum of off-resonance IS and I mixture solution. Integrated area (H1 stands for upper panel, H1' stands for lower panel. Similarly, hereinafter): IS, H1(1.97), H2(1.07), H3(1.14), H4(1.19), H5(1.17). H1'(4.03), H2'(4.22), H3'(4.15), H4'(3.95), H5'(3.83). PCS, H1 and H7 (1.12), H2 and H6 (1.74), H3-H5(2.54). H1' and H7' (7.14), H2'and H6' (7.12), H3'-H5' (10.9).	61
Figure 2.7 1H NMR spectrum: A(a), C(a): IS. B(a), D(a): PCS. A(b), B(b): warfarin. C(b), D(b) ibuprofen. STD spectrum ($[I]=0.1$ mM, $[IS]=[PCS]=0.1$ mM, n(Site indicator): n(Toxin)= 0.5, 1, 2, 5 for (c) to (f)): A(c)-A(f): warfarin with gradient concentration is added into I+IS mixtrure. B(c)-B(f): warfarin with gradient concentration is added into I+PCS mixtrure. C(c)-C(f): ibuprofen with gradient concentration is added into I+IS mixtrure. D(c)-D(f): ibuprofen with gradient concentration is added into I+PCS mixtrure. Arrows denoted the signal increasing or decreasing peak intensity.....	63
Figure 3.2 Representative TGA curves for bare and coated MNPs. Monomer ratio of PM β CD to MPC and the weight loss are A (1:0), 37.42%; B (3:1), 40.1%; C (1:1), 43.0%; D (1:3), 32.1%; E (0:1), 24.1%. The weight loss of bare MNP was 7.4%.	81
Figure 3.3 Representative FTIR spectra of pure MPC, PM β CD, bare MNP, and particles A to E. Monomer ratio of PM β CD to MPC are A (1:0), B (3:1), C (1:1), D (1:3), E (0:1).	83
Figure 3.4 Representative TEM, SEM, and SAED characterization of bare and coated -MNPs. (A) - (E) TEM image of synthesized polymer modified nanoparticles of sample A-E; Right lower inset: Corresponding SEM image of sample A-E. White arrow indicated the polymer layer and black arrow indicated the MNP core size (15 nm). (F) TEM image of bare MNP with SEM inset. (G) Particle size distribution of bare MNP in (F). (H) SAED pattern of MNP. (I) SAED pattern of particle A.	84
Figure 3.5 Total adsorbed amounts of toxins (nmol) for all modified MNP systems, given similar surface areas and incubation times of 1 or 4 hr. Note that repeats were only performed on a subset of data to reduce costs of data collection. Data represent average +/- 1 STD. STD was determined using n=3 and error propagation calculation.	89
Figure 4.1 Illustration of MNPs grafted with poly(2-(methacryloyloxy)ethyl phosphorylcholine) and poly(β -cyclodextrin).	104
Figure 4.2 Representative TEM and SAED characterization of bare and polymer coated MNPs. (A) - (E) TEM image of synthesized polymer modified nanoparticles of sample A-E; Black arrow indicated the polymer layer. (F) TEM image of bare MNP. (G) Particle size distribution of bare MNP in (F). (H) SAED pattern of particle E. (I) SAED pattern of MNP.	112
Figure 4.3 Representative zeta potential test of bare MNP and particles A to E. Unpaired <i>t</i> -tests were conducted to compare results across each pair of groups. Comparisons that are not displayed	

were not statistically significant (* $p < 0.05$, ** $p < 0.01$, *** $p < 0.001$, data presented as mean \pm 1 SD, $n = 3$). 113

Figure 4.4 Circular dichroism spectrum of (A) lysozyme, (B) HSA, and (C) α -lactalbumin in the presence of particles A to E and bare MNP ($n = 3$).Circular dichroism spectrum of (A) lysozyme, (B) HSA, and (C) α -lactalbumin in the presence of particles A to E and bare MNP ($n = 3$)...... 115

Figure 4.5 Study of the interaction of HSA protein with MNPs via quenching of the intrinsic fluorescence of HSA in the presence of different concentrations of MNPs. (A) Fluorescence emission spectra of HSA solution titrated against increasing concentrations of MNPs in the solution (0–70 $\mu\text{g}/\text{mL}$). (B) Binding constant (K_a) and number of binding sites (n) obtained from the plot, $\log [(F_0 - F)/(F - F_s)]$ vs. $\log [S]$. RFU = relative fluorescence units, $[S]$ = MNP concentration, F_0 = relative fluorescence intensity (F) of protein solution alone, and F_s = relative fluorescence intensity of protein saturated with MNPs. Data represent mean \pm 1 SD, $n \geq 3$ 118

Figure 4.6 Representative results showing the amount of adsorbed protein determined using the BCA assay. * Represents $p < 0.05$, data represent mean \pm 1 SD, $n \geq 3$ 120

Figure 4.7 Presence of MNPs reduces clotting time driven by plasma proteins. (a) Representative plots of baseline-corrected average clot formation in platelet-poor human plasma over 60 minutes, with particles A to E or bare MNP present. (b) Whole blood ROTEM results for clotting time – reflective of fibrinogen polymerization. Shapes reflect biological replicates. Results were compared across groups with repeated measures ANOVA to compare differences within biological replicates, across groups, and paired t-tests were used for pairwise comparisons to the water control (* $p < 0.05$, ** $p < 0.01$). Comparisons not shown were not statistically significant. 122

Figure 4.8 C3a ELISA results of MNP-depleted plasma from whole-blood hemocompatibility studies. Whole blood from $n = 3$ healthy donors was incubated with 0.18 mg/mL of each MNP formulation, and MNP-depleted plasma was assayed for C3a. Results were compared across groups with repeated-measures ANOVA to compare differences within biological replicates across groups, and paired t -tests were used for pairwise comparisons to the water control. Comparisons not shown were not statistically significant. 126

Figure 4.9 Complete blood counts and hemolysis in response to whole-blood MNP treatment. Whole blood from $n = 3$ healthy donors was incubated with 0.18 mg/mL of each MNP formulation, and complete blood counts were measured on the Sysmex XN-550 hematology analyzer. Results for (a) platelets, (b) white blood cells, and (c) red blood cells are shown. Hemolysis was assayed in MNP-depleted plasma via the Harboe method (d). Results were compared across groups with repeated-measures ANOVA to compare differences within biological replicates across groups, and paired t -tests were used for pairwise comparisons to the water control (* $p < 0.05$). Comparisons not shown were not statistically significant. 133

Figure 4.10 Trend toward increased platelet activation with lower PM β CD content, without robust impact on platelet function in coagulation. Whole blood from $n = 3$ healthy donors was incubated with 0.18 mg/mL of each MNP formulation, then assessed for platelet-related outcomes. (a) Baseline platelet activation reflected by surface expression of CD62P detected by flow cytometry. Percentage of CD62P+ platelets displayed. (b) Platelet degranulation in response to 10 μM ADP,

reflected by surface expression of CD62P detected by flow cytometry. Baseline activation was subtracted from the % CD62P+ platelets to yield the increase in degranulated platelets, as a measure of the platelet response. (c) Platelet function in coagulation reflected by ROTEM maximum clot firmness and (d) clot formation time. Dashed lines indicate normal ranges as per manufacturer's information, and shapes reflect biological replicates. Results were compared across groups with repeated measures ANOVA to compare differences within biological replicates, across groups, and paired t-tests were used for pairwise comparisons to the..... 135

Figure 5.1 Representative TEM and SAED results for bare and polymer-coated samples. TEM images (A) to (E) show the of the synthesized polymer-modified nanoparticles of sample A to E. TEM image (F) is of control bare MNP, and (G) shows the particle size distribution of the bare MNP in (F). Representative SAED patterns were obtained for particle E (Fig. 1H) and the control MNP (Fig. 1I)...... 158

Figure 5.2 Representative zeta potential test of bare MNP and A to E. Unpaired T test was performed and results were compared across groups for each two groups. Comparisons not shown were not statistically significant (* $p < 0.05$, ** $p < 0.01$, *** $p < 0.001$, data represents mean \pm 1 SD, $n = 3$). 159

Figure 5.3 The amount of adsorbed protein to all MNP systems (0.18 mg/mL MNP) was determined using a BCA assay. Repeated measures ANOVA were used for statistical analysis across groups (* represents $p < 0.01$, data represents mean \pm 1 SD, $n \geq 3$)..... 163

Figure 5.4 Representative immunoblot for fibrinogen eluted from MNPs incubated with (A) normal platelet poor plasma control and (B) uremic plasma. 169

Chapter 1

Introduction [1]

[1] A portion of this chapter was published as “Ma, Y., et al., Adsorption-based strategies for removing uremic toxins from blood. 2021. 319: p. 111035.”

Author List: Ma, Yuhao, Shuhui Li, Marcello Tonelli, and Larry D. Unsworth.*

Contribution: Ma, Yuhao wrote the manuscript, conducted literature review and data visualization. Shuhui Li conducted literature review, data visualization, manuscript editing. Marcello Tonelli reviewed and edited the manuscript. Larry D. Unsworth reviewed and edited the manuscript. Conceptualized and supervised the research.

1.1 Chronic Kidney Disease

Chronic kidney disease (CKD) is a prevalent medical condition with a global estimated prevalence of 13.4%. However, this estimate may vary, particularly in developing countries where the epidemiology of CKD is not fully characterized due to insufficient public health attention and investment [1]. The incidence of CKD is found to be more prevalent among individuals over the age of 65 years. Although males are reported to have a lower incidence of CKD compared to females, they possess higher chances of disease progression [2]. CKD is a complex medical condition characterized by heterogeneous functional and structural abnormalities of the kidneys. It is a slowly progressive disease that often remains asymptomatic until it has reached an advanced stage. The severity of CKD is determined by stages that are classified according to the reduction in kidney function, typically estimated by the glomerular filtration rate (GFR): stage 1 – more than 90 mL/min per 1.73 m², stage 2 – 60~89 mL/min per 1.73 m², stage 3 – 30~59 mL/min per 1.73 m², stage 4 – 15~29 mL/min per 1.73 m², stage 5 – less than 15 mL/min per 1.73 m² [3]. In the kidney biopsy, the common changes, such as tubular atrophy and interstitial fibrosis, are present in the samples from CKD patients. These structural deformations of the kidney impair its function, leading to a range of complications. The most prevalent underlying diseases associated with CKD include diabetes, hypertension, and anemia. Notably, a considerable proportion of diabetes patients, up to 30%-40%, develop CKD [1, 4]. Whereas in developing countries, infectious disease and drug misuse are account for the prevalence of CKD [5].

1.1.1 Treatment of CKD

Early intervention in the treatment of chronic kidney disease (CKD) can effectively slow its progression. The primary objective of early-stage treatment is to regulate the concentration levels of substances that may trigger complications, including vitamin D, blood sugar, and acid-

base balance. However, in the advanced stages of CKD, dialysis is necessary. Hemodialysis and peritoneal dialysis are two options available for patients. The cost of these treatments is significant, with annual expenses reaching \$77,506 and \$57,639 for hemodialysis and peritoneal dialysis, respectively [6]. Despite receiving dialysis treatment, the mortality rate among patients on dialysis remains high, with a rate of approximately 40%. The causes of death are grouped into six categories: cardiac, vascular, sudden death, infectious, withdrawal of dialysis, and other, in which cardiac deaths account for 14.4% of the death rate [7].

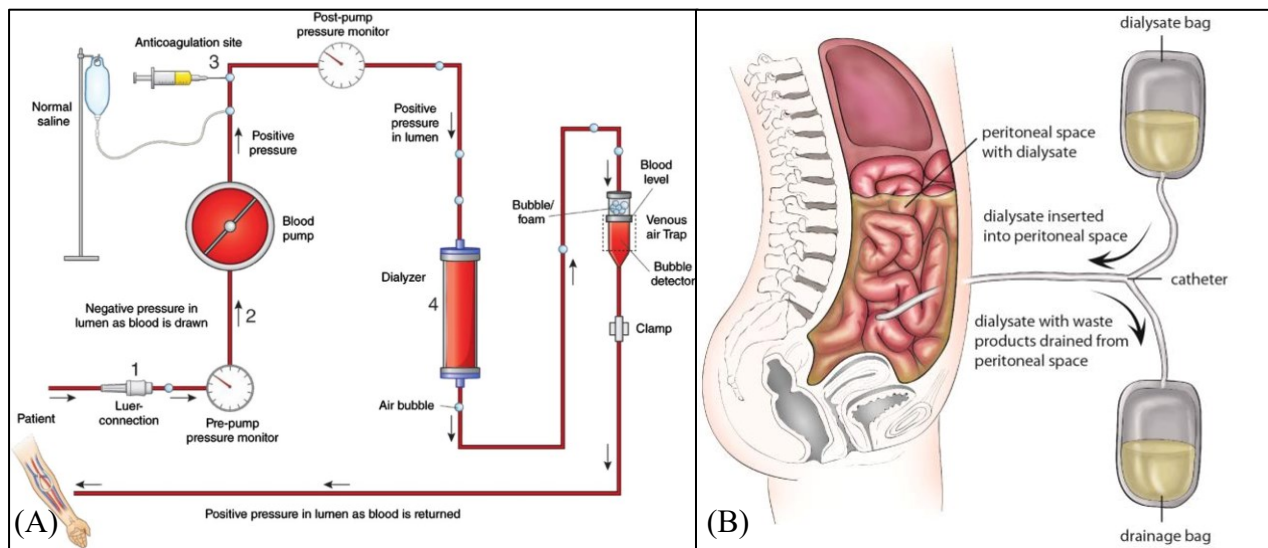


Figure 1.1 Schematically illustration of (A) Hemodialysis [8], (B) Peritoneal dialysis [9].

1.2 Uremic Toxins

Ever since Richard Bright first discovered urea and articulated its subsequent effects on kidney disease, research on uremia has been at the forefront of scientific investigation. The application of advanced techniques for the detection of organic molecules and isolation of toxic substances has led to a significant expansion in the characterization of uremic toxins. The number of known uremic toxins has increased from 32 in 2007 to 88 in 2012 [10, 11]. Uremic toxins are a

complex mixture of organic and inorganic substances that originate from various sources, including dietary intake and endogenous metabolic processes [12, 13]. Organic sources undergo the intestinal digestion and are transferred to liver by the portal circulation. Within the liver, the protein mediates undergo conjugation and sulfation, then excreted into the blood circulation. Once in the bloodstream, food metabolites, including urea from amino acid metabolism, ureic acid from nucleic acid metabolism, and creatine from muscle metabolism, merge with other metabolites. When blood fluid enters the kidneys, nephrons filter the blood, remove waste products and toxins, and screen the blood content for any abnormalities [14]. The quantification of uremic toxins holds substantial significance in clinical, as the deviant levels of these toxins are regarded as a pivotal clinical diagnostic indicator for the presence of disease.

1.2.1 Classification of Uremic Toxins

Uremic toxins are commonly classified into three distinct categories based on their physicochemical properties and molecular weight: free water-soluble low molecular weight solutes (<500 Da, N=45), protein-bound solutes (<500 Da except for leptin and retinol-binding proteins, N=25), and middle molecule solutes (N=22) [10]. Among the 88 uremic toxins, 68 possess a molecular weight of less than 500 Da while 12 exceed 120 kDa. The free water-soluble low molecular weight solutes category encompasses ribonucleosides, guanidines, polyols, peptides, purines, and pyridines. Protein-bound solutes consist of phenols, AGE, Hippurates, indoles, peptides, and polyamines. Peptides and cytokines are the primary components of the middle molecule solutes category [11].

1.2.2 The Association of Uremic Toxins with Disease

As stated previously, uremic toxins serve as an important indicator for abnormal metabolomic behavior within the human body, and their association with disease has been extensively investigated. While the level of creatinine and blood urea nitrogen tests is typically used to diagnose uremia directly, the presence of other diseases and complications, such as anemia, thrombosis, and cardiovascular disease, can also be induced by elevated serum uremic toxin levels [15, 16]. The elevated intracellular levels of reactive oxygen species (ROS) lead by the increasing concentration of uremic toxins played a role in resulting in these diseases and complications. The increasing concentration of uremic toxins can lead to elevated intracellular levels of reactive oxygen species (ROS), which play a role in the development of these diseases and complications [17]. Additionally, a link between elevated uremic toxins and depression is also reported by Heng-Jung Hsu et al [18].

1.2.3. Protein-Bound Uremic Toxins

Protein-bound uremic toxins (PBUTs) represent a subset of uremic toxins that tend to accumulate in the blood of patients with CKD and are not efficiently cleared by dialysis. The retention of PBUTs can result in toxic effects on various vital organs, including the heart, blood vessels, and kidneys themselves [19]. Among the 25 PBUTs that have been reported, as mentioned in section 1.2.1, phenols, indoles, and hippurates represent the non-peptide categories that contain a benzene ring and account for approximately 48% of the total number [11]. The remaining PBUTs consist of peptides, polyamines, and advanced glycation end products (AGEs) that possess relatively diverse structures and abundant electron clouds.

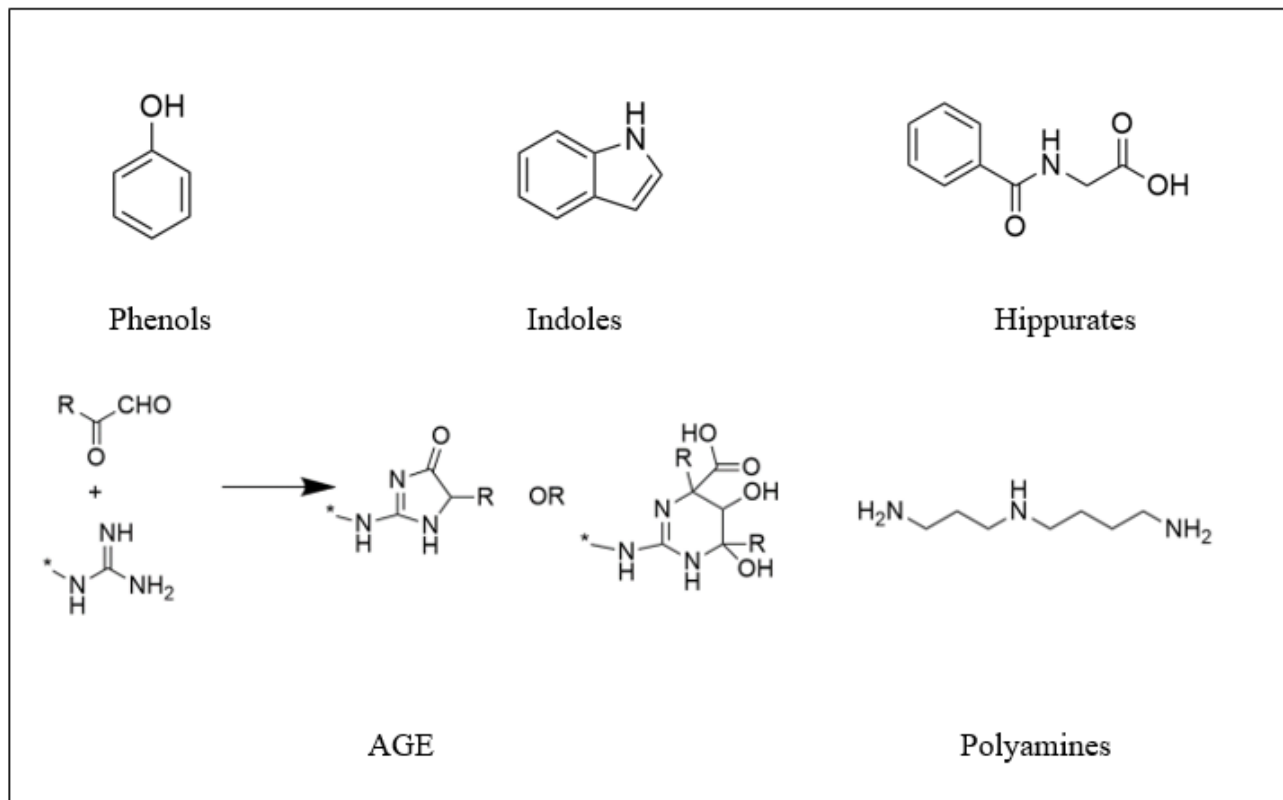


Figure 1.2 Chemical structure of categories of PBTUs.

1.3. Human Serum Albumin

1.3.1. Structure of Human serum albumin

Human serum albumin (HSA) is the most prevalent protein (35-50 g/L) in human blood serum and serves multiple functions, including the maintenance of oncotic pressure and the transport of nutrients. Composed of 585 amino acids, HSA displays a multi-domain structure that facilitates the binding of both endogenous and exogenous ligands. Within each molecule, the residues of cysteine, leucine, glutamic acid, and lysine outnumber methionine, glycine, and isoleucine, resulting in a high ion charge of 215 ions per HSA molecule and increased solubility. Moreover, HSA has 83 positively charged residues and 98 negatively charged residues, rendering

its surface charge negative. These features suggest that electrostatic forces may play a role in HSA binding activity.

1.3.2. Binding site on HSA

The unique sequence of amino acids in human serum albumin (HSA) leads to the formation of three homologous domains, which can be further subdivided into six helical subdomains (Figure 1.3): IA (5~112), IB (112-195), IIA (196~303), IIB (303~383), IIIA (384~500), IIIB (500~582) [20]. Numerous studies have been conducted to identify the type of ligands that bind to these different subdomains [21-27]. The study of HSA has a lengthy history, dating back to the precipitation of HSA from urine in 1500 A.D [28]. Native HSA has been extensively studied at first, and the advent of biosynthesized HSA in 1996 prompted research into modifications aimed at altering binding properties and conferring antigenicity [29]. Due to the greater structural flexibility of the HSA molecule surface compared to its core, and the fact that the excessive loading of ligands does not significantly alter the HSA structure, HSA is an ideal host molecule for studying ligand binding [30].

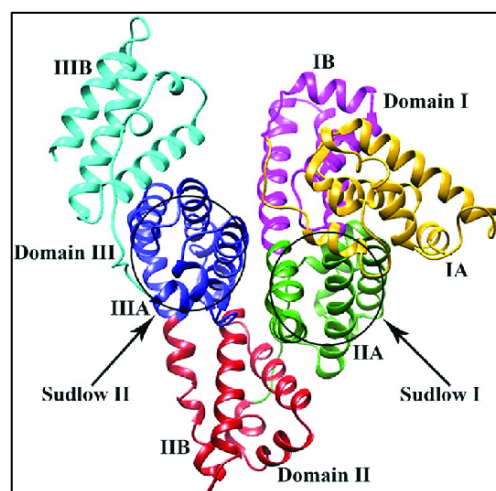


Figure 1.3 Illustration of domains, subdomains, and Sudlow's sites on HSA [31].

1.3.3. A close look to Sudlow's site I and Sudlow's site II

Intensive research is being done on Sudlow's site I (found at IIA) and Sudlow's site II (located at IIIA), two binding sites that bind to various ligands. Sudlow's site I is known as the seventh binding site for fatty acids. The amino acids of this site, Tyr150, Lys199, Arg222, and His242, endow this binding site with a hydrophobic core. Sudlow's site II contains the third and fourth fatty acid binding sites composed of residues Tyr411, Arg410, and Ser489. Aromatic carboxylates were proven to be the preferred ligands for this site, and the apolar region on the third fatty acid binding site is mainly responsible for the drug binding. Indoxyl sulfate, the PBUT associated with cardiac and vascular disease, binds to Sudlow's II [27]. Except for the hydrophobicity of the core, Sudlow's site I and II are positively charged and attractive to anions because of the existence of Lys and Arg residues. The Asp and Glu, which account for the negative charges, are not included in Sudlow's site I and II [32].

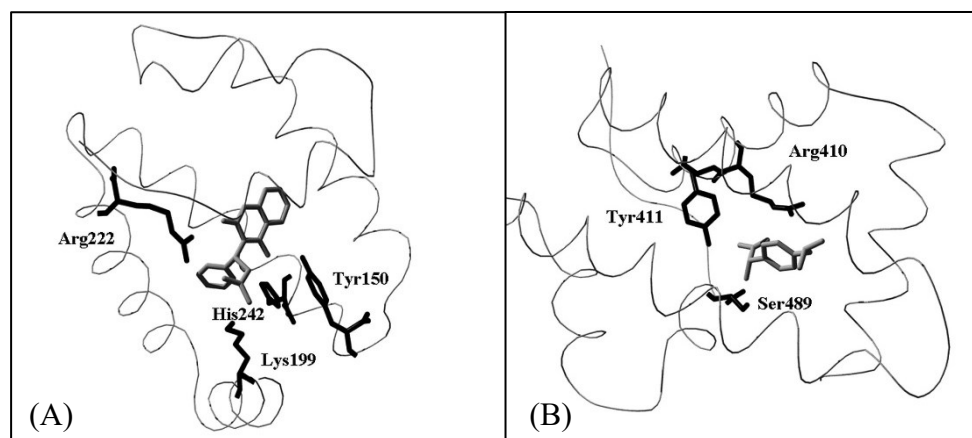


Figure 1.4 Illustration of (A) Sudlow's site I bind with warfarin and (B) Sudlow's site II bind with ibuprofen. Ligands are represented in grey [20].

1.4 Driving Forces Responsible for Ligands-HSA binding

Herein, I direct the attention toward three primary types of intermolecular interactions involved between ligands and HSA, namely, hydrophobic interactions, hydrogen bonding, and electrostatic interactions. The thermodynamic properties of non-covalent interactions can typically be assessed using the Gibbs free energy equation:

$$\Delta G = \Delta H - T\Delta S \quad (\text{Equation 1.1})$$

Where ΔG represents the Gibbs free energy change, ΔH represents the enthalpy change and ΔS is the entropy change. The interaction is spontaneous when ΔG is negative ($\Delta G < 0$). Enthalpy is defined by two components, internal energy and the product of pressure and volume of the system, where the internal energy of the system is comprised of bond energy and thermal energy. Negative ΔH represents the exothermic procedure. While entropy is dependent on temperature, molecular weight, and complexity of the substance. It is defined as heat transferred to the system (ΔQ) divided by system temperature:

$$\Delta S = \frac{\Delta Q}{T} \quad (\text{Equation 1.2})$$

1.4.1. Hydrophobic Interactions

Based on the examination of the chemical structures of the HSA binding sites as mentioned earlier, it can be inferred that the nonpolar residues of amino acids are responsible for the major component of each domain. This finding supports the notion that hydrophobic interactions play a significant role in facilitating the formation of ligand-HSA complexes [33, 34]. The specific type of interaction that occurs between ligands and HSA is influenced by the chemical composition of the ligands. For instance, a ligand lacking hydrogen bonding capability is more likely to induce hydrophobic interactions, while an aromatic compound with ring structures is more likely to induce pi-stacking under the desired conformation.

The strength of hydrophobic interaction can be quantified using calorimetry, which evaluates the free energy change resulting from enthalpy and entropy changes. At room temperature, hydrophobic interaction is typically considered entropy-driven due to the reduced mobility and entropy of water molecules on non-polar surfaces. This occurs when hydrophobic compounds are bound to a surface, which disrupts the water molecule shell surrounding the non-polar surface and releases water molecules with restricted mobility. As a result, the entropy of the system usually increases.

In hydrophobic interaction, positive ΔH and positive ΔS is usually observed, the release of restricted water molecules increased the entropy of the system as liberated water forms new hydrogen bonding with the surrounding water molecules, leading an increasing in internal energy. The increasing entropy is considered the cause of increasing enthalpy in this case, therefore called entropy-driven, but is that always the case in hydrophobic interaction? The addition of hydrophobic species to water leads to an increase in entropy that is proportional to the volume of water excluded by the hydrophobic species. During this process, hydrogen bonds are reorganized without breaking, resulting in a minor change in enthalpy. However, when a large hydrophobic cluster is formed, hydrogen bonds are broken to accommodate the hydrophobic species, leading to an increase in enthalpy that is proportional to the surface area of the cluster. Therefore, the accumulation and aggregation of hydrophobic species can transform the hydrophobic interaction from an entropy-driven process to an enthalpy-driven process. This explained why positive ΔH and positive ΔS are usually observed. However, it is important to note that other combinations of ΔH and ΔS are also possible.

1.4.2. Electrostatic Interaction

In addition to hydrophobic interaction, electrostatic interaction participates in the ligand-HSA complex formation. As stated above, the distribution of amino acid residues in HSA leads to negatively charged regions, with Sudlow's site being a prominent example, making electrostatic interactions highly relevant for ligand binding. Electrostatic interaction is a large family, including hydrogen bonding, ionic interaction, and Van der Waals forces. While hydrophobic interaction and Van der Waals forces are responsible for most nonspecific interactions, specific interactions are dominated by electrostatic forces [35]. The strength of electrostatic interaction is influenced by various factors, such as the ionic strength of the solvent, pH, chemical reactivity, and biological activity [36]. These factors can be broadly categorized into two groups: medium properties and compound properties. The underlying mechanisms of these factors affecting electrostatic force can be explained through Coulomb's law and the Van der Waals force equation:

$$F_{VdW}(Z) = -\frac{A}{6} \frac{64R_1^3R_2^3z}{[Z^2-(R_1+R_2)^2]^2[Z^2-(R_1-R_2)^2]^2} \quad (\text{Equation 1.3})$$

$$|F_e| = k_e \frac{|q_1||q_2|}{r^2} \quad (\text{Equation 1.4})$$

Where F_{VdW} is Van Der Waals force, A is the Hamaker coefficient, which is a constant ($\sim 10^{-19} - 10^{-20}$ J) that depends on the material properties and intervening medium. z is the center-to-center distance. R_1 and R_2 represent the radii of spherical bodies. F_e is the electrostatic force and k_e is Coulomb's constant ($k_e \approx 8.988 \times 10^9 \text{ N} \cdot \text{m}^2 \cdot \text{C}^{-2}$). q_1, q_2 and r are the charges and the distance between the charges. When two charged particles approach each other in colloids, their stability is influenced by both Van Der Waals force and electrostatic force. To describe this interplay, the DLVO theory has been established. However, the assumption made in the DLVO theory that the

surface of particles is uniformly charged may limit its applicability in portraying the ligands-HSA interaction process.

Hydrogen bonding is also a subset of electrostatic interaction owing to the dipole-dipole attraction between the highly electronegative oxygen, nitrogen, sulfur, or fluorine atom and a partially positive hydrogen atom. However, its behavior is more characteristic of charge-dipole interaction. The electron distribution of the "donor" and "acceptor" atoms is believed to play a role, although the underlying reasons are not yet fully understood. In the case where the donor and acceptor are located in the same molecule, the hydrogen atom acts as the acceptor, while the electronegative moiety serves as the donor. Despite the absence of a covalent bond, the strength of hydrogen bonding is typically greater than that of Van Der Waals force, ranging from 4 KJ to 50 KJ per mole of hydrogen bonds [37]. The distribution of various amino acid residues allows HSA to be a natural "donor-acceptor" complex that maintains protein folding and stability.

1.4.3. Current Methodology for Assessing Binding Mechanisms

Techniques that are being used in detecting macromolecules interaction are developed based on various mechanisms. Surface plasmon resonance (SPR) and UV-Vis spectroscopy (UV-Vis) are used to detect optical properties changes such as reflective index and absorbance in order to calculate the association constant. Nuclear magnetic resonance (NMR) can also be used to capture the chemical shift of residues within the interacted molecules and then demonstrate the association constant [38]. Analytical ultracentrifugation (AUC) adopts gravity as the tool to separate bounded and unbounded molecules and determines the association constant by investigating the association state and equilibrium constant [39]. Isothermal titration calorimetry (ITC) is another technique that can directly capture the heat fluctuation and generate a complete thermodynamic profile including enthalpy, entropy, Gibbs free energy, number of binding sites,

and affinity. A detailed comparison of the advantages and disadvantages of these techniques has been recently published [40].

1.4.4. Mechanism of ITC

As described earlier, ITC quantifies the heat produced or consumed during a physical or chemical reaction. In order to achieve this goal, an ITC instrument has a reference and the sample cell. The reference cell is utilized to balance the heat generated or absorbed by the sample cell. In order to keep the consistency of the heat capacity in both cells, degassed water is typically injected as the reference fluid instead of the buffer for cleaning consideration. The addition of salt in buffer solutions typically decreases the heat capacity, but this effect is negligible as the salt concentration in buffer solutions is usually low (20 mM-50 mM). During an ITC experiment, small aliquots of titrant are gradually titrated into the sample cell through a syringe. The introduction of the titrant causes a disturbance in the thermal equilibrium between the two cells. A feedback circuit detects the resulting heat changes and adjusts the thermal equilibrium by producing or consuming heat to eliminate the heat difference. The amount of heat applied is monitored and recorded during the experiment. ITC data is further analyzed using the first law of thermodynamics:

$$\Delta U = Q - W \quad (\text{Equation 1.5})$$

Where U is the internal energy of the system, Q denotes the heat that are transferred to the system and W is the amount of thermal dynamics work done by the system on the surrounding. The system is defined as the composition of the sample cell and the reference cell (Figure 1.5). No energy is transferred from the system to the surrounding; therefore, no work is done by the system to the surrounding, leading to $\Delta U = Q$. By combining equation 1.5 with the following equation, the association constant K_a is obtained:

$$\Delta G = RT \ln K_a \quad (\text{Equation 1.6})$$

As the binding process of ligands to protein is dynamic and reversible, the determination of concentration played an important role here. The relationship between the concentration of host and ligands should fit into a theoretical “c-window” in order to obtain the analyzable data, meaning either ligands or host is consumed up and no further binding heat is generated. It is acceptable when c-window is $1 < c < 1000$, and $5 < c < 500$ is considered ideal. The c-window is described by the following equation 1.7, where n represents the number of ligands binds to the host molecule, K_d is the disassociation:

$$c = nK_d[\text{titrand}] = n[\text{titrand}]/K_d \quad (\text{Equation 1.7})$$

When processing data, the raw heat signal is fitted in a selected model chosen based on the number of binding sites. The independent binding site model is usually chosen to analyze the raw data in this research as the binding sites on HSA possess different affinity and are considered unique.

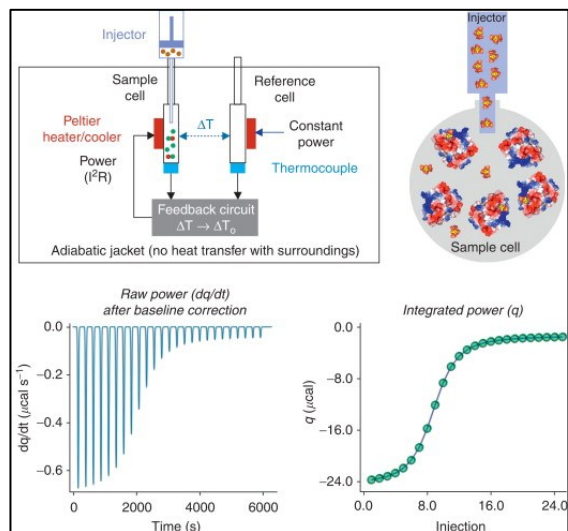


Figure 1.5 Scheme of an isothermal titration calorimetry and the typical data set (Copyright 2012 by D.G. Lambright) [41].

1.5. Overview of Polymer Adsorbents in Uremic Toxins Removal

In general, three strategies are commonly adopted in renal failure management using polymer-assisted technologies (Figure 1.6). Dialysis membrane, which operates based on concentration gradients, has traditionally relied on pore size selection as the primary mechanism. As a result, much research in dialysis materials has focused on controlling pore sizes of various polymers. Another types of UTX remover are adsorbent in either beads or membrane state, which are often applied to adsorption cassettes with the beads fitted into columns to assist in toxin adsorption or adopted as a extra layer to the traditional dialysis membrane [42]. The advantage of polymer is self-evident by being used in enormous industries. The flexibility of polymer enables the production of various forms, including membrane, resin, gel, and liquid. The surface chemistry and copolymerization capability of polymers offer a great potential for modification according to specific requirements. Current functional polymer materials applied in UTX removal can be categorized into pure polymer, molecular imprinted polymer, mix matrix membrane, and polymer coated beads. In this section, I will review polymer-assisted UTX removal methods to provide insights for future polymer-based materials development. A summary of current polymer-based adsorbents for uremic toxins removal is presented in Table 1.1.

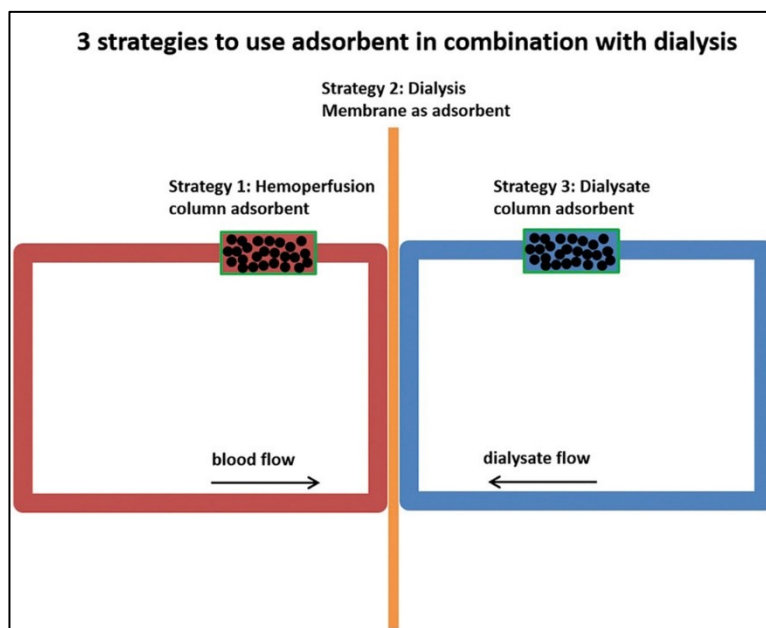


Figure 1.6 Three adsorbent strategies used for removal UTX [43].

1.5.1. Pure Polymer and Polymer Coated Adsorbent

Pure polymer and polymer coated adsorbent have two mechanisms that assist in UTX removal. Apart from pore size selection, the chemical property of the monomer also determines the mechanisms of adsorption. Even for the same ligands, the adsorption capacity of the adsorbent can vary significantly depending on the polymer composition. For example, polyamide membrane, poly(acrylonitrile) membrane, and polysulfone membrane are three types of polymers developed to adsorb p-cresol, among which the polysulfone exhibits superior adsorption capability towards p-cresol [44]. This can be attributed to multiple interactions occurring between the p-cresol and sulfone. The sulfone contains S=O bonds, enabling electrostatic interactions, and benzo groups that facilitate $\pi - \pi$ stacking (as depicted in Figure 1.7). Similarly, the selection of the polymer-coated adsorbent follows the same principle. Materials with a large surface area, such as activated carbon, zeolite, and silica, are commonly used as the core of polymer-coated adsorbents to accommodate

polymer deposition. The combined advantages of polymer composite and core structure have addressed one of the drawbacks of polymer materials, namely, their uncontrollable shape.

In recent years, extensive research has been conducted to overcome the limitations of polymers. One of the drawbacks, uneven pore size, has been addressed by the development of novel manufacturing processes. Guo et al. proposed the use of crystallization-driven phase separation methods to achieve precise control over the pore size of porous films of poly(3-hexylthiophene) based on specific requirements. This approach has proven successful in producing films with controlled pore size and morphology, which is essential for various applications, including filtration, separation, and catalysis [45]. In the meanwhile, Sáfrány et al. developed a γ -radiation-initiated synthesis routine and obtained monoliths with the same chemical structure in various sizes, shapes, and porous characteristics. Another limitation of polymers is their limited hemocompatibility. To overcome this problem, researchers have developed biomimetic and bioinspired materials that are more biocompatible than traditional bioinert materials. Factors that affect the biocompatibility of polymer materials include surface composition (functional groups and density/sign of charge), surface degradation, hydrophilic-hydrophobic character, wettability and surface free energy, topography (roughness, stiffness), and competitive protein binding. Among various biocompatible polymer candidates, zwitterions have gained significant attention due to their unique water shield formed by the opposite charges. When removing uremic toxins, the abundance of proteins and cells in the environment can lead to unfavorable interactions, making zwitterions an excellent copolymer component for performing the anti-fouling function [46].

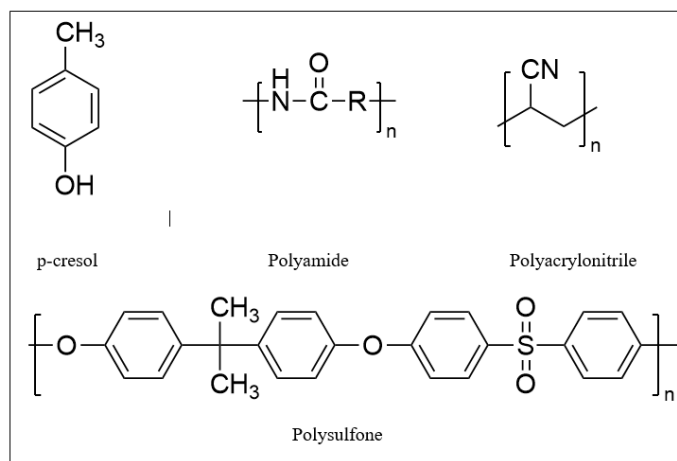


Figure 1.7 Representative chemical structure of p-cresol, polyamide, polyacrylonitrile, and polysulfone.

1.5.2. Molecular imprinted polymer (MIP)

MIPs have demonstrated great potential in addressing specific adsorption and have been utilized in biosensor development and adsorbent applications. The MIPs function by positioning the template molecules during polymerization, resulting in the formation of a polymer with customized pore sizes. Upon removal of the template, the MIP can selectively reabsorb the template molecules to the specific pocket through non-covalent or reversible covalent interactions [47]. In the field of uremic toxin removal, creatinine imprinted polymers have shown promise. Syu et al. developed a creatinine imprinted polymer using β -Cyclodextrin (β -CD) as the monomer and epichlorohydrin as the crosslinker. In competitive binding experiments with creatinine, N-hydroxysuccinimide, and 2-pyrrolidinone, the creatinine imprinted polymer exhibited a superior removal rate for creatinine compared to other solutes, indicating specific binding [48]. Even though MIP possess high specific binding pocket for template, the removal rate of MIP is not as desired as other adsorbent due to the limited accessibility of the pocket. Moreover, the MIP using proteins or protein-bound uremic toxins as the template is seldom synthesized even though the proteins and

protein-bound uremic toxins are recognized as an important party of uremic toxins. The reason is believed to be the flexible structures of protein disabled the size selection of the pocket and the complex adsorption environment reduced the capability of specific binding [49].

1.5.3. Mixed matrix membrane (MMM)

MMM is a type of material that integrates both diffusion and adsorption mechanisms for efficient removal of organic molecules. Typically, a ternary system is employed, with the adsorbent incorporated into the microporous matrix and then covered by an additional layer of polymer coating that provides hemocompatibility. The representative application of MMM in UTX removal is developed by Dimitrio's group, where three generations of poly(ethersulfone)/poly(vinylpyrrolidone) dual-layer hollow fibers have been developed for the removal of protein-bound uremic toxins. After the improvement of successive generation, the flux rate is improved while protein adsorption is decreased. MMM3 now exhibit an great ability to remove indoxyl sulfate, p-cresol sulfate and hippuric acid [50-52]. However, for what is worth mentioning, the blood flow passes through the hemocompatibility layer prior to reaching the adsorbent embedded layer. This arrangement can hinder the passage of protein-bound uremic toxins through the membrane, thereby limiting their removal, compromising the efficacy of the treatment, and increasing the likelihood of complications arising from the accumulation of PBUTs during clinical application.

Table 1.1 Summary of *in vitro* research using adsorbent for removal of uremic toxins.

Adsorbent type	Suitable strategy ¹	Uremic toxins	Maximum removal capacity in amount of adsorbed toxin/per gram or square meter of adsorbent (Initial toxin concentration, Medium)	Ref
Polymer				
polyamide membrane	2	<i>p</i> -cresol	21 mg/g (22 mg/l, PBS)	[44]
polyacrylonitrile membrane	2	<i>p</i> -cresol	0.3 mg/g (22 mg/l, PBS)	[44]
polysulfone membrane	2	<i>p</i> -cresol	37.3 mg/g (22 mg/l, PBS)	[44]
urease-immobilized polyethersulfone beads	1,3	urea	75.1 mg/g (800 mg/l, water)	[53]
polysulfone-poly(methyl methacrylate) dual layer hollow fiber	1,3	urea	27.6 mg/g (2500 mg/l, water)	[54]
polystyrene column	1	β_2 -microglobulin (β_2M)	1.3 mg/g (63.5 mg/l, PBS)	[55]
seed-conjugated polymer Beads	1	β_2 -microglobulin (β_2M)	7.3 mg/g (440 mg/l, PBS)	[56]
poly(cyclodextrins)	1	indoxyl sulfate	45 mg/g (780 mg/l, PBS)	[57]
oxidized poly(vinylindanone) beads with ninhydrin groups	1,3	urea	192 mg/g (1800 mg/l, PBS)	[58]
poly(carboxybetaine) (PCB) coated polystyrene resin (H103) microparticles	1	bilirubin	20.75 mg/g (150 mg/l, BSA solution) 6.59 mg/g (150 mg/l, 100% FBS)	[59]
CaCO ₃ nanoparticle/polystyrene composite	1	interleukin-6	25.6 ng/g (1000 ng/l, human plasma)	[60]
carbonylated hypercrosslinked chloromethylated poly(styrene-co-divinylbenzene)	1	<i>p</i> -cresol	141.5 mg/g (100 mg/l, NaCl solution)	[61]
Molecularly imprinted polymer (MIP)				

creatinine-imprinted poly(β -cyclodextrin)	3	creatinine	6 mg/g (180 mg/l, PB)	[48]
creatinine-imprinted poly (tetraethoxysilanol) sol-gel	3	creatinine	0.8 mg/g (100 mg/l, water)	[62]
uric acid-imprinted poly(acrylamide-hydroxyethyl methacrylate) p(AAm-MMA) cryogel	3	uric acid	687.6 mg/g (40 mg/l, water) 148.6-186.6 mg/g (35 mg/l, human serum)	[63]
Mixed matrix membrane (MMM)				
cellulose acetate matrix	2	Creatinine indoxyl sulfate	25 mg/g membrane (12-136 mg/l, water) 13 mg/g membrane (53-247 mg/l, water)	[64]
poly(ethersulfone)/poly(vinylpyrrolidone) dual layer hollow fiber (MMM1)	2	Creatinine indoxyl sulfate <i>p</i> -cresyl sulfate hippuric acid	2825 mg/m ² (136 mg/l, human plasma) 255 mg/m ² , or 12.85 mg/g membrane (247 mg/l, human plasma) 160 mg/m ² , or 2.68 mg/g membrane (uremic concentrations, human plasma) 784 mg/m ² (471 mg/l, human plasma)	[50]
poly(ethersulfone)/poly(vinylpyrrolidone) dual layer hollow fiber (MMM2)	2	Creatinine indoxyl sulfate <i>p</i> -cresyl sulfate	2549 mg/m ² (100 mg/l, PBS) 367 mg/m ² (40 mg/l, human plasma) 380 mg/m ² (40 mg/l, human plasma)	[51]
poly(ethersulfone)/poly(vinylpyrrolidone) dual layer hollow fiber (MMM3)	2	indoxyl sulfate hippuric acid	500 mg/m ² (40 mg/l, human plasma) 2478 mg/m ² (110 mg/l, human plasma)	[52]

heparin-mimicking polymers grafted carbon nanotube/poly(ethersulfone) composite membrane	2	creatinine	1.4 mg/g membrane (50 mg/l, PBS)	[65]
polyethersulfone matrix	2	<i>p</i> -cresol	108.7 mg/g membrane (400 mg/l, PB)	[66]
		creatinine	133.3 mg/g membrane (700 mg/l, PB)	
Polymer coated adsorbent				
zwitterionic poly-carboxybetaine (PCB) hydrogel coating	1	bilirubin	8 mg/g (150 mg/l, BSA solution)	[46]
poly (hydroxyethyl methacrylate) coating	1,3	creatinine	10 mg/g (20 mg/l, PBS)	[67]
poly (hydroxyethyl methacrylate) coating	1,3	creatinine	175 mg/g (100 mg/l, PB)	[68]
4% poly (vinylidene chloride/vinyl chloride) coating	3	creatinine	2.5 mg/g (100 mg/l, PBS)	[69]
polyvinylpyrrolidone coating	1	phenylacetic acid	38.9 mg/g (474 mg/l, BSA solution)	[70]
poly (ether sulfone)/activated carbon (PES-AC) hybrid beads	1,3	creatinine	87 mg/g (500 mg/l, Tyrode buffer)	[71]
poly (ethylene-co-vinyl alcohol) (EVOH)-zeolite-polymer composite nanofibers	3	creatinine	25 mg/g (22 mg/l, water)	[72]
polyacrylonitrile (PAN)-zeolite composite nanofiber	3	creatinine	880 mg/m ² (23 mg/l, water)	[73]
zeolites and polyethersulfone-zeolite composite membranes	2	indoxyl sulfate	1.3 mg/g (35 mg/l, PBS)	[74]

1.6 Cyclodextrin (CD)

Cyclodextrins are a group of edible functional materials that have been commercialized as small molecular encapsulation agents in various applications, such as wastewater treatment, odor control, food stabilization, drug delivery, and the manufacturing of chromatography columns [75-78]. α -, β -, and γ -CD are the most common cyclodextrin that contained 6, 7, and 8 glucose units, respectively. Since the middle of the 20th century, cyclodextrins have been used as auxiliary substances to boost the solubility of drugs with poor solubility [79]. The cyclic oligosaccharide structure of cyclodextrins enabled the core with a relative hydrophobicity compared to its hydrophilic outer surface [80]. Due to the existence of the hydrophobic cavity and resourceful hydroxyl groups in CD molecules, hydrophobic interaction and hydrogen bonding are considered the possible driving force when suitable ligands are introduced. In each CD molecule, the free electron pairs of glycosidic oxygen are positioned directly towards the cavity, creating a high local electron density at the core. This not only endows the CD with the characteristic of Lewis base but also indicates the greater chemistry reactivity of the primary hydroxyl groups compared to the secondary hydroxyl groups [81]. Indeed, the modification of primary hydroxyl group on β -CD is wildly practiced in order to generate derivatives that can meet certain needs [82-84].

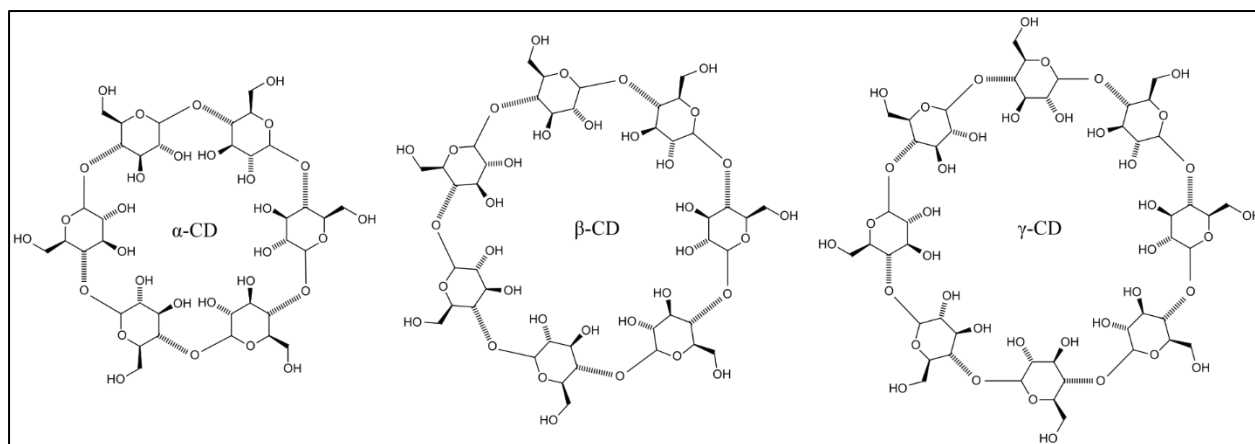


Figure 1.8 Chemistry structure of α -, β -, and γ -CD.

1.6.1 Cyclodextrin Polymers

Polymerization techniques have boosted the development of technology in countless areas. Utilizing the functional materials as monomers further enhanced the application of polymerization technique. To date, mainly four types of CD polymers are designed to serve the needs, which are crosslinked CDs, linear-linked CDs, CD star polymers, and CD polyrotaxanes (Figure 1.9).

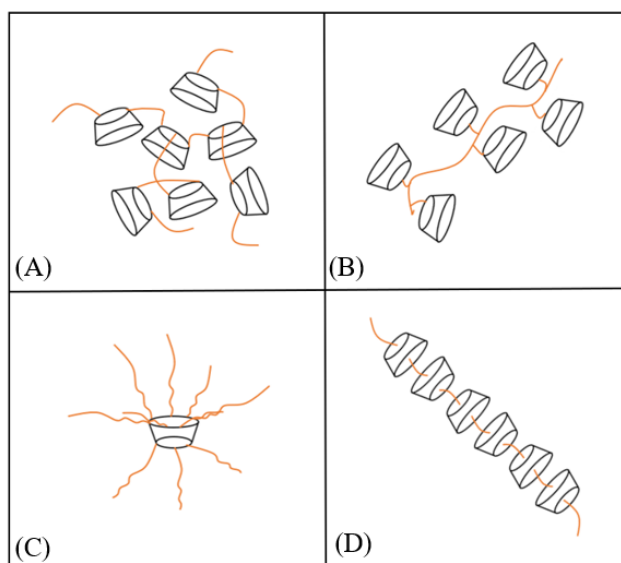


Figure 1.9 Illustration of types of cyclodextrin polymers.

1.6.1.1 Crosslinked Cyclodextrin Polymers

Crosslinked CDs are usually synthesized through the method of cross-linking of primary hydroxyl groups. The principal synthesis route for cyclodextrin crosslinking involves chloride substitution and hydroxyl-epoxy addition. This material is particularly suitable for organic multipollutant absorption and exhibits a performance 15-200 times greater than that of both activated carbon and non-porous cyclodextrin polymers [85]. This is accredited to the supercritical liquid CO₂-assisted drying process that produced a high surface area by removing surface tension [86]. Nanosponges represent a type of nanoparticle gel that has garnered significant research attention for drug delivery applications. In this context, beta-CD-based nanosponges have been developed by Elham et al. for curcumin delivery, aiming to enhance the pharmacokinetic profile, anticancer activity, and solubility of curcumin. Epiclone was adopted to crosslink with beta-CD in a ratio of 1:8 and resulting in the average 31.35% w/w curcumin load rate. The introduction of cyclodextrin nanosponge improved the selective toxicity against malignant cells, while also minimizing the adverse effects of curcumin on tissue [87]. CD-based metal-organic frameworks are also researched. However, due to the fact that the crosslinking is achieved through physical positioning as opposed to chemical bonding, the application is constrained by utilization conditions and is viewed as lacking practical potential.

1.6.1.2 Linear-linked Cyclodextrin Polymers

Linear-linked cyclodextrin polymers are distinct from crosslinked cyclodextrin polymers in that each monomer only has one main hydroxyl modification. These linear polymers are either attached to the surface or form the self-assembled hydrogels/supramolecules in order to serve different functional demands. Before polymerization, CDs are commonly decorated with p-

toluenesulfonyl chloride group as a leaving group. This step enabled the further add-on of the functional groups for polymerization [88, 89]. Nanoparticles (NP) of various diameters are commonly utilized in CD polymer fixation due to their high surface area. Ali et. al synthesised recyclable β -CD polymers grafted magnetic nanoparticles (MNP) for benzyl halides inclusion in an aqueous solution for the purpose of catalyzing solid-liquid phase-transition [90]. Yuan et. al reported a voltage-responsive dextran- β -CD polymer micelle for controlling drug release. Ferrocene terminated poly(ϵ -caprolactone) molecules bind to the hydrophobic cavity of dextran- β -CD polymer and self-assembled as micelle in the drug solution. Under the voltage of +1.0 V, the micelle is disassembled and released the ferrocene-terminated poly(ϵ -caprolactone) that is loaded with drugs [91].

1.6.1.3 Cyclodextrin Star Polymers

In this instance, the hydrophobic core was used to fulfill various functional requirements, such as the encapsulation of ligands, while the polymer arms developed on the primary and secondary faces of the CD molecule to serve antifouling function [92, 93]. The fact that CD contains abundant hydroxyl groups made CD an ideal chemistry reaction initiator. For example, hydroxyl groups can initiate the ring-opening polymerization of cyclic lactones, substitution reaction for chloride/bromide atomic transfer radical polymerization (ATRP) initiator fixation, and reversible addition-fragmentation chain-transfer (RAFT) polymerization [94-97]. Martina et. al successfully synthesized star polymer with β -CD core through RAFT reaction at 100 °C-120 °C using the native hydroxyl group as the initiator. The molecular weight is determined using gel permeation chromatography (GPC) and exhibited an overall lower value compared to the theoretical value, which might be resulted from the steric hindrance [98]. CD Star Polymer can

also be used to tackle the drug resistance problem. Clinical trials pointed out that drug resistance in malignant treatment forces patients to seek alternative drugs or even apply multiple drugs that worsen the impairing effect of chemotherapy. Fan et. al designed a novel “V”-shaped armed β -CD star polymer that is composed of poly(N-isopropylacrylamide) (PNIPAAm) and biocompatible poly(ethylene glycol) (PEG). The drug inclusion is not only induced by the hydrophobic core of the β -CD cavity, the association of the “V” shaped polymer chain has also accelerated the process. Moreover, the anti-fouling and biocompatible properties of the PEG segment also stabilized the inclusion state and further improved intracellular retention and drug delivery efficiency. In vivo study shows the largest reduced tumor volume in the group using β -CD-g-(PEG-v-PNIPAAm) ($84 \text{ mm}^3 \pm 69 \text{ mm}^3$) compared to the control ($391 \text{ mm}^3 \pm 154 \text{ mm}^3$) [92].

1.6.1.4 Cyclodextrin polyrotaxanes

The native CD polyrotaxanes is a necklace-like supramolecule that is seldom used in application owing to its high steric hindrance and strong hydrogen bonds between the neighbor CD molecules. Due to the same reason, the CD polyrotaxanes only dissolve in DMSO and DMF in which the hydrogen bond between the neighboring molecules is destroyed [99-101]. Consequently, researchers explored multiple modification schemes to improve the solubility of CD polyrotaxanes, in which methylation of the hydroxyl group is considered the easiest route. The decoration groups have evolved from simple groups, such as hydroxypropyl group and carboxyethyl ether group, to functional polymer chains. A bio-cleavable hydroxypropyl- β -CD (HP- β -CD) based polyrotaxanes is designed by Tamura et. al aiming at capturing cholesterol. After PEG threaded the CD units, terminal bulky molecules are further added through disulfide linkages. Disulfide linkages are cleaved when encountered L-glutathione in the intracellular environment and enabled the release of CD to capture cholesterol [102]. As mentioned above, the hydrogen bond between neighboring

CDs resulted in reduced solubility as fewer hydroxyl groups are available for forming hydrogen bonds with water molecules. Wang et. al utilized this property to crosslinked multiple α -CD polyrotaxanes using CD itself as a crosslinker and synthesized porous hydrogel for bioengineering applications [103].

1.6.2 β -Cyclodextrin

β CD is the most utilized cyclodextrin due to its ideal core size to form drug complex even though it is the least soluble cyclodextrin among α -, β -, and γ -CD. The elucidation of this poor solubility is the molecular rigidity of β CD and the formation of intramolecular hydrogen bonding in the crystal state. The complete secondary belt was formed by C2-OH and C3-OH which reduced the flexibility of β CD. 21 hydroxyl groups are categorized into primary groups and secondary groups, each containing 7 and 14 hydroxyls [83].

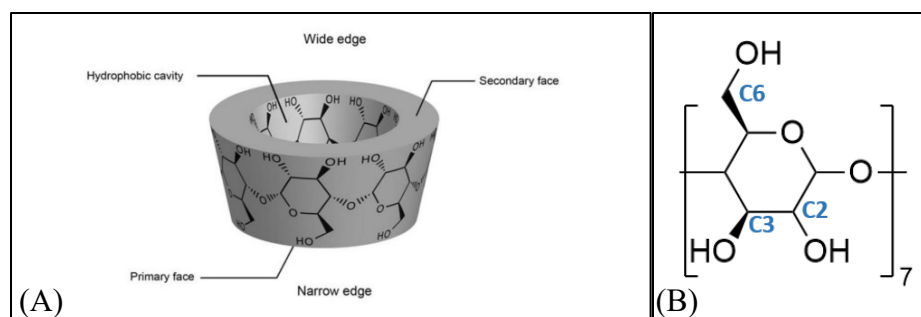


Figure 1.10 Structural illustration of β CD. (A) The primary hydroxyl groups composed primary face, the secondary hydroxyl groups composed secondary face [104]. (B) Illustration of C2, C3, C6 on each glucose unit.

1.7 Magnetic Nanoparticle Technology

Nanoparticle technology starts growing public attention in the early 2000s. It contributes to multiple scientific areas including chemistry, biology, materials science, and engineering. The most recent application of NPs has been expanded to human health. The promising results of NP-involved research implied the commercial value of NP-based treatment methods. The Greek prefix ‘nano’ depicts one thousand millionth of a meter (10^{-9}). NPs refer to particles with a diameter between 1 and 100 nm. The history of NP application can be traced back to the fourth century AD when Au and Ag nanoparticles were first applied to ancient glass artwork. The invention of various microscopies, such as transmission electron microscopy (TEM) and scanning probe microscopes (SPM), visualized the NPs and expanded the research scope of NP.

The combination of polymer science and nanoparticles is considered the highlight of materials science in recent years. The superior biocompatibility and cost-efficiency of NP make it an ideal candidate for in vivo application. Magnetic NP (MNP) is widely used in the biomedical areas due to the property of controlled positioning, surface functional potential, and biocompatibility. The naturally formed hydroxyl groups on the MNP surface enabled the decoration of polymers. Polymer-coated MNP has been used in cancer diagnosis and therapy, selective extraction, sensor probe invention, and drug carrier. Abolfazl et. al synthesized poly (N-isopropylacrylamide-methyl methacrylic acid, PNIPAAm-MAA)-grafted MNP (core size: 100nm) for controlled delivery of doxorubicin and evaluated the cytotoxicity and uptake rate of the A549 lung cancer cell line. (PNIPAAm-MAA)-grafted MNP exhibit the drug inclusion efficiency of 75%. In the targeted area, the drug release is controlled to be 43% in 200 hrs under 37 °C [105]. Born from a similar concept, reusable ligand absorbents are designed to perform the “reverse delivery”. Fei et. al developed the acrylic acid and crotonic acid copolymerized MNP for absorbing cationic dyes through the mechanisms of ionic interaction and hydrophobic interaction. The clearance rate

of 90% was achieved within 4 hrs. The recycling of used absorbent is accomplished by the desorption of dyes using a 50 ml mixture of 5% (V/V) acetic acid and methanol [106].

1.8 Research Proposal

1.8.1 Rationale

The complex nature of ligands-host interaction makes it harder to determine the binding driving force. However, the binding driving force determination is of great importance to designing a proper host for ligands capture purposes. Prior to designing the host of PBUT, it is necessary to articulate the interaction mechanisms in PBUT- HSA system. To further develop the ideal host molecule, surface chemistry should be considered other than functionality design as it profoundly impacts the efficiency of the host-guest system as well as the blood cell behavior and hemocompatibility. This thesis will investigate the PBUT-HSA system and UTX-CD system using the combined technology of isothermal titration calorimetry, LC/MS, and other characteristic methods. p-cresol sulfate and indoxyl sulfate are chosen to represent PBUT in this research as they hasten the stages of CKD by inducing multiple complications, thus the clearance of them is of great importance and well-spread researched. However, no profound interpretation of binding driving force and binding conformation has been reported. With that in mind, herein we present the investigation of PBUT-HSA system to improve the current understanding of the binding mechanism and enlighten the following design - a cyclodextrin-based host-guest system that assists in the removal of UTX. This project will definitely expand the understanding of the driving force in PBUT-HSA system and leads to the future development of bioengineering materials for uremic toxins removal.

1.8.2. Objectives

This thesis is synthesised for the purpose of answering the following questions:

1. What is the driving force of p-cresol sulfate and indoxyl sulfate binding with HSA?
(Chapter 2)
 - a. Why does the thermodynamic data of p-cresol sulfate and indoxyl sulfate binding with HSA exhibit such a pattern?
 - b. What is the quenching mechanism of p-cresol sulfate and indoxyl sulfate to HSA?
2. How does the binding of p-cresol sulfate and indoxyl sulfate to HSA influence the HSA conformational structure? (Chapter 2)
 - a. Is p-cresol sulfate and indoxyl sulfate binds to totally different sites?
 - b. what is the conformation of p-cresol sulfate and indoxyl sulfate in the binding sites?
3. What is the characteristics and functionality of the novel CD-based polymer-coated magnetic nanoparticles? (Chapter 3, Chapter4 and Chapter 5)
 - a. What are the chemical and physical properties of the novel CD-based polymer-coated magnetic nanoparticles and their efficiency in binding uremic toxins?
 - b. What is the biocompatibility of CD polymer, zwitterion polymer, and the CD-zwitterion hybrid polymer under the presence/absence of uremic toxins? What ratio of copolymerization represents the best application value?
 - c. What is the cyclodextrin selection binding pattern in a profile of uremic toxins?
Does it have preferred chemical groups to bind?
4. How will the zwitterion in the polymer chain influence the bounded type of uremic toxins and the uremic toxins bound rate overall? (Chapter 3)

1.8.3 Scope of Dissertation

In the following chapter, the driving force of indoxyl sulfate and p-cresol sulfate will be thermodynamically investigated. In order to evaluate the overall influence of indoxyl sulfate and p-cresol sulfate on HSA, other binding features should be studied as well. The binding conformation, HSA quenching mechanism, and HSA secondary and tertiary structures will be systematically assessed. For the purpose of determining the quenching mechanism, experiment should be performed at a variant temperature in order to obtain the association constant that is comparable to the ITC yield association constant. Furthermore, the competitive binding of indoxyl sulfate and p-cresol sulfate on Sudlow's site I and II should be investigated to identify the precise binding sites of these two toxins, and the binding conformation of indoxyl sulfate and p-cresol sulfate in the pocket should be articulated to further determine which driving force is responsible for such a conformation (**Chapter 2**).

In order to remove the uremic toxins and improve the hemocompatibility, magnetic nanoparticles modified with cyclodextrin and zwitterionic phosphorylcholine polymer will be synthesized. After copolymerization with different cyclodextrin and 2-(methacryloyloxy)ethyl phosphorylcholine ratio, the chemical and physical properties can be determined of each. Since the composition of polymer impact the particle dispersion as well as the interactions with uremic toxins and/or serum proteins, the adsorption profile can be further evaluated and discussed with the polymer composition to determine the overall best copolymerization ratio in adsorption capability (**Chapter 3**). In order to evaluate the biocompatibility of a series of particles, in vitro biocompatibility tests, such as platelet activation, plasma calcification, and the serum protein's structure assessment, will be performed (**Chapter 4**). A subsequent research project will be conducted to evaluate the biocompatibility of engineered particles in the presence of uremic toxins (**Chapter 5**).

1.9 References

1. Klefter, R., et al., *Savings in dialysis treatment?* Artificial Organs, 2002. **26**(1): p. 49-54.
2. Pavlenko, D., et al., *Carbon adsorbents with dual porosity for efficient removal of uremic toxins and cytokines from human plasma.* Scientific Reports, 2017. **7**(1): p. 1-7.
3. Lv, J., et al., *Prevalence and disease burden of chronic kidney disease.* Renal Fibrosis: Mechanisms Therapies, 2019: p. 3-15.
4. Ma, Y., et al., *Adsorption-based strategies for removing uremic toxins from blood.* Microporous Mesoporous Materials, 2021. **319**: p. 111035.
5. Bellringer, M., et al., *beta-Cyclodextrin: 52-week toxicity studies in the rat and dog.* Food Chemical Toxicology, 1995. **33**(5): p. 367-376.
6. Zhou, Y., et al., *Enhanced removal of bisphenol A by cyclodextrin in photocatalytic systems: degradation intermediates and toxicity evaluation.* Chinese Chemical Letters, 2020. **31**(10): p. 2623-2626.
7. Yu, Q., et al., *Anti-fouling bioactive surfaces.* Acta Biomaterialia, 2011. **7**(4): p. 1550-1557.
8. Zhang, H., et al., *Anti-fouling coatings of poly (dimethylsiloxane) devices for biological and biomedical applications.* Journal of Medical Biological Engineering, 2015. **35**(2): p. 143-155.
9. Bhakta, S.A., et al., *Protein adsorption onto nanomaterials for the development of biosensors and analytical devices: A review.* Analytica Chimica Acta, 2015. **872**: p. 7-25.
10. Silva-Bermudez, P., et al., *An overview of protein adsorption on metal oxide coatings for biomedical implants.* Surface Coatings Technology, 2013. **233**: p. 147-158.

11. Pinholt, C., et al., *The importance of interfaces in protein drug delivery-why is protein adsorption of interest in pharmaceutical formulations?* Expert Opinion on Drug Delivery, 2011. **8**(7): p. 949-964.
12. Chen, S., et al., *Surface hydration: Principles and applications toward low-fouling/nonfouling biomaterials.* Polymer, 2010. **51**(23): p. 5283-5293.
13. Mohanty, J., et al., *Cyclodextrins in Anti-Biofouling Applications*, in *Supramolecular Chemistry in Corrosion and Biofouling Protection*. 2021, CRC Press. p. 335-346.
14. Liu, Y., et al., *Molecular simulations and understanding of antifouling zwitterionic polymer brushes.* Journal of Materials Chemistry B, 2020. **8**(17): p. 3814-3828.
15. He, M., et al., *Zwitterionic materials for antifouling membrane surface construction.* Acta Biomaterialia, 2016. **40**: p. 142-152.
16. Burns, N.L., et al., *Influence of surface charge on protein adsorption at an amphoteric surface: effects of varying acid to base ratio.* Journal of Colloid Interface Science, 1996. **178**(1): p. 116-122.
17. Phillips, S., et al., *Acrylamide and iodide fluorescence quenching as a structural probe of tryptophan microenvironment in bovine lens crystallins.* Current Eye Research, 1986. **5**(8): p. 611-620.
18. Krebs, H.A., *Chemical composition of blood plasma and serum.* Annual Review of Biochemistry, 1950. **19**(1): p. 409-430.
19. Sperling, C., et al., *Blood coagulation on biomaterials requires the combination of distinct activation processes.* Biomaterials, 2009. **30**(27): p. 4447-4456.
20. Fischer, M., et al., *Synergistic effect of hydrophobic and anionic surface groups triggers blood coagulation in vitro.* Journal of Materials Science: Materials in Medicine, 2010. **21**: p. 931-937.

21. Le, H.T., et al., *Synthesis, cytotoxicity, and phase-solubility study of cyclodextrin click clusters*. Journal of Pharmaceutical Sciences, 2014. **103**(10): p. 3183-3189.
22. Diget, J.S., et al., *Direct synthesis of well-defined zwitterionic cyclodextrin polymers via atom transfer radical polymerization*. European Polymer Journal, 2019. **116**: p. 84-90.
23. Goszczyński, T.M., et al., *Synthesis of beta-cyclodextrin-lysozyme conjugates and their physicochemical and biochemical properties*. Journal of Inclusion Phenomena, 2017. **87**: p. 341-348.
24. Dong, H., et al., *Recyclable antibacterial magnetic nanoparticles grafted with quaternized poly (2-(dimethylamino) ethyl methacrylate) brushes*. Biomacromolecules, 2011. **12**(4): p. 1305-1311.
25. Yallapu, M.M., et al., *Multi-functional magnetic nanoparticles for magnetic resonance imaging and cancer therapy*. Biomaterials, 2011. **32**(7): p. 1890-1905.
26. Beaven, G.H., et al., *A spectroscopic study of the haemin-human-serum-albumin system*. European Journal of Biochemistry, 1974. **41**(3): p. 539-546.
27. Chipman, D.M., et al., *The binding of oligosaccharides containing n-acetylglucosamine and n-acetylmuramic acid to lysozyme: the specificity of binding subsites*. Journal of Biological Chemistry, 1967. **242**(19): p. 4388-4394.
28. Bahniuk, M.S., et al., *Human plasma protein adsorption to elastinlike polypeptide nanoparticles*. Biointerphases, 2020. **15**(2): p. 021007.
29. Bahniuk, M.S., et al., *Bioactive glass 45S5 powders: effect of synthesis route and resultant surface chemistry and crystallinity on protein adsorption from human plasma*. Biointerphases, 2012. **7**(1): p. 41.
30. Han, V., et al., *A comparative study of common techniques used to measure haemolysis in stored red cell concentrates*. Vox Sanguinis, 2010. **98**(2): p. 116-123.

31. Mahmoud, W.E., et al., *A facile method to syntheses monodisperse gamma-Fe₂O₃ nanocubes with high magnetic anisotropy density*. Superlattices Microstructures, 2014. **68**: p. 1-5.
32. RÅ¶sner, H.I., et al., *The human alpha-lactalbumin molten globule: comparison of structural preferences at pH 2 and pH 7*. Journal of Molecular Biology, 2009. **394**(2): p. 351-362.
33. Cadenas, E., et al., *Thiol redox transitions in cell signaling, part A: chemistry and biochemistry of low molecular weight and protein thiols*. 2010: Academic Press.
34. Steudle, A., et al., *Modelling of lysozyme binding to a cation exchange surface at atomic detail: the role of flexibility*. Biophysical Journal, 2011. **100**(12): p. 3016-3024.
35. Jain, T.K., et al., *Magnetic resonance imaging of multifunctional pluronic stabilized iron-oxide nanoparticles in tumor-bearing mice*. Biomaterials, 2009. **30**(35): p. 6748-6756.
36. Dobrovolskaia, M.A., et al., *Interaction of colloidal gold nanoparticles with human blood: effects on particle size and analysis of plasma protein binding profiles*. Nanomedicine: Nanotechnology, Biology and Medicine, 2009. **5**(2): p. 106-117.
37. Konno, T., et al., *Preparation of nanoparticles composed with bioinspired 2-methacryloyloxyethyl phosphorylcholine polymer*. Biomaterials, 2001. **22**(13): p. 1883-1889.
38. Ishihara, K., et al., *Hemocompatibility of human whole blood on polymers with a phospholipid polar group and its mechanism*. Journal of Biomedical Materials Research, 1992. **26**(12): p. 1543-1552.
39. Yang, J., et al., *How does biological sex affect the physiological response to nanomaterials?* Nano Today, 2021. **41**: p. 101292.

40. Davie, E.W., et al., *The coagulation cascade: initiation, maintenance, and regulation*. *Biochemistry*, 1991. **30**(43): p. 10363-10370.
41. Kratz, F., *Albumin as a drug carrier: design of prodrugs, drug conjugates and nanoparticles*. *Journal of Controlled Release*, 2008. **132**(3): p. 171-183.
42. Kowalczyńska, H.M., et al., *Albumin adsorption on unmodified and sulfonated polystyrene surfaces, in relation to cell–substratum adhesion*. *Colloids and Surfaces B: Biointerfaces*, 2011. **84**(2): p. 536-544.
43. Dabare, P.R.L., et al., *Surface nanotopography mediated albumin adsorption, unfolding and modulation of early innate immune responses*. *Materials Today Advances*, 2021. **12**: p. 100187.
44. Lin, W., et al., *Hemocompatibility of polyacrylonitrile dialysis membrane immobilized with chitosan and heparin conjugate*. *Biomaterials*, 2004. **25**(10): p. 1947-1957.
45. Henry, M., et al., *Conformation change of albumin adsorbed on polycarbonate membranes as revealed by ToF-SIMS*. *Langmuir*, 2003. **19**(15): p. 6271-6276.
46. Van Dulm, P., et al., *The adsorption of human plasma albumin on solid surfaces, with special attention to the kinetic aspects*. *Journal of Colloid and Interface Science*, 1983. **91**(1): p. 248-255.
47. Victor, S.P., et al., *Development and evaluation of cyclodextrin complexed hydroxyapatite nanoparticles for preferential albumin adsorption*. *Colloids and Surfaces B: Biointerfaces*, 2011. **85**(2): p. 221-228.
48. Walport, M.J., *Advances in immunology: complement (first of two parts)*. *New England Journal of Medicine*, 2001. **344**(14): p. 1058-1066.

49. Andersson, J., et al., *Binding of C3 fragments on top of adsorbed plasma proteins during complement activation on a model biomaterial surface*. *Biomaterials*, 2005. **26**(13): p. 1477-1485.
50. Melchior, P., et al., *Complement activation by dialysis membranes and its association with secondary membrane formation and surface charge*. *Artificial Organs*, 2021. **45**(7): p. 770-778.
51. Vidarsson, G., et al., *IgG subclasses and allotypes: from structure to effector functions*. *Frontiers in Immunology*, 2014. **5**: p. 520.
52. Harrison, P.M., et al., *The ferritins: molecular properties, iron storage function and cellular regulation*. *Biochimica et Biophysica Acta (BBA)-Bioenergetics*, 1996. **1275**(3): p. 161-203.
53. Ogun, A.S., et al., *Biochemistry, transferrin*, in *StatPearls [Internet]*. 2022, StatPearls Publishing.
54. Stafford, J.L., et al., *Transferrin and the innate immune response of fish: identification of a novel mechanism of macrophage activation*. *Developmental & Comparative Immunology*, 2003. **27**(6-7): p. 539-554.
55. Bale, M.D., et al., *Identification of vitronectin as a major plasma protein adsorbed on polymer surfaces of different copolymer composition*. *Blood*, 1989.
56. Berclaz, P., et al., *Rare Childhood Lung Disorders: α 1-Antitrypsin Deficiency, Pulmonary Alveolar Proteinosis, and Pulmonary Alveolar Microlithiasis*, in *Kendig's Disorders of the Respiratory Tract in Children*. 2006, Elsevier. p. 747-761.
57. Chidambaranathan-Reghupaty, S., et al., *Hepatocellular carcinoma (HCC): Epidemiology, etiology and molecular classification*. *Advances in Cancer Research*, 2021. **149**: p. 1-61.

58. Li, W., et al., *Cyclodextrin based unimolecular micelles with targeting and biocleavable abilities as chemotherapeutic carrier to overcome drug resistance*. Materials Science Engineering: C, 2019. **105**: p. 110047.
59. Papa, E., et al., *Investigation of the influence of protein corona composition on gold nanoparticle bioactivity using machine learning approaches*. SAR and QSAR in Environmental Research, 2016. **27**(7): p. 521–538.
60. Samir, D., et al., *Cell cooperation and role of the P2X7 receptor in pulmonary inflammation induced by nanoparticles*. Nanotoxicology, 2012. **7**(8): p. 1302–1314.
61. Liu, R., et al., *Prediction of nanoparticles-cell association based on corona proteins and physicochemical properties*. Nanoscale, 2015. **7**(21): p. 9664-9675.
62. Armstrong, P.B., et al., *α 2-macroglobulin: an evolutionarily conserved arm of the innate immune system*. Developmental & Comparative Immunology, 1999. **23**(4-5): p. 375-390.
63. Vandooren, J., et al., *Alpha-2-macroglobulin in inflammation, immunity and infections*. Frontiers in Immunology, 2021. **12**: p. 803244.
64. Levy, J.H., et al., *Fibrinogen as a therapeutic target for bleeding: a review of critical levels and replacement therapy*. Transfusion, 2014. **54**(5): p. 1389-1405.
65. Lowe, G.D., et al., *Plasma fibrinogen*. Annals of Clinical Biochemistry, 2004. **41**(6): p. 430-440.
66. Nava-Ortiz, C.A., et al., *Cyclodextrin-functionalized biomaterials loaded with miconazole prevent Candida albicans biofilm formation in vitro*. Acta Biomaterialia, 2010. **6**(4): p. 1398-1404.
67. Austen, D., *Clinical Biochemistry of Blood Coagulation*, in *Scientific Foundations of Biochemistry in Clinical Practice*. 1994, Elsevier. p. 495-513.

68. Ashikaga, H., et al., *chapter 28 - Blood Coagulation and Atherothrombosis*, in *Molecular Basis of Cardiovascular Disease (Second Edition)*, K.R. Chien, Editor. 2004, W.B. Saunders: Philadelphia. p. 498-518.
69. Wu, Y., *Contact pathway of coagulation and inflammation*. *Thrombosis journal*, 2015. **13**(1): p. 1-9.
70. Ortega, V.A., et al., *Polymer-coated nanoparticle protein corona formation potentiates phagocytosis of bacteria by innate immune cells and inhibits coagulation in human plasma*. *Biointerphases*, 2020. **15**(5): p. 051003.
71. Ivanov, I., et al., *Protease activity in single-chain prekallikrein*. *Blood, The Journal of the American Society of Hematology*, 2020. **135**(8): p. 558-567.
72. Veloso, D., et al., *Western blot analyses of prekallikrein and its activation products in human plasma*. *Thrombosis and Haemostasis*, 1991. **65**(04): p. 382-388.
73. Yun, Y., et al., *Initial hemocompatibility studies of titanium and zirconium alloys: Prekallikrein activation, fibrinogen adsorption, and their correlation with surface electrochemical properties*. *Journal of Biomedical Materials Research: An Official Journal of The Society for Biomaterials and The Japanese Society for Biomaterials*, 1996. **32**(1): p. 77-85.
74. To, W.S., et al., *Plasma and cellular fibronectin: distinct and independent functions during tissue repair*. *Fibrogenesis & Tissue Repair*, 2011. **4**: p. 1-17.
75. Rogers, H.J., et al., *Hemostasis and thrombosis*, in *Hematopathology*. 2018, Elsevier. p. 57-105. e4.
76. Woodhouse, K., et al., *Adsorption of plasminogen from plasma to lysine-derivatized polyurethane surfaces*. *Biomaterials*, 1992. **13**(15): p. 1103-1108.

77. Quandt, J., et al., *Interactive Hemocompatible Nanocoating to Prevent Surface-Induced Coagulation in Medical Devices*. *Advanced Materials Interfaces*, 2022. **9**(33): p. 2201055.
78. Nalezinková , M., *In vitro hemocompatibility testing of medical devices*. *Thrombosis Research*, 2020. **195**: p. 146-150.
79. Lippi, G., *Systematic assessment of the hemolysis index: pros and cons*. *Advances in Clinical Chemistry*, 2015. **71**: p. 157-170.
80. Thomas, M., et al., *High molecular weight kininogen adsorption on hemodialysis membranes: influence of pH and relationship with contact phase activation of blood plasma. Influence of pre-treatment with poly (ethyleneimine)*. *The International Journal of Artificial Organs*, 2000. **23**(1): p. 20-26.
81. Renaux, J., et al., *Activation of the kallikrein-kinin system in hemodialysis: role of membrane electronegativity, blood dilution, and pH*. *Kidney International*, 1999. **55**(3): p. 1097-1103.
82. Dobrovolskaia, M.A., et al., *Nanoparticle size and surface charge determine effects of PAMAM dendrimers on human platelets in vitro*. *Molecular Pharmaceutics*, 2012. **9**(3): p. 382-393.
83. Koziara, J., et al., *Blood compatibility of cetyl alcohol/polysorbate-based nanoparticles*. *Pharmaceutical Research*, 2005. **22**: p. 1821-1828.
84. Wang, J., et al., *Cyclic molecule aerogels: a robust cyclodextrin monolith with hierarchically porous structures for removal of micropollutants from water*. *Journal of Materials Chemistry A*, 2017. **5**(9): p. 4308-4313.

85. Gholibegloo, E., et al., *Improved curcumin loading, release, solubility and toxicity by tuning the molar ratio of cross-linker to beta-cyclodextrin*. Carbohydrate Polymers, 2019. **213**: p. 70-78.
86. Yuan, Z., et al., *Chitosan-graft-beta-cyclodextrin nanoparticles as a carrier for controlled drug release*. International Journal of Pharmaceutics, 2013. **446**(1-2): p. 191-198.
87. Namazi, H., et al., *Synthesis of beta-cyclodextrin-based dendrimer as a novel encapsulation agent*. Polymer International, 2014. **63**(8): p. 1447-1455.
88. Kiasat, A.R., et al., *Magnetic nanoparticles grafted with beta-cyclodextrin-polyurethane polymer as a novel nanomagnetic polymer brush catalyst for nucleophilic substitution reactions of benzyl halides in water*. Journal of Molecular Catalysis A: Chemical, 2012. **365**: p. 80-86.
89. Yuan, Z., et al., *Redox-controlled voltage responsive micelles assembled by noncovalently grafted polymers for controlled drug release*. Macromolecules, 2019. **52**(4): p. 1400-1407.
90. Fan, X., et al., *Thermoresponsive Supramolecular Chemotherapy by "V"-Shaped Armed β -Cyclodextrin Star Polymer to Overcome Drug Resistance*. Advanced Healthcare Materials, 2018. **7**(7): p. 1701143.
91. Xu, Z., et al., *Unimolecular micelles of amphiphilic cyclodextrin-core star-like block copolymers for anticancer drug delivery*. Chemical Communications, 2015. **51**(87): p. 15768-15771.
92. Chmielarz, P., et al., *Synthesis of beta-cyclodextrin-based star polymers via a simplified electrochemically mediated ATRP*. Polymer, 2016. **88**: p. 36-42.

93. Miura, Y., et al., *Synthesis of well-defined AB₂₀-type star polymers with cyclodextrin-core by combination of NMP and ATRP*. *Journal of Polymer Science Part A: Polymer Chemistry*, 2005. **43**(18): p. 4271-4279.
94. Pan, Y., et al., *Tailor-Made Antimicrobial/Antiviral Star Polymer via ATRP of Cyclodextrin and Guanidine-Based Macromonomer*. *Macromolecular Chemistry Physics*, 2015. **216**(5): p. 511-518.
95. Stenzel, M.H., et al., *Star polymer synthesis using trithiocarbonate functional β -cyclodextrin cores (reversible addition–fragmentation chain-transfer polymerization)*. *Journal of Polymer Science Part A: Polymer Chemistry*, 2002. **40**(24): p. 4498-4512.
96. Araki, J., et al., *Recent advances in the preparation of cyclodextrin-based polyrotaxanes and their applications to soft materials*. *Soft Matter*, 2007. **3**(12): p. 1456-1473.
97. Samitsu, S., et al., *New solvent for polyrotaxane. II. Dissolution behavior of polyrotaxane in ionic liquids and preparation of ionic liquid-containing slide-ring gels*. *Journal of Polymer Science Part B: Polymer Physics*, 2006. **44**(14): p. 1985-1994.
98. Mondjinou, Y.A., et al., *Synthesis of 2-hydroxypropyl- β -cyclodextrin/pluronic-based polyrotaxanes via heterogeneous reaction as potential Niemann-Pick type C therapeutics*. *Biomacromolecules*, 2013. **14**(12): p. 4189-4197.
99. Tamura, A., et al., *Lysosomal-specific cholesterol reduction by biocleavable polyrotaxanes for ameliorating Niemann-Pick type C disease*. *Scientific Reports*, 2014. **4**(1): p. 1-8.
100. Wang, J., et al., *The intrinsic microstructure of supramolecular hydrogels derived from α -cyclodextrin and pluronic F127: nanosheet building blocks and hierarchically self-assembled structures*. *Soft Matter*, 2020. **16**(25): p. 5906-5909.

101. Boger, J., et al., *Cyclodextrin chemistry. Selective modification of all primary hydroxyl groups of alpha- and beta-cyclodextrins*. Helvetica Chimica Acta, 1978. **61**(6): p. 2190-2218.
102. Hammoud, Z., et al., *Cyclodextrin-membrane interaction in drug delivery and membrane structure maintenance*. International Journal of Pharmaceutics, 2019. **564**: p. 59-76.
103. Akbarzadeh, A., et al., *Synthesis, characterization, and in vitro evaluation of novel polymer-coated magnetic nanoparticles for controlled delivery of doxorubicin*. Nanotechnology, Science Applications, 2012. **5**: p. 13.
104. Ge, F., et al., *Efficient removal of cationic dyes from aqueous solution by polymer-modified magnetic nanoparticles*. Chemical Engineering Journal, 2012. **198**: p. 11-17.

Chapter 2

Indoxyl and p-cresol sulfate binding with human serum albumin [1].

[1] This chapter was published as “Li, S., et al., Indoxyl and p-cresol sulfate binding with human serum

albumin. 2022. 635: p. 128042.

Author List: Li, Shuhui, Marcello Tonelli, and Larry D. Unsworth.*

Contribution: Li, Shuhui wrote the manuscript and performed all experiments as well as the data analysis. Marcello Tonelli reviewed and edited the manuscript. Larry D. Unsworth reviewed and edited the manuscript. Conceptualized and supervised the research.

2.1 Introduction

Despite the successful application of hemodialysis (HD) to treat patients with kidney failure and the decades of research conducted in developing HD therapies, morbidity and mortality among HD populations remain regrettably high. This high burden of illness, premature death and disability is driven by accelerated cardiovascular disease [1, 2], which is felt to arise from the continued accumulation of metabolically-derived compounds despite ongoing HD treatment. In particular, compounds that become tightly bound by blood proteins (as known as protein bound uremic toxins, PBUTs) are notoriously hard to clear from the blood compartment using membrane-based techniques. Here the protein phase within the plasma component of the blood acts like a reservoir, where after being cleared by HD their solution concentrations may be re-established through their release from the protein-bound phase [2]. A complete list of PBUTs, their concentration profiles in HD patients as a function of disease progression, or a full understanding of how these molecules either induce or are the result of cellular dysfunction has only been provided. Nevertheless, p-cresol sulfate (PCS) and indoxyl sulfate (IS) are two, well-recognized, PBUTs that accumulate in patients that undergo HD treatments, which have been linked with inflammation, bone damage, increased oxidative stress, and exacerbating kidney damage [3]. It is thought that understanding how these PBUTs interact with serum HSA will allow for the development of molecules that compete with HSA as binders of these small molecules, or molecules that can compete with PBUTs in binding HSA.

HSA is an abundant blood protein, accounting for 50%-60% (35–50 g/L) of the total plasma proteins and is responsible for ~80% of the colloid osmotic pressure of blood [4, 5]. X-ray crystallography has shown HSA predominantly adopts an heart-shaped tertiary structure, which is considered the result of joint action of three homologous domains (I–III) and 17 disulfide bridges

[6]. These three domains are subdivided into A and B groups, composed of 4 and 6 α -helices, respectively. The α -helix of each subdomain are found to line a number of hydrophobic cavities that bind a wide variety of endogenous and exogenous compounds [7], such as thyroid hormones, fatty acids. Sudlow's site I is located in the hydrophobic cavity of subdomain IIA and preferentially binds heterocyclic anions, such as warfarin [8, 9]. In site I, drugs reside between apolar side-chains of Leu238 and Ala291 and hydroxyl group of Tyr150 [10]. Sudlow's site II is found within subdomain IIIA and has a high affinity for aromatic carboxylates, like ibuprofen [10]. In site II, the hydroxyl group of Tyr411, Arg410 and Ser489 residues contribute to drug binding via the formation of salt-bridges and hydrogen bonds. The binding site includes a polar patch that could potentially interact with carboxyl ligands [11-13]. For patients with kidney dysfunction, native and post-translationally modified HSA coexist; the relative ratio of these as a function of disease progression has yet to be fully determined. Post-translational modification of HSA is known to contribute to the progression of CKD [14, 15]. Herein, we focus on native HSA interactions with IS and PCS, but others have studied the effect of post-translational modification of HSA and have observed decreased binding affinities for some PBUTs compared to native HSA [15-17].

The development of materials to augment the clearance of IS and PCS from the blood compartment of HD patients depends upon obtaining a fundamental understanding of the mechanisms involved in that interaction. Previous literature has largely focused on IS or PCS clearance rates using different types of materials (membrane or other), without fully outlining the mechanisms responsible for their retention [3, 18-21]. Binding affinity for PCS or IS to HSA has been reported previously, but the binding mechanisms, specific binding site and resultant conformational changes of HSA have not been fully considered [22, 23]. Herein, we provide an accurate and full data set for interpreting the binding mechanism and conformation of PCS or IS

with HSA by combining isothermal titration calorimetry, fluorescence spectroscopy, circular dichroism, and saturation transfer difference NMR.

2.2 Experimental

2.2.1 Materials and methods

Human serum albumin (HSA, purity $\geq 98\%$, fatty acid free, 66.5 kDa), IS and warfarin were purchased from Sigma-Aldrich Chemicals Company (USA) and used without further modification. ibuprofen was purchased from Oakwood Chemical (USA). PCS is purchased from Musechem (USA). Protein solutions were prepared fresh for each experiment, where HSA was directly dissolved in phosphate buffer solution of pH 7.2 (0.1 M PBS). The stock solutions were prepared and stored at 4 °C, pH was evaluated using EcoSence® model pH10A (EcoSence, USA) as calibrated using buffer pack. All PBS buffers were syringe filtered (0.2 μm) prior to use.

2.2.2 Fluorescence

Protein solutions (0.1 M PBS, pH 7.2) were aliquoted into a 96 well plate with black walls and transparent bottom. Measurements were performed at 25, 30, and 37°C. Steady-state fluorescence was measured using the PTI fluorescence spectrometer FelixTM (company, country). Samples were excited at 285 nm and the emission spectrum measured between 290 to 500 nm (2 nm resolution). A series of IS or PCS buffered solutions with increasing concentrations (0-20 μM and 0-40 μM , respectively) were prepared. HSA (2 μM) was chosen as the concentration for fluorescence quenching experiments.

2.2.3 Circular dichroism

Far-UV circular dichroism spectra of HSA with IS or PCS (1:20 molar ratio) were obtained using a circular dichroism/ORD spectrometer (JASCO, J810). The spectra were recorded from 180

to 260 nm using a 0.5 mm quartz cell. The concentrations of HSA solution were 1.5 mM and ligand concentration of 3.2 mM. HSA solution (100 μ L) added to the cuvette and followed by adding 10, 20, 30, and 40 μ L of ligands. Measurement was set at three times repeat, the results presented are average value. CDNN 2.0 software is used to determine the secondary structure changing upon adding toxins.

2.2.4 Isothermal titration calorimetry

ITC experiments were performed using a VP-ITC instrument (TA instrument, USA). All samples were prepared in PBS buffer (pH 7.2) and degassed immediately prior to use. Two equilibrium processes are required, namely the instrument was stabilized for 1hr after the addition of the ligands into the sample cell. After the fluctuation range stabilized within 0.2 μ J/sec, the syringe filled with titrant was inserted. One hour of equilibrium time was allowed to pass prior to titration. A total of 50 μ L of ligand solution was injected into the 170 μ L cell. In the simulation, cumulative heat corresponding to each injection was used. According to the thermodynamic formulas:

$$\Delta G = -RT \ln K \quad (\text{Equation 2.1})$$

$$\Delta G = \Delta H - T\Delta S \quad (\text{Equation 2.2})$$

standard changes of Gibbs free energy ($\Delta G, kJ mol^{-1}$), enthalpy effect ($\Delta H, kJ mol^{-1}$), and entropy effect ($\Delta S, J mol^{-1} K^{-1}$) for the binding process of ligands to HSA was derived. An independent binding model was used for fitting the data and the association constant (K_a) was further calculated.

2.2.5 Saturation transfer difference (STD) NMR

1D ^1H STD spectra were acquired at 27 °C on Agilent/Varian VNMRS four-channel 600 MHz i600 equipped with AutoXID probe. All samples were prepared using PBS (D_2O solvent). Chemical shifts were referenced to the external signal of Acetone at 2.26 ppm. Selective saturation of HSA was performed using Gaussian-shaped pulses of 50 ms each. The on-resonance irradiation of HSA was performed at a chemical shift of -1 ppm and off-resonance irradiation at 35 ppm.

2.3 Results and discussion

2.3.1 Binding of IS and PCS to HSA

Thermodynamic parameters and resultant stoichiometry were evaluated as a means of characterizing the mode of interaction between IS or PCS with HSA. ITC was used to directly measure the evolving heat during the titration (Figure 2.1), which can be used in Eq'ns (1) and (2) to evaluate the binding affinity and stoichiometry (n) in aqueous phase without the need for probe addition or artificial ligand immobilization (Table 2.1) [24]. Each peak in the resulting isotherm represents a single injection of IS or PCS into the HSA solution, subtracting any heat effects related to dilution for each component injected into blank PBS buffer.

Isotherms were fitted to a binding model to yield the association constant (K_a), binding stoichiometry (n), enthalpy change (ΔH), entropy change (ΔS), and free energy change (ΔG). Based on the isotherm profile, an independent site model was employed (Table 2.1), where it was observed that IS had a higher binding affinity for HSA compared to PCS [25, 26]. However, both toxins had a lower binding affinity compared to the experimentally determined values for warfarin ($3.41 \times 10^4 \text{ L mol}^{-1}$) and ibuprofen ($1.39 \times 10^5 \text{ L mol}^{-1}$). Experimentally determined binding affinities for warfarin and ibuprofen were in good agreement with previous literature ($\sim 10^4 \text{ L mol}^{-1}$ and $\sim 10^5 \text{ L mol}^{-1}$) [27-29].

In order to discern the binding mechanism the change in enthalpy and entropy are scrutinized, where if ΔH and ΔS are both positive, binding was dominated by hydrophobic interaction [30]. In the case of IS or PCS interactions with HSA, a negative ΔH and ΔS (Table 2.1) were obtained, which suggested the involvement of electrostatic interactions and a disorder-to-order transition in the ligand-protein-water complex [23, 31-33]. The binding for both IS or PCS was enthalpy-driven with an unfavorable entropy change. A similar trend was observed for warfarin-HSA interactions, where both ΔH and ΔS were negative. However, ibuprofen-HSA interactions had a negative ΔH and positive ΔS , indicating an interaction that is different than for IS or PCS. In the case of ibuprofen-HSA interactions, positive entropy and negative enthalpy reflect the combined effects of hydrophobic and electrostatic interactions. Though ibuprofen has been reported as a potential competitor for removing toxins from HSA [34], ITC results indicated that the binding mechanism between ibuprofen and PCS or IS was different; indicating that a different binding site may be involved. That said, ibuprofen binding to HSA had a lower Gibb's free energy than either IS or PCS ($\Delta G_{\text{ibuprofen-HSA}} = -23.16$, $\Delta G_{\text{IS-HSA}} = -20.11$, and $\Delta G_{\text{PCS-HSA}} = -17.69$ kJ mol⁻¹).

Table 2.1 Thermodynamic parameters for the interaction of IS or PCS with HSA obtained from ITC at 298 K and pH 7.20.

Toxins	K_a ($\times 10^3$ L mol ⁻¹)	n	ΔH (kJ mol ⁻¹)	ΔG (kJ mol ⁻¹)	ΔS (kJ mol ⁻¹ K ⁻¹)
IS	10.06±0.04	1.08 ±0.21	-70.09	-20.11	-0.168
PCS	1.39±0.08	1.03±0.15	-115.2	-17.69	-0.327

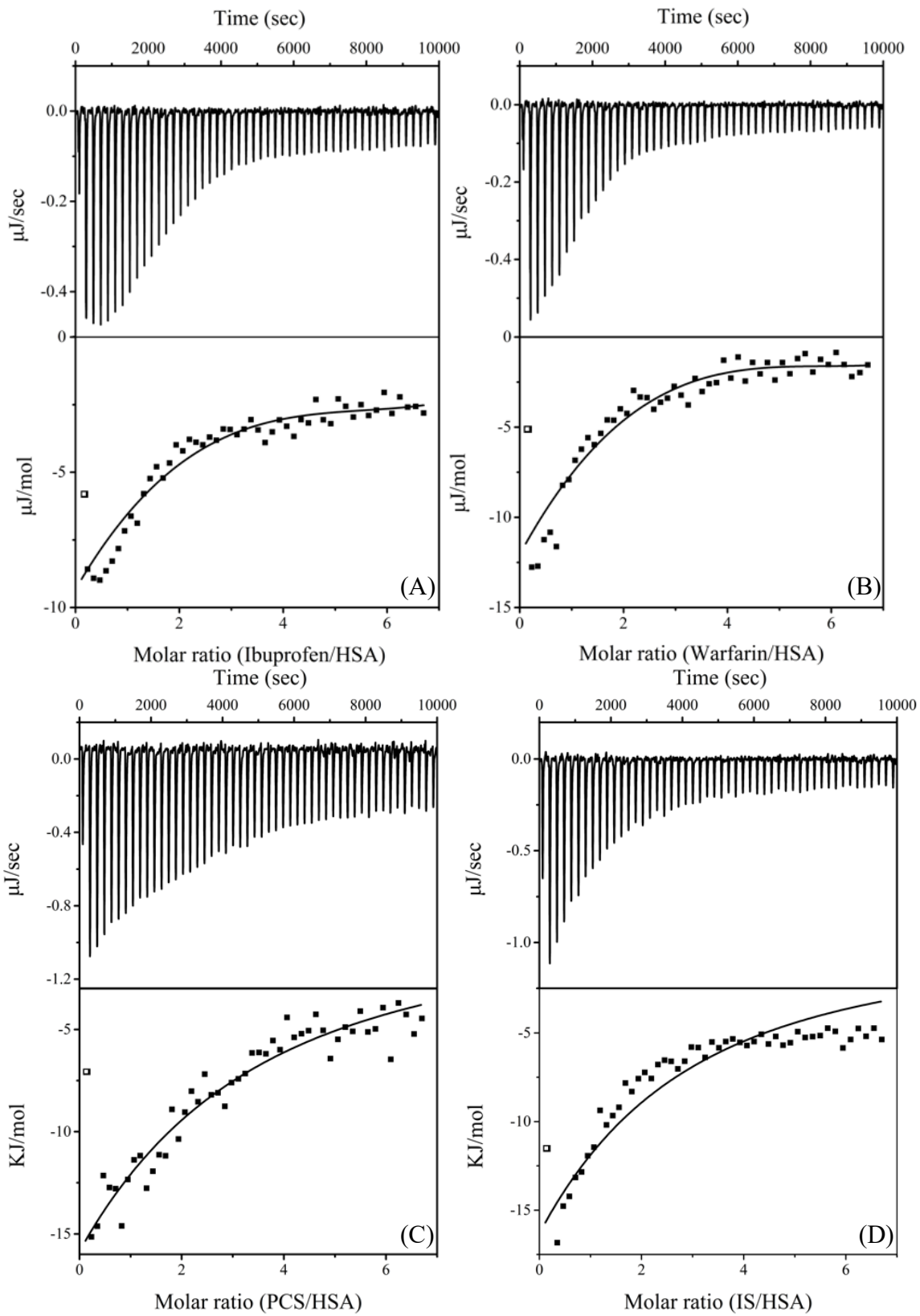


Figure 2.1 ITC thermogram (upper panel) and fitting (lower panel) of HAS with single ligand. ITC thermogram (upper panel) and fitting (lower panel) of HAS with single ligands. The solid line represents the best nonlinear least-squares fit to the independent binding site model, where fit quality is represented as R^2 . The initial concentration is 2×10^{-3} mol L⁻¹ for ibuprofen or warfarin and 1×10^{-4} mol L⁻¹ for HSA. T=298 K, pH=7.20. (A) Left panel: Corrected heat data for the titration of ibuprofen with HSA, with an $R^2=0.88$. (B) Right panel: Corrected heat data for the titration of warfarin with HSA, with an $R^2=0.84$. (C) Left panel: Corrected heat data for the titration of PCS with HSA, with an $R^2=0.99$. (D) Right panel: Corrected heat data for the titration of IS with HSA, with an $R^2=0.99$.

Competitive experiments using warfarin or ibuprofen with IS or PCS were conducted using ITC, where warfarin or ibuprofen was injected into a solution containing HSA and IS or PCS; subtracted background was PBS injection into IS/PCS-HSA solution. The presence of both endo- and exothermal peaks (Figure 2.2A) suggested the displacement of IS by ibuprofen within the same site. A minor endothermal effect occurred in the inceptive 5 and 11 injections for warfarin to HSA-IS complex and ibuprofen to HSA-PCS, respectively. The heat then tended toward a steady level, indicating the saturation of the system, as expected for low-affinity binding [35]. For the experiment of warfarin to HSA-PCS complex (Figure 2.2D), split peaks are observed for the inceptive 2 to 4 injections. This is considered as an exothermic binding reaction and a low-affinity unbinding occurred simultaneously in different sites. One reasonable interpretation for this observation is that PCS rebound to a different site or randomly bound to HSA after being displaced by warfarin from site I.

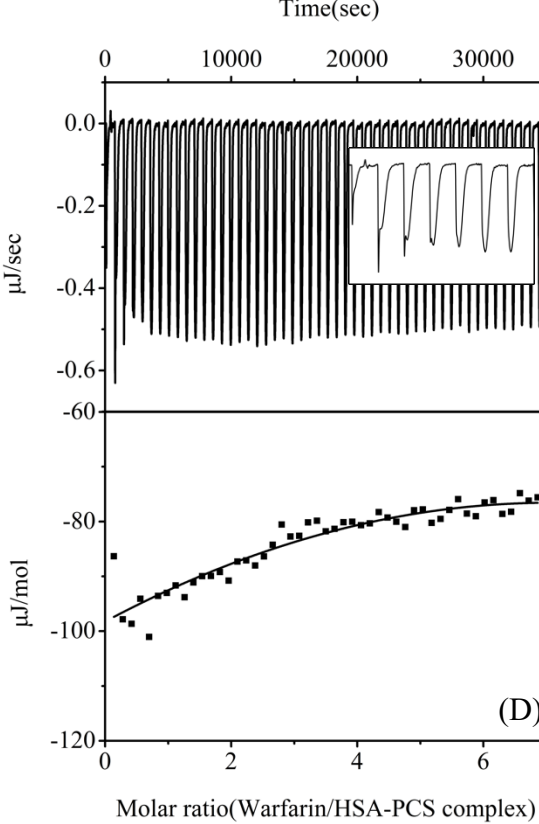
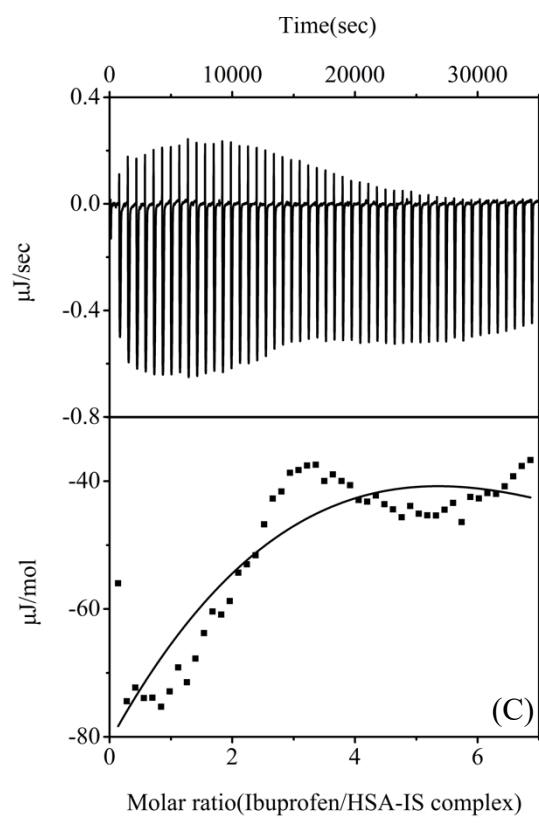
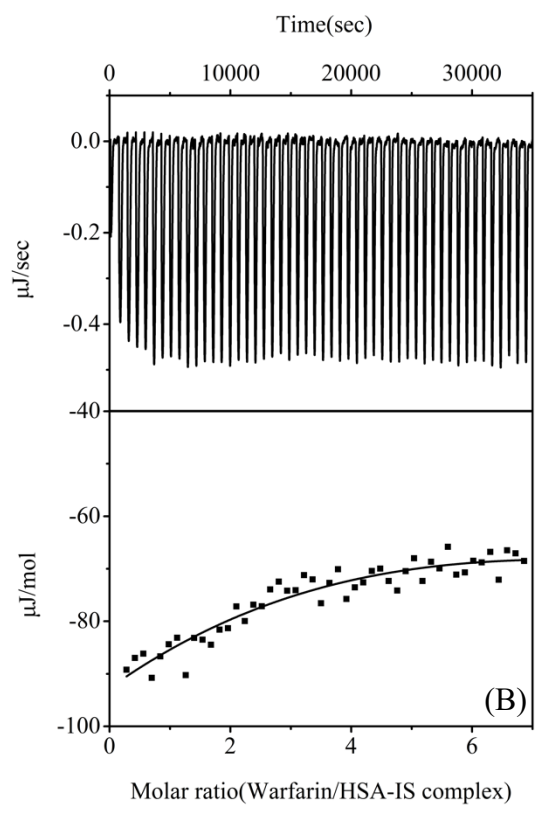
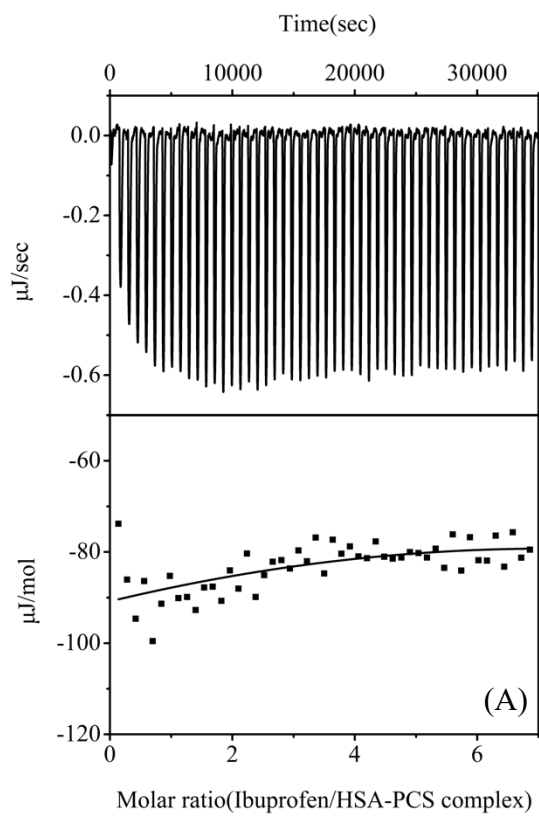


Figure 2.2 ITC thermogram (upper panel) and fitting (lower panel) of I with double ligands. The solid line represents the best nonlinear least-squares fit to the competitive binding model. The initial concentration is $2 \times 10^{-3} \text{ mol L}^{-1}$ for IS/PCS/ibuprofen/warfarin, and $1 \times 10^{-4} \text{ mol L}^{-1}$ for I. T=298 K, pH=7.20. (A) Corrected heat data for the titration of ibuprofen with I and IS mixture, with an $R^2=0.91$ (B) Corrected heat data for the titration of warfarin with I and IS mixture, with an $R^2=0.99$ (C) Corrected heat data for the titration of ibuprofen with I and PCS mixture, with an $R^2=0.82$ (D) Corrected heat data for the titration of IS with I and PCS mixture, with an $R^2=0.95$.

2.3.2 Fluorescence

2.3.2.1 Effect of IS and PCS on fluorescence

Intrinsic fluorescence is measured through quenching, where intensity and peak position can be used to understand the protein-ligand interaction [36]. Fluorescence emission spectra for I in the presence of IS or PCS (Figure 2.3) used an excitation wavelength of 285 nm. It was observed that I fluorescence intensity decreased as IS or PCS concentration increased (Figure 2.3A and 2.3B). The fluorescence of IS and PCS was observed using emission wavelengths of 390 and 325 nm, respectively (Figure 2.3C and 2.3D) [37]. The fluorescence spectra for IS has a shoulder at 420 nm, which is attributed to an unresolved vibrational-electronic transition [38]. A slight red shift is observed upon PCS being bound by I (from 352 to 356 nm), indicating the I structure was altered such that more water was incorporated and an increased polarity near the tryptophan residue occurred [39]. Furthermore, a blue shift (from 364 to 358 nm) in the peak position occurred with increasing IS concentration, which indicated the fluorophore is in a hydrophobic environment upon IS addition [40]; where the protein rearranged so that the water content decreased, which led to a decreased polarity [41]. However, the inclusion of cations in the protein has also been shown to

cause a blue shift [42]. STD NMR experiments were conducted to further explain the environmental changes local to the binding event.

2.3.2.2 Fluorescence quenching mechanism

The Stern-Volmer equation (Eq'n 2.3) can be used to determine whether the quenching mechanism was dynamic or static:

$$F^0/F = 1 + K_{SV}[Q] \quad (\text{Equation 2.3})$$

where F^0 is the fluorescence intensity in the absence of a quencher, F is in the presence of the quencher, K_{SV} is the Stern–Volmer quenching constant, and $[Q]$ is the concentration of the quencher. The results of which are illustrated in the Stern-Volmer plot of quenching by IS and PCS (Figure 2.3E and 2.3F). Quenching experiments at three different temperatures yielded a linear relationship between $[Q]$ and F^0/F , which suggested that static quenching was the dominant mechanism at play: dynamic and static quenching can be discerned through temperature effects. Static quenching represents a strong coupling between host and ligand (i.e. I and toxins), where increasing temperature tends to yield a decreasing Stern–Volmer quenching constant K_{SV} (Table 2.2) [43].

Table 2.2 Stern–Volmer quenching constant K_{SV} and association constant K_a for IS and PCS binding with I at 298, 303, and 310 K.

$T(K)$	PCS		IS	
	K_{SV} (L mol ⁻¹)	K_a (L mol ⁻¹)	K_{SV} (L mol ⁻¹)	K_a (L mol ⁻¹)
298	7.01×10^3	7.7×10^3	5.88×10^4	5.75×10^4
303	5.25×10^3	5.71×10^3	4.76×10^4	4.63×10^4
310	3.75×10^3	5.01×10^3	3.95×10^4	3.79×10^4

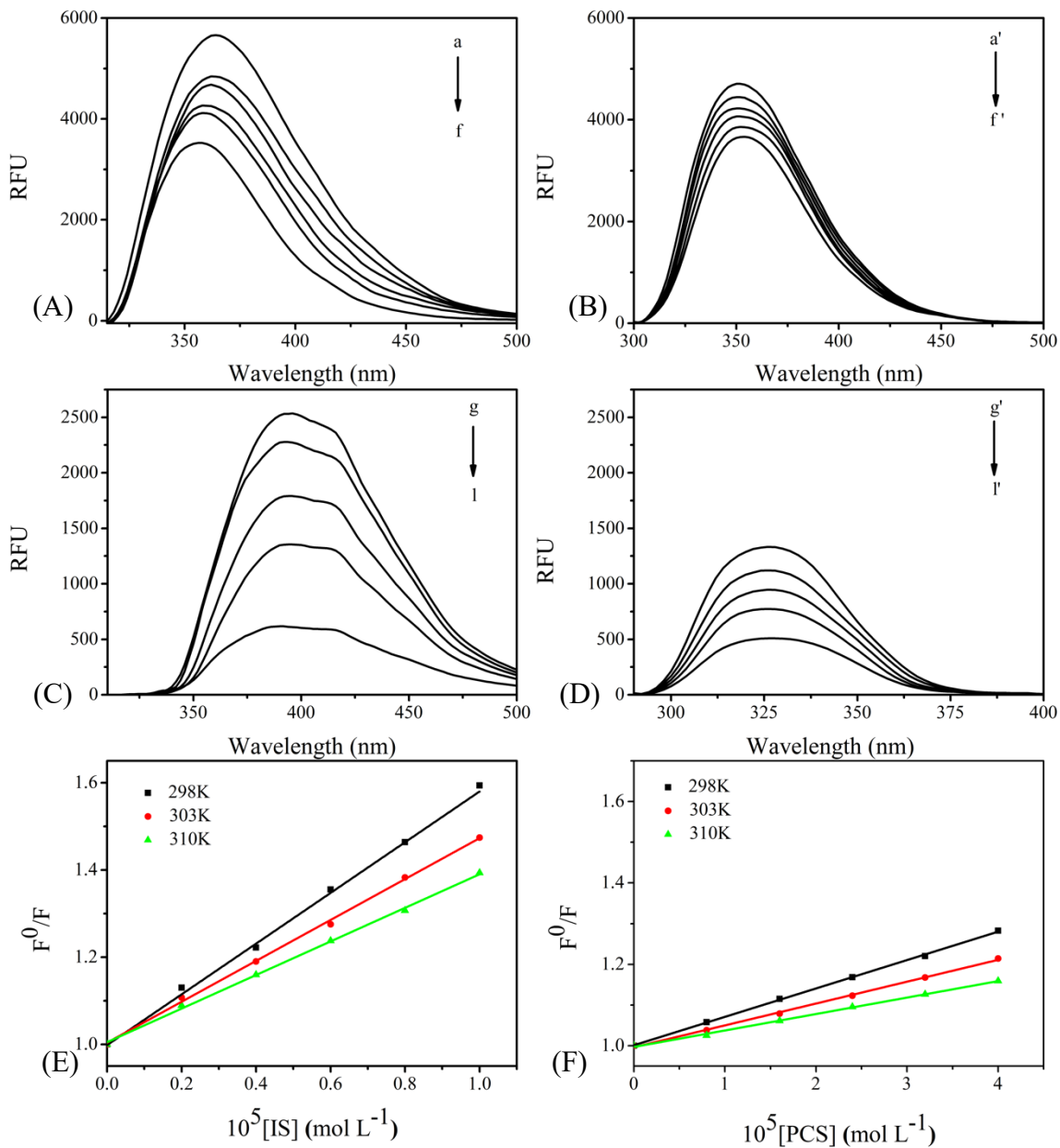


Figure 2.3 Fluorescence emission spectra results for I (2×10^{-6} mol L⁻¹, pH=7.20) and IS or PCS. (A) I emission in the presence of different concentrations of IS (a-f: 0-1 mM) at 298 K. (B) I emission in the presence of different concentrations of PCS (a'-f': 0-4 mM) at 298 K. (C)(D): IS (g-l: 1-0.2 mM) and PCS (g'-l': 4-0.8 mM) in PBS; I(F): Stern–Volmer plots for I quenching by IS or PCS with temperature.

2.3.2.3 Binding Parameters

Further analysis of the quenching data was done to determine the association constant (K_a) and the average number of binding sites (n) [44]:

$$\log \frac{F^0 - F}{F} = n \log K_a - n \log \frac{1}{[Q] - \frac{(F^0 - F)[P]}{F^0}} \quad (\text{Equation 2.4})$$

where $[P]$ represents protein concentration. Fitting equation 2.4 to trends shown in Figure 2.4 resulted in a K_a of IS and PCS at 298K to be determined as $\sim 10^4$ and $\sim 10^3$ L mol⁻¹, with an n of 0.89 and 0.93, respectively. These results agreed with the independent ITC results.

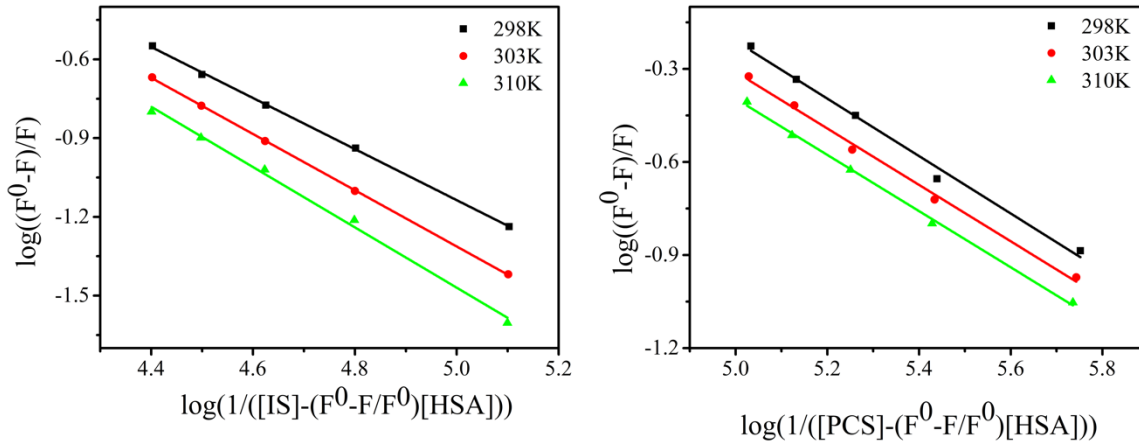


Figure 2.4 The plots of $\log((F_0 - F)/F)$ vs. $\log(1/([Q] - (F_0 - F)[P]/F_0))$ for IS/PCS-I system at three different temperatures and pH 7.2.

2.3.3 Effect of PBUT on I structure

Increasing IS or PCS concentration resulted in a decrease in CD peak intensity of I at 208 and 223 nm, a result commonly attributed to the α -helix structure (Figure 2.5, Table 2.3); where the α -helix in native I was decreased by 40.8% or 47% with the addition of IS or PCS, respectively. However, the beta-sheet content of I increased 15.6% upon IS addition and 23.1% for PCS. An α -

helix secondary structure dominated the IS-I complex, whereas a random coil structure evolved for PCS-I.

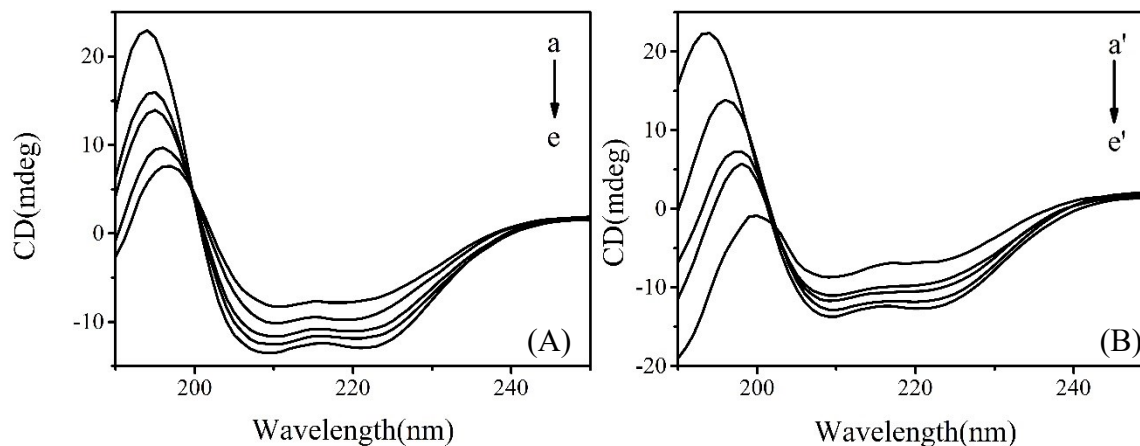


Figure 2.5 Circular dichroism spectrum of I in the absence and presence of IS (A) or PCS (B), where the $[I] = 1.0 \times 10^{-5} \text{ mol L}^{-1}$, $[IS]$ (a–e) or $[PCS]$ (a’–e’) was 0.32 to 0 mM.

Table 2.3 Representative results for the effect of IS or PCS on the secondary structure of I, as determined using CD spectra between 190 to 260 nm. Results are an average of three repeated scans.

	<i>IS</i>		<i>PCS</i>	
	0 mM	0.32 mM	0 mM	0.32 mM
Alpha-Helix	73%	32.2%	70.7%	23.7%
Beta sheet	3.8%	19.4%	4.2%	27.3%
Beta turn	12.7%	17.6%	12.7%	18.4%
Random coil	10.5%	30.7%	12.5%	30.6%

2.3.4 Analysis of STD-NMR experiments

The addition of these uremic toxins to the protein solution could affect their secondary and tertiary structure without directly binding to the protein. Although ITC results do show direct

interactions between these PBUTs and I, it doesn't give any indication of where this binding is occurring or what domains of either the PBUT or the protein are involved in the interaction. To further clarify the physicochemical properties of the interaction between I and IS or PCS, STD-NMR (^1H NMR) is used to characterize the magnetization transfer from I, when under an induced magnetic field, onto IS or PCS. Herein, STD was used to selectively transfer the magnetic-field induced resonance of protein protons to the protons of bound IS or PCS, without affecting those that are solution free (i.e., unbound), where the intensity of this binding event is determined through the difference between the on- and off-resonance spectra. Thus, the difference between the on- and off- resonance spectra highlight only the ligands that received resonance from protein (Figure 2.6). The observed magnetization transfer confirmed the binding between IS or PCS and I as well as provided the integrated area for each proton (Figure 2.6). It was observed that 32.5 or 23.8% of IS or PCS molecules interacted with HSA.

Moreover, from the STD spectra it was possible to discern the protons involved in the resonance transfer, highlighting the positional characteristics of IS or PCS in the region of I. STD spectrum for IS showed a that a higher percentage of H2 on IS (Figure 2.6A) was involved than other protons: H2 – 48.88%, H3 – 30.54%, H4 – 30.12%, H5 – 27.47%, and H6 – 25.35%. Therefore, binding most likely involved the sulfated group. This result is in good agreement with our ITC results that showed an electrostatic interaction was the main driving force of IS binding with HAS. For PCS, H3 and H4 was 24.78%, H1 and H7 was 23.52%, H2 and H6 was 24.44%, which suggested no significant enhancement of local proton signals. This can be explained by the relative linear and symmetrical spatial configuration of PCS, leading to a smaller steric hinderance compared with IS, and a more homogeneous fit within the binding site as evidenced by an equal resonance transfer over the entire molecule.

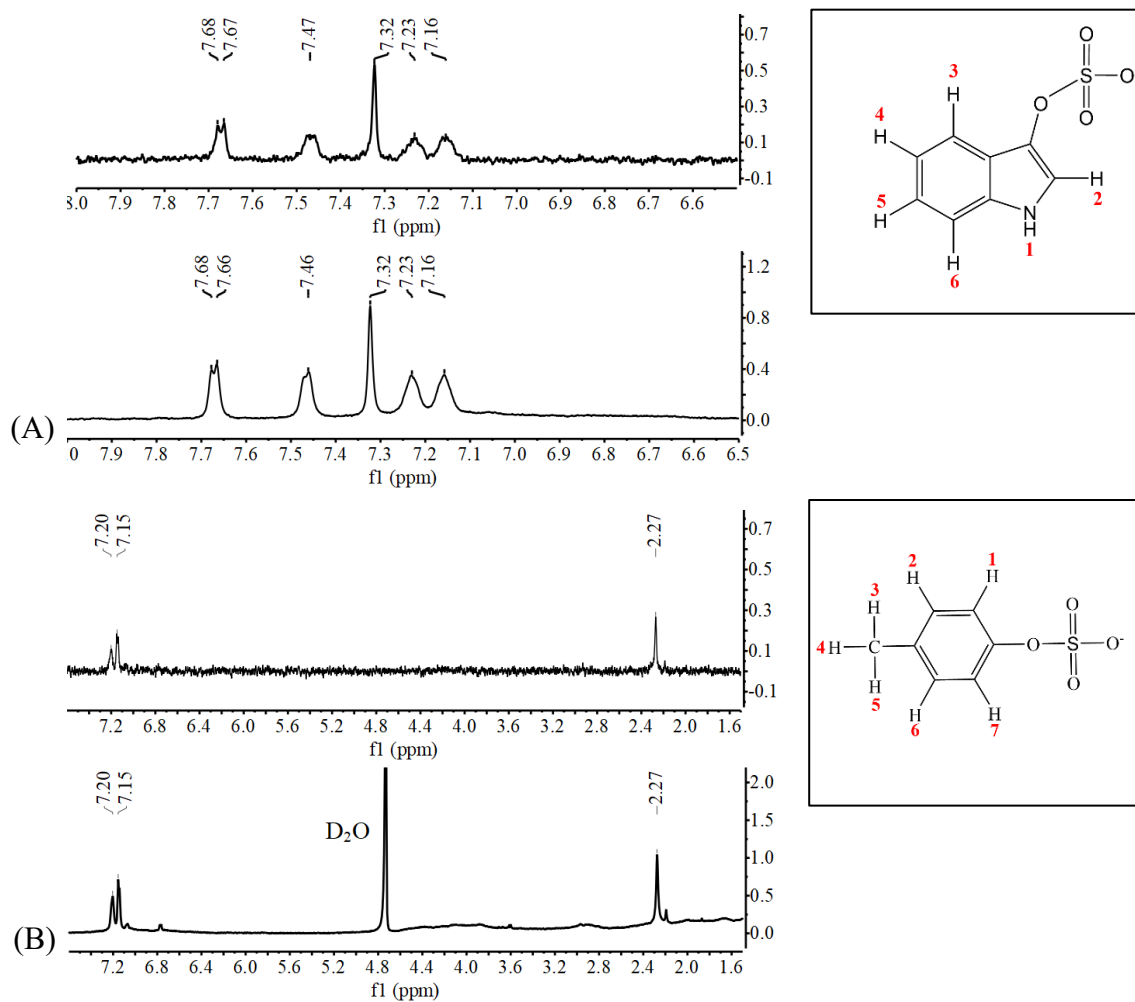


Figure 2.6 Detection of IS and PCS bind with I. $[I] = 30 \text{ mM}$, $[IS] = [PCS] = 1.5 \text{ mM}$. (A). Upper panel: STD spectrum of IS with I. Lower panel: NMR spectrum of off-resonance IS and I mixture solution. (B) Upper panel: STD spectrum of PCS with I. Lower panel: NMR spectrum of off-resonance IS and I mixture solution. Integrated area (H1 stands for upper panel, H1' stands for lower panel. Similarly, hereinafter): IS, H1(1.97), H2(1.07), H3(1.14), H4(1.19), H5(1.17). H1'(4.03), H2'(4.22), H3'(4.15), H4'(3.95), H5'(3.83). PCS, H1 and H7 (1.12), H2 and H6 (1.74), H3-H5(2.54). H1' and H7' (7.14), H2'and H6' (7.12), H3'-H5' (10.9).

2.3.5 Identification of IS or PCS binding site on I

A competitive STD-NMR displacement experiment was conducted to further confirm the preferred I binding site for IS or PCS. Upon adding warfarin to an I+IS solution it was observed that the IS signal intensity decreased ~42.9% (Figure 2.7 A). Furthermore, as the concentration of ibuprofen increased in an I-IS solution, the IS signal intensity decreased ~64.3% (Figure 2.7 C(c-f)). These results indicated the differential displacement of IS due to the competing presence of ibuprofen or warfarin, proving that IS was largely present in both the site I and site II of I. This result stands in contrast to previous reports that IS was only found in site II [45, 46]. Similarly, only a slight decrease of ~12.5% in PCS signal intensity occurred upon the addition of ibuprofen to an I+PCS solution (Figure 2.7 D) and no significant change was observed upon warfarin addition to a similar solution (Figure 2.7 B); indicating that PCS seemed to reside only within site II, as previously reported [47, 48]. Moreover, ITC results indicated that both ibuprofen and warfarin were able to displace IS and PCS, whereas only ibuprofen displaced both IS and PCS in STD-NMR experiment. This result suggested that IS and PCS share binding site II. Furthermore, due to the fact that IS possessed a higher binding affinity than PCS (ITC results), and ibuprofen and warfarin had the capability of displacing IS and not PCS indicates that neither site are the preferred binding site for PCS. This is further evidenced by the fact that our ITC results showed an unbinding activity due to the introduction of warfarin to I+PCS solutions. Thus, we can conclude that there is an unknown binding site on I for PCS that was unaffected by warfarin addition.

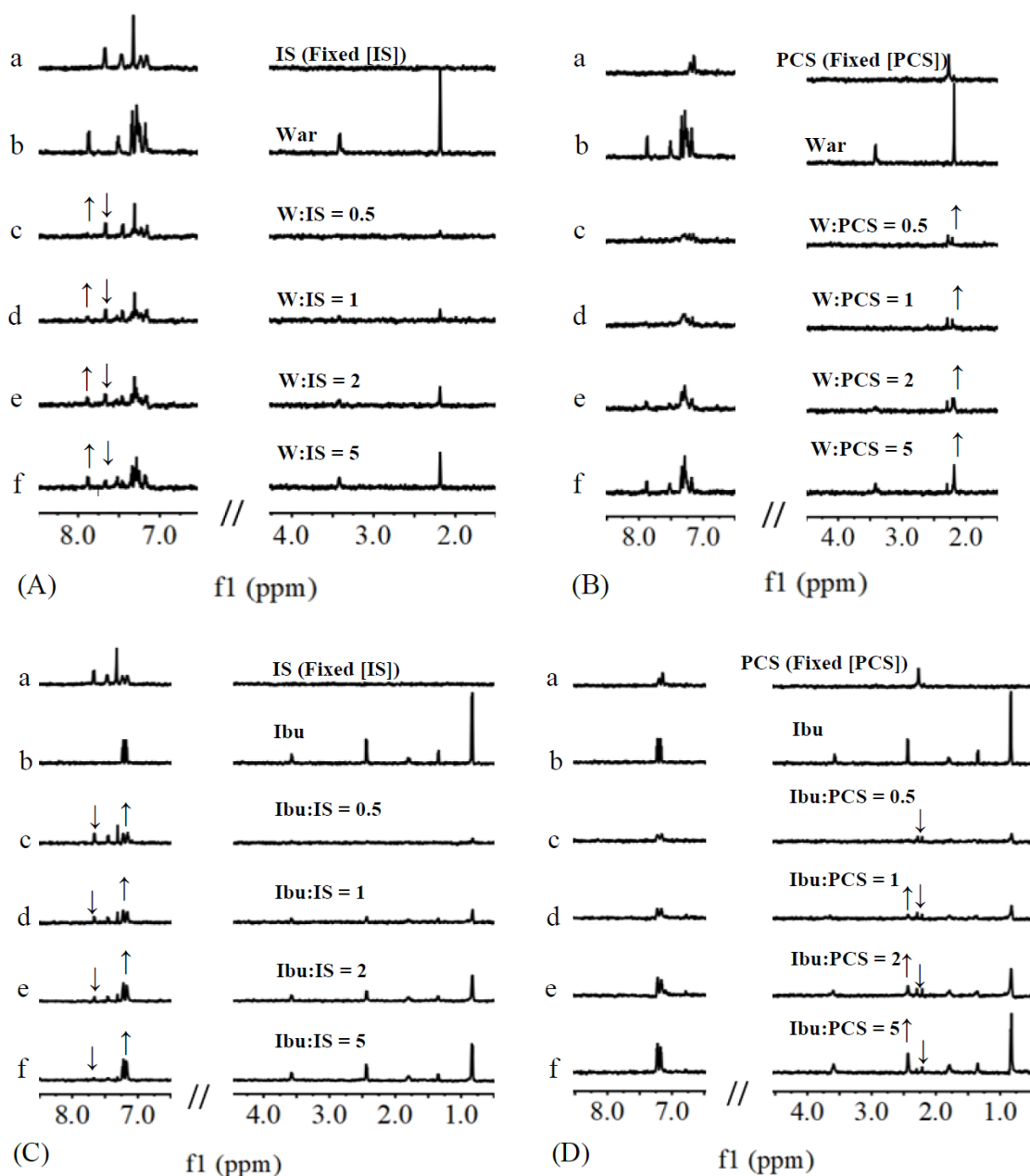


Figure 2.7 ^1H NMR spectrum: A(a), C(a): IS. B(a), D(a): PCS. A(b), B(b): warfarin. C(b), D(b) ibuprofen. STD spectrum ($[\text{I}]=0.1\text{mM}$, $[\text{IS}]=[\text{PCS}]=0.1\text{mM}$, $n(\text{Site indicator})$: $n(\text{Toxin})= 0.5, 1, 2, 5$ for (c) to (f)): A(c)-A(f): warfarin with gradient concentration is added into I+IS mixtrure. B(c)-B(f): warfarin with gradient concentration is added into I+PCS mixtrure. C(c)-C(f): ibuprofen with gradient concentration is added into I+IS mixtrure. D(c)-D(f): ibuprofen with

gradient concentration is added into I+PCS mixture. Arrows denoted the signal increasing or decreasing peak intensity.

2.4 Conclusion

The mechanisms responsible for IS and PCS interactions with human serum albumin were investigated using isothermal titration calorimetry, NMR, as well as several spectroscopic techniques under simulated physiological conditions. An electrostatic interaction was indicated *via* ITC results to be the main driver for IS or PCS binding with HSA, and was further verified using STD NMR. Though ibuprofen possessed a higher binding affinity to I, compared to PCS and IS, the binding mechanism arose from the combined effects of hydrophobic and electrostatic interactions. Fluorescence experiments indicated that I was statically quenched by IS or PCS. Circular dichroism results indicated that the addition of IS or PCS significantly altered the secondary structure of I, with decreased α -helix content of 40.77% and 47%, respectively. STD NMR directly verified binding of IS or PCS to I and indicated the most possible binding position was the sulfated group end. The competitive displacement experiment suggested IS and PCS share binding site II, where site II is the preferred site for IS interaction with I. Whereas, PCS was located on site II and an unknown binding site. It is thought that the complete characterization of how IS or PCS interacts with I will lead to the development of better methods for inhibiting PBUT bound with I, and lead to better clinical outcomes for hemodialysis patients.

2.5 References

1. Liabeuf, S., et al., *Protein-bound uremic toxins: new insight from clinical studies*. *Toxins*, 2011. **3**(7): p. 911-919.
2. Shi, Y., et al., *Increasing the removal of protein-bound uremic toxins by liposome-supported hemodialysis*. *Artificial Organs*, 2019. **43**(5): p. 490-503.
3. Liu, W., et al., *Impacts of indoxyl sulfate and p-cresol sulfate on chronic kidney disease and mitigating effects of AST-120*. *Toxins*, 2018. **10**(9): p. 367.
4. Khan, M.W.A., et al., *Biochemical, biophysical, and thermodynamic analysis of in vitro glycated human serum albumin*. *Biochemistry (Moscow)*, 2007. **72**(2): p. 146-152.
5. Morissette, M., *Colloid osmotic pressure: its measurement and clinical value*. *Canadian Medical Association Journal*, 1977. **116**(8): p. 897.
6. Quinlan, G.J., et al., *Albumin: biochemical properties and therapeutic potential*. *Hepatology*, 2005. **41**(6): p. 1211-1219.
7. Kragh-Hansen, U., et al., *Detergents as probes of hydrophobic binding cavities in serum albumin and other water-soluble proteins*. *Biophysical Journal*, 2001. **80**(6): p. 2898-2911.
8. Sudlow, G., et al., *The characterization of two specific drug binding sites on human serum albumin*. *Molecular Pharmacology*, 1975. **11**(6): p. 824-832.
9. Peters Jr, T., *All about albumin: biochemistry, genetics, and medical applications*. 1995: Academic Press.
10. Fanali, G., et al., *Human serum albumin: from bench to bedside*. *Molecular Aspects of Medicine*, 2012. **33**(3): p. 209-290.
11. Sudlow, G., et al., *Further characterization of specific drug binding sites on human serum albumin*. *Molecular Pharmacology*, 1976. **12**(6): p. 1052-1061.

12. Ghuman, J., et al., *Structural basis of the drug-binding specificity of human serum albumin*. Journal of Molecular Biology, 2005. **353**(1): p. 38-52.
13. Bhattacharya, A.A., et al., *Binding of the general anesthetics propofol and halothane to human serum albumin: high resolution crystal structures*. Journal of Biological Chemistry, 2000. **275**(49): p. 38731-38738.
14. Wang, C., et al., *Skin autofluorescence is associated with endothelial dysfunction in uremic subjects on hemodialysis*. PloS One, 2016. **11**(1): p. e0147771.
15. Gajjala, P.R., et al., *Emerging role of post-translational modifications in chronic kidney disease and cardiovascular disease*. Nephrology Dialysis Transplantation, 2015. **30**(11): p. 1814-1824.
16. Rueth, M., et al., *Guanidinylation of albumin decreased binding capacity of hydrophobic metabolites*. Acta Physiologica, 2015. **215**(1): p. 13-23.
17. Badar, A., et al., *Carbamylation of human serum albumin generates high-molecular weight aggregates: fine characterization by multi-spectroscopic methods and electron microscopy*. International Journal of Biological Macromolecules, 2020. **164**: p. 2380-2388.
18. Martinez, A.W., et al., *Removal of P-cresol sulfate by hemodialysis*. Journal of the American Society of Nephrology, 2005. **16**(11): p. 3430-3436.
19. Pham, N.M., et al., *Removal of the protein-bound solutes indican and p-cresol sulfate by peritoneal dialysis*. Clinical Journal of the American Society of Nephrology, 2008. **3**(1): p. 85-90.
20. Rocchetti, M.T., et al., *Efficacy of Divinylbenzenic Resin in Removing Indoxyl Sulfate and P-cresol Sulfate in Hemodialysis Patients: Results from an In Vitro Study and an In Vivo Pilot Trial (xuanro4-Nature 3.2)*. Toxins, 2020. **12**(3): p. 170.

21. Patel, K.P., et al., *The production of p-cresol sulfate and indoxyl sulfate in vegetarians versus omnivores*. Clinical Journal of the American Society of Nephrology, 2012. **7**(6): p. 982-988.
22. Devine, E., et al., *Binding affinity and capacity for the uremic toxin indoxyl sulfate*. Toxins, 2014. **6**(2): p. 416-429.
23. Bergé-Lefranc, D., et al., *Binding of p-cresylsulfate and p-cresol to human serum albumin studied by microcalorimetry*. The Journal of Physical Chemistry B, 2010. **114**(4): p. 1661-1665.
24. Frazier, R.A., et al., *Isothermal titration calorimetry study of epicatechin binding to serum albumin*. Journal of Pharmaceutical Biomedical Analysis, 2006. **41**(5): p. 1602-1605.
25. Nakamura, S., et al., *A new multi-binding model for isothermal titration calorimetry analysis of the interaction between adenosine 5'-triphosphate and magnesium ion*. Thermochimica Acta, 2013. **563**: p. 82-89.
26. Dehkordi, M.N., et al., *Comprehensive study on the binding of iron Schiff base complex with DNA and determining the binding mode*. Journal of Fluorescence, 2013. **23**(4): p. 813-821.
27. Ràfols, C., et al., *Molecular interactions between warfarin and human (HSA) or bovine (BSA) serum albumin evaluated by isothermal titration calorimetry (ITC), fluorescence spectrometry (FS) and frontal analysis capillary electrophoresis (FA/CE)*. Journal of Pharmaceutical Biomedical Analysis, 2018. **150**: p. 452-459.
28. Honoré, B., et al., *Albumin binding of anti-inflammatory drugs. Utility of a site-oriented versus a stoichiometric analysis*. Molecular Pharmacology, 1984. **25**(1): p. 137-150.

29. Hage, D.S., et al., *Characterization of the protein binding of chiral drugs by high-performance affinity chromatography interactions of R-and S-ibuprofen with human serum albumin*. Journal of Chromatography A, 1995. **693**(1): p. 23-32.
30. Fatima, S., et al., *Hydrophobic interaction between domain I of albumin and B chain of detemir may support myristate-dependent detemir-albumin binding*. Applied Biochemistry Biotechnology, 2017. **182**(1): p. 82-96.
31. Zhang, G., et al., *Polyoxometalate binding to human serum albumin: a thermodynamic and spectroscopic approach*. The Journal of Physical Chemistry B, 2007. **111**(38): p. 11253-11259.
32. Demers, J., et al., *Binding mechanism of an SH3 domain studied by NMR and ITC*. Journal of the American Chemical Society, 2009. **131**(12): p. 4355-4367.
33. Jourde-Chiche, N., et al. *PROGRESS IN UREMIC TOXIN RESEARCH: Protein-Bound Toxins—Update 2009*. in *Seminars in dialysis*. 2009. Wiley Online Library.
34. Madero, M., et al., *Removal of protein-bound uremic toxins during hemodialysis using a binding competitor*. Clinical Journal of the American Society of Nephrology, 2019. **14**(3): p. 394-402.
35. Li, J., et al., *Response regulators CheB and CheY exhibit competitive binding to the kinase CheA*. Biochemistry, 1995. **34**(45): p. 14626-14636.
36. Zhang, G., et al., *Study of the interaction between icariin and human serum albumin by fluorescence spectroscopy*. Journal of Molecular Structure, 2008. **881**(1-3): p. 132-138.
37. Melamed, M.L., et al., *Retained organic solutes, patient characteristics and all-cause and cardiovascular mortality in hemodialysis: results from the retained organic solutes and clinical outcomes (ROSCO) investigators*. BMC Nephrology, 2013. **14**(1): p. 1-10.

38. Lakowicz, J.R., *Principles of Fluorescence Spectroscopy 3rd ed.* New York City. 2011, USA: Springer Science.
39. Tang, J., et al., *Binding analysis of glycyrrhetic acid to human serum albumin: Fluorescence spectroscopy, FTIR, and molecular modeling.* Bioorganic Medicinal Chemistry, 2006. **14**(9): p. 3210-3217.
40. Samari, F., et al., *Affinity of two novel five-coordinated anticancer Pt (II) complexes to human and bovine serum albumins: a spectroscopic approach.* Inorganic Chemistry, 2012. **51**(6): p. 3454-3464.
41. Lakowicz, J.R., *Protein fluorescence*, in *Principles of fluorescence spectroscopy*. 1983, Springer. p. 341-381.
42. Vivian, J.T., et al., *Mechanisms of tryptophan fluorescence shifts in proteins.* Biophysical Journal, 2001. **80**(5): p. 2093-2109.
43. Zhang, G., et al., *Probing the binding of the flavonoid diosmetin to human serum albumin by multispectroscopic techniques.* Journal of Agricultural Food Chemistry, 2012. **60**(10): p. 2721-2729.
44. Bakar, K.A., et al., *A critical view on the analysis of fluorescence quenching data for determining ligand–protein binding affinity.* Spectrochimica Acta Part A: Molecular Biomolecular Spectroscopy, 2019. **223**: p. 117337.
45. Sakai, T., et al., *Interaction mechanism between indoxyl sulfate, a typical uremic toxin bound to site II, and ligands bound to site I of human serum albumin.* Pharmaceutical Research, 2001. **18**(4): p. 520-524.
46. Sakai, T., et al., *Characterization of binding site of uremic toxins on human serum albumin.* Biological Pharmaceutical Bulletin, 1995. **18**(12): p. 1755-1761.

47. Watanabe, H., et al., *Interaction between two sulfate-conjugated uremic toxins, p-cresyl sulfate and indoxyl sulfate, during binding with human serum albumin*. *Drug Metabolism Disposition*, 2012. **40**(7): p. 1423-1428.
48. Viaene, L., et al., *Albumin is the main plasma binding protein for indoxyl sulfate and p-cresyl sulfate*. *Biopharmaceutics Drug Disposition*, 2013. **34**(3): p. 165-175.

Chapter 3

Dynamic adsorption profile for uremic toxins to beta-cyclodextrin, 2-(methacryloyloxy)ethyl phosphorylcholine modified magnetic nanoparticles.

This chapter was submitted to Macromolecular Bioscience as “Adsorption dynamics of uremic toxins to novel modified magnetic nanoparticles.”, and it is currently in revision.

*Author List: Shuhui Li, Mehdi Ghaffari Sharaf, Lun Zhang, David S. Wishart, Marcello Tonelli, and Larry D. Unsworth **

Contribution: Li, Shuhui conceptualized the research, wrote and edited the manuscript, conducted the experiment of synthesis, characterization, and analyzed and visualized the data. Mehdi Ghaffari Sharaf performed experiments, Lun Zhang conducted LC/MS experiment, David S. Wishart supervised LC/MS work, Marcello Tonelli reviewed and edited the manuscript, Larry D. Unsworth reviewed, edited the manuscript, visualized data, conceptualized and supervised the research.

3.1 Introduction

Reduced glomerular filtration rate is often referred to as “kidney dysfunction”, which causes the accumulation of certain molecules in the blood compartment. These molecules are colloquially referred to as “uremic toxins” despite the fact that direct links to toxicity for all of these metabolites has not been accomplished. Chronic kidney disease (CKD) is a globally prevalent disease, with multi-factorial pathogenesis; diabetes and hypertension being recognized as the most common etiological factors [1]. Hemodialysis is the most common treatment worldwide for this disease. Although it is life-saving, hemodialysis is associated with adverse health outcomes and unacceptably poor quality of life, while creating excessive plastic and water waste and costing >\$72,000 USD per patient per year [2]. Wearable devices that use adsorbents to clear toxins from the blood are considered the future of dialysis treatments and could potentially overcome many of the limitations associated with membrane-based hemodialysis. The design of the adsorbent for these devices is key to uremic toxin removal. A recent and comprehensive review of adsorbent-assisted uremic toxins removal from our lab has surveyed the current technology that span a range of sophistication, from activated carbon to molecular imprinted polymers, zeolites, and a variety of nanoparticles [3].

Previous work has evaluated solutions like carbon adsorbents with both micro and meso porosity that achieved the adsorption of uremic toxins of different molecular weight ranges [4]. Polymeric chemisorbents, abundant in ninhydrin groups, have been studied for urea adsorption [5]. Magnetic nanoparticles have inherently advantageous properties that make them amenable for toxin adsorption: cost-efficient, easy to regenerate, biodegradable, ability to control their location, ease in surface modification, high surface area for capturing toxins, and general biocompatibility [6-9]. Moreover, the abundant hydroxyl groups on the surface of MNPs allow for polymerization,

making MNPs highly versatile and applicable to a variety of uses. That said, there is a dearth in the literature investigating the adsorption of uremic toxins, and existing studies usually consider only indoxyl sulfate or p-cresol sulfate adsorption [3]; even then usually only from single component buffers. Truly the accumulation of indoxyl sulfate and p-cresol sulfate in the blood compartment leads to severe health complications [10-12], but these are not the only identified uremic toxins retained in kidney dysfunction [13-16]. For example, organic acids and polyamines are other types of protein-bound uremic toxins that may be related to acidosis, cancer, and the progression of chronic kidney disease [11, 17, 18]. New methods for specific compound adsorption could potentially fill this gap, but no work has shown the effect of surface properties on toxin adsorption from complex solutions. Progress in the field of engineered surface adsorption may allow the widespread utilization of wearable kidney devices, providing a more convenient and efficacious treatment option for patients with CKD.

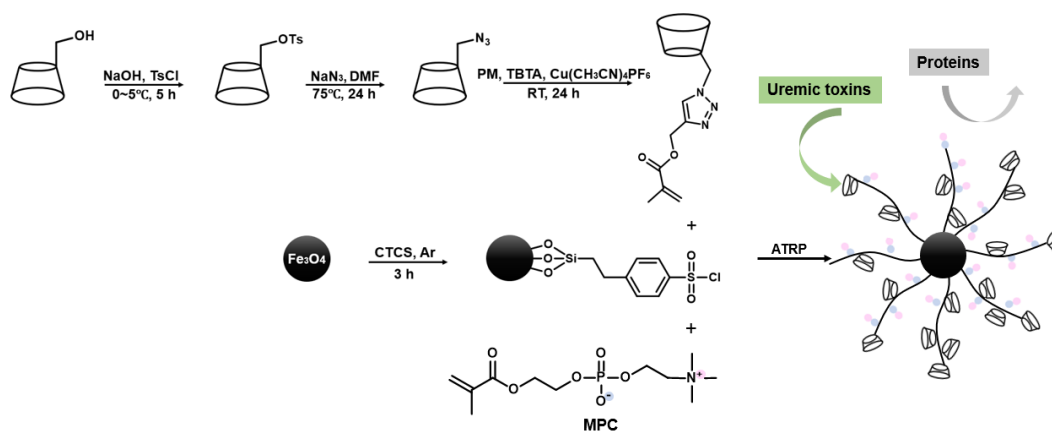
Given that these engineered surfaces need to contact blood, protein adsorption will be crucial to developing toxin-adsorbing surfaces. As such, 2-(methacryloyloxy)ethyl phosphorylcholine (MPC) is a low-fouling polymer that stands out due to its zwitterionic properties, hydration, and net neutral charge [19-23]; crucial attributes for inhibiting protein adsorption at MPC-modified surfaces [24-26]. β -Cyclodextrin (β -CD) was copolymerized with MPC so as to enhance the film's ability to bind uremic toxins. Moreover, compared to the other cyclodextrins, β -CD has an increased ability to bind to small hydrophobic ligands due to its optimal internal diameter size [27]. Therefore, previous research has utilized β -CD as a functional decoration for the inclusion of uremic toxins. For example, a multi-site polycyclodextrin adsorbent, achieving a 96% adsorption rate for p-cresol sulfate was developed [16]. In another study, an adsorption membrane layer for the elimination of bilirubin, demonstrating an adsorption rate of

97.8% was tested [28]. Additionally, β -cyclodextrin-co-toluene diisocyanate was used to form a nanosponge that adsorbed 90% indole [15]. That said, the adsorption from a complex solution with different incubation times remain largely ill-defined.

Based on these earlier results and making use of new innovations in magnetic nanoparticles, we synthesized poly(β -cyclodextrin-co-2-(methacryloyloxy)ethyl phosphorylcholine) (p(β -CD-co-MPC)) coated magnetic nanoparticles. This represents a novel, multifunctional copolymer that could serve as an effective engineered adsorbent for uremic toxin removal. Using ATRP synthesis and click-chemistry (Scheme.1), magnetic particles were modified with p(β -CD-co-MPC) with controlled amounts of β -CD within the film. The film properties were characterized using Fourier-transform infrared spectroscopy (FT-IR), thermogravimetric testing (TGA), transmission electron microscopy (TEM), and Gel permeation chromatography (GPC). To better simulate true uremia, a chemically diverse uremic toxin solution, comprised of organic acids, polyamines, and sulfates (Table 3.1) was constructed for measuring the adsorption capacity of these engineered adsorbents. Uremic toxin adsorption was evaluated using quantitative liquid chromatography–mass spectrometry (LC-MS) to quantify the adsorption of uremic toxins relative to their differing surface chemistry and incubation time. This systematic study comprehensively evaluated the chemical/physical characteristics of the p(MPC-co-PM β CD) MNPs, the effect that differing surface chemistries has on uremic toxin adsorption, as well as revealing if the toxin adsorption is dynamic. This information will inform the future development of engineered adsorbents for these and other uremic toxins.

Table 3.1 Composition of uremic toxin solutions developed based on literature analysis of the blood of patients with kidney dysfunction.

Uremic toxins	Solution composition (mol%)	Experimental concentration (mg/L)	Literature concentration (mg/L)	Ref
3-Deoxyglucosone	0.36	1.7	1.7 ± 1.0	[29]
4-Ethylphenyl sulfate	0.04	0.25	0.242 ± 0.044	[30]
4-Hydroxyphenylacetic acid	0.57	2.5	2.43 ± 2.28	[31]
Dimethyl glycine	0.20	0.59	0.5768	[29]
Guanidinopropionic acid	0.08	0.29	0.288 ± 0.0183	[29]
Hippuric acid	45.79	236.0	247.0 ± 112	[29]
Indole-3-acetic acid	0.40	2.03	2.03 ± 0.38	[32]
Indoxyl glucuronide	0.28	2.5	2.5 ± 0.3	[32]
Indoxyl sulfate	8.64	53.0	53.0 ± 91.5	[29]
p-Cresol sulfate	3.46	20.9	20.9 ± 12.2	[32]
Phenylalanine	1.95	9.25	8.92 ± 1.81	[33]
p-Hydroxyhippuric acid	0.76	4.25	4.43 ± 2.79	[34]
Pyruvic acid	4.62	11.7	5~11.7 ± 8.6	[35]
Quinolinic acid	0.02	0.084	0.0835	[36]
Spermidine	0.02	0.096	0.097 ± 0.045	[32]
Trimethylamine N-oxide	3.47	7.5	7.49 ± 2.39	[37]
Uric acid	17.17	83	83 ± 13	[38]
Xanthine	0.34	1.5	1.5 ± 0.8	[39]
Xanthosine	11.82	96.6	96.6 ± 62.9	[40]



Scheme 1. Synthesis route for p(MPC-co-PMβCD) coated magnetic nanoparticles.

3.2 Experimental

3.2.1 Materials

p-Toluenesulfonyl chloride (TsCl, reagent grade, $\geq 98\%$, Sigma Aldrich), 2-(4-Chlorosulfonylphenyl) ethyl trichlorosilane (CTCS, 50% in toluene, Gelest), Sodium azide ($\geq 99\%$, Fisher Scientific), propargyl methacrylate (PM, 98%, Alfa Aesar), β -Cyclodextrin ($\geq 97\%$, Sigma Aldrich), 2,2'-bipyridyl (bpy, $> 99\%$, copper(I)bromide ($> 98\%$), copper(II)bromide (99%), Tris[(1-benzyl-1H-1,2,3-triazol-4-yl)methyl]amine (TBTA, Trichemicals), Dialysis Tubing 500 MWCO (Cole-Parmer), Lewatit TP 207 adsorbent, TetrakisacetonitrilecopperI hexafluorophosphate ($\text{Cu}(\text{CH}_3\text{CN})_4\text{PF}_6$, Sigma Aldrich), 2-Methacryloyloxyethyl phosphorylcholine (MPC, Sigma Aldrich), ultra-thin carbon-coated copper grid (150 mesh, Ted pella, Inc.), Sodium Hydroxide (Fisher Scientific), $\text{FeCl}_2 \cdot 4\text{H}_2\text{O}$, $\text{FeCl}_3 \cdot 6\text{H}_2\text{O}$ and of ammonium hydroxide solution (25%) were purchased from Sigma Aldrich. Uremic toxin solution compounds: 3-Deoxyglucosone, 4-Ethylphenyl sulfate, Argininic acid, Asymmetric dimethylarginine, Creatinine, Dimethyl glycine, Guanidinopropionic acid, Hippuric acid, Homocysteine, Hypoxanthine, Indole acetic acid, Indoxyl glucuronide, Indoxyl sulfate, Kynurenine, Methyl histidine, Orotic acid, *p*-Cresol sulfate, Phenylacetic acid, Phenylalanine, *p*-Hydroxyhippuric acid, *p*-Hydroxyl phenylacetic acid, Putrescine, Pyruvic acid, Quinolinic acid, Spermidine, Spermine, Trimethylamine N-oxide, Uric acid, Uridine, Xanthine, Xanthosine, l-Tyrosine, l-Asparagine were all purchased from Sigma Aldrich. Optima™ LC/MS grade formic acid and HPLC grade water were purchased from Fisher Scientific. HPLC grade pyridine, LC/MS grade methanol, LC/MS grade ethanol, Tetrahydrofuran (THF) and LC/MS grade acetonitrile (ACN) were purchased from Sigma-Aldrich. Argon and nitrogen (99.999%) were used as blanket gases for all chemical reactions and some characterization techniques.

3.2.2 Molecular Characterization

Nuclear magnetic resonance (NMR) analysis was carried out using an Agilent 400 NMR (Agilent Technologies, USA) at 298K. Samples were dissolved in CDCl_3 , DMSO-d_6 or D_2O . FTIR spectra were recorded using Agilent Cary 670 FTIR Microscope (Agilent Technologies, USA), samples were dried in vacuum overnight prior to measurements as conducted under N_2 blanket using ATR mode. TGA was conducted on samples dried in vacuum overnight prior to measurement using TA Q50 TGA (TA instrument, USA). The heating range was set between 30 ~ 900 °C, with ramp of 10°C/min in nitrogen atmosphere. Error was calculated using data from different batches but same experimental conditions.

TEM was conducted using a JEM-ARM200CF S/TEM (JEOL, USA) with an accelerating voltage of 200 kV to collect images of particles that were further analyzed using ImageJ. Samples were prepared by depositing a droplet of a well-dispersed sample onto an ultra-thin carbon-coated copper grid and allowed to dry for 24 hrs in open air prior to characterization.

GPC was conducted with a Waters gel permeation chromatography system (Waters, USA) to obtain the molecular weight (MW) and polydispersity index (PDI) of grafted polymers once cleaved from the nanoparticle surface by etching the magnetic core with hydrochloric acid [41]. T6000m column from Viscotek was equipped with the Waters 1515 Isocratic HPLC Pump and Waters 2414 Refractive Index Detector to measure the MW at 40 °C. The eluent fluid (toluene) was used with a flow rate of 1 mL/min. Six polystyrene polymers with different MWs (1,000 - 200,000) and PDI (1.1 -1.2) were used to calibrate the column so as to quantify the MW of formed polymer.

Zeta potential measurements were performed using a Malvern Zetasizer Nano-ZS (Nano ZS, Malvern Instruments, Malvern, UK) to determine the zeta potential of the engineered surface. A sample was prepared by adding 25 μL of 1 mg/mL MNPs suspension into 3 mL DI water and applying 30 s of ultrasound prior to measuring the zeta potential. An average zeta potential was obtained from three repetitions, with 12 runs in each repetition.

3.2.3 Toxin solution

A concentrated stock solution of individual uremic toxins (Table 3.1) was made immediately prior to use and stored at 4 $^{\circ}\text{C}$ (or on ice) for a limited time between handlings. Concentrated stock solutions were added into the 200 mL cylinder, except uric acid, and the volume increased to 90 mL using HPLC grade water. Uric acid powder was added before finalizing the solution to 100 mL, an equal volume of 20 mM PBS solution was used to dilute the solution, yielding a uremic toxin in 10 mM PBS, pH 7.4, that was aliquoted and stored at -80 $^{\circ}\text{C}$ until used.

3.2.4 LC/MS quantification of adsorbed toxin profile

Constant surface area ($\sim 287 \text{ m}^2$) of polymer coated MNP samples (0.25 mg by mass) were incubated with the uremic toxin solution (0.5 mL) for 1 and 4 hr, respectively. Prior to experiment, all tubes were washed twice using HPLC grade methanol and vacuum dried. After incubation with the uremic toxin solution the MNPs were magnetically separated, and remaining water droplets gently blown off using nitrogen flow to avoid spurious readings due to entrapped water. HPLC grade methanol (100 μL) was added to the MNPs and allowed to mix for 24 hr to ensure desorption of uremic toxins.

A quantitative MS-based metabolomics approach, reverse-phase high performance liquid chromatography (HPLC) tandem mass spectroscopy, was used to analyze the uremic toxins eluted

from the MNPs using methanol. An Agilent 1290 series UHPLC system and an Agilent reversed-phase Zorbax Eclipse XDB C18 column (3.0 mm × 100 mm, 3.5 μm particle size, 80 Å pore size) were used for online LC-MS/MS with an AB SCIEX QTRAP® 5500 mass spectrometer. Analyst® 1.6.3 was used as the controlling software. Positive/negative electrospray ionization was applied with multiple reaction monitoring (MRM) mode. The profiling of the metabolomics raw data was performed using Multi Quant™ 3.0.3. Notably, 20% error in LC/MS is considered normal [42].

3.3 Results and discussion

3.3.1 Synthesis

3.3.1.1 Synthesis of Fe₃O₄ nanoparticles (MNP)

A three-neck round-bottom flask was filled with N₂, FeCl₂·4H₂O (1 g, 5.0 mmol) and FeCl₃·6H₂O (2.6 g, 9.6 mmol) dissolved in 25 mL degassed water, stirred at 400 rpm (75°C) for 10 min, 10 mL of ammonium hydroxide solution (25%) added slowly, and stirring increased to 600 rpm. The reaction was terminated after stirring for 1.5 hr. Resulting nanoparticles were washed with water and ethanol thrice, magnetically separated from solution, and vacuum dried.

3.3.2 Surface polymer synthesis

3.3.2.1 ATRP initiator fixation on MNP

A three-neck flask was degassed and refilled with argon prior to use. Dehydrated toluene (200 mL) used to suspend MNP (500 mg) under ultrasound and argon atmosphere. Dropwise addition of CTCS (5 mL) was done after 15 min and left to react for 3 hrs. Modified MNP were washed three times with THF and twice with ethanol *via* consecutive separation and redispersion. Finally, MNP-CTCS was dried under vacuum overnight and stored under argon blanket.

3.3.3 Thermogravimetric analysis of bare and coated MNPs

TGA spectra for all MNPs are summarized in Figure 3.2 and the percent weight loss for each system as a function of temperature range are summarized in Table 3.3. The mass loss before 100 °C was due to the loss of bulk water, likely entrapped within the matrix of particles. Mass loss between 100-200 °C coincides with the loss of vicinal water, bare MNP has a lower bulk and vicinal water content due to the lack of the polymer film. The mass loss between 200-380 °C arose from the breaking of C–O bond and C–C bonds, the mass loss in this range was highest for p(PM β CD)-MNP (16 %) and decreased as the PM β CD component reduced; this is expected given PM β CD has 50 C–O bonds in each monomer whereas MPC only has 2. The breakdown of C–O bonds will lead to the large mass loss of PM β CD monomer. The mass loss observed at 380-500 °C was due to the breaking of C=O that exist in both PM β CD and MPC monomers [43]. The loss above 590°C from decomposition of the triazole groups and glucose monomers [44]. After the fixation of initiator, the O-H group on the virgin MNP surface was replaced by O-Si group, resulting in an increased particle electronegativity. Bond energy for the O-H group is 79 KJ/mol less than that of O-Si, thus the degradation temperature was higher for O-Si rich chemistry [45]. The average weight loss (n=3) for these particles was in good agreement with the GPC results for MW, where C accounted for the highest weight loss followed by B, A, D, and E. These results suggest that a similar number of chains were on each type of particle.

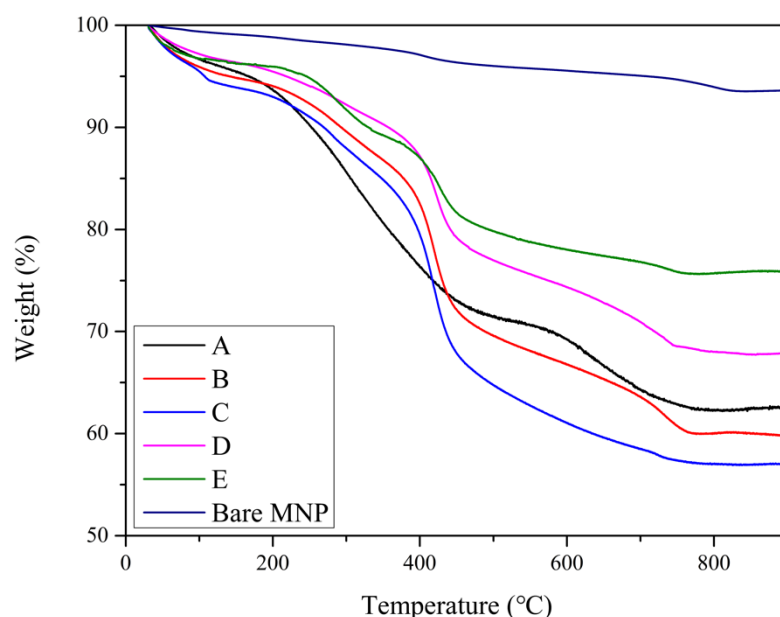


Figure 3.1 Representative TGA curves for bare and coated MNPs. Monomer ratio of PM β CD to MPC and the weight loss are A (1:0), 37.42%; B (3:1), 40.1%; C (1:1), 43.0%; D (1:3), 32.1%; E (0:1), 24.1%. The weight loss of bare MNP was 7.4%.

Table 3.2 Average percent weight loss from particles within specific temperature regimes as determined using TGA.

<i>T</i> (°C)	<100	100-200	200-380	380-500	>590
<i>Particle</i>					
<i>MNP</i>	1±0.2	1±0.1	1±0.0	1±0.1	2±0.0
<i>A</i>	3±1.1	3±0.7	16±1.2	7±0.0	7±0.1
<i>B</i>	4±0.5	2±1.1	12±1.0	15±0.5	7±0.2
<i>C</i>	5±0.8	2±0.7	11±0.9	18±1.1	4±0.0
<i>D</i>	3±0.3	2±0.3	9±0.2	12±0.6	3±0.1
<i>E</i>	3±0.4	1±0.6	8±0.2	8±0.4	2±0.0

3.3.4 Chemical composition and charge of coatings

FTIR spectra were collected for all systems and changes attributed to the presence of different bonds (Figure 3.3). FTIR spectra for pure MPC and PM β CD were collected for reference and the band at 560 cm⁻¹ attributed to the Fe–O bond for all MNPs [46]. The common intense peak at 1728 cm⁻¹ was related to the C=O of the ester group in both PM β CD and MPC monomers. The peaks for POCH₂ and N⁺(CH₃), located at 1253 and 1074 cm⁻¹, were used to confirm the presence of the MPC segment [47]. It was difficult to distinguish PM β CD from MPC or MNP as its characteristic bonds (i.e., carbon backbone, ester group, C–O and –OH) were common for all. The combination of the ester group with triazole was used to confirm the presence of PM β CD, as evidenced through the new peaks for the C–H bond of triazole ring at 2955 cm⁻¹ [48]. In Particle A, the presence of the triazole group and ester group peaks, coupled with the absence of POCH₂ and N⁺(CH₃) peaks, confirmed the presence of the PM β CD segment only. In contrast, the presence of POCH₂ and N⁺(CH₃) related peaks, in the absence of triazole group peak for Particle E, confirmed deposition of only MPC. Particles B, C, and D possessed all the functional peaks of PM β CD and MPC, suggesting co-polymer formation. Zeta potential of the series of engineered surface were characterized and recorded as follow: A: -6.4 \pm 0.63; B: -22.9 \pm 1.14; C: -24.7 \pm 1.67; D: -28.3 \pm 0.12; E: -23.1 \pm 0.94; Bare MNP: -11.3 \pm 0.99.

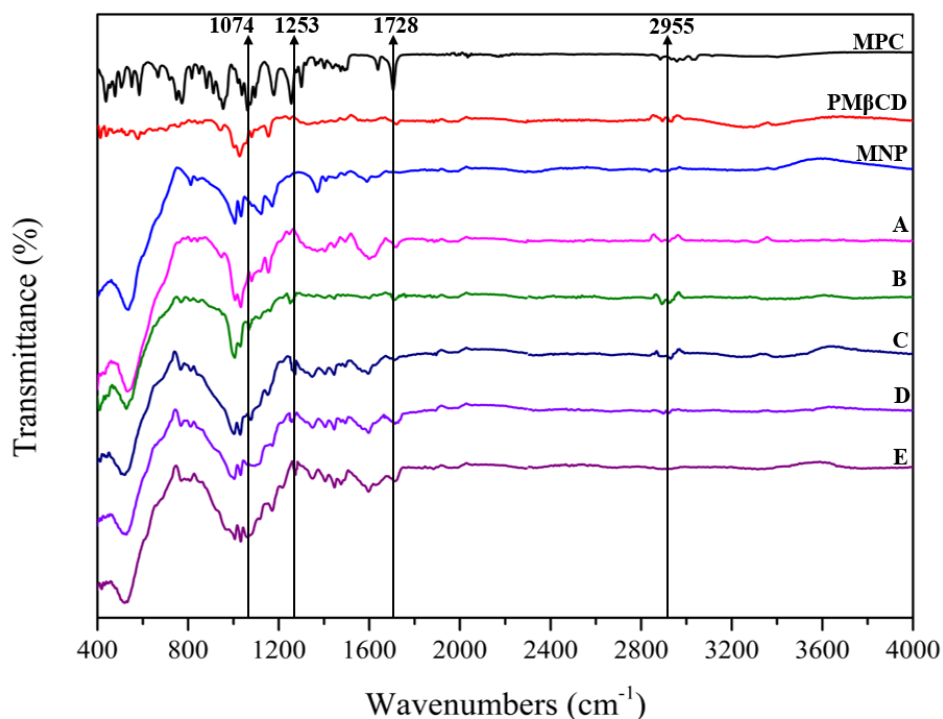


Figure 3.2 Representative FTIR spectra of pure MPC, PM β CD, bare MNP, and particles A to E. Monomer ratio of PM β CD to MPC are A (1:0), B (3:1), C (1:1), D (1:3), E (0:1).

3.3.5 Coating morphology analysis

The effect of coating on particle morphology was characterized using transmission (TEM) and scanning electron microscopy (SEM) (Figure 3.4). A total of 58 particles were selected for each system for determining both particle and film sizes, where virgin MNP had an average diameter of 11.87 ± 2.37 nm, with a normal distribution (Figure 3.4. (G)). The dried film thickness was estimated to range between 4.5 – 6 nm thick and its presence seemed to yield a smoother particle surface, qualitatively (Figure 3.4. (E)). The selected-area electron diffraction (SAED) pattern was typical for the crystal structure of magnetite, where both bare and polymer-coated MNP had a ring diffraction pattern that corresponded to (220), (311), (400), (420), (511) and (440) planes (JCPDS card No. 19-0629); this indicated a polycrystalline structure for the magnetic core [49].

Bare MNP also had a spot diffraction pattern that is common to Fe_3O_4 : both crystalline FeO and Fe_2O_3 .

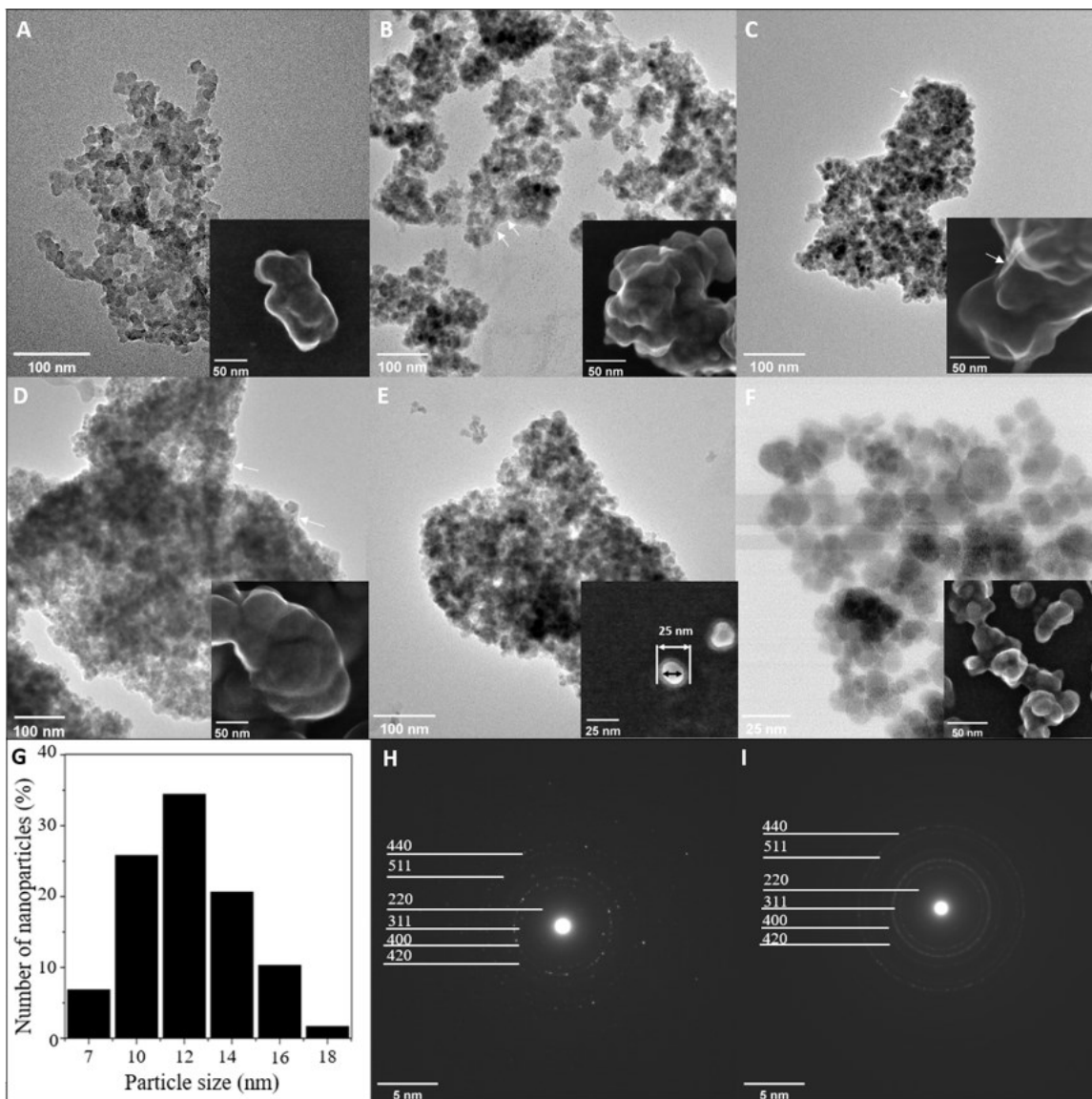


Figure 3.3 Representative TEM, SEM, and SAED characterization of bare and coated -MNPs. (A) - (E) TEM image of synthesized polymer modified nanoparticles of sample A-E; Right lower inset: Corresponding SEM image of sample A-E. White arrow indicated the polymer layer and black arrow indicated the MNP core size (15 nm). (F) TEM image of bare MNP with SEM inset.

(G) Particle size distribution of bare MNP in (F). (H) SAED pattern of MNP. (I) SAED pattern of particle A.

3.3.6 Profile of adsorbed uremic toxins for all particle systems

In order to understand the adsorption profile of the select uremic toxins to CD modified MPC films, films composed of MPC and PM β CD in various ratios were studied, *viz.*, A (0:4), B (1:3), C (1:1), D (3:1), and E (4:0). The binding capacity and binding dynamics for all systems were evaluated by incubating modified MNPs for 1 or 4 hr in the model uremic toxin solution (Table 3.1). The time point set-up fits the upper-limit of dialysis time duration. All particles adsorbed toxins from solution (Table 3.1), with obvious differences in the adsorbed toxinome as a function of the coating composition and incubation time (Tables 3.4 and 3.5). These differences in adsorption likely arose from a multitude of factors, including: (i) the chemical variety within the toxic compounds; (ii) solution concentration differences between toxins; and (iii) chemical composition differences between copolymers for different particles. Even though cyclodextrin was employed to be the main binding element for toxins, MPC itself has a phosphate anion and a trimethylammonium cation that may facilitate toxin capture directly.

Table 3.3 Quantitative LC/MS evaluation of adsorbed toxinome from Particles A through E, for 1 and 4 hr incubation times, respectively. Note that all values represent μM concentrations of eluted toxins, <LOD indicating a response below the level of detection for that species. Note that the experimental repeats yielded standard deviations less than the expected 20% inherent to targeted mass spectroscopy, however, an error of 20% in these values were used for all analysis.

(MPC:PM β CD)	A (0:4)			B (1:3)			C (1:1)		
	1 hr	4 hr (stdev)	Adsorption Amount	1 hr (stdev)	4 hr	Adsorption Amount	1 hr	4 hr (stdev)	Adsorption Amount
3-Deoxyglucosone	0.88	1.11 (0.18)	0.33	0.68 (0.17)	0.51	0.16	0.53	0.44 (0.08)	0.15
4-Ethylphenyl sulfate	0.15	0.23 (0.04)	0.06	0.14 (0.06)	0.09	0.03	0.09	0.08 (0.01)	0.03
4-Hydroxyphenylacetic acid	1.26	2.06 (0.76)	0.52	1.05 (0.44)	0.50	0.16	0.36	0.32 (0.25)	0.06
Dimethyl glycine	0.83	1.37 (0.38)	0.37	0.82 (0.22)	0.49	0.16	0.56	0.47 (0.05)	0.14
Guanidinopropionic acid	1.62	3.34 (0.71)	0.94	1.56 (0.89)	0.94	0.30	1.10	0.83 (0.20)	0.30
Hippuric acid	118.83	161.22 (26.57)	46.76	92.96 (30.81)	63.62	20.36	62.29	50.51 (17.08)	13.28
Indole-3-acetic acid	0.98	1.67 (0.33)	0.48	0.90 (0.42)	0.54	0.17	0.48	0.62 (0.20)	0.20
Indoxyl glucuronide	1.10	1.93 (0.66)	0.50	0.96 (0.42)	0.61	0.19	<LOD	0.65 (0.001)	0.21
Indoxyl sulfate	28.08	47.05 (10.99)	13.03	24.22 (9.74)	15.11	4.84	15.40	12.84 (4.57)	3.31
p-Cresol sulfate	5.54	11.40 (3.13)	3.08	1.64 (0.68)	1.72	0.55	1.20	1.61 (0.44)	0.52
Phenylalanine	0.34	1.85 (1.71)	0.59	1.28 (1.01)	1.01	0.32	0.14	0.25 (0.08)	0.08
p-Hydroxyhippuric acid	1.54	2.74 (0.66)	0.76	1.30 (0.56)	0.73	0.24	0.85	0.68 (0.25)	0.18
Pyruvic acid	850.11	1244.11 (193.04)	398.12	1226.78 (152.41)	2175.50	696.16	2251.62	1807.45 (363.40)	640.22
Quinolinic acid	0.02	0.08 (0.02)	0.02	0.03 (0.01)	0.02	0.01	0.04	0.02 (0.004)	0.01
Spermidine	<LOD	<LOD	NA	0.36 (0.13)	<LOD	NA	0.13	<LOD	NA
Trimethylamine N-oxide	4.88	7.65 (2.50)	1.99	4.47 (2.06)	0.90	0.90	2.55	2.15 (0.46)	0.77
Uric acid	17.66	46.72 (2.42)	14.52	47.59 (22.29)	11.83	11.83	8.31	15.15 (4.32)	5.64
Xanthine	1.33	2.80 (0.13)	0.87	1.36 (0.98)	0.23	0.23	0.71	1.17 (0.20)	0.41
Xanthosine	24.84	40.54 (9.50)	11.22	18.91 (9.34)	4.31	4.31	12.90	10.78 (3.93)	2.79

(MPC:PMβCD)	D (3:1)			E (4:0)		
	1 hr (stdev)	4 hr	Adsorption Amount	1 hr	4 hr (stdev)	Adsorption Amount
3-Deoxyglucosone	0.54 (0.08)	1.05	0.34	0.62	0.74 (0.10)	0.23
4-Ethylphenyl sulfate	0.10 (0.02)	0.21	0.07	0.10	0.16 (0.05)	0.04
4-Hydroxyphenylacetic acid	0.75 (0.07)	2.29	0.73	0.80	1.35 (0.47)	0.41
Dimethyl glycine	0.73 (0.08)	0.64	0.20	0.84	0.88 (0.40)	0.24
Guanidinopropionic acid	0.88 (0.25)	2.82	0.90	1.09	2.17 (0.33)	0.50
Hippuric acid	64.11 (13.72)	150.81	48.26	68.68	110.89 (31.63)	29.41
Indole-3-acetic acid	0.60 (0.25)	1.78	0.57	0.82	1.06 (0.46)	0.33
Indoxyl glucuronide	0.71 (-)	1.31	0.42	<LOD	1.13 (0.35)	0.32
Indoxyl sulfate	15.23 (3.47)	41.22	13.19	17.04	29.87 (9.77)	7.63
p-Cresol sulfate	2.64 (0.87)	9.11	2.91	1.70	5.52 (2.55)	1.43
Phenylalanine	0.77 (0.29)	2.07	0.66	0.77	1.94 (0.88)	0.62
p-Hydroxyhippuric acid	0.86 (0.18)	2.36	0.75	1.04	1.64 (0.60)	0.44
Pyruvic acid	2060.94 (84.23)	2599.43	831.82	1859.63	853.13 (44.75)	700.55
Quinolinic acid	0.03 (0.01)	0.09	0.03	0.04	0.06 (0.03)	0.02
Spermidine	0.17 (0.04)	0.25	0.08	0.23	0.11 (0.04)	0.07
Trimethylamine N-oxide	2.94 (0.48)	7.07	2.26	3.06	4.80 (1.33)	1.37
Uric acid	38.58 (10.82)	85.63	27.40	42.90	62.07 (19.49)	17.16
Xanthine	0.71 (0.26)	2.16	0.69	0.71	1.82 (0.85)	0.37
Xanthosine	14.32 (3.14)	34.81	11.14	14.29	24.38 (7.89)	6.57

Table 3.4 Heat map highlighted selectivity of binding as determined by taking the experimentally adsorbed mol% and dividing by the mol% for each compound in the original solution. Data greater than unity (red) indicates an increased adsorption relative to the compound's initial concentration, less than 0.2 (light blue) and less than 0.1 (dark blue) highlights adsorbed amounts much less than initial concentrations, and - shows compounds where calculations could not be done due to values being lower than the detectable level.

(MPC:PM β CD)	A (0:4)		B (1:3)		C (1:1)		D (3:1)		E (4:0)	
	1 hr	4 hr								
3-Deoxyglucosone	0.23	0.19	0.13	0.06	0.06	0.06	0.07	0.10	0.08	0.18
4-Ethylphenyl sulfate	0.33	0.33	0.23	0.09	0.09	0.10	0.10	0.16	0.11	0.34
4-Hydroxyphenylacetic acid	0.21	0.23	0.13	0.04	0.03	0.03	0.06	0.14	0.07	0.21
Dimethyl glycine	0.39	0.44	0.29	0.11	0.12	0.12	0.17	0.11	0.21	0.40
Guanidinopropionic acid	1.99	2.75	1.42	0.53	0.61	0.57	0.52	1.24	0.70	2.55
Hippuric acid	0.24	0.22	0.14	0.06	0.06	0.06	0.06	0.11	0.07	0.22
Indole-3-acetic acid	0.23	0.26	0.16	0.06	0.05	0.08	0.07	0.15	0.10	0.24
Indoxyl glucuronide	0.37	0.43	0.24	0.09	-	0.12	0.11	0.16	-	0.36
Indoxyl sulfate	0.31	0.34	0.20	0.08	0.08	0.08	0.08	0.16	0.10	0.31
p-Cresol sulfate	0.15	0.21	0.03	0.02	0.01	0.02	0.03	0.09	0.02	0.14
Phenylalanine	0.02	0.06	0.05	0.02	0.00	0.01	0.02	0.04	0.02	0.09
p-Hydroxyhippuric acid	0.19	0.23	0.12	0.04	0.05	0.05	0.05	0.11	0.07	0.20
Pyruvic acid	17.36	17.07	18.61	20.34	20.66	20.53	20.23	19.11	19.98	16.73
Quinolinic acid	0.13	0.27	0.13	0.06	0.09	0.07	0.09	0.17	0.10	0.32
Spermidine	-	-	1.09	-	0.24	-	0.33	0.37	0.49	0.45
Trimethylamine N-oxide	0.13	0.14	0.09	0.03	0.03	0.03	0.04	0.07	0.04	0.13
Uric acid	0.10	0.17	0.19	0.09	0.02	0.05	0.10	0.17	0.12	0.33
Xanthine	0.36	0.52	0.28	0.09	0.09	0.18	0.09	0.21	0.10	0.48
Xanthosine	0.20	0.22	0.11	0.05	0.05	0.05	0.05	0.10	0.06	0.19

The total average amount of toxins adsorbed to the modified MNPs did not stabilize within 1 hr of incubation, but substantial changes were observed with increased incubation time (Table 3.3, Figure 3.5). Given that all MNP systems utilized similar particle sizes, it was apparent that type D adsorbed among the highest amounts of uremic toxins per surface area, whereas A and E

showed the lowest amount of adsorption. Moreover, A, B, and D types showed a large average increase in total adsorbed amount and type E showed a substantial decrease in adsorbed amount with incubation time.

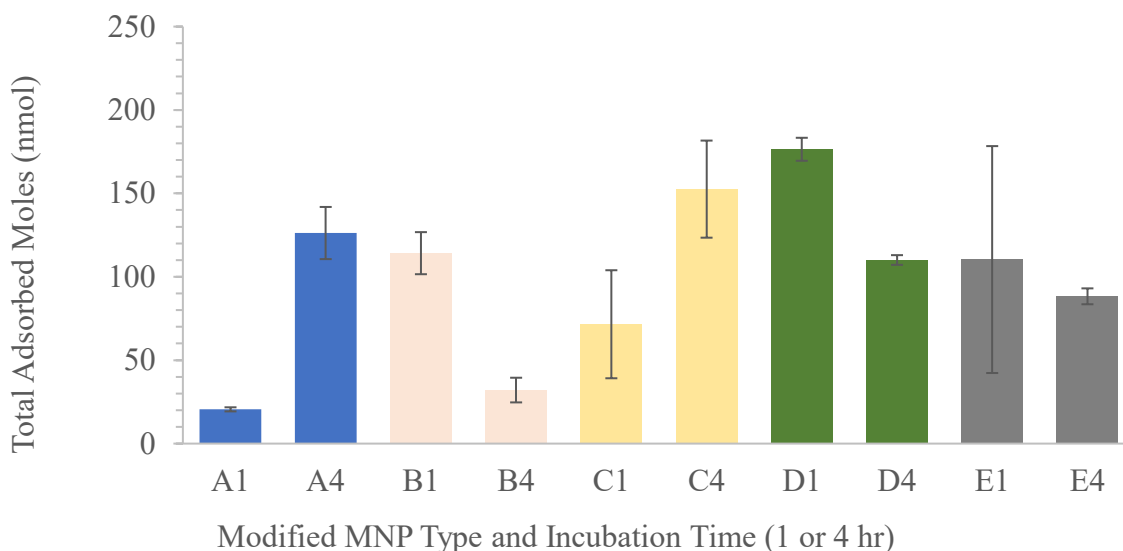


Figure 3.4 Total adsorbed amounts of toxins (nmol) for all modified MNP systems, given similar surface areas and incubation times of 1 or 4 hr. Note that repeats were only performed on a subset of data to reduce costs of data collection. Data represent average \pm 1 STD. STD was determined using $n=3$ and error propagation calculation.

Changes in the total adsorbed amount were broken down to understand individual toxin content as a function of incubation time. This was done by calculating the relative change in mol% from 1 to 4 hrs of adsorption (Table 3.6). The increased and decreased mol% of compounds are marked with red and blue, respectively. When interpreting Table 3.6, it is important to remember that these amounts are influenced heavily by Pyruvic acid due to the large amount that was adsorbed by these systems. For example, type B shows large percent decrease for every compound,

with only a moderate increase in the relative amounts of Pyruvic acid. However, if the mole number is examined, a trend of increase in total mole number is observed as demonstrated by the total mole of adsorbed toxins for B is 141.85 nmol at 1 hr and 188.22 nmol at 4 hrs. Nevertheless, trends can be observed from the data in Table 3.6. Type A nanoparticles exhibited a general increase in mol% for most toxins with increasing adsorption time. In this case, a substantial increase in mol% was observed for phenylalanine>quinolinic acid>uric acid>xanthine, guanidinopropionic acid and p-Cresol sulfate. Guanidionpropionic acid and p-Cresol sulfate are charged species that may be interacting with different domains of the film. Uric acid and Xanthine have a common purine base, but differences in charge structure seem to provide Uric acid an increased interaction with the β -CDs. Quinolinic acid changes seem large, but the absolute values for their concentration are very low, thus this significant increase may be associated with the limited measurement precision associated of these low concentrations more than physicochemical reasons. Increased Phenylalanine adsorption was likely due to the readily exposed terminal aromatic that can directly interact hydrophobically with the internal β -CD domain. This was in stark contrast to Type B nanoparticles, where just a small amount of MPC content led to a moderate increase in mol% of pyruvic acid with substantial decreases in all other compounds; likely a result of electrostatic interactions. Balancing the content of β -CD to MPC in Type C nanoparticles led to a similar response as seen for Type A nanoparticles, except that Uric acid and Xanthine changes in mol% were greater. Surprisingly, both D and E nanoparticles showed an obvious and dramatic increase in almost all compounds with increased adsorption time. Suggesting that the increased presence of MPC may be facilitating relatively non-specific interactions with these toxins. Chemical moieties within these uremic toxins seem to greatly impact their retention at the engineered surface. Sulfate-containing toxin adsorption to both A and E particles may suggest a dual binding mechanism that

utilizes both hydrophobic and electrostatic interactions. Thus, for the other particles that have both CD and MPC in the films, sulfate adsorption may also rely on these interaction mechanisms. Particle D exhibited the highest adsorption rate of both acid and sulfate compounds among the other three co-polymer coated particles (B, C, D). Toxins with less hydrophobic functional groups but considerable adsorption rate, such as 3-deoxyglucosone and xanthosine, contain hydroxyl or carbonyl groups, suggesting that hydrogen bonding may contribute to the variation of adsorbed toxin profiles. Our investigation of the chemical property of toxins showed that the existence of aromatics groups will decrease net adsorption, whereas amino, imino, hydroxyl groups, and carboxyl groups seem to be favoured. Hippuric acid is a good example as it contains a benzene ring yet has relatively high adsorbed amounts from this complex solution. The fused bicyclic is another common structure in the compounds that are desorption unfavorable. However, the existence of hydroxyl groups made a major difference in fused bicyclic compounds adsorption; comparing toxins with low amounts of hydroxyl groups (Xanthine and uric acid) to those of abundant hydroxyl groups (Xanthosine).

Table 3.5 Percent change in mol% from 1 to 4 hr incubation time. Red indicates an increase in mol% of compound, blue a decrease, and white a nominal change.

(MPC:PM β CD)	A (0:4)	B (1:3)	C (1:1)	D (3:1)	E (4:0)	
3-Deoxyglucosone	-17.5	-116.4	2.6	32.0	54.5	> 50
4-Ethylphenyl sulfate	-0.6	-156.4	13.9	37.4	67.3	30 to 49
4-Hydroxyphenylacetic acid	8.6	-240.6	10.2	56.0	67.7	10 to 29
Dimethyl glycine	10.1	-173.7	4.5	-54.2	47.8	9 to -9
Guanidinopropionic acid	27.8	-169.4	-6.4	58.4	72.5	-10 to -39
Hippuric acid	-9.7	-137.1	0.4	43.2	66.1	-40 to -69
Indole-3-acetic acid	12.9	-167.0	37.2	54.8	57.5	-70 to -99
Indoxyl glucuronide	15.0	-155.3	-	28.0	-	< -100
Indoxyl sulfate	11.1	-160.0	3.1	50.7	68.7	
p-Cresol sulfate	27.7	-54.5	39.9	61.3	83.1	
Phenylalanine	72.8	-105.9	53.8	50.6	78.2	
p-Hydroxyhippuric acid	16.5	-187.7	-0.3	51.3	65.5	
Pyruvic acid	-1.7	8.5	-0.6	-5.9	-19.4	
Quinolinic acid	53.9	-122.3	-14.9	47.4	67.1	
Spermidine	-	-	-	11.5	-9.3	
Trimethylamine N-oxide	5.0	-158.4	4.5	44.5	65.0	
Uric acid	43.7	-108.8	55.7	39.8	62.1	
Xanthine	29.5	-211.0	50.5	56.1	78.5	
Xanthosine	8.8	-128.0	3.3	45.1	67.9	

In order to understand the competitive binding characteristics of these systems, a heat map for selectivity of adsorbed species was developed where the experimentally determined mol% for each adsorbed species was normalized by the corresponding mol% in the incubation solution (Table 3.5). It was observed that pyruvic acid adsorption reached as high as 20 times that of the original solution; a surprising result given that the original incubation mol% for pyruvic acid was only 4.26 mol%, suggesting a significant binding event with pyruvic acid for all conditions. Whereas hippuric acid, which started with a ~46 mol% in solution, only represented a very small fraction of the adsorbed toxinome. These results suggest that the interactions are not largely driven

by concentration effects alone. Guandinopropionic acid adsorption to these materials showed upwards of 3 times that found in the original solutions, suggesting a highly competitive binding event. Otherwise, it was observed that a large fraction of the surfaces did not lead to a binding of 0.1 that of the compounds in the original solution (dark blue, Table 3.5).

3.4 Conclusion

A series of novel polymer-modified particles were synthesized using ATRP polymerization. The chemical and physical properties of these particles were characterized using various analytical techniques such as FTIR, TGA, GPC, and TEM. The signature peaks of POCH_2 and $\text{N}^+(\text{CH}_3)$ group in MPC and the ester group and triazole group in $\text{PM}\beta\text{CD}$ were utilized to confirm the successful deposition of successful deposition in FTIR experiment. TGA analysis illustrated the chemical composition and weight loss ratio of the particles. The average weight losses of each particle are A, 37.42%; B, 40.1%; C, 43.0%; D, 32.1%; E, 24.1%. The molecular weight and PDI were obtained from the GPC. The molecular weights of cleaved polymers are ranging from 47.0 to 144.7 kg/mol. The modified particles showed correlating results in both GPC and TGA, suggesting the higher chemical reactivity of MPC than $\text{PM}\beta\text{CD}$. TEM results showed the rough morphology of bare MNPs and smooth morphology of polymer-modified MNPs, with an average core size of 11.87 ± 2.37 nm and coated polymer layer of 4.5-6 nm. Fresh uremic toxin solution (Table 3.1) that aligned with the typical concentration of uremic toxins in patients with kidney failure was formulated in our lab. . LC-MS/MS results confirmed the adsorption of uremic toxins by all 5 nanoparticles, with nanoparticle D exhibiting the highest overall adsorption rate towards all the compounds in the profile. This may attribute to two reasons: the synergy adsorption effect between CD content and MPC, and the high zeta potential on the surface of particle D. Firstly, in section 3.1, we estimated that particle A has 88 monomers per chain and particle E has

159. Assuming equal chain numbers due to the initiator density, the adsorption ratio on each PM β CD and MPC monomer is $(132.67/88) : (193.67/159) = 1.23$. This implies better adsorption ability of CDs compared to MPC. Therefore, the high adsorption rate on particle D may be due to a synergistic effect between CD and MPC content in binding uremic toxins, which requires further investigation. Secondly, the zeta potential analysis suggest that particle D has the highest zeta potential (-28.3 mV) compared to all coated surfaces. This indicates that particle D has a stronger electrostatic interaction with its surroundings, which may have contributed to its overall increased adsorption. The adsorption of Pyruvic acid and Guanidinopropionic acid was found to have the highest rate among all toxins, with both concentration-driven binding and specific binding involved. Further analysis of the physiochemical property of removed compounds revealed the involvement of electrostatic forces in the mechanisms of carboxylic acid compound removal by MPC, while hydrophobic interaction and hydrogen bonding were responsible for compounds adsorbed by the PM β CD component. In conclusion, we have successfully synthesized p(MPC-co-PM β CD) coated MNPs in this study and measured the chemical property and the functionality of the series of particles. The adsorption result emphasizes the potential of p(MPC-co-PM β CD) coated MNPs as an adsorbent that can assist in the treatment of CKD.

3.5 References

1. Lv, J., et al., *Prevalence and disease burden of chronic kidney disease*. Renal Fibrosis: Mechanisms Therapies, 2019: p. 3-15.
2. Klefter, R., et al., *Savings in dialysis treatment?* Artificial organs, 2002. **26**(1): p. 49-54.
3. Ma, Y., et al., *Adsorption-based strategies for removing uremic toxins from blood*. Microporous Mesoporous Materials, 2021. **319**: p. 111035.
4. Pavlenko, D., et al., *Carbon adsorbents with dual porosity for efficient removal of uremic toxins and cytokines from human plasma*. Scientific Reports, 2017. **7**(1): p. 1-7.
5. Jong, J.A., et al., *A Ninhydrin-Type Urea Sorbent for the Development of a Wearable Artificial Kidney*. Macromolecular Bioscience, 2020. **20**(3): p. 1900396.
6. Keçili, R., et al., *The use of magnetic nanoparticles in sample preparation devices and tools*, in *Handbook of Nanomaterials in Analytical Chemistry*. 2020, Elsevier. p. 75-95.
7. Kainz, Q.M., et al., *Polymer-and dendrimer-coated magnetic nanoparticles as versatile supports for catalysts, scavengers, and reagents*. Accounts of Chemical Research, 2014. **47**(2): p. 667-677.
8. Wang, X., et al., *A molecularly imprinted polymer-coated nanocomposite of magnetic nanoparticles for estrone recognition*. Talanta, 2009. **78**(2): p. 327-332.
9. Urbina, M.C., et al., *Investigation of magnetic nanoparticle-polymer composites for multiple-controlled drug delivery*. The Journal of Physical Chemistry C, 2008. **112**(30): p. 11102-11108.
10. Sarnak, M.J., *Cardiovascular complications in chronic kidney disease*. American Journal of Kidney Diseases, 2003. **41**: p. 11-17.
11. Kraut, J.A., et al., *Adverse effects of the metabolic acidosis of chronic kidney disease*. Advances in Chronic Kidney Disease, 2017. **24**(5): p. 289-297.

12. Patel, S.S., et al., *Serum creatinine as a marker of muscle mass in chronic kidney disease: results of a cross-sectional study and review of literature*. Journal of Cachexia, Sarcopenia Muscle, 2013. **4**(1): p. 19-29.
13. Namekawa, K., et al., *Fabrication of zeolite–polymer composite nanofibers for removal of uremic toxins from kidney failure patients*. Biomaterials Science, 2014. **2**(5): p. 674-679.
14. Yen, S., et al., *Carbon nanotube/conducting polymer hybrid nanofibers as novel organic bioelectronic interfaces for efficient removal of protein-bound uremic toxins*. ACS Applied Materials & Interfaces, 2019. **11**(47): p. 43843-43856.
15. Varan, C., et al., *Preparation and characterization of cyclodextrin nanosponges for organic toxic molecule removal*. International Journal of Pharmaceutics, 2020. **585**: p. 119485.
16. Li, J., et al., *Multi-sites polycyclodextrin adsorbents for removal of protein-bound uremic toxins combining with hemodialysis*. Carbohydrate Polymers, 2020. **247**: p. 116665.
17. Tsoi, T., et al., *Urinary polyamines: a pilot study on their roles as prostate cancer detection biomarkers*. PLoS One, 2016. **11**(9): p. e0162217.
18. Kopple, J.D., et al., *Risks of chronic metabolic acidosis in patients with chronic kidney disease*. Kidney International, 2005. **67**: p. S21-S27.
19. Schlenoff, J.B., *Zwitteration: coating surfaces with zwitterionic functionality to reduce nonspecific adsorption*. Langmuir, 2014. **30**(32): p. 9625-9636.
20. Ueda, T., et al., *Preparation of 2-methacryloyloxyethyl phosphorylcholine copolymers with alkyl methacrylates and their blood compatibility*. Polymer Journal, 1992. **24**(11): p. 1259-1269.

21. Ishihara, K., *Revolutionary advances in 2-methacryloyloxyethyl phosphorylcholine polymers as biomaterials*. Journal of Biomedical Materials Research Part A, 2019. **107**(5): p. 933-943.
22. Konno, T., et al., *Enhanced solubility of paclitaxel using water-soluble and biocompatible 2-methacryloyloxyethyl phosphorylcholine polymers*. Journal of Biomedical Materials Research Part A, 2003. **65**(2): p. 209-214.
23. Ishihara, K., et al., *Inhibition of fibroblast cell adhesion on substrate by coating with 2-methacryloyloxyethyl phosphorylcholine polymers*. Journal of Biomaterials Science, Polymer Edition, 1999. **10**(10): p. 1047-1061.
24. Ishihara, K., et al., *Preparation of phospholipid polymers and their properties as polymer hydrogel membranes*. Polymer Journal, 1990. **22**(5): p. 355-360.
25. Ishihara, K., et al., *Reduced thrombogenicity of polymers having phospholipid polar groups*. Journal of Biomedical Materials Research, 1990. **24**(8): p. 1069-1077.
26. Campbell, E.J., et al., *Biocompatible surfaces using methacryloylphosphorylcholine laurylmethacrylate copolymer*. ASAIO Journal, 1994. **40**(3): p. M853-7.
27. Hedges, A., *Cyclodextrins: properties and applications*, in *Starch*. 2009, Elsevier. p. 833-851.
28. Liu, J., et al., *Structure design and performance study on filtration-adsorption bifunctional blood purification membrane*. Journal of Membrane Science, 2021. **636**: p. 119535.
29. Vanholder, R., et al., *Review on uremic toxins: classification, concentration, interindividual variability*. Kidney International, 2003. **63**: p. 1934-1943.

30. Itoh, Y., et al., *Protein-bound uremic toxins in hemodialysis patients measured by liquid chromatography/tandem mass spectrometry and their effects on endothelial ROS production*. Analytical Bioanalytical Chemistry, 2012. **403**(7): p. 1841-1850.
31. Toshimitsu, N., et al., *A gas chromatographic-mass spectrometric assay for nine hydroxyphenolic acids in uremic serum*. Clinica Chimica Acta, 1979. **96**(3): p. 247-254.
32. Duranton, F., et al., *Normal and pathologic concentrations of uremic toxins*. Journal of the American Society of Nephrology, 2012. **23**(7): p. 1258-1270.
33. Wolfson, M., et al., *Amino acid losses during hemodialysis with infusion of amino acids and glucose*. Kidney International, 1982. **21**(3): p. 500-506.
34. Schools, A., et al., *Biochemical and neurophysiological parameters in hemodialyzed patients with chronic renal failure*. Clinica Chimica Acta, 1989. **185**(1): p. 91-107.
35. Landon, J., et al., *Blood pyruvate concentration measured by a specific method in control subjects*. Journal of Clinical Pathology, 1962. **15**(6): p. 579-584.
36. Saito, K., et al., *Mechanism of increases in l-kynurenine quinolinic acid in renal insufficiency*. American Journal of Physiology-Renal Physiology, 2000. **279**: p. F565-F572.
37. Bain, M.A., et al., *Accumulation of trimethylamine and trimethylamine-N-oxide in end-stage renal disease patients undergoing haemodialysis*. Nephrology Dialysis Transplantation, 2006. **21**(5): p. 1300-1304.
38. Taki, K., et al., *Indoxyl sulfate and atherosclerotic risk factors in hemodialysis patients*. American Journal of Nephrology, 2007. **27**(1): p. 30-35.
39. Vanholder, R.C., et al., *Assessment of urea and other uremic markers for quantification of dialysis efficacy*. Clinical Chemistry, 1992. **38**(8): p. 1429-1436.

40. Toshimitsu, N., et al., *RNA metabolism in uremic patients: accumulation of modified ribonucleosides in uremic serum*. *Kidney International*, 1998. **53**: p. 1801-1806.
41. Dong, H., et al., *Recyclable antibacterial magnetic nanoparticles grafted with quaternized poly (2-(dimethylamino) ethyl methacrylate) brushes*. *Biomacromolecules*, 2011. **12**(4): p. 1305-1311.
42. Zhang, L., et al., *A high-performing plasma metabolite panel for early-stage lung cancer detection*. *Cancers*, 2020. **12**(3): p. 622.
43. Tan, J., et al., *Facile preparation of hybrid vesicles loaded with silica nanoparticles via aqueous photoinitiated polymerization-induced self-assembly*. *RSC Advances*, 2017. **7**(37): p. 23114-23121.
44. Shown, I., et al. *Synthesis of Cyclodextrin and Sugar-Based Oligomers for the Efavirenz Drug Delivery*. in *Macromolecular symposia*. 2010. Wiley Online Library.
45. Sun, X., et al., *Facile graft of poly (2-methacryloyloxyethyl phosphorylcholine) onto Fe₃O₄ nanoparticles by ATRP: Synthesis, properties, and biocompatibility*. *Journal of Biomedical Materials Research Part A*, 2013. **101**(2): p. 607-612.
46. Santos, E.C., et al., *Guanidine-functionalized Fe₃O₄ magnetic nanoparticles as basic recyclable catalysts for biodiesel production*. *RSC Advances*, 2015. **5**(59): p. 48031-48038.
47. Han, G., et al., *Advanced anti-fouling membranes for osmotic power generation from wastewater via pressure retarded osmosis (PRO)*. *Environmental Science Technology*, 2018. **52**(11): p. 6686-6694.
48. Burujeny, S.B., et al., *Bactericidal dental nanocomposites containing 1, 2, 3-triazolium-functionalized POSS additive prepared through thiol-ene click polymerization*. *Dental Materials*, 2017. **33**(1): p. 119-131.

49. Mahmoud, W.E., et al., *A facile method to syntheses monodisperse gamma-Fe₂O₃ nanocubes with high magnetic anisotropy density*. Superlattices Microstructures, 2014. **68**: p. 1-5.

Chapter 4

Hemocompatibility of β -cyclodextrin modified (methacryloyloxy)ethyl phosphorylcholine coated magnetic nanoparticles.

This chapter is published in Biomolecules as “Hemocompatibility of β -cyclodextrin modified (methacryloyloxy)ethyl phosphorylcholine coated magnetic nanoparticles.”

Author List: Shuhui Li, Mehdi Ghaffari Sharaf, Elyn M. Rowe, Katherine Serrano, Dana V. Devine, and Larry D. Unsworth

Contribution: Conceptualization, S.L., K.S. and L.D.U.; methodology, S.L., M.G., E.M.R.; software, Origin, CDNN 2.0, ImageJ; validation, S.L., M.G., E.M.R., L.D.U.; formal analysis, S.L., M.G., E.M.R.; investigation, S.L., M.G., E.M.R.; resources, D.V.D., and L.D.U.; data curation, S.L., M.G., E.M.R.; writing—original draft preparation, S.L., M.G., E.M.R.; writing—review and editing, S.L., M.G., E.M.R., L.D.U.; visualization, S.L., M.G., E.M.R.; supervision, L.D.U.; project administration, L.D.U.; funding acquisition, D.V.D., L.D.U.. All authors have read and agreed to the published version of the manuscript.

4.1 Introduction

Hemodialysis is a costly and time-consuming therapy that ultimately cannot clear all accumulated molecules from the blood of patients with kidney dysfunction [1]. The buildup of these compounds (i.e., uremic toxins [2]) exacerbates kidney dysfunction and directly leads to the progression of chronic kidney disease [3]. Adsorbent surfaces are designed to clear these compounds from the blood, which may transform both treatment costs and patient outcomes associated with hemodialysis [4]. While 2-(methacryloyloxy)ethyl phosphorylcholine (MPC) is a gold-standard low-fouling film [5, 6], it is not optimized for uremic toxin clearance. Herein, we synthesized copolymers of β -cyclodextrin (CD) and MPC on magnetic nanoparticles (MNPs) (Figure 4.1) for the express purpose of studying the effect that CD incorporation has on the hemocompatibility of the particles as an initial screen to determine their potential utility in the context of treating patients with kidney failure. The MNPs provide a platform for removing adsorbed toxins from the blood. General hemocompatibility of these engineered surfaces were assessed through investigating protein–surface interactions and the response of cellular components of the blood.

Nonspecific protein adsorption at the interface of blood-contacting biomaterials can lead to undesired host responses and functional failure of the device [7, 8]. For example, plasma protein adsorption on engineered surfaces can lead to microenvironmental changes and protein denaturation, making the introduction of anti-fouling properties essential for the prolonged functionality of various biomaterials, including biomedical implants, biosensors, and membranes [9-11]. Common surface modifications used to inhibit protein adsorption include hydrophilic polymers like zwitterionic polymers, including poly(sulfobetaine methacrylate) (pSBMA) and pMPC [12]. However, it is unclear how the formation of surface films composed of CDs and pMPC interact with blood components. Although both CD and MPC monomers exhibit properties that are

associated with inhibiting protein adsorption, such as abundant hydroxyl groups found on CDs [13], and the properties associated with the zwitterion of MPC [14, 15], further examination of their joint contribution to outcomes related to both proteins and blood cells is crucial to their application in capturing uremic toxins. Circular dichroism was used to examine the effect film properties had on the adsorbed protein structure using albumin (HSA), α -lactalbumin, and lysozyme. These three proteins allow for the surface to be interrogated on different size scales, as HSA and α -lactalbumin have similar charges but different sizes. In a complementary manner, through using lysozyme and α -lactalbumin, the film was evaluated for proteins of a similar size but a different charge [16]. Adsorption-induced rearrangement of HSA was also evaluated using the changes in the fluorescence of tryptophan [17].

In addition to single-protein experiments, understanding how plasma proteins are affected by surface chemistry is crucial to their eventual application. Plasma is a highly intricate fluid that contains a plethora of proteins that can, upon interacting with surfaces, trigger a multitude of deleterious host responses [18]. When combined with platelet activation, these surfaces could initiate thrombus formation, leading to embolisms [19,20]. Therefore, a comprehensive understanding of the interaction between biomaterials, plasma proteins, and platelets is crucial for developing safe and effective medical devices. To this end, the adsorbed plasma proteome was assessed *via* incubation of MNPs with platelet-poor human plasma using sodium dodecyl-sulfate polyacrylamide gel electrophoresis (SDS-PAGE) and immunoblot. The BCA protein assay was employed to determine the total amount of plasma protein adsorbed by different types of MNPs. To probe the platelet function and the more general hemocompatibility of the series of coated MNPs, several complementary techniques were used following incubation with whole blood: complete blood counts, whole-blood rotational thromboelastometry (ROTEM), platelet activation and responsiveness to adenosine diphosphate (ADP) through flow cytometry, and hemolysis

methacrylate (PM, 98%, Alfa Aesar, Tewksbury, USA), β -cyclodextrin ($\geq 97\%$, Sigma Aldrich), 2,2'-bipyridyl (bpy, $>99\%$, copper(I)bromide ($> 98\%$), copper(II)bromide (99%), Tris[(1-benzyl-1H-1,2,3-triazol-4-yl)methyl]amine (TBTA, Trichemicals, Edmonds, USA), Dialysis Tubing 500 MWCO (Cole-Parmer, Illinois, USA), Lewatit TP 207 adsorbent, TetrakisacetonitrilecopperI hexafluorophosphate ($\text{Cu}(\text{CH}_3\text{CN})_4\text{PF}_6$, Sigma Aldrich, St. Louis, USA), 2-methacryloyloxyethyl phosphorylcholine (MPC, Sigma Aldrich, St. Louis, USA), ultra-thin carbon-coated copper grid (150 mesh, Ted Pella, Inc., Redding, USA), sodium hydroxide (Fisher Scientific, Waltham, USA), $\text{FeCl}_2 \cdot 4\text{H}_2\text{O}$, $\text{FeCl}_3 \cdot 6\text{H}_2\text{O}$, and ammonium hydroxide solution (25%) were purchased from Sigma Aldrich, St. Louis, USA.

Chemicals for experiments: Sodium phosphate dibasic heptahydrate, sodium phosphate monobasic monohydrate, and PBS tablet were purchased from Fisher Scientific. Platelet-poor human plasma was procured via the Blood4Research program from Canadian Blood Services. Sodium dodecyl sulfate (SDS) and polyvinylidene fluoride (PVDF) membrane were from Bio-Rad, Hercules, USA. The TMB-stabilized substrate was from Promega, Madison, USA, and the BCA protein assay from the Pierce™ BCA Protein Assay Kit (Thermo Fisher Scientific Inc., Waltham, USA) was used. Statistical analysis of protein adsorption data was performed using one-way ANOVA, followed by a post-hoc Tukey's HSD test, with a significance level of $p < 0.05$.

4.2.2 Methods

4.2.2.1 Polymer synthesis and fixation

PM β CD monomer and bare MNPs were prepared following previously reported methods [21-23]. Bare MNPs were decorated with CTCS: 500 mg of bare MNPs were placed in an argon-filled three-neck flask, and 5 mL of CTCS solution was added drop-wise and left to react for 3 h. MNP-CTC was washed thrice with THF and twice with ethanol through consecutive separation

and redispersion. The MNP-CTC product was dried in the vacuum overnight and sealed under an argon blanket for storage. Atom transfer radical polymerization (ATRP) synthesis methods were applied for polymer synthesis, as presented in Table 4.1. Before the experiment, argon was added to a round-bottom flask thrice to remove any gas present and ensure an argon blanket. MPC and PM β CD were then dissolved in a 10 mL mixed solvent, which contained an even volume of water and ethanol. The solution was stirred and bubbled with argon for 20 min to form the MPC-PM β CD complex.

Table 4.1 The representative synthesis scheme for A to E particle series.

	<i>A</i>	<i>B</i>	<i>C</i>	<i>D</i>	<i>E</i>
<i>PMβCD:MPC</i>	4:0	3:1	2:2	1:3	0:4
<i>PMβCD (mmol)</i>	1.25	0.9375	0.625	0.3125	0
<i>MPC (mmol)</i>	0	0.3125	0.625	0.9375	1.25

4.2.2.2 Polymer Characterization

TEM (JEM-ARM200CF S/TEM, JEOL, Houston, USA) analysis used an accelerating voltage of 200 kV to obtain images of particles. These images were further analyzed using ImageJ. To prepare the samples, a droplet of a well-dispersed sample was deposited onto an ultra-thin carbon-coated copper grid and allowed to air-dry for 24 h prior to characterization.

The zeta potential of the engineered surfaces was evaluated using the Malvern Zetasizer Nano-ZS (Nano ZS, Malvern Instruments, Malvern, UK). To prepare the sample, 25 μ L of a 1 mg/mL MNPs suspension was mixed with 3 mL of DI water and subjected to 30 s of ultrasonication before the zeta potential measurement. Three repeats were conducted, with each measurement comprising 12 runs each. These were averaged to obtain the reported zeta potential.

4.2.2.3 Circular Dichroism

Far-UV circular dichroism (DSM 17 Circular Dichroism spectrometer, Olis, Athens, USA) spectra of HSA, α -lactalbumin, and lysosome with the polymer-coated MNPs were obtained using human serum albumin: 1.25 mg/mL, and α -lactalbumin and lysozyme: 0.25 mg/mL. The MNP concentration was 0.25 mg/mL. The same volumes of protein solution and MNP solution were incubated for 3 h at 37 °C before the test. The spectra were recorded from 180 to 260 nm. The presented results are an average value of three independent repeats. CDNN 2.0 software was used to determine the secondary structure changes upon adding MNPs.

4.2.2.4 Fluorescence spectroscopy

The binding interaction study of nanoparticles synthesized with HSA was conducted in vitro using a previously described procedure [24]. Briefly, a solution of HSA (330 μ g/mL in 10 mM of PB, pH 7.4) was titrated with different formulations of nanoparticles (1 mg/mL). Fluorescence spectroscopy (FlexStation 3 multimode plate reader) was used to study the interaction between the protein and the nanoparticles. The reduction of fluorescence intensity was recorded at emission scanning wavelengths from 300 to 500 nm, $\lambda_{ex} = 295$ nm. The binding constant (K_b) and the number of binding sites (n) were determined according to previously published methods (Equation 4.1) [25-27]:

$$(F_0 - F) / (F_0 - F_s) = [(S) / K_d]n \quad (\text{Equation 4.1})$$

Where F_0 is relative fluorescence intensity (F) of protein solution alone, F_s is relative fluorescence intensity of protein saturated with MNPs, and $[S]$ is concentration of MNPs. n is the number of binding sites and was determined from the slope of plot, $\log [(F_0-F)/(F-F_s)]$ vs $\log [S]$. The $\log [S]$

at $\log [(F_0-F)/(F-F_s)] = 0$ determines the logarithm of dissociation constant (K_d), where K_b is reciprocal of K_d .

4.2.2.5 SDS-PAGE and immunoblot

Upon pooled platelet-poor plasma arrival, plasma samples were aliquoted and stored at -80 °C until use. The study was approved and conducted per the guidelines set by the research ethics board of the University of Alberta. Nanoparticle and platelet-poor plasma incubation was carried out according to existing protocols [28]. Briefly, different magnetic particles were added to 37 °C plasma at the same concentration used for the recalcification turbidimetric assay (0.18 mg/mL) and incubated at 37 °C for 2 h. Samples were subsequently centrifuged at $20,000\times g$ for 10 min. The supernatant was removed, and nanoparticles were washed twice with 1 mL of PBS to remove loosely bound proteins. The final pellets of particles and adsorbed proteins were resuspended in 100 μ L of 10% SDS in PBS and incubated at 50 °C for 2 h to elute the adsorbed proteins from the surface of the nanoparticles. The eluted protein sample concentration was quantified using the Pierce™ BCA protein (detergent-compatible) assay. The final sample was further analyzed using SDS-PAGE and immunoblotting.

The analysis of samples using SDS-PAGE and immunoblot techniques was conducted using a protocol described previously [28, 29]. Before SDS-PAGE, a denaturing sample buffer containing SDS and 0.5 M β -mercaptoethanol was added to each sample and heated at 95 °C for 5 min. A constant amount of each protein sample (30 μ g) was run on 12% polyacrylamide gels. Samples were transferred onto 0.2 μ m-pore size immunoblot polyvinylidene difluoride membranes (Bio-Rad Laboratories, Inc, Hercules, USA). Upon electro-transfer, each membrane was divided into 23 strips, with 2 used for colloidal gold staining and the rest for immunoblot, using 21 individual proteins. Each primary antibody was used at a $1:1000$ dilution. Horseradish peroxidase (HRP)-

conjugated secondary antibodies and 3,3',5,5'-tetramethylbenzidine (TMB)-stabilized chromogen substrate (Promega) were used for the visualization of the immunoblot results. The color development time was kept consistent between immunoblots to compare the results between different samples. The strips were dried, assembled, and digitized immediately after stopping the color development with water.

4.2.2.6 Fibrin clot formation in plasma

Clot formation was assessed using the plasma calcification turbidimetric assay. Plasma (100 μ L) was incubated with MNPs. Plasma was incubated with PBS (10 mM) for 30 min, then incubated with MNPs for 1 h prior to testing. Then, 100 μ L of 0.025 M CaCl_2 was injected into a 96-well plate for the turbidity reading. A BioTek ELx808 plate reader was used to measure the absorbance at 405 nm at 1 min intervals over 1 hour. All steps were performed at 37 $^\circ\text{C}$, with three independent repeats.

4.2.2.7 Whole blood hemocompatibility testing

Venous blood from three healthy donors was collected into 2.7 mL BD vacutainers containing buffered sodium citrate (0.109 M, 3.2%) for hemocompatibility evaluation. This study was approved by the UBC Clinical Research Ethics Board (H22-00215), and all donors provided informed consent. For whole-blood hemocompatibility testing, MNPs dispersed in water (or an equal volume of deionized water, as a control) were added to 2.7 mL of citrated whole blood at a final concentration of 0.18 mg/mL and incubated on a rocker for 1 h at 37 $^\circ\text{C}$.

Following incubation, complete blood counts were obtained using a Sysmex XN-550 hematology analyzer (Sysmex Corporation). Coagulation was assessed in the treated citrated whole

blood using rotational thromboelastometry (ROTEM; Instrumentation Laboratory), where 300 μL of whole blood was mixed with the STAR-TEM and EXTEM reagents to re-calcify and activate the extrinsic coagulation pathway, respectively. Primary readouts included: the clotting time (the period from the beginning of coagulation to the start of fibrin polymerization), the clot formation time (velocity of clot formation—platelet-dependent), and the maximum clot firmness (mechanical strength of the clot—dependent on platelet function fibrin polymerization, and Factor XIII activity).

Platelet activation and responsiveness were evaluated using flow cytometry on a BD FACSCanto II flow cytometer (BD Biosciences). For baseline activation, 3 μL of whole blood was incubated with 5 μL of mouse anti-CD62P (IM1759U, Beckman Coulter) in 0.22 μm -filtered PBS at a total volume of 50 μL . For responsiveness, 3 μL of whole blood was incubated with ADP (Chrono-Log) at a final concentration of 10 μM and 5 μL of antibody in 0.22 μm -filtered PBS, at a total volume of 50 μL . After a 30-min incubation at room temperature, samples were diluted with 1 mL of 0.22 μm -filtered PBS before measurement. The platelet population was confirmed with a CD41 stain and gated for the remainder of the experiments. Gates for a positive CD62P signal in the platelet population were determined for each experiment based on an isotype control (IgG1; IM0670U, Beckman Coulter).

The remaining whole blood was centrifuged at 3000 rpm for 10 min at 4 $^{\circ}\text{C}$ to obtain platelet-poor plasma (PPP), then the PPP was spun again at 20,000 $\times g$ for 20 min at 4 $^{\circ}\text{C}$ to pellet the remaining microparticles before exposure to a magnet for 15 min at room temperature. Hemolysis was assessed in PPP using the previously described Harboe method [30], and C3a levels reflecting complement activation were assessed in plasma aliquots frozen at -70°C using a commercial ELISA (#A031, Quidel), following the kit instructions for plasma. All diluted samples were within the detection limits of the ELISA.

Graphing and statistical analysis for the hemocompatibility outcomes were performed in RStudio using R version 4.0.5, with the packages `rstatix`, `dplyr`, `grid`, and `ggplot2`. Due to the innate variability across donors, hemocompatibility results were evaluated using a repeated-measures ANOVA, with the donor as the identifier and treatment (MNP) as the within-subject variable. Post hoc pairwise comparisons were performed using paired *t*-tests, where each MNP formulation was compared to the water control. *p*-values were not adjusted for multiple comparisons in post hoc testing, as the goal was to identify any MNP formulations that showed indications of hemoincompatibility with high sensitivity.

4.3 Results and discussions

4.3.1 Properties and characterization of the modified MNPs

A series of polymer-modified particles were synthesized using ATRP techniques. Figure 4.2 illustrates the representative TEM results for the modified MNPs, where an average particle size of 13.45 ± 2.52 nm was found through analyzing a random subset of particles ($n = 33$). The selected-area electron diffraction (SAED) pattern indicated that both the bare and polymer-coated MNPs had a ring pattern consistent with a polycrystalline structure of magnetite, matching the (220), (311), (400), (420), (511), and (440) planes, as specified by the JCPDS Card No. 19-0629 [31, 32]. All particles' engineered surfaces exhibited a negative net charge, as demonstrated by their zeta potential data (Figure 4.3). The bare MNP's zeta potential was significantly different ($p < 0.05$) than all modified surfaces. No significant difference in the zeta potentials of surfaces B, C, and E was observed. The zeta potential of the surface on particle D was significantly ($p < 0.05$) more negative but still similar to other CD:MPC surfaces. Surfaces B–E had a sufficient surface charge to inhibit rapid flocculation in buffers, compared to the control and A surfaces [33, 34].

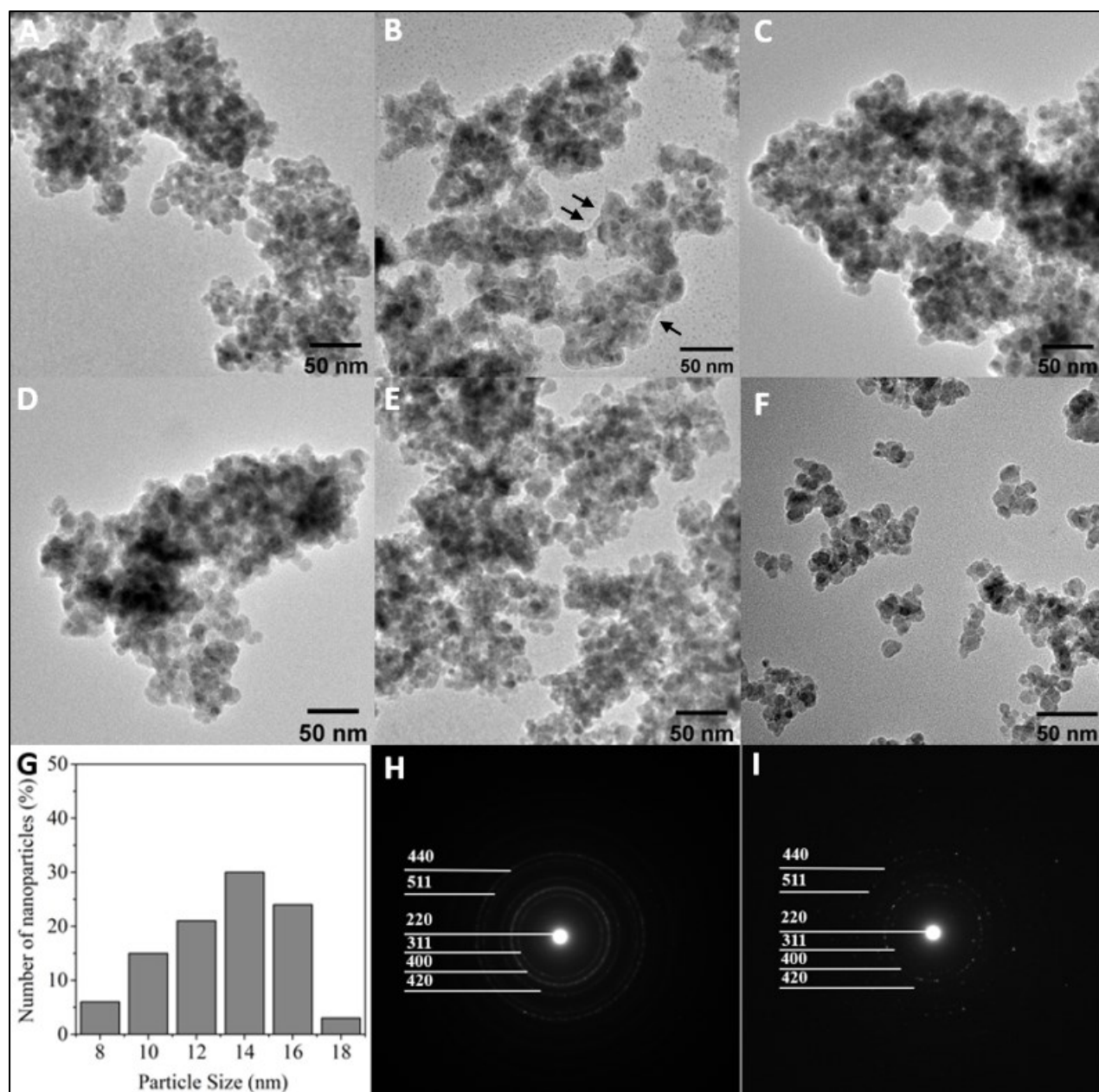


Figure 4.2 Representative TEM and SAED characterization of bare and polymer coated MNPs. (A) - (E) TEM image of synthesized polymer modified nanoparticles of sample A-E; Black arrow indicated the polymer layer. (F) TEM image of bare MNP. (G) Particle size distribution of bare MNP in (F). (H) SAED pattern of particle E. (I) SAED pattern of MNP.

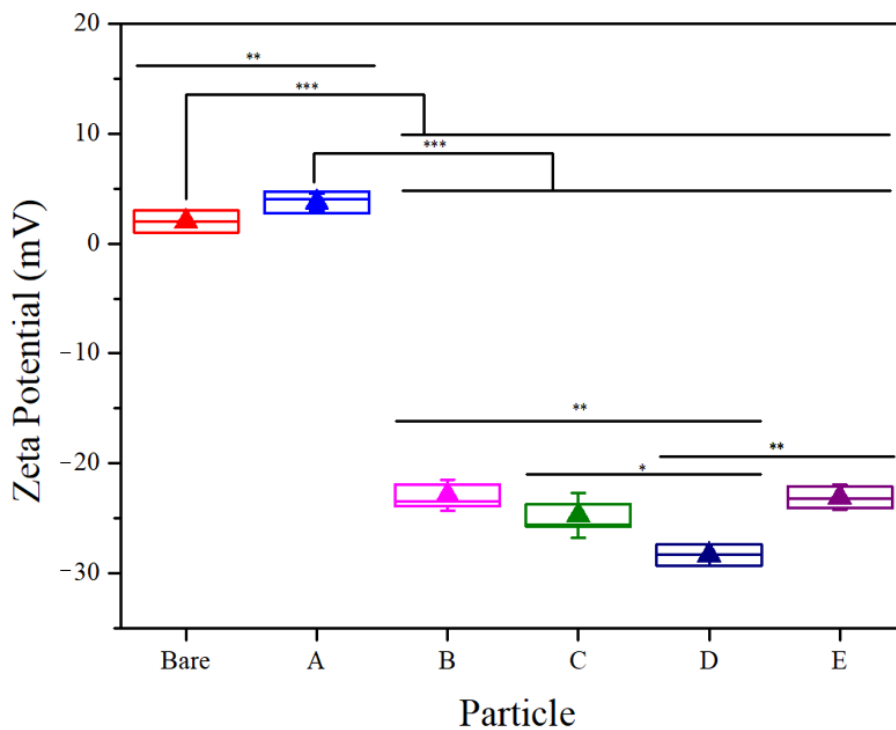


Figure 4.3 Representative zeta potential test of bare MNP and particles A to E. Unpaired *t*-tests were conducted to compare results across each pair of groups. Comparisons that are not displayed were not statistically significant (* $p < 0.05$, ** $p < 0.01$, *** $p < 0.001$, data presented as mean \pm 1 SD, $n = 3$).

4.3.2 Circular Dichroism

The effect of surface chemistry differences between particles A to E and the bare MNP control on the lysozyme, HSA, and α -lactalbumin structure were evaluated (Figure 4.4, Table 4.2). Overall, modified MNPs exhibited negligible effects on the secondary structure of all three proteins. In the case of lysozyme, peak absorbance occurred at 192 nm, and a reduction of 2.4~3.4% in the helix and an increase of 1.7~2.4% in the beta-sheet were observed compared to the native

protein reference. Concerning HSA, particle D induced the largest reduction in the helix (8.4%), followed by C (3.6%) and E (2.3%). The random coil structure for HSA with particle D was notably increased, by 5.7%. α -Lactalbumin had a peak at 188 nm and minima around 218~223 nm. For α -lactalbumin, the conformational change induced by the engineered surface was less than 1% compared to the native control, except for a 1.7% decrease in the helix with particle D. Bare MNPs induced the most conformational changes in α -lactalbumin, reducing the helix by 3.5%. Among these three proteins, the net-negative-charged HAS structure was affected the most. As a carrier of many substances in the blood, HSA can bind to substances of varied characteristics and have its structure perturbed through this interaction. In contrast, lysozyme and α -lactalbumin remained relatively stable, perhaps due to the smaller sizes (HSA: 66.5 kDa, lysozyme and α -lactalbumin: 14 kDa) and charge densities (HSA: -19, lysozyme (+8), and α -lactalbumin (-7)) relative to HSA [23, 35-37].

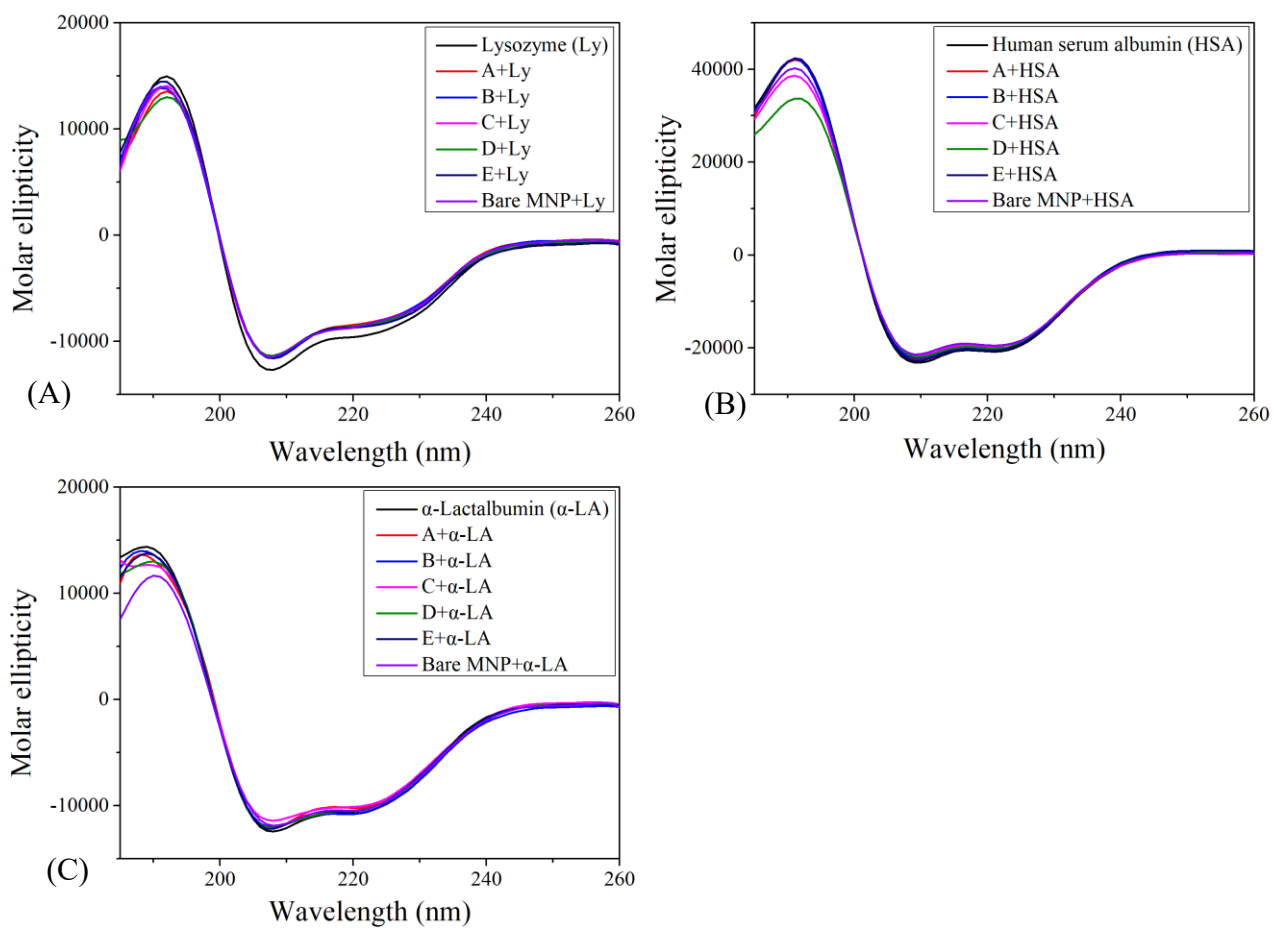


Figure 4.4 Circular dichroism spectrum of (A) lysozyme, (B) HSA, and (C) α -lactalbumin in the presence of particles A to E and bare MNP ($n = 3$).Circular dichroism spectrum of (A) lysozyme, (B) HSA, and (C) α -lactalbumin in the presence of particles A to E and bare MNP ($n = 3$).

Table 4.2 Representative results for the effects of particles A to E and MNP on the secondary structure of α -lactalbumin, human serum albumin, and lysozyme, as determined using circular dichroism spectra between 190 and 260 nm. The results are an average of three repeated scans. The unit is in percentage (%). Data represent mean \pm 1 SD, n = 3.

	<i>Particle</i>	<i>Helix</i>	<i>Beta sheet</i>	<i>Beta turn</i>	<i>Random coil</i>
<i>Lysozyme</i>	<i>Blank</i>	33.8 \pm 0.1	19.7 \pm 0.2	18.1 \pm 0.0	28.4 \pm 0.3
	<i>A</i>	30.4 \pm 0.2	22.1 \pm 0.1	18.0 \pm 0.1	29.6 \pm 0.1
	<i>B</i>	30.7 \pm 0.1	21.8 \pm 0.3	18.0 \pm 0.0	29.5 \pm 0.0
	<i>C</i>	31.1 \pm 0.1	21.3 \pm 0.2	18.0 \pm 0.0	29.6 \pm 0.3
	<i>D</i>	30.6 \pm 0.3	21.9 \pm 0.2	18.0 \pm 0.0	29.9 \pm 0.5
	<i>E</i>	31.4 \pm 0.1	21.0 \pm 0.1	17.9 \pm 0.1	29.7 \pm 0.2
	<i>Bare MNP</i>	30.7 \pm 0.2	21.8 \pm 0.3	17.9 \pm 0.1	29.5 \pm 0.1
<i>Human serum albumin</i>	<i>Blank</i>	71.0 \pm 0.1	4.1 \pm 0.2	12.6 \pm 0.0	12.3 \pm 0.2
	<i>A</i>	71.0 \pm 0.2	4.1 \pm 0.1	12.6 \pm 0.1	12.3 \pm 0.2
	<i>B</i>	71.1 \pm 0.3	4.1 \pm 0.4	12.6 \pm 0.0	12.3 \pm 0.2
	<i>C</i>	67.4 \pm 0.1	5.4 \pm 0.2	12.9 \pm 0.2	14.3 \pm 0.3
	<i>D</i>	62.6 \pm 0.5	6.0 \pm 0.1	13.4 \pm 0.3	18.0 \pm 0.2
	<i>E</i>	68.7 \pm 0.2	6.5 \pm 0.2	13.0 \pm 0.2	11.8 \pm 0.1
	<i>Bare MNP</i>	70.3 \pm 0.1	4.2 \pm 0.3	12.7 \pm 0.1	12.7 \pm 0.1
<i>α-Lactalbumin</i>	<i>Blank</i>	31.7 \pm 0.2	22.1 \pm 0.3	18.2 \pm 0.0	28.0 \pm 0.3
	<i>A</i>	31.7 \pm 0.1	22.1 \pm 0.2	18.2 \pm 0.1	28.0 \pm 0.2
	<i>B</i>	30.8 \pm 0.3	22.4 \pm 0.2	18.2 \pm 0.1	28.6 \pm 0.1
	<i>C</i>	31.4 \pm 0.4	21.7 \pm 0.2	18.1 \pm 0.1	28.7 \pm 0.2
	<i>D</i>	30.0 \pm 0.1	22.9 \pm 0.3	18.1 \pm 0.0	29.0 \pm 0.3
	<i>E</i>	31.3 \pm 0.2	22.1 \pm 0.4	18.2 \pm 0.1	28.5 \pm 0.2
	<i>Bare MNP</i>	28.2 \pm 0.2	22.4 \pm 0.3	21.1 \pm 0.1	28.4 \pm 0.1

The values of SDs in this table are the modeling results.

4.3.3 Changes in intrinsic fluorescence of HSA upon adsorption

Previous studies have shown that the intrinsic fluorescence intensity of tryptophan located in HSA can be reduced with increased adsorption to MNPs, and that this is potentially dependent upon the surface chemistry of particles [25, 38]. In this fluorescence study, the quenching effect (Figure 4.5A) for HSA upon incubation with engineered MNPs and bare MNPs allowed for the determination of the number of binding sites on nanoparticles (n) and the binding constant (K_a) for each type of MNP (Figure 4.5B). Particles A and B showed the same number of binding sites, close to the number of binding sites on particle C (ranging from 1.23 to 1.26). Among different types of MNP formulations, particles E and D had the lowest and highest number of binding sites, respectively. Furthermore, we found that particle C had the weakest binding affinity towards HSA, whereas bare MNPs without surface modification exhibited the strongest binding affinity towards HSA (Figure 4.5B).

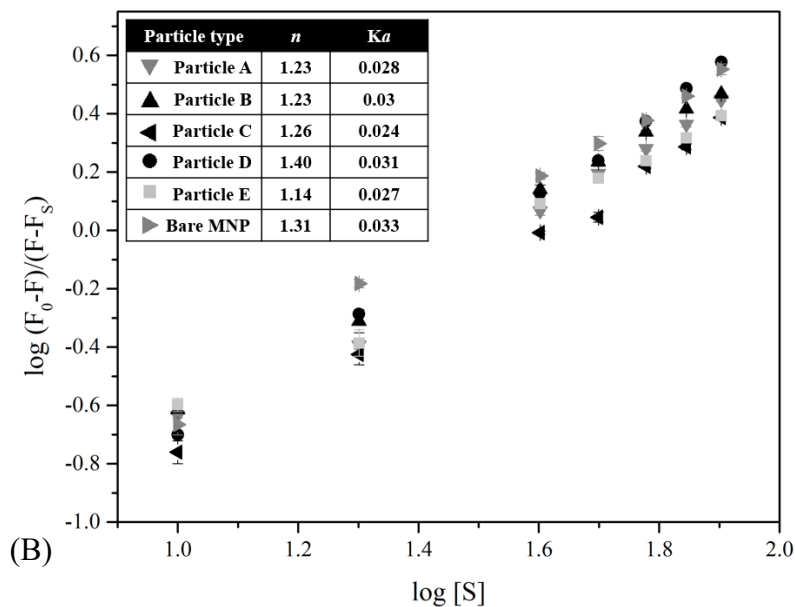
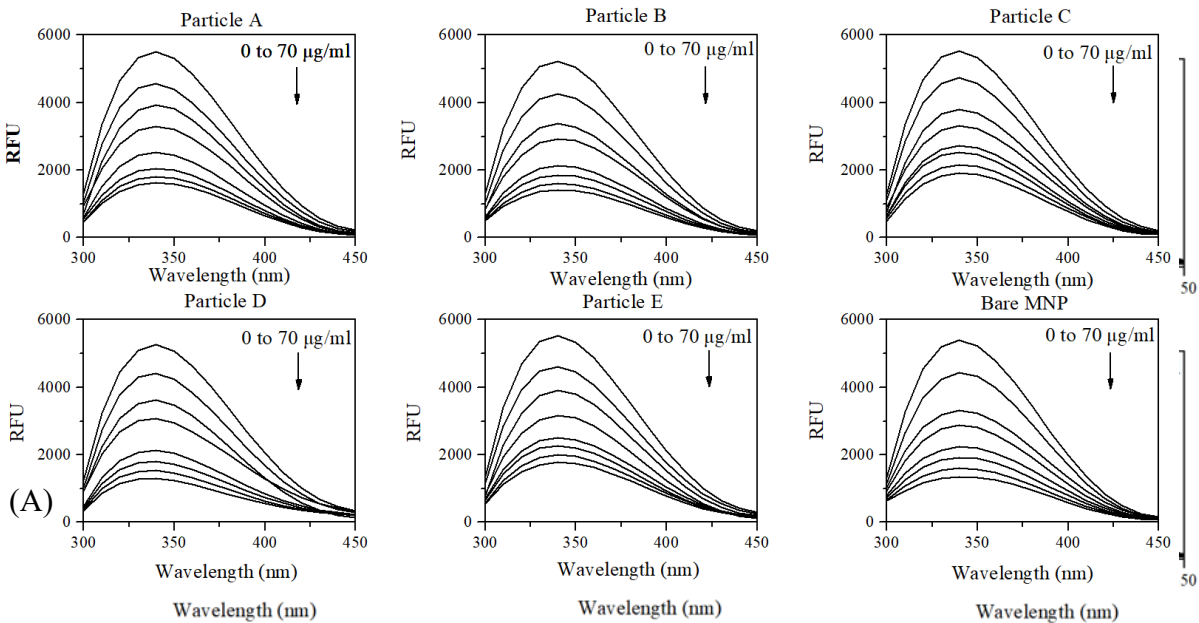


Figure 4.5 Study of the interaction of HSA protein with MNPs via quenching of the intrinsic fluorescence of HSA in the presence of different concentrations of MNPs. (A) Fluorescence emission spectra of HSA solution titrated against increasing concentrations of MNPs in the solution (0–70 µg/mL). (B) Binding constant (K_a) and number of binding sites (n) obtained from

the plot, $\log [(F_0 - F)/(F - F_s)]$ vs. $\log [S]$. RFU = relative fluorescence units, $[S]$ = MNP concentration, F_0 = relative fluorescence intensity (F) of protein solution alone, and F_s = relative fluorescence intensity of protein saturated with MNPs. Data represent mean \pm 1 SD, $n \geq 3$.

4.3.4 Total adsorbed protein

A detergent-compatible BCA assay was used to quantify the concentration of eluted plasma proteins from each type of MNP (Figure 4.6), which ranged from 0.17 to 0.3 mg/mL for a constant surface area of MNP. Bare MNP showed the highest, and particle E showed the lowest values of eluted proteins. A significant reduction ($p < 0.05$) in protein adsorption occurred for all modified nanoparticles compared to the unmodified bare nanoparticles. Although particle size has been shown to influence protein binding [39], the particle size and surface area of these MNP systems were relatively similar, and surface chemistry likely dominated the adsorption of proteins. Notably, the protein adsorption of MNPs displayed an inverse relationship with the content of MPC, with bare particles exhibiting the highest plasma protein adsorption and particle E showing the lowest. Intermediate MPC-containing films displayed a gradual decline in the total adsorbed amount of protein, except for particle D. Nonetheless, there was a significant difference between the protein content adsorbed by bare particles and particle D. These findings correlate with previously reported results, where MPC-only modified surfaces have shown significantly improved inhibition of protein adsorption [40, 41].

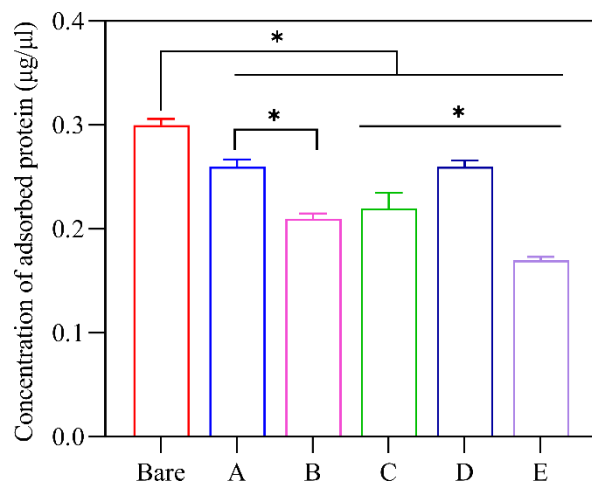


Figure 4.6 Representative results showing the amount of adsorbed protein determined using the BCA assay. * Represents $p < 0.05$, data represent mean \pm 1 SD, $n \geq 3$.

4.3.5 Plasma clotting in the presence of polymer-coated nanoparticles

Intrinsic contact activation through the interaction of the surface, Factor XII, high-molecular-weight kininogen, and prekallikrein is a known humoral response to artificial materials that leads to thrombus formation [42, 43]. Plasma clotting experiments were conducted for bare and engineered MNPs (Figure 4.7, Table 4.3). Considering the obvious surface area effect on clot kinetics, clot formation upon MNP incubation was much quicker than that of the plasma control, but surprisingly led to a reduced clot intensity. Native plasma showed that clotting initiated at 10 min and reached a plateau at 30 min, with a turbidity of 0.93. Overall, adding MNPs advanced the clotting time but inhibited the final clot turbidity. Internal comparisons of the polymer film on systems with similar surface areas showed that particles A, D, and E showed a clotting start time at 2 min, whereas particles B and C showed clotting at 1 min. The plateaus were reached at 5 min for particles A, B, and C, and 6 min for D, E, and bare MNP. From the turbidity results, it was observed that particle D inhibited clot formation the most compared to the other particles. Particle

E exhibited the best compatibility, as demonstrated by the lowest clotting inhibition effect. This was predictable as it was coated with solely the MPC polymer, which was introduced to improve the overall anti-fouling and biocompatibility. In the co-polymer groups, particle C showed the highest clotting inhibition effect. Coagulation was also assessed in whole blood through rotational thromboelastometry (ROTEM), where a similar effect was observed—the addition of any type of MNP decreased the time to fibrinogen polymerization (clotting time) compared to the control (whole blood with an equivalent volume of water added) (Figure 4.7B).

Table 4.3 Summary of platelet-poor plasma clotting initiation and completion time of non-uremic toxin group, 1 hr incubation group and 4 hr incubation group. (n = 3, all SDs are less than 3 seconds).

	A	B	C	D	E	Bare MNP	Plasma
	0.67	0.57	0.64	0.45	0.74	0.79	0.93
<i>Clotting starting point (min)</i>	2	1	1	2	2	2	10
<i>Plateau reach point (min)</i>	5	5	5	6	6	6	30

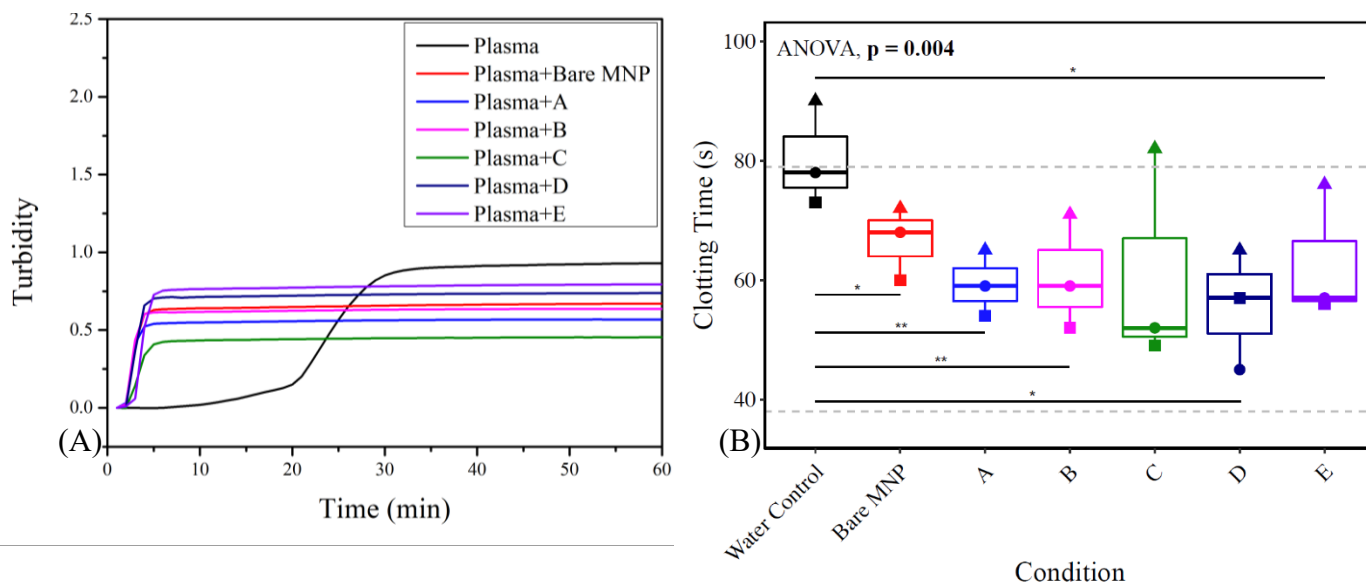


Figure 4.7 Presence of MNPs reduces clotting time driven by plasma proteins. (a) Representative plots of baseline-corrected average clot formation in platelet-poor human plasma over 60 minutes, with particles A to E or bare MNP present. (b) Whole blood ROTEM results for clotting time – reflective of fibrinogen polymerization. Shapes reflect biological replicates. Results were compared across groups with repeated measures ANOVA to compare differences within biological replicates, across groups, and paired t-tests were used for pairwise comparisons to the water control (* $p < 0.05$, ** $p < 0.01$). Comparisons not shown were not statistically significant.

4.3.6 Quantification of protein adsorption

The immunoblot band intensity data for all MNPs were quantified using a 13-step gray-scale system, where zero indicates no visible band, and 12 indicates the highest band intensity. To facilitate the band intensity comparison between different systems, the amount of loaded protein and the color development time were kept constants for all systems studied (Table 4.4)

Table 4.2 Relative intensities of immunoblot of plasma proteins adsorbed to different types of MNPs.

Plasma Protein	Fragment Size (kDa)	Bare MNP	A	B	C	D	E
			PM β CD:MPC (4:0)	(3:1)	(2:2)	(1:3)	(0:4)
Fibrinogen	68	7	8	8	7	7	6
	56	6	8	8	7	4	4
	48	6	7	8	6	4	4
	<48	4	3	5	2	0	0
α_1 -Antitrypsin	54	9	8	9	8	5	5
Prothrombin	72	2	2	2	2	1	2
Vitronectin	54	8	8	10	8	5	6
Prekallikrein	85	5	2	5	2	1	2
	50	10	8	9	7	2	5
Antithrombin	53	6	6	4	4	3	3
IgG	55	7	4	3	8	5	5
	27	8	7	8	9	5	5
Albumin	66	9	7	7	8	9	9
Plasminogen	91	9	8	7	8	5	3
C3	187	0	0	0	0	0	0

	115	5	4	4	5	3	2
	70	10	10	10	9	7	8
	42	5	8	8	7	3	3
Factor XII	80	3	2	1	2	1	1
Factor XI	70	9	8	9	10	8	8
Transferrin	77	8	8	7	10	10	8

Albumin (66.5 kDa) is the most prevalent plasma protein (35–50 g/L) and is largely responsible for binding various metabolic compounds, lipids, and even medications [44]. Moreover, albumin is known to adsorb to surfaces, which alters the subsequent binding of other proteins and even affects coagulation [45, 46]. For example, albumin adsorption to polyacrylonitrile hemodialysis membranes has reduced the adhesion and aggregation of platelets to the membrane [47]. Previous research using immunoblotting techniques has shown that albumin has a high affinity to elastin-like polypeptide nanoparticles, requiring the dilution of primary and secondary antibodies [28]. Herein, albumin adsorption was not sufficient enough to require a dilution of antibodies for characterization. Studies conducted on siliconized glass and polycarbonate membrane surfaces have shown that albumin has a higher affinity for hydrophobic surfaces [48, 49]. Our results surprisingly showed that as the MPC content in the film increased, the adsorbed albumin increased to levels similar to the control bare MNP surface. This is contrary to studies that have shown that the addition of β -cyclodextrin to hydroxyapatite nanoparticles enhanced albumin adsorption [50].

4.3.6.1 Immune response-related proteins

The activation of the complement system is accomplished through the concerted action of multiple proteins, which operate through three distinct activation pathways: the classical pathway, the alternative pathway, and the mannose-binding lectin pathway [51]. These cascades mount a defense against bacterial infection and the clearance of immune complexes and apoptotic cells. It also links innate and adaptive immune responses as complement component 3 (C3) plays a key role in all three activation pathways, particularly in the alternative pathway, which is involved in biomaterial-induced complement activation [28, 52]. Prolonged blood exposure to synthetic surfaces during hemodialysis can lead to chronic inflammation due to chronic activation of the complement system [53]. Four distinct bands can be seen for C3: whole C3, 187 kDa, α chain, 115 kDa, β chain, 70 kDa, and an activation fragment, 42 kDa [28]. Herein, intact C3 was not observed for any MNP system. All other bands were present and abruptly decreased in intensity for particles D and E. Bare MNP controls were similar in band intensity to the CD-only film (particle A). The activation fragment (42 kDa) was present for all MNP types and showed a drastic decrease for particles D and E. This suggests that particle D and E MNPs induced less activation of C3 than other surfaces. C3a was also independently assayed via ELISA in three biological replicates of MNP-depleted plasma from whole-blood hemocompatibility studies (Figure 4.8). One replicate mirrored the results of decreased C3a in bare MNP and particles D and E, but these results were inconsistent in the other two replicates. Taken together with the protein adsorption results from the immunoblot analysis, the independent C3a ELISA results may indicate that while there was an increased presence of C3a with the increased PM β CD:MPC ratio in the MNP coating, there may also be donor-dependent increases in C3a generation with these formulations, considering that the ELISA results on MNP-depleted plasma were not significantly different. However, consistent with

the blotting results, a trend toward decreased C3a in the MNP-treated plasma compared to the untreated control was observed, indicating adsorption to all MNP surfaces.

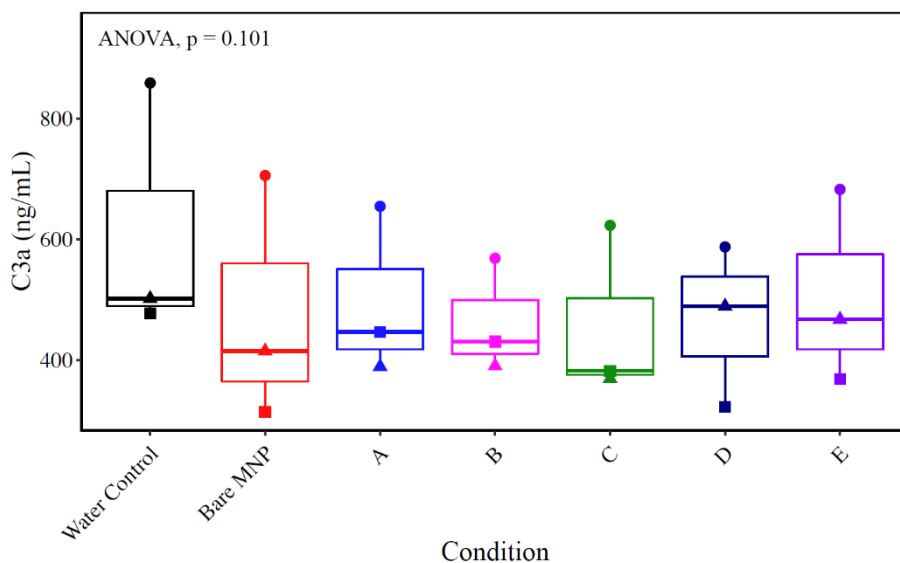


Figure 4.8 C3a ELISA results of MNP-depleted plasma from whole-blood hemocompatibility studies. Whole blood from $n = 3$ healthy donors was incubated with 0.18 mg/mL of each MNP formulation, and MNP-depleted plasma was assayed for C3a. Results were compared across groups with repeated-measures ANOVA to compare differences within biological replicates across groups, and paired t -tests were used for pairwise comparisons to the water control. Comparisons not shown were not statistically significant.

Of the five distinct isotypes of serum immunoglobulins (IgM, IgD, IgG, IgA, and IgE), IgG is the most prevalent in human serum: ~10–20% of total plasma protein [54]. IgG presence leads to the activation of the classical pathway of complement [28]. The light chain of IgG (27 kDa) again showed a step decrease in intensity for particles D and E compared to all other systems. The heavy chain of IgG (55 kDa) was relatively low for all MNP systems, with no trend associated with

the MPC content of the surface film. This result is consistent with the role of the content of MPC in inhibiting protein adsorption.

Transferrin (77 kDa) carries iron (ferric iron) throughout the body, is a component of the innate immune system, can activate macrophages, and acts to restrict the survival of bacteria [28, 55-57]. All types of MNPs showed relatively high and consistent transferrin adsorption, suggesting that this protein's binding may trigger macrophage activation.

Vitronectin is a multifunctional glycoprotein and, in plasma, acts as a complement regulatory component. Different types of MNPs, including bare particles, showed relatively high-intensity values associated with vitronectin, compared to the low levels observed for particles D and E. Vitronectin is known as a major plasma protein in association with polymer surfaces. Although fibronectin and vitronectin have similar plasma concentrations, studies conducted on various polystyrene-based surfaces have shown that vitronectin has a greater propensity to bind to surfaces [58]. Although MNPs showed moderate to high values for vitronectin, none of the MNPs were found to adsorb fibronectin.

α_1 -Antitrypsin is the most abundant serine protease inhibitor in human plasma, constituting 95% of the trypsin inhibitory capacity. As a serine protease inhibitor, the primary role of α_1 -antitrypsin is to inhibit the proteolytic activity of serine protease neutrophil elastase. Aside from its primary role as a protease inhibitor, α_1 -antitrypsin has other immunomodulatory functions, including anti-inflammatory properties and regulation of T- and B-lymphocytes [59, 60]. α_1 -Antitrypsin has been previously found absorbed in large amounts to elastin-like polypeptide nanoparticles, suggesting its inhibitory role in preventing the nanoparticles from degradation by elastase [28]. This protein was found in high binding levels to bare MNP, and particles A, B, and C, but particles D and E showed moderate adsorption levels. It has been previously shown that α_1 -antitrypsin in the protein corona of Au nanoparticles could act as a cell-binding-promoting factor

[61-63]. Considering the anti-inflammatory role of α_1 -antitrypsin, this protein may reduce macrophage activity [64].

α_2 -Macroglobulin is another component of the innate immune system, regulating proteases by clearing them from the blood [65, 66]. No visible immunoblot was identified for this protease. The lack of α_2 -macroglobulin may suggest that MNP surfaces are not playing an active role in promoting either clotting or fibrinolysis, as it acts as an inhibitor for both processes [29].

4.3.6.2 Coagulation-related proteins

Fibrinogen (340 kDa) has a key role in coagulation and is a substrate for three related enzymes, including Factor XIIIa, thrombin, and plasmin. It is a heterodimer, each half consisting of three polypeptide chains (A α , B β , and γ), linked via disulfide bonds. Thrombin enzymatically cleaves A α and B β chains from the N-terminal, which ultimately leads to the initiation of clot formation. Factor XIIIa stabilizes the fibrin polymers via cross-linking, thus increasing its resistance to degradation through fibrinolysis [67, 68]. Fibrinogen appears as three distinct bands: A α , 68 kDa, B β , 56 kDa, and γ , 48 kDa. In addition, cleavage fragments appear as bands at <48 kDa [28]. In all MNP systems, the band intensity for all fibrinogen fragments remained relatively constant but decreased for particles D and E. Particles D and E showed no fibrinogen cleavage fragments (<48 kDa). It has been previously shown that coating of polyethylene and polypropylene surfaces with β -CD decreased the adsorption of fibrinogen, potentially enhancing the blood compatibility of those surfaces [69]. However, in this case, it is apparent that films with higher amounts of MPC showed a lower amount of related fibrinogen.

Prothrombin (72 kDa) is a single-chain glycoprotein that is an inactive precursor for thrombin. The proteolytic conversion of prothrombin to thrombin is induced by Factor Xa in the presence of Factor V, phospholipid, and Ca²⁺ [70]. Low levels of prothrombin were observed for all MNP

systems, whereas the amount of antithrombin decreased with the increasing MPC composition of the engineered films. Antithrombin (53 kDa) is a serine protease inhibitor that is an endogenous anticoagulant that complexes with thrombin, and other activated coagulation factors, to inhibit coagulation [71].

The contact pathway of coagulation comprises three serine proteinases, namely coagulation Factors XII and XI, prekallikrein, and the non-enzymatic cofactor high-molecular-weight kininogen [72]. Factors XII and XI have been previously reported in low quantities in protein corona of poly(acrylic acid)-coated TiO₂ nanoparticles. Herein, low and consistent amounts of Factor XII were found on all MNPs, where bare particles showed the highest intensity. Factor XI was relatively strongly bound to all MNP surfaces, with no decrease observed for particles D and E, similar to previous reports for poly(acrylic acid)-coated Fe₂O₃ nanoparticles [73]. Prekallikrein, the precursor of kallikrein, cleaves high-molecular-weight kininogen [74] and may be found at 85 kDa, with consistent levels for all modified MNPs that were much lower than the bare MNP control. The kallikrein band (50 kDa) was relatively higher than prekallikrein (85 kDa) for all MNP types. The particle D and E films again showed a sharp decrease in kallikrein intensity. Previous studies have established that the activation of the contact system results in a decrease in the intensity of prekallikrein immunoblot bands, with the formation of complexes of kallikrein with the C1 inhibitor and α_2 -macroglobulin [75].

Fibronectin is a critical component of the fibrin clot, binding to fibrin via non-covalent interactions and covalent cross-linking, leading to the regulation of platelet function and hemostasis [76]. Protein S regulates coagulation, exhibiting anticoagulant function independent of activated protein C, which directly inhibits intrinsic tenase and prothrombinase complexes [77]. None of the MNPs showed adsorption of fibronectin, protein S, or protein C, suggesting a limited clot formation and fibrinolytic response [28].

Plasminogen (91 kDa) is the inactive precursor of plasmin, the major protease that catalyzes the degradation of fibrin clots. Again, particles D and E showed a sharp decline in adsorbed plasminogen compared to the other MNP types. It is thought that surface adsorption of plasminogen might indicate fibrinolytic activity [78, 79].

3.7. Whole blood hemocompatibility and impact on platelet function

Further characterization was performed in whole blood to assess the hemocompatibility of the MNP formulations based on the published criteria of leukocyte presence, hemolysis, and platelet function—in addition to the results reported above on complement activation and coagulation [80]. Whole blood collected in 2.7 mL of sodium citrate vacutainers from $n = 3$ biological replicates was incubated at 37 °C for 1 h with the same concentration of MNPs as the previous experiments in plasma (0.18 mg/mL), and complete blood counts were performed on the Sysmex XN-550 hematology analyzer. A trend toward a decrease in the platelet number was observed in particle D (Figure 4.9a), which could reflect platelet aggregation, rendering individual platelets undetectable. No evident trends emerged for differences in leukocyte (Figure 4.9b) or red cell (Figure 4.9c) counts, despite a statistically significant repeated-measures ANOVA result for leukocyte counts.

Supernatant hemoglobin levels were measured in MNP-depleted plasma from the MNP-treated whole blood *via* the Harboe spectrophotometric method for quantification of percent hemolysis, based on the total hemoglobin content of the blood measured on the hematology analyzer. Results in Figure 4.9d demonstrate a trend toward increased hemolysis in MNP-treated whole blood, with a statistically significant increase in the presence of particle A and a larger effect size for particle C, just below statistical significance ($p = 0.057$). Important to note, however, is

that the supernatant hemoglobin content for all specimens remained below 0.2 g/L, which is considered to be insignificant hemolysis [81]. Therefore, MNP treatment did not appear to result in a concerning level of hemolysis.

The impact of the series of MNPs on platelets was further investigated through flow cytometry and ROTEM (Figure 4.10). CD62P (P-selectin) is stored in platelet alpha-granules and mobilized to the platelet surface upon platelet activation and subsequent degranulation. Flow cytometry was used for the detection of the surface expression of CD62P (P-selectin) on unstimulated platelets (Figure 4.10a) and platelets stimulated with 10 μ M of ADP (Figure 4.10b) to measure the baseline activation and the response to an agonist, respectively. Results of the baseline activation illustrated a trend toward increased platelet activation in all MNP-treated conditions, with statistically significant but small effect sizes observed in bare, A, and E MNPs. While not statistically significant due to the small sample size tested here, baseline platelet activation increases with large effect sizes were observed for particle C and, most prominently, particle D. This trend suggests increased platelet activation with coatings consisting of lower concentrations of CD in the presence of MPC. It is unclear why these formulations induce platelet activation, but it may be attributed to the inhomogeneous surface composition indicated by the PDI. Results of baseline platelet activation were largely mirrored in the platelets stimulated with ADP, demonstrating lower levels of additional degranulation in the conditions that had considerable baseline degranulation. If platelets were degranulated in response to the MNPs, it tracks that they would have a reduced additional response to agonists and may show functional deficits in clot formation.

The impact of the series of MNPs on platelets was further investigated through flow cytometry and ROTEM. CD62P (P-selectin) is stored in platelet alpha-granules and mobilized to the platelet surface upon platelet activation and subsequent degranulation. Flow cytometry was

used for the detection of surface expression of CD62P (P-selectin) on unstimulated platelets (Figure 4.9a), and platelets stimulated with 10 μ M ADP (Figure 4.9b), to measure baseline activation and response to an agonist, respectively. Results of baseline activation illustrate a trend toward increased platelet activation in all MNP-treated conditions, with statistically significant but small effect sizes observed in bare, A, and E MNPs. While not statistically significant due to the small sample size tested here, baseline platelet activation increases with large effect sizes were observed for particle C and most prominently in particle D. This trend suggests increased platelet activation with coatings consisting of lower concentrations of CD in the presence of MPC. It is unclear why these formulations induce platelet activation, but it may be attributed to the inhomogeneous surface composition indicated by the PDI. Results of baseline platelet activation were largely mirrored in the platelets stimulated with ADP, demonstrating lower levels of additional degranulation in the conditions that had considerable baseline degranulation. If platelets are degranulated in response to the MNPs, it tracks that they would have a reduced additional response to agonists and may show functional deficits in clot formation.

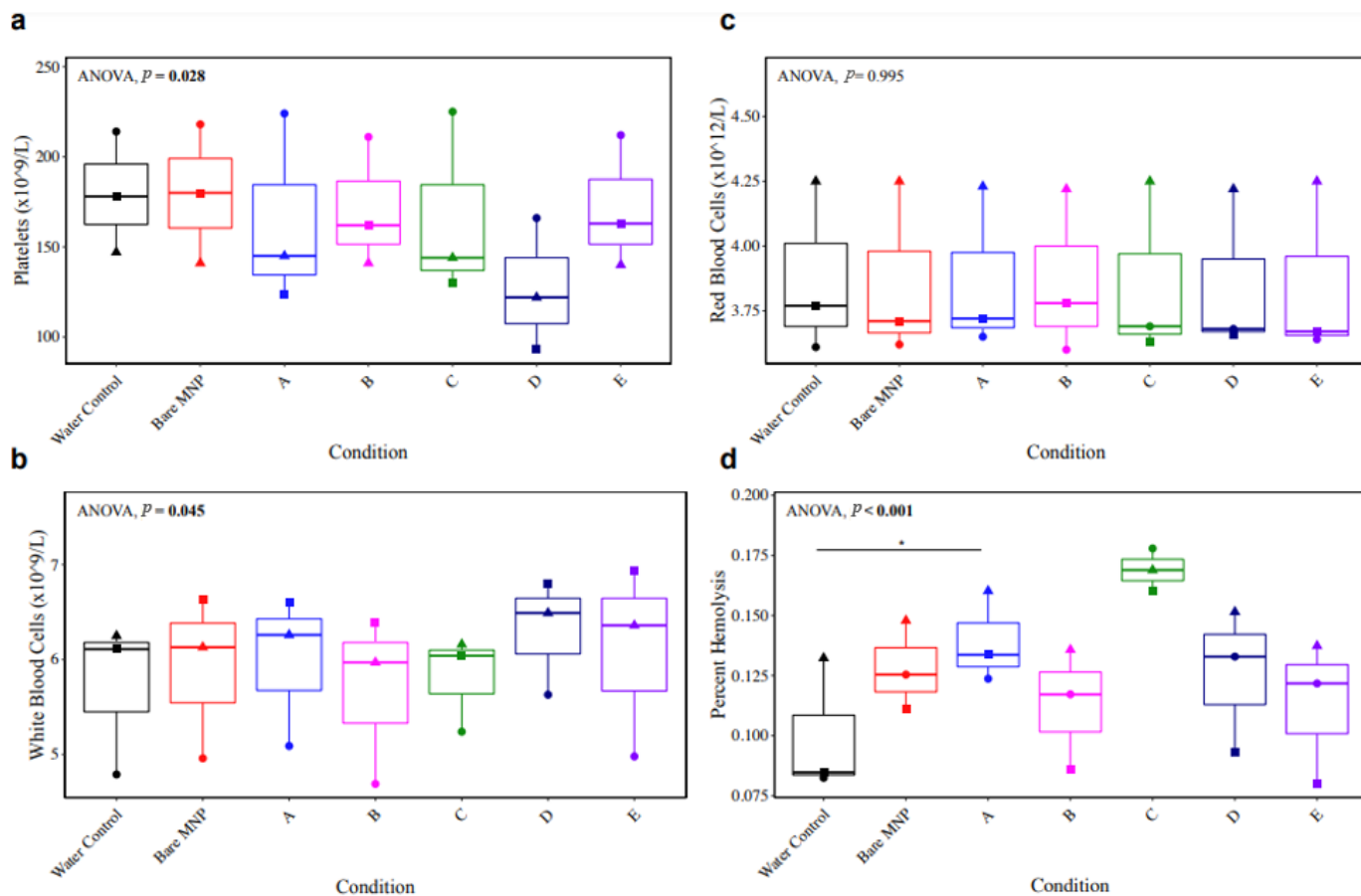


Figure 4.9 Complete blood counts and hemolysis in response to whole-blood MNP treatment.

Whole blood from $n = 3$ healthy donors was incubated with 0.18 mg/mL of each MNP formulation, and complete blood counts were measured on the Sysmex XN-550 hematology analyzer. Results for (a) platelets, (b) white blood cells, and (c) red blood cells are shown. Hemolysis was assayed in MNP-depleted plasma via the Harboe method (d). Results were compared across groups with repeated-measures ANOVA to compare differences within biological replicates across groups, and paired t -tests were used for pairwise comparisons to the water control ($* p < 0.05$). Comparisons not shown were not statistically significant.

Next, we analyzed the platelet function in whole-blood coagulation using ROTEM, with platelet-mediated outcomes of the maximum clot firmness and clot formation time. The *EXTEM* ROTEM reagent was used to probe the function of the extrinsically activated coagulation pathway. Increases in platelet activation with particle C did translate to a statistically significant increase in clot formation time, indicating reduced platelet function, but this was limited to a trend with particle D. No observable trends across replicates were present for the maximum clot firmness. All platelet-dependent ROTEM results remained within the normal ranges, as per the manufacturer's instructions.

Interestingly, the biological replicate that showed the largest reduction in the platelet count (illustrated in graphs with squares) also showed the most pronounced changes in the platelet function assays, with the largest increase in the unstimulated CD62P surface expression, largest decrease in the maximum clot firmness, and largest increase in the clot formation time for MNP particle D. While the other replicates did not demonstrate effects of the same magnitude, due to the limited sample size tested in these experiments, there is reason to believe that particle D had adverse effects on platelets. This was further supported by additional experiments tested at higher MNP concentrations (0.5 mg/mL), where particle D's adverse effects were exaggerated with much larger effect sizes, reaching a statistically significant decrease in the maximum clot firmness.

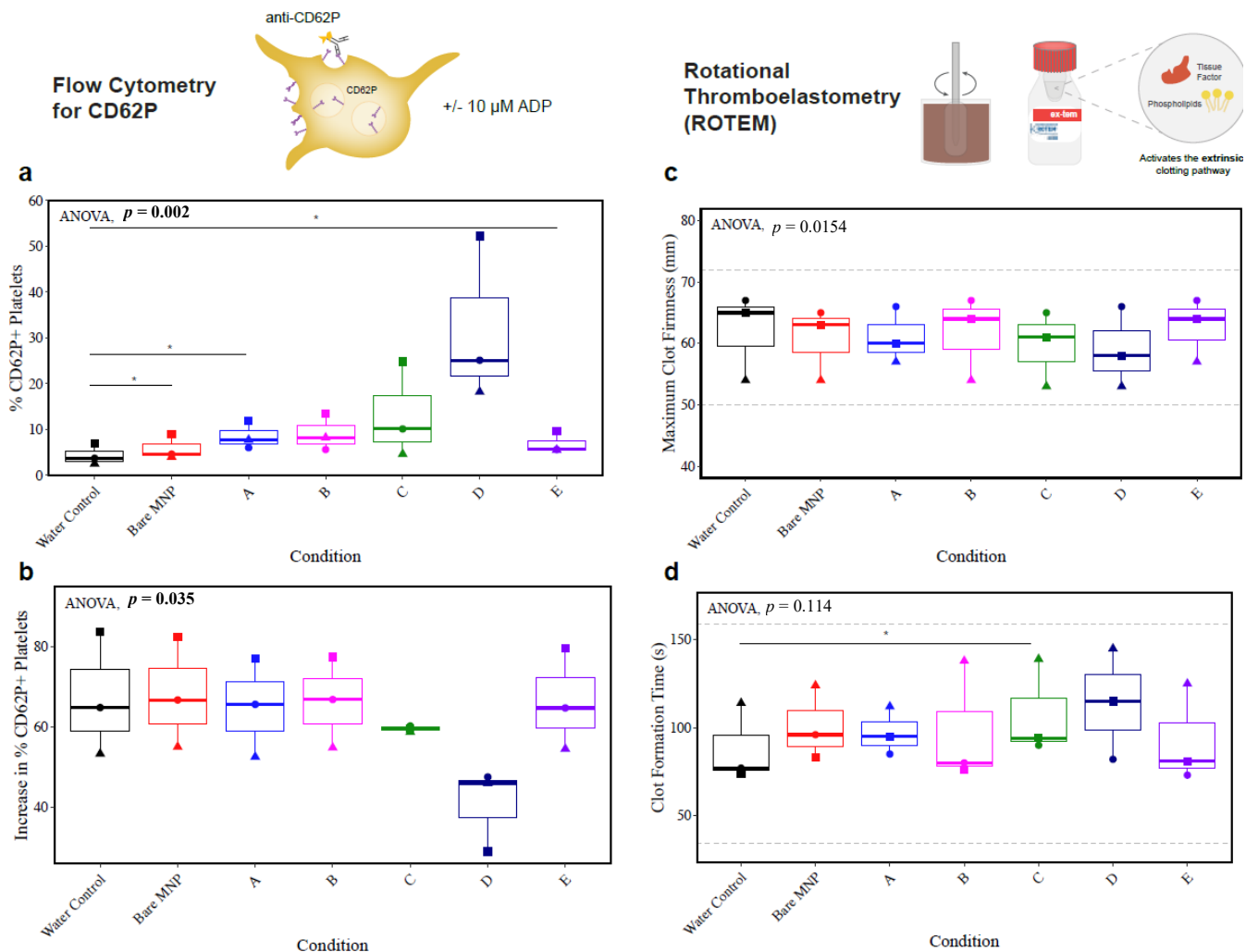


Figure 4.10 Trend toward increased platelet activation with lower PM β CD content, without robust impact on platelet function in coagulation. Whole blood from $n = 3$ healthy donors was incubated with 0.18 mg/mL of each MNP formulation, then assessed for platelet-related outcomes. (a) Baseline platelet activation reflected by surface expression of CD62P detected by flow cytometry. Percentage of CD62P+ platelets displayed. (b) Platelet degranulation in response to 10 μ M ADP, reflected by surface expression of CD62P detected by flow cytometry. Baseline activation was subtracted from the % CD62P+ platelets to yield the increase in degranulated platelets, as a measure of the platelet response. (c) Platelet function in coagulation reflected by

ROTEM maximum clot firmness and (d) clot formation time. Dashed lines indicate normal ranges as per manufacturer's information, and shapes reflect biological replicates. Results were compared across groups with repeated measures ANOVA to compare differences within biological replicates, across groups, and paired t-tests were used for pairwise comparisons to the

4.4 Conclusion

We assessed the biocompatibility of novel p(PM β CD-co-MPC) magnetic nanoparticles through various techniques, including circular dichroism, fluorescence spectrometry, plasma calcification, the BCA assay, and immunoblot. Circular dichroism showed that bare MNPs caused the highest decrease (3.5%) in the helix structure of α -lactalbumin, while other modified particles caused less than a 1.7% decrease. Particle D caused an 8.4% reduction in the helix structure and a 5.7% increase in the random coil structure. No significant structural alterations were observed in lysozyme. Fluorescence experiments showed that all particles quenched the tryptophan of HSA as the concentration increased. Particle C had the weakest binding affinity towards HSA, whereas bare MNPs exhibited the strongest binding affinity. Particle E had the lowest number of binding sites, whereas particle D had the highest. The zeta potential results showed that all coatings had an effect on the surface charge. However, surfaces B, C, and E were statistically similar, and even though D was statistically more negative, the difference was less than 10 mV.

We observed an obvious resuming effect in the plasma clotting experiment, mirrored by a fibrinogen-dependent outcome in whole-blood coagulation tests. The incubation of modified particles with uremic plasma resumed the turbidity and prolonged the clotting formation time point, among which particles B, C, and D represented the best results. The BCA assay indicated that the modified particles had less protein adsorption compared to the bare MNP. Furthermore, we assessed the adsorption of 21 plasma proteins to MNPs through immunoblot analysis. It was found

that only 12 proteins were adsorbed to MNPs. The lack of proteins S and C in the samples could imply a limited fibrinolytic response. Kininogen, which participates in initiating the contact activation pathway, was not found. The absence of kininogen in the protein corona of MNPs might provide insight into more suitable surfaces for blood-contacting materials. It is even more pertinent to note that kininogen (high molecular weight) can be adsorbed to hemodialysis membranes, where surface modification and ionic strength play an essential role in tuning the surface [82, 83]. In terms of the whole-blood hemocompatibility tested on $n = 3$ biological replicates, no robust MNP-dependent effects were observed on the erythrocyte or leukocyte counts. Particle D showed a trend toward decreased platelet counts, suggesting increased aggregation, which was mirrored in the flow cytometry results, suggesting increased platelet activation. Contradictory results from the previous literature make it difficult to ascertain if a small change in the surface charge accounts for increased platelet activity [84, 85]. It is likely mediated by the bound proteins more than the underlying surface charge. Particle C caused a statistically significant increase in hemolysis, though the results remained within acceptable levels of hemolysis and slight activation of platelets, which resulted in a statistically significant increase in the clot formation time. Overall, this work provided a comprehensive evaluation of the hemocompatibility of p(PM β CD-co-MPC)-engineered surfaces, reinforcing this polymer combination's potential for use in the context of chronic kidney disease.

4.5 References

1. Klefter, R., et al., *Savings in dialysis treatment?* Artificial Organs, 2002. **26**(1): p. 49-54.
2. Pavlenko, D., et al., *Carbon adsorbents with dual porosity for efficient removal of uremic toxins and cytokines from human plasma.* Scientific Reports, 2017. **7**(1): p. 1-7.
3. Lv, J., et al., *Prevalence and disease burden of chronic kidney disease.* Renal Fibrosis: Mechanisms Therapies, 2019: p. 3-15.
4. Ma, Y., et al., *Adsorption-based strategies for removing uremic toxins from blood.* Microporous Mesoporous Materials, 2021. **319**: p. 111035.
5. Bellringer, M., et al., *Beta-Cyclodextrin: 52-week toxicity studies in the rat and dog.* Food Chemical Toxicology, 1995. **33**(5): p. 367-376.
6. Zhou, Y., et al., *Enhanced removal of bisphenol A by cyclodextrin in photocatalytic systems: degradation intermediates and toxicity evaluation.* Chinese Chemical Letters, 2020. **31**(10): p. 2623-2626.
7. Yu, Q., et al., *Anti-fouling bioactive surfaces.* Acta Biomaterialia, 2011. **7**(4): p. 1550-1557.
8. Zhang, H., et al., *Anti-fouling coatings of poly (dimethylsiloxane) devices for biological and biomedical applications.* Journal of Medical Biological Engineering, 2015. **35**(2): p. 143-155.
9. Bhakta, S.A., et al., *Protein adsorption onto nanomaterials for the development of biosensors and analytical devices: A review.* Analytica Chimica Acta, 2015. **872**: p. 7-25.
10. Silva-Bermudez, P., et al., *An overview of protein adsorption on metal oxide coatings for biomedical implants.* Surface Coatings Technology, 2013. **233**: p. 147-158.

11. Pinholt, C., et al., *The importance of interfaces in protein drug delivery-why is protein adsorption of interest in pharmaceutical formulations?* Expert Opinion on Drug Delivery, 2011. **8**(7): p. 949-964.
12. Chen, S., et al., *Surface hydration: Principles and applications toward low-fouling/nonfouling biomaterials.* Polymer, 2010. **51**(23): p. 5283-5293.
13. Mohanty, J., et al., *Cyclodextrins in Anti-Biofouling Applications*, in *Supramolecular Chemistry in Corrosion and Biofouling Protection*. 2021, CRC Press. p. 335-346.
14. Liu, Y., et al., *Molecular simulations and understanding of antifouling zwitterionic polymer brushes.* Journal of Materials Chemistry B, 2020. **8**(17): p. 3814-3828.
15. He, M., et al., *Zwitterionic materials for antifouling membrane surface construction.* Acta Biomaterialia, 2016. **40**: p. 142-152.
16. Burns, N.L., et al., *Influence of surface charge on protein adsorption at an amphoteric surface: effects of varying acid to base ratio.* Journal of Colloid Interface Science, 1996. **178**(1): p. 116-122.
17. Phillips, S., et al., *Acrylamide and iodide fluorescence quenching as a structural probe of tryptophan microenvironment in bovine lens crystallins.* Current Eye Research, 1986. **5**(8): p. 611-620.
18. Krebs, H.A., *Chemical composition of blood plasma and serum.* Pharmaceutical Research, 1950. **19**(1): p. 409-430.
19. Sperling, C., et al., *Blood coagulation on biomaterials requires the combination of distinct activation processes.* Biomaterials, 2009. **30**(27): p. 4447-4456.
20. Fischer, M., et al., *Synergistic effect of hydrophobic and anionic surface groups triggers blood coagulation in vitro.* Journal of Materials Science: Materials in Medicine, 2010. **21**: p. 931-937.

21. Le, H.T., et al., *Synthesis, cytotoxicity, and phase-solubility study of cyclodextrin click clusters*. Journal of Pharmaceutical Sciences, 2014. **103**(10): p. 3183-3189.
22. Diget, J.S., et al., *Direct synthesis of well-defined zwitterionic cyclodextrin polymers via atom transfer radical polymerization*. European Polymer Journal, 2019. **116**: p. 84-90.
23. Goszczyński, T.M., et al., *Synthesis of beta-cyclodextrin-lysozyme conjugates and their physicochemical and biochemical properties*. Journal of Inclusion Phenomena Macrocyclic Chemistry, 2017. **87**: p. 341-348.
24. Dong, H., et al., *Recyclable antibacterial magnetic nanoparticles grafted with quaternized poly (2-(dimethylamino) ethyl methacrylate) brushes*. Biomacromolecules, 2011. **12**(4): p. 1305-1311.
25. Yallapu, M.M., et al., *Multi-functional magnetic nanoparticles for magnetic resonance imaging and cancer therapy*. Biomaterials, 2011. **32**(7): p. 1890-1905.
26. Beaven, G.H., et al., *A spectroscopic study of the haemin-human-serum-albumin system*. European Journal of Biochemistry, 1974. **41**(3): p. 539-546.
27. Chipman, D.M., et al., *The binding of oligosaccharides containing n-acetylglucosamine and n-acetylmuramic acid to lysozyme: the specificity of binding subsites*. Journal of Biological Chemistry, 1967. **242**(19): p. 4388-4394.
28. Bahniuk, M.S., et al., *Human plasma protein adsorption to elastinlike polypeptide nanoparticles*. Biointerphases, 2020. **15**(2): p. 021007.
29. Bahniuk, M.S., et al., *Bioactive glass 45S5 powders: effect of synthesis route and resultant surface chemistry and crystallinity on protein adsorption from human plasma*. Biointerphases, 2012. **7**(1): p. 41.
30. Han, V., et al., *A comparative study of common techniques used to measure haemolysis in stored red cell concentrates*. Vox Sanguinis, 2010. **98**(2): p. 116-123.

31. Mahmoud, W.E., et al., *A facile method to syntheses monodisperse gamma-Fe₂O₃ nanocubes with high magnetic anisotropy density*. Superlattices Microstructures, 2014. **68**: p. 1-5.
32. Tombuloglu, H., et al., *Fate and impact of maghemite (γ -Fe₂O₃) and magnetite (Fe₃O₄) nanoparticles in barley (*Hordeum vulgare L.*)*. Environmental Science Pollution Research, 2022. **29**(3): p. 4710-4721.
33. Al-Harbi, L., et al., *Functionalized iron oxide nanoparticles: synthesis through ultrasonic-assisted co-precipitation and performance as hyperthermic agents for biomedical applications*. Heliyon, 2022. **8**(6): p. e09654.
34. Kmita, A., et al., *One-step synthesis of long term stable superparamagnetic colloid of zinc ferrite nanorods in water*. Materials, 2019. **12**(7): p. 1048.
35. Rösner, H.I., et al., *The human alpha-lactalbumin molten globule: comparison of structural preferences at pH 2 and pH 7*. Journal of Molecular Biology, 2009. **394**(2): p. 351-362.
36. Cadenas, E., et al., *Thiol redox transitions in cell signaling, part A: chemistry and biochemistry of low molecular weight and protein thiols*. 2010: Academic Press.
37. Steudle, A., et al., *Modelling of lysozyme binding to a cation exchange surface at atomic detail: the role of flexibility*. Biophysical Journal, 2011. **100**(12): p. 3016-3024.
38. Jain, T.K., et al., *Magnetic resonance imaging of multifunctional pluronic stabilized iron-oxide nanoparticles in tumor-bearing mice*. Biomaterials, 2009. **30**(35): p. 6748-6756.
39. Dobrovolskaia, M.A., et al., *Interaction of colloidal gold nanoparticles with human blood: effects on particle size and analysis of plasma protein binding profiles*. Nanomedicine: Nanotechnology, Biology and Medicine, 2009. **5**(2): p. 106-117.

40. Konno, T., et al., *Preparation of nanoparticles composed with bioinspired 2-methacryloyloxyethyl phosphorylcholine polymer*. *Biomaterials*, 2001. **22**(13): p. 1883-1889.
41. Ishihara, K., et al., *Hemocompatibility of human whole blood on polymers with a phospholipid polar group and its mechanism*. *Journal of Biomedical Materials Research*, 1992. **26**(12): p. 1543-1552.
42. Yang, J.J., et al., *How does biological sex affect the physiological response to nanomaterials?* *Nano Today*, 2021. **41**: p. 101292.
43. Davie, E.W., et al., *The coagulation cascade: initiation, maintenance, and regulation*. *Biochemistry*, 1991. **30**(43): p. 10363-10370.
44. Kratz, F., *Albumin as a drug carrier: design of prodrugs, drug conjugates and nanoparticles*. *Journal of Controlled Release*, 2008. **132**(3): p. 171-183.
45. Kowalczyńska, H.M., et al., *Albumin adsorption on unmodified and sulfonated polystyrene surfaces, in relation to cell–substratum adhesion*. *Colloids and Surfaces B: Biointerfaces*, 2011. **84**(2): p. 536-544.
46. Dabare, P.R.L., et al., *Surface nanotopography mediated albumin adsorption, unfolding and modulation of early innate immune responses*. *Materials Today Advances*, 2021. **12**: p. 100187.
47. Lin, W., et al., *Hemocompatibility of polyacrylonitrile dialysis membrane immobilized with chitosan and heparin conjugate*. *Biomaterials*, 2004. **25**(10): p. 1947-1957.
48. Henry, M., et al., *Conformation change of albumin adsorbed on polycarbonate membranes as revealed by ToF-SIMS*. *Langmuir*, 2003. **19**(15): p. 6271-6276.

49. Van Dulm, P., et al., *The adsorption of human plasma albumin on solid surfaces, with special attention to the kinetic aspects*. Journal of Colloid and Interface Science, 1983. **91**(1): p. 248-255.
50. Victor, S.P., et al., *Development and evaluation of cyclodextrin complexed hydroxyapatite nanoparticles for preferential albumin adsorption*. Colloids and Surfaces B: Biointerfaces, 2011. **85**(2): p. 221-228.
51. Walport, M.J., *Advances in immunology: complement (first of two parts)*. New England Journal of Medicine, 2001. **344**(14): p. 1058-1066.
52. Andersson, J., et al., *Binding of C3 fragments on top of adsorbed plasma proteins during complement activation on a model biomaterial surface*. Biomaterials, 2005. **26**(13): p. 1477-1485.
53. Melchior, P., et al., *Complement activation by dialysis membranes and its association with secondary membrane formation and surface charge*. Artificial Organs, 2021. **45**(7): p. 770-778.
54. Vidarsson, G., et al., *IgG subclasses and allotypes: from structure to effector functions*. Frontiers in Immunology, 2014. **5**: p. 520.
55. Harrison, P.M., et al., *The ferritins: molecular properties, iron storage function and cellular regulation*. Biochimica et Biophysica Acta (BBA)-Bioenergetics, 1996. **1275**(3): p. 161-203.
56. Ogun, A.S., et al., *Biochemistry, transferrin*, in *StatPearls [Internet]*. 2022, StatPearls Publishing.
57. Stafford, J.L., et al., *Transferrin and the innate immune response of fish: identification of a novel mechanism of macrophage activation*. Developmental & Comparative Immunology, 2003. **27**(6-7): p. 539-554.

58. Bale, M.D., et al., *Identification of vitronectin as a major plasma protein adsorbed on polymer surfaces of different copolymer composition*. *Blood*, 1989.
59. Berclaz, P., et al., *Rare Childhood Lung Disorders: α 1-Antitrypsin Deficiency, Pulmonary Alveolar Proteinosis, and Pulmonary Alveolar Microlithiasis*, in *Kendig's Disorders of the Respiratory Tract in Children*. 2006, Elsevier. p. 747-761.
60. Chidambaranathan-Reghupaty, S., et al., *Hepatocellular carcinoma (HCC): Epidemiology, etiology and molecular classification*. *Advances in Cancer Research*, 2021. **149**: p. 1-61.
61. Charbgoon, F., et al., *Gold nanoparticle should understand protein corona for being a clinical nanomaterial*. *Journal of Controlled Release*, 2018. **272**: p. 39-53.
62. Papa, E., et al., *Investigation of the influence of protein corona composition on gold nanoparticle bioactivity using machine learning approaches*. *SAR and QSAR in Environmental Research*, 2016. **27**(7): p. 521–538.
63. Samir, D., et al., *Cell cooperation and role of the P2X7 receptor in pulmonary inflammation induced by nanoparticles*. *Nanotoxicology*, 2012. **7**(8): p. 1302–1314.
64. Liu, R., et al., *Prediction of nanoparticles-cell association based on corona proteins and physicochemical properties*. *Nanoscale*, 2015. **7**(21): p. 9664-9675.
65. Armstrong, P.B., et al., *α 2-macroglobulin: an evolutionarily conserved arm of the innate immune system*. *Developmental & Comparative Immunology*, 1999. **23**(4-5): p. 375-390.
66. Vandooren, J., et al., *Alpha-2-macroglobulin in inflammation, immunity and infections*. *Frontiers in Immunology*, 2021. **12**: p. 803244.
67. Levy, J.H., et al., *Fibrinogen as a therapeutic target for bleeding: a review of critical levels and replacement therapy*. *Transfusion*, 2014. **54**(5): p. 1389-1405.

68. Lowe, G.D., et al., *Plasma fibrinogen*. *Annals of Clinical Biochemistry*, 2004. **41**(6): p. 430-440.
69. Nava-Ortiz, C.A., et al., *Cyclodextrin-functionalized biomaterials loaded with miconazole prevent Candida albicans biofilm formation in vitro*. *Acta Biomaterialia*, 2010. **6**(4): p. 1398-1404.
70. Austen, D., *Clinical Biochemistry of Blood Coagulation*, in *Scientific Foundations of Biochemistry in Clinical Practice*. 1994, Elsevier. p. 495-513.
71. Ashikaga, H., et al., *Blood Coagulation and Atherothrombosis*, in *Molecular Basis of Cardiovascular Disease (Second Edition)*. 2004, W.B. Saunders: Philadelphia. p. 498-518.
72. Wu, Y., *Contact pathway of coagulation and inflammation*. *Thrombosis Journal*, 2015. **13**(1): p. 1-9.
73. Ortega, V.A., et al., *Polymer-coated nanoparticle protein corona formation potentiates phagocytosis of bacteria by innate immune cells and inhibits coagulation in human plasma*. *Biointerphases*, 2020. **15**(5): p. 051003.
74. Ivanov, I., et al., *Protease activity in single-chain prekallikrein*. *Blood, The Journal of the American Society of Hematology*, 2020. **135**(8): p. 558-567.
75. Veloso, D., et al., *Western blot analyses of prekallikrein and its activation products in human plasma*. *Thrombosis and Haemostasis*, 1991. **65**(04): p. 382-388.
76. To, W.S., et al., *Plasma and cellular fibronectin: distinct and independent functions during tissue repair*. *Fibrogenesis & Tissue Repair*, 2011. **4**: p. 1-17.
77. Rogers, H.J., et al., *Hemostasis and thrombosis*, in *Hematopathology*. 2018, Elsevier. p. 57-105.

78. Woodhouse, K., et al., *Adsorption of plasminogen from plasma to lysine-derivatized polyurethane surfaces*. *Biomaterials*, 1992. **13**(15): p. 1103-1108.
79. Quandt, J., et al., *Interactive Hemocompatible Nanocoating to Prevent Surface - Induced Coagulation in Medical Devices*. *Advanced Materials Interfaces*, 2022. **9**(33): p. 2201055.
80. Nalezinková, M., *In vitro hemocompatibility testing of medical devices*. *Thrombosis Research*, 2020. **195**: p. 146-150.
81. Lippi, G., *Systematic assessment of the hemolysis index: pros and cons*. *Advances in Clinical Chemistry*, 2015. **71**: p. 157-170.
82. Thomas, M., et al., *High molecular weight kininogen adsorption on hemodialysis membranes: influence of pH and relationship with contact phase activation of blood plasma. Influence of pre-treatment with poly (ethyleneimine)*. *The International Journal of Artificial Organs*, 2000. **23**(1): p. 20-26.
83. Renaux, J., et al., *Activation of the kallikrein-kinin system in hemodialysis: role of membrane electronegativity, blood dilution, and pH*. *Kidney International*, 1999. **55**(3): p. 1097-1103.
84. Dobrovolskaia, M.A., et al., *Nanoparticle size and surface charge determine effects of PAMAM dendrimers on human platelets in vitro*. *Molecular Pharmaceutics*, 2012. **9**(3): p. 382-393.
85. Koziara, J., et al., *Blood compatibility of cetyl alcohol/polysorbate-based nanoparticles*. *Pharmaceutical Research*, 2005. **22**: p. 1821-1828.

Chapter 5

Effect of uremic toxins on hemocompatibility of β -cyclodextrin, 2-(methacryloyloxy)ethyl phosphorylcholine grafted magnetic nanoparticles

This chapter is in progress as “Effect of Uremic toxins on hemocompatibility of β -cyclodextrin, 2-(methacryloyloxy)ethyl phosphorylcholine grafted magnetic nanoparticles.”

Author List: Shuhui Li, Mehdi Ghaffari Sharaf, Elyn M. Rowe, Katherine Serrano, Dana V. Devine, and Larry D. Unsworth

Contribution: Conceptualization, S.L., K.S. and L.D.U.; methodology, S.L., M.G., E.M.R.; software, Origin, CDNN 2.0, ImageJ; validation, S.L., M.G., E.M.R., L.D.U.; formal analysis, S.L., M.G., E.M.R.; investigation, S.L., M.G., E.M.R.; resources, D.V.D., and L.D.U.; data curation, S.L., M.G., E.M.R.; writing—original draft preparation, S.L., M.G., E.M.R.; writing—review and editing, S.L., M.G., E.M.R., L.D.U.; visualization, S.L., M.G., E.M.R.; supervision, L.D.U.; project administration, L.D.U.; funding acquisition, D.V.D., L.D.U.. All authors have read and agreed to the published version of the manuscript.

5.1 Introduction

Uremic toxins are retained in the blood compartment due to kidney dysfunction [1, 2]. Normally, uremic toxins are cleared *via* organic anion or organic cation transporters that are largely located on the proximal tubule of the kidney [3-5]. The impaired function of these transporters leads to the accumulation of toxins in the blood that are responsible for furthering kidney dysfunction leading to chronic kidney disease (CKD), as well as other severe complications like acidosis and cardiovascular disease to name a few [6, 7]. Although membrane-based dialysis is the standard treatment for patients with CKD, the ionic and hydrophobic properties of toxins facilitate their interactions with blood proteins and, thus, may inhibit their clearance. Adsorbents for the purpose of clearing toxins from blood are an active area of research. However, surfaces contacting blood may trigger a myriad of adverse host responses and themselves be thrombogenic, immunogenic, and inflammogenic [8]. The adsorbed proteome is considered the major impetus for dictating the extent to which surfaces remain hemocompatible. However, no work has investigated the extent to which small molecules retained by patients with kidney dysfunction affects these protein-surface interactions, and subsequently the cellular level events involved in the blood-material interaction; despite the fact that these events rely on enzymatic functions that demands the conservation of secondary and tertiary structures of proteins. This is further complicated by the fact that these enzymes, proenzymes, and coenzymes may be less than 1% of the composition of blood but still play a vital role in hemocompatibility [9, 10].

Previous work on adsorbents for uremic toxins has included cationic metal-organic frameworks for the adsorption of p-cresyl sulfate and indoxyl sulfate, where it was shown that electrostatic interactions play a critical role in their adsorption [11]. Due to the issues surrounding protein adsorption to these blood contacting materials, MPC polymers were employed as an

underlying substrate due to its ‘low-fouling’ nature and the effect of step-wise addition of PM β CD on blood-surface interactions in the presence of uremic toxins evaluated. MPC has been widely applied as a medical device coating and found to prevent blood coagulation without the presence of an anticoagulant [12]. The incorporation of MPC with other materials has constantly been found to inhibit deleterious biological responses and reactions [13-15]. Cyclodextrins have been applied in the blood contacting environment, such as for drug delivery. However, Yeyun et al. found that 10 mg/mL of β -cyclodextrins can cause abnormal red blood cell morphology and serious hemolysis [16]. Therefore, when employing β -cyclodextrins for copolymerization, the concentration of β -cyclodextrins can be vital. The goal being to inhibit protein adsorption using these ‘gold-standard’ surfaces and understand the effect of adding PM β CDs has on protein adsorption through to blood cell responses in the presence of uremic toxins. Li et al. developed a poly cyclodextrin-based adsorbent for capturing p-cresol sulfate *via* hydrophobic interactions [17]. That said, the effect uremic toxins have on blood components, general hemocompatibility of engineered materials, the blood-surface interaction, and hemocompatibility can be recovered using adsorbent materials when in the presence of uremic toxins is largely understudied.

Platelets are small anucleate cellular fragment that generated in the bone marrow. Once activated, platelet can release vast number of molecules in the blood stream. Recent study also suggest that the platelet plays a critical role in the host inflammation and immune responses, stimulating thrombus formation [18-20]. Therefore, the investigation of the interaction between bioengineered surface with platelet is also of great importance.

Herein, we designed a series of functional polymer coated magnetic nanoparticles for the adsorption of uremic toxins. PM β CD and MPC were employed for copolymerization with respective molar ratios of 4:0, 3:1, 2:2, 1:3, 0:4. Using a model uremic toxin solution (Table 5.1)

in platelet poor plasma to mimic CKD patient blood, the hemocompatibility of these surfaces was assessed. The adsorbed proteome was assessed *via* incubation of MNPs with using immunoblots. Clotting experiments were also carried out using platelet-poor plasma with and without the presence of uremic toxins to evaluate effects on clot formation.

Table 5.1 Composition of uremic toxin solutions based on literature values for the analysis of the blood of patients with kidney dysfunction.

Toxin	Concentration (mg/L)	Reference
3-Deoxyglucosone	1.40	[21]
4-Ethylphenyl sulfate	0.19	[22]
Argininic acid	0.06	[21]
Asymmetric dimethylarginine	0.32	[23]
Creatinine	124	[21]
Dimethyl glycine	0.20	[21]
Guanidinopropionic acid	0.29	[21]
Hippuric acid	246	[21]
Homocysteine	6.75	[21]
Hypoxanthine	0.5	[21]
Indole acetic acid	1.53	[23]
Indoxyl glucuronide	1.24	[23]
Indoxyl sulfate	52.4	[21]
p-Cresol sulfate	20.82	[23]
Phenylalanine	465.8	[24]
p-Hydroxyhippuric acid	2.32	[25]
Pyruvic acid	4680	[26]
Spermidine	0.09	[23]
Trimethylamine N-oxide	4.65	[27]
Uric acid	42.5	[28]
Uridine	8.3	[29]
Xanthosine	34.1	[30]
l-Tyrosine	37.85	[21]
l-Asparagine	3.63	[21]

5.2 Materials and Methods

5.2.1 Materials

Chemicals for synthesis: p-Toluenesulfonyl chloride (TsCl, reagent grade, $\geq 98\%$, Sigma Aldrich), 2-(4-Chlorosulfonylphenyl) ethyl trichlorosilane (CTCS, 50 % in toluene, Gelest), Sodium azide ($\geq 99\%$, Fisher Scientific), propargyl methacrylate (PM, 98 %, Alfa Aesar), β -Cyclodextrin ($\geq 97\%$, Sigma Aldrich), 2,2'-bipyridyl (bpy, $> 99\%$, copper(I)bromide ($> 98\%$), copper(II)bromide (99 %), Tris[(1-benzyl-1H-1,2,3-triazol-4-yl)methyl]amine (TBTA, Trichemicals), Dialysis Tubing 500 MWCO (Cole-Parmer), Lewatit TP 207 adsorbent, Tetrakis(acetonitrile)copper(i) hexafluorophosphate ($\text{Cu}(\text{CH}_3\text{CN})_4\text{PF}_6$, Sigma Aldrich), 2-Methacryloyloxyethyl phosphorylcholine (MPC, Sigma Aldrich), ultra-thin carbon-coated copper grid (150 mesh, Ted Pella, Inc.), Sodium Hydroxide (Fisher Scientific), $\text{FeCl}_2 \cdot 4\text{H}_2\text{O}$, $\text{FeCl}_3 \cdot 6\text{H}_2\text{O}$ and of ammonium hydroxide solution (25 %) were purchased from Sigma Aldrich.

All chemicals used for the formation of the uremic toxin solution (Table 5.1) were purchased from Sigma Aldrich and used without further purification. BCA protein assay (Pierce™ BCA Protein Assay Kit, Thermo Fisher Scientific Inc.). Sodium phosphate dibasic heptahydrate, sodium phosphate monobasic monohydrate, and PBS tablets were purchased from Fisher Scientific. Platelet-poor human plasma was procured via the Blood4Research program from Canadian Blood Services. Sodium dodecyl sulfate (SDS) and PVDF membrane (Bio-Rad, Hercules, CA). TMB stabilized substrate (Promega, Madison, WI).

5.2.2 Methods

5.2.2.1 Toxin solution preparation and lyophilization

A graduated cylinder was washed and dried overnight, dry uremic toxins added (Table 5.1), and the final solution brought to a total volume of 100 mL with DI water. The resulting uremic toxin solution was aliquoted into 3 mL tubes and lyophilized for mixing into plasma directly. To avoid plasma dilution, lyophilized uremic toxin powder was resuspended in the corresponding plasma volume. The pH of the plasma was tested and found to be around 7.4.

5.2.2.2 Polymer coated particle preparation

We have prepared a series of PM β CD-co-MPC coated particles. PM β CD monomers were synthesised from the native β CD, following the literature [31-33]. Bare MNP were prepared through the co-precipitation method. After bare MNP being prepared, 5 ml CTC were added dropwise to the argon-filled three-neck flask that hold 500 mg dried bare MNP. Upon the completion of CTC titration, the reaction was kept for 3 hrs. Cease the reaction by exposing the flask under the air. MNP-CTC was washed three times with THF and two times with ethanol through the consecutive separation and redispersion. The co-polymerization is conducted through ATRP. A series of polymer coated particles were synthesised. The ratio of PM β CD and MPC of the 5 types are stated as following: Type A, 4:0 (1.25 mmol, 0); Type B, 3:1 (0.9375 mmol, 0.3125 mmol); Type C, 2:2 (0.625 mmol, 0.625 mmol); Type D, 1:3 (0.3125 mmol, 0.9375 mmol); Type E, 0:4 (0, 1.25 mmol). The polymerization is conducted under the argon blanket. PM β CD and MPC were dissolved in a 10 mL mixed solvent with the ratio of water and ethanol of 1:1. The solution was stirred under the argon blanket for 20 min before adding to the flask containing the MNP-CTC.

5.2.2.3 Polymer Characterization

Thermogravimetric analysis (TGA): Samples were subjected to thermogravimetric analysis (TGA) after being dried in a vacuum overnight. The TA Q50 TGA instrument from TA Instruments (USA) was used, and the heating range was set between 30 and 900 °C with a ramp of 10 °C/min under a nitrogen atmosphere. The error was determined using data from multiple batches under the same experimental conditions.

Transmission electron microscopy (TEM): For imaging particles, a JEM-ARM200CF S/TEM instrument from JEOL (USA) with an accelerating voltage of 200 kV was used, and the resulting images were analyzed using ImageJ. To prepare the samples, a droplet of a well-dispersed sample was deposited onto an ultra-thin carbon-coated copper grid. Excessive water was removed using Kim Wipe gently from the edges. The sample grids were further air-dried for 24 hrs before characterization.

Gel permeation chromatography (GPC): To determine the molecular weight (MW) and polydispersity index (PDI) of grafted polymers, cleaved from the nanoparticle surface by etching the magnetic core with hydrochloric acid [31], a GPC system from Waters (USA) was used. The T6000m column from Viscotek was equipped with the Waters 1515 Isocratic HPLC Pump and Waters 2414 Refractive Index Detector and operated at 40 °C using toluene as the eluent at a flow rate of 1 mL/min. To calibrate the column and quantify the MW of the formed polymer, six polystyrene polymers with various MWs (ranging from 1,000 to 200,000) and PDI values (ranging from 1.1 to 1.2) were used.

Zeta potential: To determine the zeta potential of the engineered surface, the zeta potentials were measured using Malvern Zetasizer Nano-ZS (Nano ZS, Malvern Instruments, Malvern, UK). To

making the sample, 25 μL of 1 mg/mL MNPs suspension was added into 3 mL DI water and ultrasonication was applied for 30 s immediately prior to determining the zeta potential. An average zeta potential was reported from 3 repeats, with 12 runs in each repeat.

5.2.2.4 Plasma Calcification

In this experiment, 100 μL of plasma was incubated with MNPs in the presence or absence of uremic toxins for different time points to evaluate the impact of MNPs on plasma behavior. In the group using non-UTX-treated plasma, plasma was first incubated with PBS at a concentration of 10 mM for 30 min, followed by adsorption evaluation, incubating MNPs for 1 hr and 4 hrs prior to the test. In the group using UTX-treated plasma, plasma was first incubated with lyophilized uremic toxins powder for 30 min, followed by adsorption evaluation, incubating MNPs for 1 hr and 4 hr prior to the test.

After the incubation and adsorption, 100 μL of a 0.025 M calcium chloride solution was injected into a 96-well plate to measure turbidity. The turbidity readings were obtained using a BioTek ELx808 plate reader at an absorbance of 405 nm. The readings were taken every minute for a 60-minute period. All steps were conducted at 37 $^{\circ}\text{C}$, with the entire experiment repeated three times.

5.2.2.5 SDS-PAGE and Immunoblot

Platelet-poor human plasma was procured from Canadian Blood Services, aliquoted and stored at -80 $^{\circ}\text{C}$ until use. The research complied with the ethical guidelines set forth by the University of Alberta's research ethics board. The uremic toxin model solution was lyophilized, added to the platelet-poor plasma, mixed by inversion, and incubated at 37 $^{\circ}\text{C}$ for 30 min. MNPs were added to the plasma using established protocols [32]. Briefly, plasma incubation with

magnetic particles at 37 °C, using the same concentration as for the recalcification turbidimetric assay. After centrifugation at 20,000 × G for 10 minutes, nanoparticles were washed twice with 1 mL of PBS to remove weakly attached proteins. The resulting pellet of particles and adsorbed proteins were resuspended in 100 µL of 10 % SDS in PBS and incubated for 2 hours at 50 °C to elute the adsorbed proteins from the surface of the MNPs. The protein concentration of the eluted protein sample was determined using Pierce™ BCA protein (detergent-compatible) assay. Further analysis of the final sample was performed *via* SDS-PAGE and immunoblotting.

The SDS-PAGE and immunoblot analysis of samples was performed according to a previously described protocol [33, 34]. Before performing SDS-PAGE, each sample was mixed with a denaturing buffer containing SDS and 0.5 M β-mercaptoethanol and then heated at 95 °C for 5 minutes. A consistent quantity of each protein sample was then subjected to electrophoresis on 12 % polyacrylamide gels. Afterward, the samples were transferred onto immunoblot polyvinylidene difluoride membranes with a pore size of 0.2 µm (Bio-Rad Laboratories, Inc). After transfer, the membrane was cut into 23 strips, out of which two strips were utilized for colloidal gold staining, and the remaining 21 strips were used for the immunoblotting analysis of individual proteins. The primary antibody was diluted at 1:1000 for each experiment. Horseradish peroxidase (HRP)-conjugated secondary antibodies and a chromogen substrate stabilized with 3,3',5,5'-tetramethylbenzidine (TMB) from Promega were utilized to visualize the outcomes of the immunoblot assays. To ensure consistency across different samples, the color development time was maintained constant throughout the immunoblot experiments. Following the cessation of color development with water, the strips were immediately dried, arranged, and digitized for analysis.

5.3 Result and Discussion

5.3.1 Properties and characterization of the modified MNPs

MPC-PM β CD polymer-modified particles were synthesized using Atom Transfer Radical Polymerization (ATRP) techniques (Table 5.2). Representative TEM results for the modified MNPs show an average particle size of 13.3 ± 3.23 nm ($n = 27$, Figure 5.1). The selected-area electron diffraction (SAED) pattern revealed that both the bare and polymer-coated magnetic nanoparticles exhibited a ring pattern indicative of a polycrystalline structure of magnetite, matching the (220), (311), (400), (420), (511), and (440) planes as identified by the JCPDS card No. 19-0629 (refer to supplemental information) [35]. The theoretical M_w was estimated using the mole ratio of reactants. The M_w should decrease as the ratio of MPC increases in the systems due to the significant difference in molecular weight between monomers: PM β CD (1282 g/mol) and MPC (295.27 g/mol). In fact, this was not observed and MPC addition led to an increased M_w , suggesting that MPC is more readily incorporated into the growing polymer than PM β CD. Using the M_w yield from GPC, it was possible to estimate that the number of monomers per chain was 88 for A vs. 159 for E, which also suggests that the MPC monomer is more reactive than PM β CD.

The engineered surfaces of all particles have a negative net charge, as indicated by their zeta potential data (Figure 5.2). The zeta potential of the bare MNP differed significantly ($p < 0.05$) from that of all modified surfaces. However, there is no significant difference between the zeta potentials of surfaces B, C, and E. The zeta potential of the surface on particle D has a statistically significant difference ($p < 0.05$) from the other modified surfaces.

Table 5.2 Summary of TGA, GPC and molecular weight results for polymers cleaved from MNPs.

System	Bare	A	B	C	D	E
Mol Ratio PM β CD:MPC	-	1:0	3:1	1:1	1:3	0:1
Total Weight Loss, % (± 1 SD), n=3	7.6 (0.8)	37.0 (1.4)	41.2 (2.2)	45.3 (2.1)	33.4 (1.5)	25.0 (1.0)
GPC - M _w ($\times 10^3$ g/mol)	-	115.3	144.8	138.4	72.1	47.0
Theoretical M _w ($\times 10^3$ g/mol)	-	115.3	97.9	86.7	63.9	47.0
GPC - M _n ($\times 10^3$ g/mol)	-	85.4	96.5	101.7	55.4	46.4
PDI	-	1.3	1.5	1.4	1.3	1.0

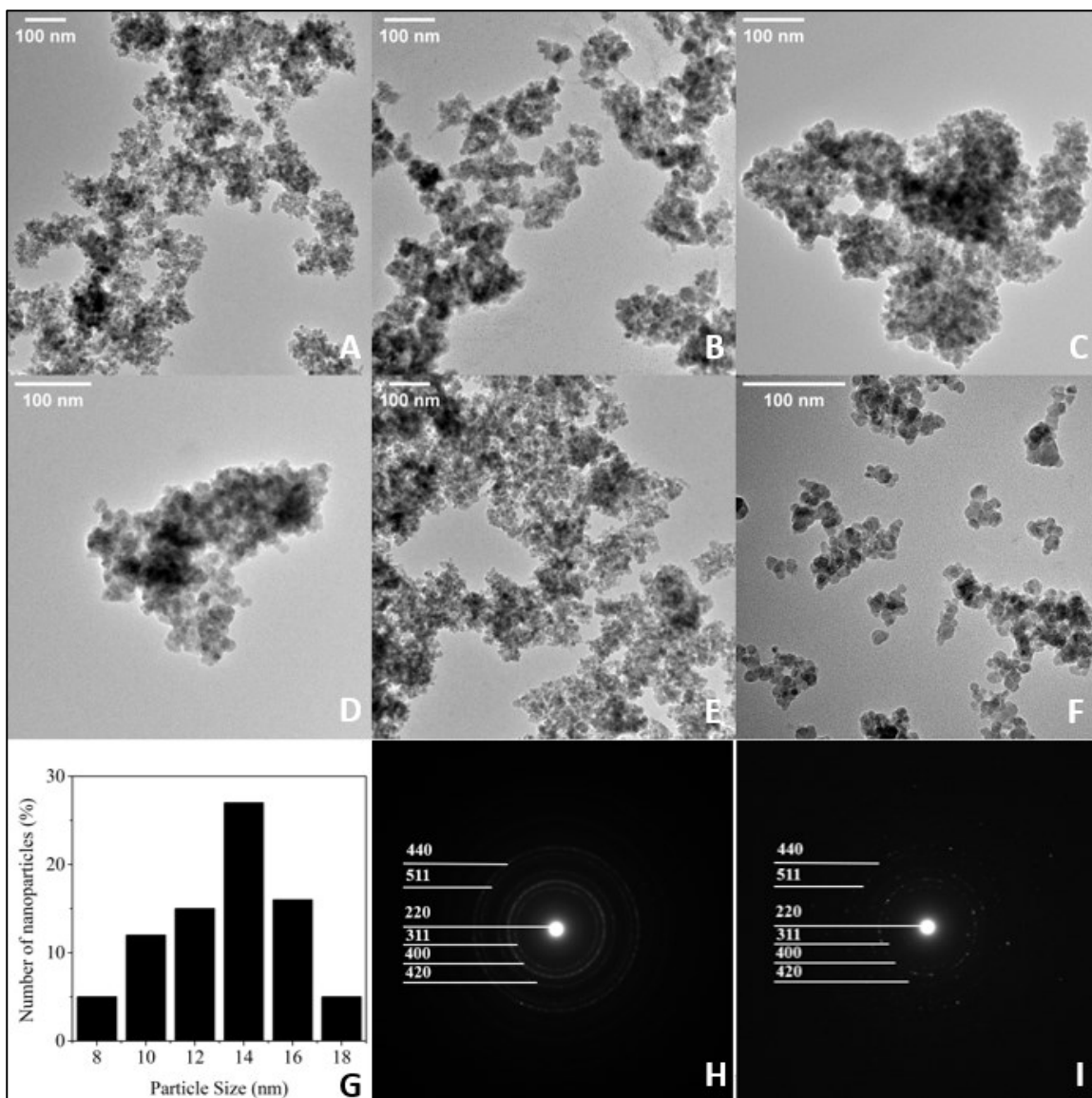


Figure 5.1 Representative TEM and SAED results for bare and polymer-coated samples. TEM images (A) to (E) show the of the synthesized polymer-modified nanoparticles of sample A to E. TEM image (F) is of control bare MNP, and (G) shows the particle size distribution of the bare MNP in (F). Representative SAED patterns were obtained for particle E (Fig. 1H) and the control MNP (Fig. 1I).

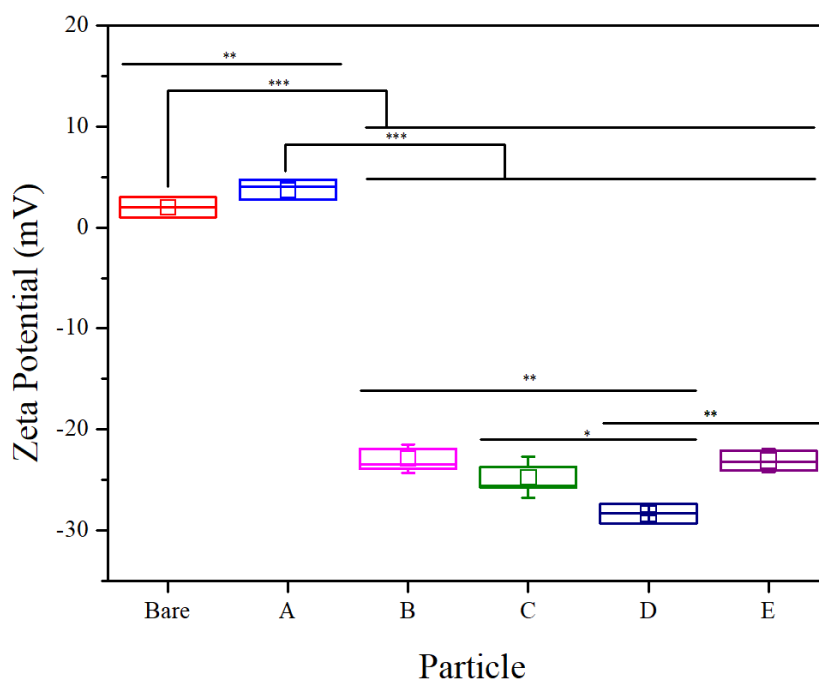


Figure 5.2 Representative zeta potential test of bare MNP and A to E. Unpaired T test was performed and results were compared across groups for each two groups. Comparisons not shown were not statistically significant (* $p < 0.05$, ** $p < 0.01$, *** $p < 0.001$, data represents mean \pm 1 SD, $n = 3$).

5.3.2 Plasma clotting in the presence of polymer coated nanoparticles

The uremic plasma showed clot formation at 13 minutes and reached a plateau at 21 minutes, whereas the native platelet poor plasma exhibited clotting within 20 minutes and reached a plateau at 32 minutes. The introduction of uremic toxin to otherwise healthy plasma caused a delay in clot formation and plateau onset, indicating an inhibitory effect on clotting formation. Clot onset and plateau onset time for all particles without uremic toxins (non-UTX) and with toxins (UTX-treated) are summarized in Table 5.3. As clot formation kinetics are directly related to surface area the presence of MNPs yielded a rapid clot formation compared to plasma samples alone, regardless of presence of the toxins. However, for all systems with MNPs present the clot

formation kinetics upon introducing toxins was significantly delayed compared to the same system without toxin; clot initiation was delayed between 1.5x to 6x of that without toxins present. This is much greater than the 1.5x delay observed for clot formation associated with these toxins in plasma alone, suggesting that the rate of clot formation is much more sensitive to the presence of uremic toxins when surfaces are present. Systems B and C showed the greatest relative delay in clot formation upon introduction of toxins and system E showed the absolute longest delay in clot formation. For all systems it was observed that incubation time of the MNPs in the toxin solution led to a delay in clot formation. Similar to the time for clot formation to start, plateau onset was also delayed upon introduction of uremic toxins, thus the difference between clot formation and plateau onset was determined and was similar for all systems studied.

Table 5.3 Summary of clot formation kinetics and plateau onset for MNP in platelet poor plasma without uremic toxins and after 1 and 4 hr incubation with uremic toxin laden plasma (n=3, all SDs are less than 3 seconds). The ratio in the bracket represents the mole ratio of PM β CD: MPC.

	Plasma		A (4:0)			B (3:1)			C (1:1)		
	No UTX	UTX	No UTX	1 hr	4 hr	No UTX	1 hr	4 hr	No UTX	1 hr	4 hr
Turbidity	1.71	1.60	1.44	1.38	1.40	1.34	1.29	1.35	1.47	1.36	1.40
Clot formation (min)	20	13	2	4	6	1	4	6	1	3	6
Plateau onset (min)	32	21	5	8	11	5	8	11	5	8	11
Plateau onset – clot formation time (min)	12	12.5	3	4	5	4	4	5	4	5	5

	D (1:3)			E (0:4)			Bare MNP		
	No UTX	1 hr	4 hr	No UTX	1 hr	4 hr	No UTX	1 hr	4 hr
Turbidity	1.22	1.23	1.29	1.5	1.53	1.54	1.55	1.52	1.53
Clot formation (min)	2	3	5	2	5	8	2	5	7
Plateau onset (min)	6	7	9	6	9	14	6	9	12
Plateau onset – clot formation time (min)	4	4	4	4	4	6	4	4	5

5.3.3 Total adsorbed protein

Eluted protein amounts for each MNP system were determined using a detergent-compatible bicinchoninic acid (BCA) assay (Figure 5.3) so that the effects of the surface chemistry and toxin on the total adsorbed amount could be characterized. In all cases, the incorporation of uremic toxins leads to a significant increase in adsorbed protein ($p < 0.01$). Protein adsorption to MNP surfaces without toxins showed a somewhat expected result, where fully unmodified MNPs adsorbed the most protein, and adsorbed protein amounts decreased with increasing ratios of MPC in the engineered film, except for particle D where a significant increase in adsorbed protein was observed (Figure 5.3A). However, this order was not retained when looking at protein adsorption to these surfaces in the presence of uremic toxins. In this case the adsorption of proteins to PM β CD-MNP (A) and (B) were the least, significantly less than the MPC-MNP system (E). Also, no statistical difference was found in the amount of adsorbed protein between E and the bare MNPs (Figure 5.3B). Given the fact that MPC was expected to provide the lowest adsorbed amounts, as seen in the native protein adsorption case, these results reveal that uremic toxins strongly affect protein-surface interactions. Finally, systems C and D showed a substantial increase in adsorbed protein upon introducing uremic toxins to the plasma. Although it is not clear why C and D systems showed such a dramatic increase in adsorbed amounts of protein, it remains clear that the increased fraction of MPC from C to E led to a decrease in adsorbed protein. Some uremic toxins exhibit a

high affinity for plasma proteins, mainly serum albumin, and have been shown to cause changes in the secondary and tertiary structure of HSA, resulting in an inhibition of its hydrolase activity [31, 32, 34, 36]. Thus, uremic toxins may alter the structure of plasma proteins, impacting both protein adsorption and protein digestion [37].

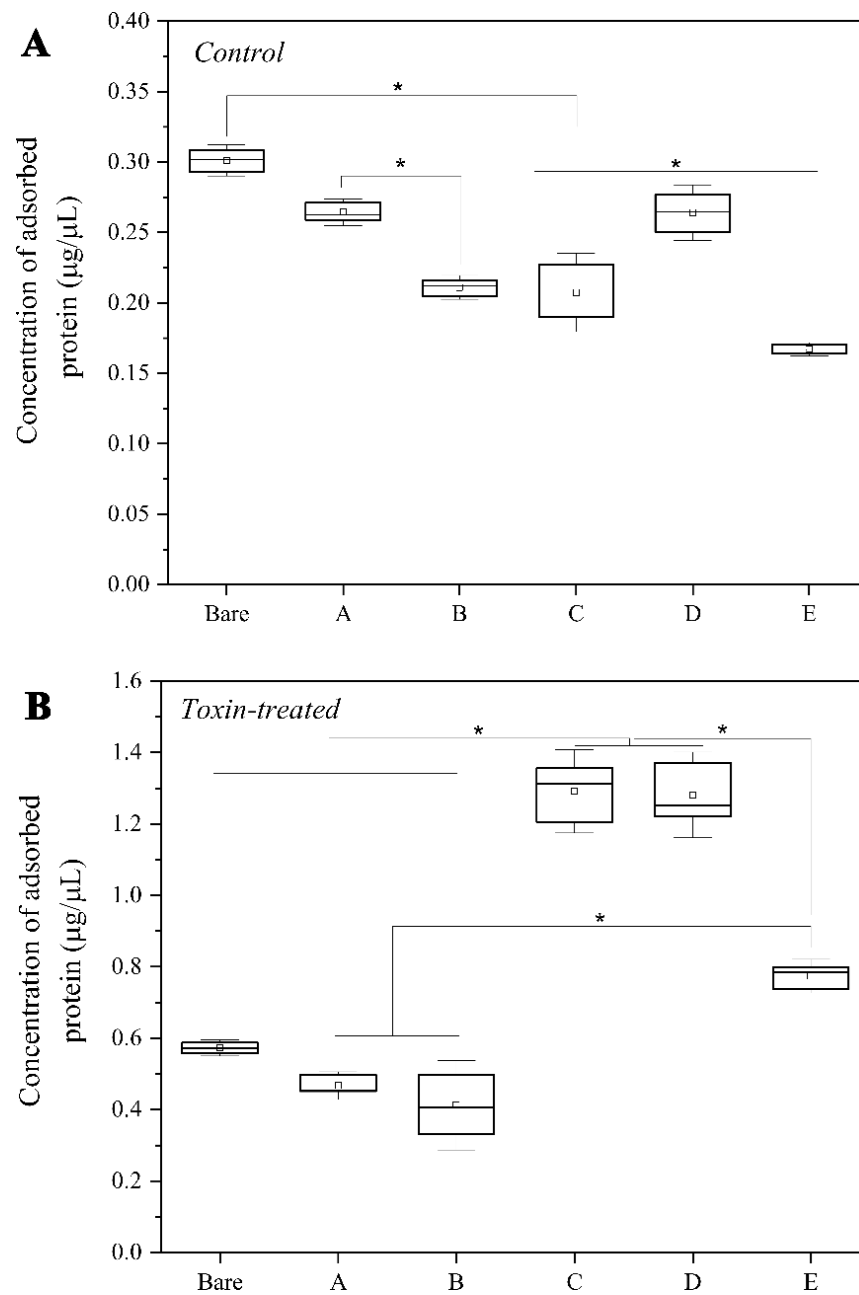


Figure 5.3 The amount of adsorbed protein to all MNP systems (0.18 mg/mL MNP) was determined using a BCA assay. Repeated measures ANOVA were used for statistical analysis across groups (* represents $p < 0.01$, data represents mean \pm 1 SD, $n \geq 3$).

5.3.4 Immunoblot analysis

The intensity of the immunoblot bands for all MNPs was measured using a 13-level grayscale system (Table 5.2). To ensure comparability of band intensity across different systems, the amount of protein loaded (30 μg) and the time for color development (5 min) was kept constant. It is possible to compare band intensities for individual proteins across different surfaces, but, intensities between different proteins can be somewhat different due to the vagaries associated with antibody affinities.

Albumin (66.5 kDa) is the most abundant protein in plasma and it binds a variety of metabolic compounds, medications and lipids [38]. Albumin adsorption at surfaces can alter subsequent protein binding events and influences coagulation processes [39, 40]. In both normal and elevated levels of toxins in advanced stages of CKD, albumin serves as the primary binding protein. For example, the binding of hippuric acid to albumin impedes its clearance, thereby causing the hemodialysis efficiency to drop to 64 % [34, 41]. Albumin-coated surfaces been shown to have enhanced biocompatibility with anticoagulant properties [42]. A thin layer of albumin coated on polyacrylonitrile hemodialysis membrane has been shown to reduce the adhesion and aggregation of platelets, improving the hemocompatibility of these membranes [43]. Thus, comparing the results of the toxin-treated groups to controls, no difference in the albumin adsorption was observed for bare particles and B. A decrease in albumin adsorption was observed from C to E, where all toxin treated systems showed lower albumin adsorption than the controls. In contrast, A (only PM β CD content) showed increased adsorption of albumin upon incorporating toxins.

5.3.4.1 Immune response-related bands

The complement system is a key component of the innate immune system. The activation

of the complement system results from the coordinated activity of several proteins that operate through the classical, alternative, and mannose-binding lectin pathways [44]. These pathways serve as a defence mechanism against bacterial infections and assist in eliminating immune complexes and apoptotic cells. The complement system also plays a vital role in connecting innate and adaptive immune responses, where complement component 3 (C3) is essential in all three activation pathways, particularly the alternative pathway, which is involved in the activation of the complement system triggered by biomaterials [31, 45]. On a denaturing SDS-PAGE gel, C3 can be separated into four distinctive bands, comprising whole C3 (187 kDa), α chain (115 kDa), β chain (70 kDa), and the activation fragment (42 kDa).

Intact C3 was not present for any MNPs in toxin-free plasma; all MNPs showed a noticeable band intensity for intact C3 upon introduction of the uremic toxins. Surprisingly MNPs with higher MPC content (i.e., D and E) showed higher amounts of whole C3 compared to the other MNP systems. Also surprising was that the toxin-related systems all had increased amounts of the α chain compared to the toxin-free controls, with a similar adsorption pattern observed except for MNP-A, which had a slightly lower amount. In both control and toxin-treated systems, the β chain was present. MNP-E and D did not show changes in the band intensities upon toxin treatment, while bare, MNP-A, B, and C showed a decrease in the band intensity. All systems showed the presence of the 42 kDa activation fragment, where significant increases in amount were observed for all MNPs except B and C upon toxin addition. Although the intensity of the activation fragment was relatively high in all toxin-treated systems, MNP-A and bare MNP showed higher values, suggesting that abnormal levels of toxin compounds might increase the possibility of C3 activation. Unlike enzymatically sensitive degradation events discussed herein, surfaces carrying a high density of hydroxyl and amino groups can activate C3 directly *via* a nucleophilic

attack on the highly reactive thioester bond, which then can further active C3 [46, 47]. Thus, the presence of the activation fragment may not solely rely on enzymatic digestion, and increased activation may be a result of the hydroxyl groups associated with the incorporation of PM β CDs into these films.

That said, D and E showed the biggest increase in amount of the 42 kDa fragment upon addition of toxin. This increase is not likely related to amount adsorbed difference upon toxin addition as the total protein loaded for this analysis was the same. Although a mechanism is not understood, this highlights the importance that uremic toxins in the humoral response pathways to engineered 'low-fouling' materials.

IgG is the most prevalent among the five serum immunoglobulin isotypes (IgM, IgD, IgG, IgA, and IgE) and accounts for approximately 10-20 % of total plasma protein in humans [48]. The presence of IgG triggers the activation of the classical pathway of complement [49]. In control systems, there was a decrease in the intensity values for the light chain of IgG (27 kDa) in MNP-D and E compared to the other control system, but no clear MPC-associate trend was observed in toxin treated systems for this fragment. Toxin incubation led to an increase in the band intensity of the heavy chain of IgG (55 kDa) in all types of MNPs except for bare MNP, which remained unchanged. These findings suggest that elevated concentrations of UTX compounds may lead to increased adsorption of IgG, which could trigger an immune response.

Factor I plays a key inhibitory role in all complement pathways *via* degradation of activated complement proteins C3b and C4b. This protein was not found in either toxin treated or control groups. Neither the control nor the toxin treated group showed Kininogen, which is involved in the initiation of the contact activation pathway.

Transferrin (77 kDa) transports ferric iron and contributes to the innate immune system by triggering macrophage activation and restricting bacterial survival [45, 50]. Despite observing relatively high and consistent levels of transferrin adsorption to all MNPs in the control group, certain MNPs in the toxin treated plasma exhibited even higher amounts. While bare MNP showed a slight increase in transferrin adsorption, MNP-B and E demonstrated a notable increase. These results suggest that increased levels of toxin compounds in plasma can enhance transferrin binding, and may potentially induce macrophage activation. However, other MNP types, including A, C, and D, did not exhibit any changes in transferrin adsorption upon plasma treatment with toxins.

Vitronectin, a multifunctional glycoprotein, and in plasma functions as a complement regulatory component [51]. Vitronectin had relatively high intensity values for MNPs in control plasma, except for MPC rich MNP types D and E. Upon toxin treatment, the intensity of E did not change and remained moderately low compared to other MNPs.

α 1 antitrypsin is the predominant serine protease inhibitor in human plasma, accounting for 95 % of trypsin inhibitory capacity. Its primary function is to inhibit the activity of neutrophil elastase, a serine protease. α 1 antitrypsin has additional immunomodulatory effects, including regulation of T- and B-lymphocytes and anti-inflammatory properties [52, 53]. α 1 antitrypsin was detected in control surfaces with a relatively high binding level to bare MNPs and MNP types A, B, and C, while moderate levels of adsorption were observed for particles D and E. In uremic plasma, the adsorption profile of α 1 antitrypsin was unchanged for MNP-B but increased for other MNPs compared to the control group. It has been suggested that α 1 antitrypsin may interact with already adsorbed proteins on the surface [54]. As most proteins showed higher adsorption levels in

uremic plasma, this could explain why some MNPs had maximum adsorption of $\alpha 1$ antitrypsin, as the increased amount of proteins on the surface could facilitate further binding.

Alpha₂ macroglobulin is another constituent of the innate immune system that plays a role in regulating proteases by eliminating them from the bloodstream [55, 56]. This protease was not found adsorbed to any MNP system in control plasma, but in uremic plasma, all MNPs showed a sharp increase in adsorption. This may suggest that MNP systems are not actively involved in clotting or fibrinolysis due to the inhibitory role played by alpha₂ macroglobulin in both processes [54]. In contrast, toxin compounds appear to affect those processes.

5.3.4.2 Coagulation related bands

Fibrinogen (340 kDa) plays a critical role in coagulation and consists of three polypeptide chains (A α : 68 kDa, B β : 56 kDa, and γ : 48 kDa) linked *via* disulfide bonds. Fibrinogen serves as a substrate for three enzymes, including Factor XIIIa, thrombin, and plasmin. During coagulation, thrombin cleaves A α and B β chains, producing fibrinopeptides and soluble fibrins, which polymerize and form a loose net that entraps red blood cells to initiate clot formation. Factor XIIIa stabilizes fibrin polymers by cross-linking, making the clot more elastic and resistant to fibrinolysis. Cleaved fibrinogen can be identified by these three separate bands, with cleavage fragments potentially appearing as bands with molecular weights < 48 kDa [49, 57, 58]. In control plasma, the intensity of fibrinogen fragments exhibited a relatively consistent trend across all MNPs, except for types D and E, which showed a decrease in intensity. No detectable cleavage fragments (< 48 kDa) were identified for MNP-D and E. But in uremic plasma, immunoblots of bare MNP, D and E, besides the three standard bands, multiple connected bands appeared with relatively high intensities (Figure 5.4). Therefore, identifying individual bands was impractical (indicated as * in Table 5.4). In MNP-B and C, the intensities of A α , B β , and γ bands remained

largely unaltered, with minor variations in band intensities upon toxin treatment. Besides the connected bands, the color development was disrupted in MNP-A, making it difficult to accurately identify the band intensities (identified as - in Table 5.4). In toxin-treated plasmas, the cleavage bands appeared as multiple and sometimes as connected bands (Figure 5.4), making it difficult to measure the intensity of individual bands (indicated as * in Table 5.4). Previous studies on plasma samples have found that uremic plasma from chronic kidney disease patients contains fibrinogen fragments not found in normal plasma [59]. These fragments found in the plasma of CKD patients may bind to fibrinogen receptors on platelets, resulting in reduced platelet aggregation [59, 60]. This may explain why CKD patients have a 1.5-fold increased risk of bleeding [61]. Previous findings have shown that uremic plasma contains increased levels of fibrinogen degradation products, including fibrinopeptides, and N- and C-terminal fragments of α - and β -chains [62].

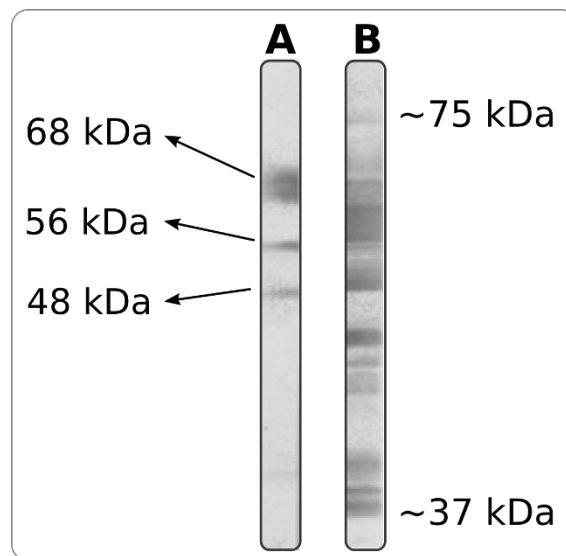


Figure 5.4 Representative immunoblot for fibrinogen eluted from MNPs incubated with (A) normal platelet poor plasma control and (B) uremic plasma.

Table 5.4 Relative intensities of immunoblot of UTX-treated and non-UTX-treated plasma proteins adsorbed to different types of MNPs.

<i>Plasma protein</i>	<i>Fragment size (kDa)</i>	<i>Bare MNP</i>		<i>A</i>		<i>B</i>		<i>C</i>		<i>D</i>		<i>E</i>	
		-	√	-	√	-	√	-	√	-	√	-	√
<i>UTX</i>	-	-	√	-	√	-	√	-	√	-	√	-	√
<i>Fibrinogen</i>	68	7	*	8	-	8	7	7	7	7	*	6	*
	56	6	*	8	-	8	7	7	7	4	*	4	*
	48	6	*	7	-	8	8	6	7	4	*	4	*
	<48	4	*	3	-	5	*	2	*	0	*	0	*
<i>Fibronectin</i>	259	0	0	0	0	0	0	0	3	0	3	0	4
<i>Alpha1 antitrypsin</i>	54	9	12	8	9	9	9	8	12	5	12	5	9
<i>Prothrombin</i>	72	2	10	2	10	2	9	2	9	1	6	2	10
<i>Vitronectin</i>	54	8	8	8	7	10	10	8	9	5	8	6	6
<i>Protein S</i>	75	0	3	0	4	0	2	0	1	0	2	0	5
<i>Prekallikrein</i>	85	5	0	2	0	5	1	2	0	1	0	2	0
	50	10	6	8	6	9	6	7	1	2	1	5	0
<i>Antithrombin</i>	53	6	9	6	9	4	9	4	9	3	9	3	10
<i>IgG</i>	55	7	7	4	7	3	7	8	7	5	7	5	7
	27	8	7	7	7	8	6	9	7	5	8	5	8
<i>Albumin</i>	66	9	9	7	9	7	7	8	7	9	6	9	8
<i>Plasminogen</i>	91	9	11	8	11	7	8	8	8	5	5	3	6
<i>C3</i>	187	0	7	0	6	0	8	0	6	0	9	0	9
	115	5	8	4	6	4	8	5	8	3	8	2	8
	70	10	9	10	7	10	8	9	7	7	7	8	8
	42	5	9	8	9	8	8	7	7	3	7	3	8
<i>Factor XII</i>	80	3	3	2	3	1	3	2	1	1	1	1	3
<i>Factor XI</i>	70	9	10	8	10	9	9	10	9	8	7	8	9
<i>Transferrin</i>	77	8	9	8	8	7	11	10	10	10	10	8	11
<i>Alpha-2-macroglobulin</i>	163	0	9	0	9	0	8	0	7	0	7	0	9

Prothrombin (72 kDa) is a precursor to thrombin in plasma. Factor Xa, with factor V, phospholipid, and Ca^{2+} , induces its proteolytic conversion [63]. In uremic plasma, most MNPs showed an increase in prothrombin band intensity, except for MNP-D, showing a moderate increase. Adsorption levels of prothrombin were low in the control plasma for all MNPs. Antithrombin blocks the coagulation cascade by inhibiting thrombin and other coagulation factors [64]. In control plasma, antithrombin band intensity decreased with increasing MPC component in the films, while in uremic plasma, all MNPs showed an increase in antithrombin adsorption.

The surface contact pathway involves three serine proteinases: coagulation factors XII and XI, plasma prekallikrein, and the high molecular weight kininogen that functions as a non-enzymatic cofactor [65]. Factor XII was detected in a consistent but very limited amount adsorbed in all MNPs in the control plasma, whereas Factor XI exhibited strong binding to the surfaces of all MNPs, consistent with prior findings for poly(acrylic acid)-coated Fe_2O_3 nanoparticles [66]. Factor XII was present in low amounts on all MNPs in uremic plasma. Bare and D showed no change in band intensity compared to controls, while A, B, C, and E displayed a slight increase in intensity after toxin treatment. Factor XI adsorption in uremic plasma showed no change in MNP-B, with a slight reduction observed in MNP-C and D, but still remained high in all MNPs similar to the controls. Prekallikrein, the precursor to kallikrein, cleaves high-molecular-weight kininogen [67]. It was detected at 85 kDa, and in control plasma, the intensity levels were consistently low in all modified MNPs compared to the bare MNP. In uremic plasma, prekallikrein band was not observed for any MNP types, with only a very faint band visible for type B. It has been shown that the activation of the contact system leads to a decrease in prekallikrein immunoblot band intensity with the formation of kallikrein complexes with α_2 -macroglobulin and C1 inhibitor [68]. In control plasma, the intensity of kallikrein band (50 kDa) was relatively higher than prekallikrein (85 kDa)

in all MNP types. The type D and E films again showed a sharp decrease in kallikrein intensity. In control plasma, all MNPs had higher kallikrein band (50 kDa) intensity than prekallikrein band (85 kDa). MNP types D and E exhibited a noticeable decrease in kallikrein band intensity. In uremic plasma, all MNPs had lower kallikrein intensity than control plasma, with types E and C having a sharp drop where no visible band was observed for MNP-E. Ti and Zr alloys have been reported to show limited prekallikrein activation, possibly due to their surface's electrochemical characteristics [69].

Plasma fibronectin, a key component of the fibrin clot, binds to fibrin through non-covalent interactions and covalent cross-linking, which is critical in regulating platelet function and hemostasis [70]. Protein S is involved in the regulation of coagulation independently of activated protein C, which works by directly inhibiting the intrinsic tenase and prothrombinase complexes [71]. MNPs did not adsorb fibronectin, protein S, or protein C in control plasma, suggesting limited fibrinolytic response and clot formation [49]. However, in uremic plasma, fibronectin was found adsorbed by MNP E, D, and C, but at low levels. MNPs showed low to moderate adsorption of protein S, while protein C was not detected.

Plasminogen (91 kDa) is the precursor to plasmin, the primary protease responsible for breaking down fibrin clots. MNP-E and D exhibited the lowest adsorption of plasminogen among the different types of MNPs in both uremic and control plasma, with most MNPs showing higher adsorption in uremic plasma than in control plasma. The adsorption of plasminogen on surfaces is considered an indicator of fibrinolytic activity [72, 73].

Kininogen, which participates in initiating the contact activation pathway, was not found in either control or UTX-treated groups.

5.4 Conclusion

We assessed the biocompatibility and hemocompatibility of novel p(PM β CD-co-MPC) magnetic nanoparticles through various techniques, including plasma calcification, BCA assay, immunoblot and platelet activation. TGA, GPC, TEM and Zetasizer were applied to characterize the surface. We observed the molecular weight of coated polymer fall between 47 to 115.3×10^3 g/mol. The average core size of MNP is 13.3 ± 3.23 nm. The zeta potential data suggest that particle D has the highest surface charge by -28.3 mv, whereas the particle A has the lowest surface charge by -6.44. This indicates the increase potential of interactions induced by particle D. We observed an obvious resuming effect in the plasma clotting experiment. The incubation of modified particles with uremic plasma resumes the turbidity and prolonged the clotting formation time point, among which particle B, C and D represents the best results. BCA assay indicated that the modified particles have less protein adsorption compared to the bare MNP. Furthermore, we analyzed 21 plasma proteins using immunoblotting to determine their adsorption onto MNPs. The results showed that treatment of plasma with uremic toxins led to an increase in the adsorption of several proteins, including fibrinogen, alpha1 antitrypsin, prothrombin, vitronectin, protein S, antithrombin, plasminogen, C3, Factor XI, and transferrin, in some or all types of MNPs. Only fibronectin, protein S, and alpha-2-macroglobulin exhibited adsorption exclusively in the plasma treated with UTX.

The absence of kininogen in the protein corona of MNPs in both studies, with and without UTX, might provide insight into more suitable surfaces for blood-contacting materials, specifically in the case of CKD patients where protein adsorption to hemodialysis membranes could lead to unfavourable and complex biochemical reactions. This is even more pertinent to note that kininogen (high molecular weight) can be adsorbed to hemodialysis membranes, where surface

modification and ionic strength play an essential role in tuning the surface [74, 75]. This paper provided a comprehensive evaluation of the biocompatibility and hemocompatibility of the p(PM β CD-co-MPC) engineered surface under the presence of uremic toxins. Depicted a holistic picture of p(PM β CD-co-MPC) engineered surface.

5.5 References

1. Burns, N.L., et al., *Influence of surface charge on protein adsorption at an amphoteric surface: effects of varying acid to base ratio*. Journal of Colloid Interface Science, 1996. **178**(1): p. 116-122.
2. Lim, Y.J., et al., *Uremic toxins in the progression of chronic kidney disease and cardiovascular disease: mechanisms and therapeutic targets*. Toxins, 2021. **13**(2): p. 142.
3. Sekine, T., et al., *The multispecific organic anion transporter (OAT) family*. European Journal of Physiology, 2000. **440**: p. 337-350.
4. Sekine, T., et al., *Molecular physiology of renal organic anion transporters*. American Journal of Physiology-Renal Physiology, 2006.
5. Lowenstein, J., et al., *Uremic toxins in organ crosstalk*. Frontiers in Medicine, 2021. **8**: p. 592602.
6. Kraut, J.A., et al., *Metabolic acidosis of CKD: an update*. American Journal of Kidney Diseases, 2016. **67**(2): p. 307-317.
7. Kim, H.J., *Metabolic acidosis in chronic kidney disease: pathogenesis, clinical consequences, and treatment*. Electrolytes Blood Pressure: E, 2021. **19**(2): p. 29.
8. Franz, S., et al., *Immune responses to implants-a review of the implications for the design of immunomodulatory biomaterials*. Biomaterials, 2011. **32**(28): p. 6692-6709.
9. Dahlbäck, B., *Blood coagulation*. The Lancet, 2000. **355**(9215): p. 1627-1632.
10. Smith, G.S., et al., *Clinical pathology in non-clinical toxicology testing*, in *Haschek and Rousseaux's Handbook of Toxicologic Pathology*. 2013, Elsevier. p. 565-594.
11. Zhang, M., et al., *Effectively Decontaminating Protein-Bound Uremic Toxins in Human Serum Albumin Using Cationic Metal-Organic Frameworks*. ACS Applied Materials Interfaces, 2022.

12. Ishihara, K., *Revolutionary advances in 2-methacryloyloxyethyl phosphorylcholine polymers as biomaterials*. Journal of Biomedical Materials Research Part A, 2019. **107**(5): p. 933-943.
13. Shigeta, M., et al., *Suppression of fibroblast and bacterial adhesion by MPC coating on acrylic intraocular lenses*. Journal of Cataract Refractive Surgery, 2006. **32**(5): p. 859-866.
14. Campbell, E.J., et al., *Biocompatible surfaces using methacryloylphosphorylcholine laurylmethacrylate copolymer*. ASAIO Journal, 1994. **40**(3): p. M853-7.
15. Ishihara, K., et al., *Photoinduced graft polymerization of 2-methacryloyloxyethyl phosphorylcholine on polyethylene membrane surface for obtaining blood cell adhesion resistance*. Colloids Surfaces B: Biointerfaces, 2000. **18**(3-4): p. 325-335.
16. Fu, Y., et al., *Effect of cyclodextrins on the structure and functions of blood components in vitro*. Journal of Bioactive Compatible Polymers, 2015. **30**(5): p. 541-554.
17. Li, J., et al., *Multi-sites polycyclodextrin adsorbents for removal of protein-bound uremic toxins combining with hemodialysis*. Carbohydrate Polymers, 2020. **247**: p. 116665.
18. Ghoshal, K., et al., *Overview of platelet physiology: its hemostatic and nonhemostatic role in disease pathogenesis*. The Scientific World Journal, 2014. **2014**.
19. Garraud, O., et al., *Platelets and cytokines: how and why?* Transfusion Clinique et Biologique, 2012. **19**(3): p. 104-108.
20. Thomas, M.R., et al., *The role of platelets in inflammation*. Thrombosis Haemostasis, 2015. **114**(09): p. 449-458.
21. Vanholder, R., et al., *European Uremic Toxin Work Group*. Kidney International, 2003. **63**: p. 1934-1943.

22. Itoh, Y., et al., *Protein-bound uremic toxins in hemodialysis patients measured by liquid chromatography/tandem mass spectrometry and their effects on endothelial ROS production*. Journal of Biomedical Materials Research Part A, 2012. **403**(7): p. 1841-1850.
23. Duranton, F., et al., *Normal and pathologic concentrations of uremic toxins*. Journal of the American Society of Nephrology, 2012. **23**(7): p. 1258-1270.
24. Wolfson, M., et al., *Amino acid losses during hemodialysis with infusion of amino acids and glucose*. Kidney International, 1982. **21**(3): p. 500-506.
25. Schools, A., et al., *Biochemical and neurophysiological parameters in hemodialyzed patients with chronic renal failure*. Clinica Chimica Acta, 1989. **185**(1): p. 91-107.
26. Landon, J., et al., *Blood pyruvate concentration measured by a specific method in control subjects*. Journal of Clinical Pathology, 1962. **15**(6): p. 579-584.
27. Bain, M.A., et al., *Accumulation of trimethylamine and trimethylamine-N-oxide in end-stage renal disease patients undergoing haemodialysis*. Nephrology Dialysis Transplantation, 2006. **21**(5): p. 1300-1304.
28. Taki, K., et al., *Indoxyl sulfate and atherosclerotic risk factors in hemodialysis patients*. American Journal of Nephrology, 2007. **27**(1): p. 30-35.
29. Daniewska-Michalska, D., et al., *Efficiency of hemodialysis of pyrimidine compounds in patients with chronic renal failure*. Nephron, 1993. **64**(2): p. 193-197.
30. Toshimitsu, N., et al., *RNA metabolism in uremic patients: accumulation of modified ribonucleosides in uremic serum*. Kidney International, 1998. **53**: p. 1801-1806.
31. Deltombe, O., et al., *Exploring binding characteristics and the related competition of different protein-bound uremic toxins*. Biochimie, 2017. **139**: p. 20-26.

32. Zaidi, N., et al., *A biophysical insight into structural and functional state of human serum albumin in uremia mimic milieu*. International Journal of Biological Macromolecules, 2019. **131**: p. 697-705.
33. Karbowska, M., et al., *The uremic toxin indoxyl sulfate accelerates thrombotic response after vascular injury in animal models*. Toxins, 2017. **9**(7): p. 229.
34. Viaene, L., et al., *Albumin is the main plasma binding protein for indoxyl sulfate and p - cresyl sulfate*. Biopharmaceutics & Drug Disposition, 2013. **34**(3): p. 165-175.
35. Mahmoud, W.E., et al., *A facile method to syntheses monodisperse gamma-Fe₂O₃ nanocubes with high magnetic anisotropy density*. Superlattices Microstructures, 2014. **68**: p. 1-5.
36. Li, S., et al., *Indoxyl and p-cresol sulfate binding with human serum albumin*. Colloids and Surfaces A: Physicochemical and Engineering Aspects, 2022. **635**: p. 128042.
37. Gessner, A., et al., *Influence of surface charge density on protein adsorption on polymeric nanoparticles: analysis by two-dimensional electrophoresis*. European Journal of Pharmaceutics and Biopharmaceutics, 2002. **54**(2): p. 165-170.
38. Kratz, F., *Albumin as a drug carrier: design of prodrugs, drug conjugates and nanoparticles*. Journal of Controlled Release, 2008. **132**(3): p. 171-183.
39. Kowalczyńska, H.M., et al., *Albumin adsorption on unmodified and sulfonated polystyrene surfaces, in relation to cell–substratum adhesion*. Colloids and Surfaces B: Biointerfaces, 2011. **84**(2): p. 536-544.
40. Dabare, P.R.L., et al., *Surface nanotopography mediated albumin adsorption, unfolding and modulation of early innate immune responses*. Materials Today Advances, 2021. **12**: p. 100187.

41. Zaidi, N., et al., *A comprehensive insight into binding of hippuric acid to human serum albumin: a study to uncover its impaired elimination through hemodialysis*. PloS One, 2013. **8**(8): p. e71422.
42. Kuten Pella, O., et al., *Albumin as a Biomaterial and Therapeutic Agent in Regenerative Medicine*. International Journal of Molecular Sciences, 2022. **23**(18): p. 10557.
43. Lin, W., et al., *Hemocompatibility of polyacrylonitrile dialysis membrane immobilized with chitosan and heparin conjugate*. Biomaterials, 2004. **25**(10): p. 1947-1957.
44. Ogun, A.S., et al., *Biochemistry, transferrin*, in *StatPearls [Internet]*. 2022, StatPearls Publishing.
45. Stafford, J.L., et al., *Transferrin and the innate immune response of fish: identification of a novel mechanism of macrophage activation*. Developmental & Comparative Immunology, 2003. **27**(6-7): p. 539-554.
46. Moghimi, S.M., et al., *Material properties in complement activation*. Advanced Drug Delivery Reviews, 2011. **63**(12): p. 1000-1007.
47. Toda, M., et al., *Complement activation on surfaces carrying amino groups*. Biomaterials, 2008. **29**(4): p. 407-417.
48. Vidarsson, G., et al., *IgG subclasses and allotypes: from structure to effector functions*. Frontiers in Immunology, 2014. **5**: p. 520.
49. Bahniuk, M.S., et al., *Human plasma protein adsorption to elastinlike polypeptide nanoparticles*. Biointerphases, 2020. **15**(2): p. 021007.
50. Harrison, P.M., et al., *The ferritins: molecular properties, iron storage function and cellular regulation*. Biochimica et Biophysica Acta (BBA)-Bioenergetics, 1996. **1275**(3): p. 161-203.

51. Sano, K., et al., *Changes in glycosylation of vitronectin modulate multimerization and collagen binding during liver regeneration*. *Glycobiology*, 2007. **17**(7): p. 784-794.
52. Berclaz, P., et al., *Rare Childhood Lung Disorders: α 1-Antitrypsin Deficiency, Pulmonary Alveolar Proteinosis, and Pulmonary Alveolar Microlithiasis*, in *Kendig's Disorders of the Respiratory Tract in Children*. 2006, Elsevier. p. 747-761.
53. Chidambaranathan-Reghupaty, S., et al., *Hepatocellular carcinoma (HCC): Epidemiology, etiology and molecular classification*. *Advances in Cancer Research*, 2021. **149**: p. 1-61.
54. Bahniuk, M.S., et al., *Bioactive glass 45S5 powders: effect of synthesis route and resultant surface chemistry and crystallinity on protein adsorption from human plasma*. *Biointerphases*, 2012. **7**(1): p. 41.
55. Armstrong, P.B., et al., *α 2-macroglobulin: an evolutionarily conserved arm of the innate immune system*. *Developmental & Comparative Immunology*, 1999. **23**(4-5): p. 375-390.
56. Vandooren, J., et al., *Alpha-2-macroglobulin in inflammation, immunity and infections*. *Frontiers in Immunology*, 2021. **12**: p. 803244.
57. Levy, J.H., et al., *Fibrinogen as a therapeutic target for bleeding: a review of critical levels and replacement therapy*. *Transfusion*, 2014. **54**(5): p. 1389-1405.
58. Lowe, G.D., et al., *Plasma fibrinogen*. *Annals of Clinical Biochemistry*, 2004. **41**(6): p. 430-440.
59. Sreedhara, R., et al., *Uremic patients have decreased shear-induced platelet aggregation mediated by decreased availability of glycoprotein IIb-IIIa receptors*. *American Journal of Kidney Diseases*, 1996. **27**(3): p. 355-364.
60. Kozek-Langenecker, S.A., et al., *Fibrinogen fragments and platelet dysfunction in uremia*. *Kidney International*, 1999. **56**(1): p. 299-305.

61. Ocak, G., et al., *Chronic kidney disease and bleeding risk in patients at high cardiovascular risk: a cohort study*. Journal of Thrombosis and Haemostasis, 2018. **16**(1): p. 65-73.
62. Kaplan, B., et al., *Search for peptidic "middle molecules" in uremic sera: isolation and chemical identification of fibrinogen fragments*. Journal of Chromatography B, 2003. **796**(1): p. 141-153.
63. Austen, D., *Clinical Biochemistry of Blood Coagulation*, in *Scientific Foundations of Biochemistry in Clinical Practice*. 1994, Elsevier. p. 495-513.
64. Ashikaga, H., et al., *Blood Coagulation and Atherothrombosis*, in *Molecular Basis of Cardiovascular Disease (Second Edition)*. 2004, W.B. Saunders: Philadelphia. p. 498-518.
65. Wu, Y., *Contact pathway of coagulation and inflammation*. Thrombosis Journal, 2015. **13**(1): p. 1-9.
66. Ortega, V.A., et al., *Polymer-coated nanoparticle protein corona formation potentiates phagocytosis of bacteria by innate immune cells and inhibits coagulation in human plasma*. Biointerphases, 2020. **15**(5): p. 051003.
67. Ivanov, I., et al., *Protease activity in single-chain prekallikrein*. Blood, The Journal of the American Society of Hematology, 2020. **135**(8): p. 558-567.
68. Veloso, D., et al., *Western blot analyses of prekallikrein and its activation products in human plasma*. Thrombosis and Haemostasis, 1991. **65**(04): p. 382-388.
69. Yun, Y., et al., *Initial hemocompatibility studies of titanium and zirconium alloys: Prekallikrein activation, fibrinogen adsorption, and their correlation with surface electrochemical properties*. Journal of Biomedical Materials Research, 1996. **32**(1): p. 77-85.

70. To, W.S., et al., *Plasma and cellular fibronectin: distinct and independent functions during tissue repair*. *Fibrogenesis & Tissue Repair*, 2011. **4**: p. 1-17.
71. Gierula, M., et al., *Anticoagulant protein S—New insights on interactions and functions*. *Journal of Thrombosis and Haemostasis*, 2020. **18**(11): p. 2801-2811.
72. Quandt, J., et al., *Interactive Hemocompatible Nanocoating to Prevent Surface - Induced Coagulation in Medical Devices*. *Advanced Materials Interfaces*, 2022. **9**(33): p. 2201055.
73. Woodhouse, K., et al., *Adsorption of plasminogen from plasma to lysine-derivatized polyurethane surfaces*. *Biomaterials*, 1992. **13**(15): p. 1103-1108.
74. Thomas, M., et al., *High molecular weight kininogen adsorption on hemodialysis membranes: influence of pH and relationship with contact phase activation of blood plasma. Influence of pre-treatment with poly (ethyleneimine)*. *The International Journal of Artificial Organs*, 2000. **23**(1): p. 20-26.
75. Renaux, J., et al., *Activation of the kallikrein-kinin system in hemodialysis: role of membrane electronegativity, blood dilution, and pH*. *Kidney International*, 1999. **55**(3): p. 1097-1103.

Chapter 6

Concluding remarks and perspectives

6.1 Major contributions

Chapter 1 of this work provides an extensive review of various adsorbents used for uremic toxin removal, highlighting the research gap in the current literature, which are improvement of adsorbent hemocompatibility and development of affordable adsorbents that can selectively bind uremic toxins. In Chapter 2, the driving force and binding pocket of IS/PCS with HSA were identified, providing key parameters for future adsorbent development. Chapter 3 describes the design, synthesis, and characterization of a series of β -cyclodextrin, 2-(methacryloyloxy)ethyl phosphorylcholine coated MNPs. For the first time, the effect of film chemistry on the adsorbed toxinome from a complex uremic toxin solution was quantified. Chapter 4 evaluates the biocompatibility and hemocompatibility of the MNPs, reinforcing the potential of the p(PM β CD-co-MPC) polymer combination for use in the context of chronic kidney disease. In Chapter 5, the behavior of the MNPs under the presence of uremic toxin solution was further evaluated, revealing that uremic toxins disturb the anti-fouling property of MPC polymers, leading to increased protein adsorption. This finding arose attention on the anti-fouling polymer application in CKD patients. Overall, this work provides a comprehensive evaluation of the hemocompatibility of p(PM β CD-co-MPC) engineered surfaces under the uremic condition that mimics the plasma of CKD patients, evaluating the difference in protein and toxin adsorption between different particle types.

This work accomplished two pivotal stages: firstly, it illuminated the driving force and binding mechanisms behind protein-bound uremic toxins binding (PBUT) with human serum albumin, thus providing invaluable insights for the development of adsorbents with targeted binding capabilities. Secondly, a comprehensive evaluation of the functionality, physicochemical

properties, and hemocompatibility of a series of innovative, hemocompatible adsorbents was conducted, culminating in the first-ever quantification of uremic adsorption on such adsorbent.

6.2 Future work

The present study evaluates the potential application of β -cyclodextrin, 2-(methacryloyloxy)ethyl phosphorylcholine coated magnetic nanoparticles (MNPs) as an adsorbent for the removal of uremic toxins. The uremic toxins removal test results indicate that the removed uremic toxins from the metabolite solution were largely composed of the water-soluble compounds pyruvic acid and guanidinopropionic acid. The next stage of the study involves the construction of a metabolite library using protein-bound uremic toxins to assess the adsorbent's ability to adsorb protein-bound uremic toxins (PBUT) and evaluate its potential as an in-line cartridge for specific removal of PBUT. Additionally, toxicity studies in animal models examining potential interactions with other medications required by chronic kidney disease (CKD) patients will be performed to bring the adsorbent a step closer to clinical trial. Although cyclodextrin has been widely used as a host molecule for the removal of organic compounds, its application as an adsorbent for uremic toxins has been limited. Thus, the uremic toxin removal efficiency of β -cyclodextrin, 2-(methacryloyloxy)ethyl phosphorylcholine coated MNPs will be compared with current existing therapy to determine its performance as literature review.

Bibliography

Chapter 1

1. Klefter, R., et al., *Savings in dialysis treatment?* Artificial Organs, 2002. **26**(1): p. 49-54.
2. Pavlenko, D., et al., *Carbon adsorbents with dual porosity for efficient removal of uremic toxins and cytokines from human plasma.* Scientific Reports, 2017. **7**(1): p. 1-7.
3. Lv, J., et al., *Prevalence and disease burden of chronic kidney disease.* Renal Fibrosis: Mechanisms Therapies, 2019: p. 3-15.
4. Ma, Y., et al., *Adsorption-based strategies for removing uremic toxins from blood.* Microporous Mesoporous Materials, 2021. **319**: p. 111035.
5. Bellringer, M., et al., *beta-Cyclodextrin: 52-week toxicity studies in the rat and dog.* Food Chemical Toxicology, 1995. **33**(5): p. 367-376.
6. Zhou, Y., et al., *Enhanced removal of bisphenol A by cyclodextrin in photocatalytic systems: degradation intermediates and toxicity evaluation.* Chinese Chemical Letters, 2020. **31**(10): p. 2623-2626.
7. Yu, Q., et al., *Anti-fouling bioactive surfaces.* Acta Biomaterialia, 2011. **7**(4): p. 1550-1557.
8. Zhang, H., et al., *Anti-fouling coatings of poly (dimethylsiloxane) devices for biological and biomedical applications.* Journal of Medical Biological Engineering, 2015. **35**(2): p. 143-155.
9. Bhakta, S.A., et al., *Protein adsorption onto nanomaterials for the development of biosensors and analytical devices: A review.* Analytica Chimica Acta, 2015. **872**: p. 7-25.
10. Silva-Bermudez, P., et al., *An overview of protein adsorption on metal oxide coatings for biomedical implants.* Surface Coatings Technology, 2013. **233**: p. 147-158.

11. Pinholt, C., et al., *The importance of interfaces in protein drug delivery-why is protein adsorption of interest in pharmaceutical formulations?* Expert Opinion on Drug Delivery, 2011. **8**(7): p. 949-964.
12. Chen, S., et al., *Surface hydration: Principles and applications toward low-fouling/nonfouling biomaterials.* Polymer, 2010. **51**(23): p. 5283-5293.
13. Mohanty, J., et al., *Cyclodextrins in Anti-Biofouling Applications*, in *Supramolecular Chemistry in Corrosion and Biofouling Protection*. 2021, CRC Press. p. 335-346.
14. Liu, Y., et al., *Molecular simulations and understanding of antifouling zwitterionic polymer brushes.* Journal of Materials Chemistry B, 2020. **8**(17): p. 3814-3828.
15. He, M., et al., *Zwitterionic materials for antifouling membrane surface construction.* Acta Biomaterialia, 2016. **40**: p. 142-152.
16. Burns, N.L., et al., *Influence of surface charge on protein adsorption at an amphoteric surface: effects of varying acid to base ratio.* Journal of Colloid Interface Science, 1996. **178**(1): p. 116-122.
17. Phillips, S., et al., *Acrylamide and iodide fluorescence quenching as a structural probe of tryptophan microenvironment in bovine lens crystallins.* Current Eye Research, 1986. **5**(8): p. 611-620.
18. Krebs, H.A., *Chemical composition of blood plasma and serum.* Annual Review of Biochemistry, 1950. **19**(1): p. 409-430.
19. Sperling, C., et al., *Blood coagulation on biomaterials requires the combination of distinct activation processes.* Biomaterials, 2009. **30**(27): p. 4447-4456.
20. Fischer, M., et al., *Synergistic effect of hydrophobic and anionic surface groups triggers blood coagulation in vitro.* Journal of Materials Science: Materials in Medicine, 2010. **21**: p. 931-937.

21. Le, H.T., et al., *Synthesis, cytotoxicity, and phase-solubility study of cyclodextrin click clusters*. Journal of Pharmaceutical Sciences, 2014. **103**(10): p. 3183-3189.
22. Diget, J.S., et al., *Direct synthesis of well-defined zwitterionic cyclodextrin polymers via atom transfer radical polymerization*. European Polymer Journal, 2019. **116**: p. 84-90.
23. Goszczyński, T.M., et al., *Synthesis of beta-cyclodextrin-lysozyme conjugates and their physicochemical and biochemical properties*. Journal of Inclusion Phenomena, 2017. **87**: p. 341-348.
24. Dong, H., et al., *Recyclable antibacterial magnetic nanoparticles grafted with quaternized poly (2-(dimethylamino) ethyl methacrylate) brushes*. Biomacromolecules, 2011. **12**(4): p. 1305-1311.
25. Yallapu, M.M., et al., *Multi-functional magnetic nanoparticles for magnetic resonance imaging and cancer therapy*. Biomaterials, 2011. **32**(7): p. 1890-1905.
26. Beaven, G.H., et al., *A spectroscopic study of the haemin-human-serum-albumin system*. European Journal of Biochemistry, 1974. **41**(3): p. 539-546.
27. Chipman, D.M., et al., *The binding of oligosaccharides containing n-acetylglucosamine and n-acetylmuramic acid to lysozyme: the specificity of binding subsites*. Journal of Biological Chemistry, 1967. **242**(19): p. 4388-4394.
28. Bahniuk, M.S., et al., *Human plasma protein adsorption to elastinlike polypeptide nanoparticles*. Biointerphases, 2020. **15**(2): p. 021007.
29. Bahniuk, M.S., et al., *Bioactive glass 45S5 powders: effect of synthesis route and resultant surface chemistry and crystallinity on protein adsorption from human plasma*. Biointerphases, 2012. **7**(1): p. 41.
30. Han, V., et al., *A comparative study of common techniques used to measure haemolysis in stored red cell concentrates*. Vox Sanguinis, 2010. **98**(2): p. 116-123.

31. Mahmoud, W.E., et al., *A facile method to syntheses monodisperse gamma-Fe₂O₃ nanocubes with high magnetic anisotropy density*. Superlattices Microstructures, 2014. **68**: p. 1-5.
32. RÅ¶sner, H.I., et al., *The human alpha-lactalbumin molten globule: comparison of structural preferences at pH 2 and pH 7*. Journal of Molecular Biology, 2009. **394**(2): p. 351-362.
33. Cadenas, E., et al., *Thiol redox transitions in cell signaling, part A: chemistry and biochemistry of low molecular weight and protein thiols*. 2010: Academic Press.
34. Steudle, A., et al., *Modelling of lysozyme binding to a cation exchange surface at atomic detail: the role of flexibility*. Biophysical Journal, 2011. **100**(12): p. 3016-3024.
35. Jain, T.K., et al., *Magnetic resonance imaging of multifunctional pluronic stabilized iron-oxide nanoparticles in tumor-bearing mice*. Biomaterials, 2009. **30**(35): p. 6748-6756.
36. Dobrovolskaia, M.A., et al., *Interaction of colloidal gold nanoparticles with human blood: effects on particle size and analysis of plasma protein binding profiles*. Nanomedicine: Nanotechnology, Biology and Medicine, 2009. **5**(2): p. 106-117.
37. Konno, T., et al., *Preparation of nanoparticles composed with bioinspired 2-methacryloyloxyethyl phosphorylcholine polymer*. Biomaterials, 2001. **22**(13): p. 1883-1889.
38. Ishihara, K., et al., *Hemocompatibility of human whole blood on polymers with a phospholipid polar group and its mechanism*. Journal of Biomedical Materials Research, 1992. **26**(12): p. 1543-1552.
39. Yang, J., et al., *How does biological sex affect the physiological response to nanomaterials?* Nano Today, 2021. **41**: p. 101292.

40. Davie, E.W., et al., *The coagulation cascade: initiation, maintenance, and regulation*. *Biochemistry*, 1991. **30**(43): p. 10363-10370.
41. Kratz, F., *Albumin as a drug carrier: design of prodrugs, drug conjugates and nanoparticles*. *Journal of Controlled Release*, 2008. **132**(3): p. 171-183.
42. Kowalczyńska, H.M., et al., *Albumin adsorption on unmodified and sulfonated polystyrene surfaces, in relation to cell–substratum adhesion*. *Colloids and Surfaces B: Biointerfaces*, 2011. **84**(2): p. 536-544.
43. Dabare, P.R.L., et al., *Surface nanotopography mediated albumin adsorption, unfolding and modulation of early innate immune responses*. *Materials Today Advances*, 2021. **12**: p. 100187.
44. Lin, W., et al., *Hemocompatibility of polyacrylonitrile dialysis membrane immobilized with chitosan and heparin conjugate*. *Biomaterials*, 2004. **25**(10): p. 1947-1957.
45. Henry, M., et al., *Conformation change of albumin adsorbed on polycarbonate membranes as revealed by ToF-SIMS*. *Langmuir*, 2003. **19**(15): p. 6271-6276.
46. Van Dulm, P., et al., *The adsorption of human plasma albumin on solid surfaces, with special attention to the kinetic aspects*. *Journal of Colloid and Interface Science*, 1983. **91**(1): p. 248-255.
47. Victor, S.P., et al., *Development and evaluation of cyclodextrin complexed hydroxyapatite nanoparticles for preferential albumin adsorption*. *Colloids and Surfaces B: Biointerfaces*, 2011. **85**(2): p. 221-228.
48. Walport, M.J., *Advances in immunology: complement (first of two parts)*. *New England Journal of Medicine*, 2001. **344**(14): p. 1058-1066.

49. Andersson, J., et al., *Binding of C3 fragments on top of adsorbed plasma proteins during complement activation on a model biomaterial surface*. *Biomaterials*, 2005. **26**(13): p. 1477-1485.
50. Melchior, P., et al., *Complement activation by dialysis membranes and its association with secondary membrane formation and surface charge*. *Artificial Organs*, 2021. **45**(7): p. 770-778.
51. Vidarsson, G., et al., *IgG subclasses and allotypes: from structure to effector functions*. *Frontiers in Immunology*, 2014. **5**: p. 520.
52. Harrison, P.M., et al., *The ferritins: molecular properties, iron storage function and cellular regulation*. *Biochimica et Biophysica Acta (BBA)-Bioenergetics*, 1996. **1275**(3): p. 161-203.
53. Ogun, A.S., et al., *Biochemistry, transferrin*, in *StatPearls [Internet]*. 2022, StatPearls Publishing.
54. Stafford, J.L., et al., *Transferrin and the innate immune response of fish: identification of a novel mechanism of macrophage activation*. *Developmental & Comparative Immunology*, 2003. **27**(6-7): p. 539-554.
55. Bale, M.D., et al., *Identification of vitronectin as a major plasma protein adsorbed on polymer surfaces of different copolymer composition*. *Blood*, 1989.
56. Berclaz, P., et al., *Rare Childhood Lung Disorders: α 1-Antitrypsin Deficiency, Pulmonary Alveolar Proteinosis, and Pulmonary Alveolar Microlithiasis*, in *Kendig's Disorders of the Respiratory Tract in Children*. 2006, Elsevier. p. 747-761.
57. Chidambaranathan-Reghupaty, S., et al., *Hepatocellular carcinoma (HCC): Epidemiology, etiology and molecular classification*. *Advances in Cancer Research*, 2021. **149**: p. 1-61.

58. Li, W., et al., *Cyclodextrin based unimolecular micelles with targeting and biocleavable abilities as chemotherapeutic carrier to overcome drug resistance*. *Materials Science Engineering: C*, 2019. **105**: p. 110047.
59. Papa, E., et al., *Investigation of the influence of protein corona composition on gold nanoparticle bioactivity using machine learning approaches*. *SAR and QSAR in Environmental Research*, 2016. **27**(7): p. 521–538.
60. Samir, D., et al., *Cell cooperation and role of the P2X7 receptor in pulmonary inflammation induced by nanoparticles*. *Nanotoxicology*, 2012. **7**(8): p. 1302–1314.
61. Liu, R., et al., *Prediction of nanoparticles-cell association based on corona proteins and physicochemical properties*. *Nanoscale*, 2015. **7**(21): p. 9664-9675.
62. Armstrong, P.B., et al., *α 2-macroglobulin: an evolutionarily conserved arm of the innate immune system*. *Developmental & Comparative Immunology*, 1999. **23**(4-5): p. 375-390.
63. Vandooren, J., et al., *Alpha-2-macroglobulin in inflammation, immunity and infections*. *Frontiers in Immunology*, 2021. **12**: p. 803244.
64. Levy, J.H., et al., *Fibrinogen as a therapeutic target for bleeding: a review of critical levels and replacement therapy*. *Transfusion*, 2014. **54**(5): p. 1389-1405.
65. Lowe, G.D., et al., *Plasma fibrinogen*. *Annals of Clinical Biochemistry*, 2004. **41**(6): p. 430-440.
66. Nava-Ortiz, C.A., et al., *Cyclodextrin-functionalized biomaterials loaded with miconazole prevent *Candida albicans* biofilm formation in vitro*. *Acta Biomaterialia*, 2010. **6**(4): p. 1398-1404.
67. Austen, D., *Clinical Biochemistry of Blood Coagulation*, in *Scientific Foundations of Biochemistry in Clinical Practice*. 1994, Elsevier. p. 495-513.

68. Ashikaga, H., et al., *chapter 28 - Blood Coagulation and Atherothrombosis*, in *Molecular Basis of Cardiovascular Disease (Second Edition)*, K.R. Chien, Editor. 2004, W.B. Saunders: Philadelphia. p. 498-518.
69. Wu, Y., *Contact pathway of coagulation and inflammation*. *Thrombosis journal*, 2015. **13**(1): p. 1-9.
70. Ortega, V.A., et al., *Polymer-coated nanoparticle protein corona formation potentiates phagocytosis of bacteria by innate immune cells and inhibits coagulation in human plasma*. *Biointerphases*, 2020. **15**(5): p. 051003.
71. Ivanov, I., et al., *Protease activity in single-chain prekallikrein*. *Blood, The Journal of the American Society of Hematology*, 2020. **135**(8): p. 558-567.
72. Veloso, D., et al., *Western blot analyses of prekallikrein and its activation products in human plasma*. *Thrombosis and Haemostasis*, 1991. **65**(04): p. 382-388.
73. Yun, Y., et al., *Initial hemocompatibility studies of titanium and zirconium alloys: Prekallikrein activation, fibrinogen adsorption, and their correlation with surface electrochemical properties*. *Journal of Biomedical Materials Research: An Official Journal of The Society for Biomaterials and The Japanese Society for Biomaterials*, 1996. **32**(1): p. 77-85.
74. To, W.S., et al., *Plasma and cellular fibronectin: distinct and independent functions during tissue repair*. *Fibrogenesis & Tissue Repair*, 2011. **4**: p. 1-17.
75. Rogers, H.J., et al., *Hemostasis and thrombosis*, in *Hematopathology*. 2018, Elsevier. p. 57-105. e4.
76. Woodhouse, K., et al., *Adsorption of plasminogen from plasma to lysine-derivatized polyurethane surfaces*. *Biomaterials*, 1992. **13**(15): p. 1103-1108.

77. Quandt, J., et al., *Interactive Hemocompatible Nanocoating to Prevent Surface-Induced Coagulation in Medical Devices*. *Advanced Materials Interfaces*, 2022. **9**(33): p. 2201055.
78. Nalezinková , M., *In vitro hemocompatibility testing of medical devices*. *Thrombosis Research*, 2020. **195**: p. 146-150.
79. Lippi, G., *Systematic assessment of the hemolysis index: pros and cons*. *Advances in Clinical Chemistry*, 2015. **71**: p. 157-170.
80. Thomas, M., et al., *High molecular weight kininogen adsorption on hemodialysis membranes: influence of pH and relationship with contact phase activation of blood plasma. Influence of pre-treatment with poly (ethyleneimine)*. *The International Journal of Artificial Organs*, 2000. **23**(1): p. 20-26.
81. Renaux, J., et al., *Activation of the kallikrein-kinin system in hemodialysis: role of membrane electronegativity, blood dilution, and pH*. *Kidney International*, 1999. **55**(3): p. 1097-1103.
82. Dobrovolskaia, M.A., et al., *Nanoparticle size and surface charge determine effects of PAMAM dendrimers on human platelets in vitro*. *Molecular Pharmaceutics*, 2012. **9**(3): p. 382-393.
83. Koziara, J., et al., *Blood compatibility of cetyl alcohol/polysorbate-based nanoparticles*. *Pharmaceutical Research*, 2005. **22**: p. 1821-1828.
84. Wang, J., et al., *Cyclic molecule aerogels: a robust cyclodextrin monolith with hierarchically porous structures for removal of micropollutants from water*. *Journal of Materials Chemistry A*, 2017. **5**(9): p. 4308-4313.

85. Gholibegloo, E., et al., *Improved curcumin loading, release, solubility and toxicity by tuning the molar ratio of cross-linker to beta-cyclodextrin*. Carbohydrate Polymers, 2019. **213**: p. 70-78.
86. Yuan, Z., et al., *Chitosan-graft-beta-cyclodextrin nanoparticles as a carrier for controlled drug release*. International Journal of Pharmaceutics, 2013. **446**(1-2): p. 191-198.
87. Namazi, H., et al., *Synthesis of beta-cyclodextrin-based dendrimer as a novel encapsulation agent*. Polymer International, 2014. **63**(8): p. 1447-1455.
88. Kiasat, A.R., et al., *Magnetic nanoparticles grafted with beta-cyclodextrin-polyurethane polymer as a novel nanomagnetic polymer brush catalyst for nucleophilic substitution reactions of benzyl halides in water*. Journal of Molecular Catalysis A: Chemical, 2012. **365**: p. 80-86.
89. Yuan, Z., et al., *Redox-controlled voltage responsive micelles assembled by noncovalently grafted polymers for controlled drug release*. Macromolecules, 2019. **52**(4): p. 1400-1407.
90. Fan, X., et al., *Thermoresponsive Supramolecular Chemotherapy by "V"-Shaped Armed β -Cyclodextrin Star Polymer to Overcome Drug Resistance*. Advanced Healthcare Materials, 2018. **7**(7): p. 1701143.
91. Xu, Z., et al., *Unimolecular micelles of amphiphilic cyclodextrin-core star-like block copolymers for anticancer drug delivery*. Chemical Communications, 2015. **51**(87): p. 15768-15771.
92. Chmielarz, P., et al., *Synthesis of beta-cyclodextrin-based star polymers via a simplified electrochemically mediated ATRP*. Polymer, 2016. **88**: p. 36-42.

93. Miura, Y., et al., *Synthesis of well-defined AB₂₀-type star polymers with cyclodextrin-core by combination of NMP and ATRP*. *Journal of Polymer Science Part A: Polymer Chemistry*, 2005. **43**(18): p. 4271-4279.
94. Pan, Y., et al., *Tailor-Made Antimicrobial/Antiviral Star Polymer via ATRP of Cyclodextrin and Guanidine-Based Macromonomer*. *Macromolecular Chemistry Physics*, 2015. **216**(5): p. 511-518.
95. Stenzel, M.H., et al., *Star polymer synthesis using trithiocarbonate functional β -cyclodextrin cores (reversible addition–fragmentation chain-transfer polymerization)*. *Journal of Polymer Science Part A: Polymer Chemistry*, 2002. **40**(24): p. 4498-4512.
96. Araki, J., et al., *Recent advances in the preparation of cyclodextrin-based polyrotaxanes and their applications to soft materials*. *Soft Matter*, 2007. **3**(12): p. 1456-1473.
97. Samitsu, S., et al., *New solvent for polyrotaxane. II. Dissolution behavior of polyrotaxane in ionic liquids and preparation of ionic liquid-containing slide-ring gels*. *Journal of Polymer Science Part B: Polymer Physics*, 2006. **44**(14): p. 1985-1994.
98. Mondjinou, Y.A., et al., *Synthesis of 2-hydroxypropyl- β -cyclodextrin/pluronic-based polyrotaxanes via heterogeneous reaction as potential Niemann-Pick type C therapeutics*. *Biomacromolecules*, 2013. **14**(12): p. 4189-4197.
99. Tamura, A., et al., *Lysosomal-specific cholesterol reduction by biocleavable polyrotaxanes for ameliorating Niemann-Pick type C disease*. *Scientific Reports*, 2014. **4**(1): p. 1-8.
100. Wang, J., et al., *The intrinsic microstructure of supramolecular hydrogels derived from α -cyclodextrin and pluronic F127: nanosheet building blocks and hierarchically self-assembled structures*. *Soft Matter*, 2020. **16**(25): p. 5906-5909.

101. Boger, J., et al., *Cyclodextrin chemistry. Selective modification of all primary hydroxyl groups of alpha- and beta-cyclodextrins*. Helvetica Chimica Acta, 1978. **61**(6): p. 2190-2218.
102. Hammoud, Z., et al., *Cyclodextrin-membrane interaction in drug delivery and membrane structure maintenance*. International Journal of Pharmaceutics, 2019. **564**: p. 59-76.
103. Akbarzadeh, A., et al., *Synthesis, characterization, and in vitro evaluation of novel polymer-coated magnetic nanoparticles for controlled delivery of doxorubicin*. Nanotechnology, Science Applications, 2012. **5**: p. 13.
104. Ge, F., et al., *Efficient removal of cationic dyes from aqueous solution by polymer-modified magnetic nanoparticles*. Chemical Engineering Journal, 2012. **198**: p. 11-17.

Chapter 2

1. Liabeuf, S., et al., *Protein-bound uremic toxins: new insight from clinical studies*. Toxins, 2011. **3**(7): p. 911-919.
2. Shi, Y., et al., *Increasing the removal of protein-bound uremic toxins by liposome-supported hemodialysis*. Artificial Organs, 2019. **43**(5): p. 490-503.
3. Liu, W., et al., *Impacts of indoxyl sulfate and p-cresol sulfate on chronic kidney disease and mitigating effects of AST-120*. Toxins, 2018. **10**(9): p. 367.
4. Khan, M.W.A., et al., *Biochemical, biophysical, and thermodynamic analysis of in vitro glycated human serum albumin*. Biochemistry (Moscow), 2007. **72**(2): p. 146-152.
5. Morissette, M., *Colloid osmotic pressure: its measurement and clinical value*. Canadian Medical Association Journal, 1977. **116**(8): p. 897.
6. Quinlan, G.J., et al., *Albumin: biochemical properties and therapeutic potential*. Hepatology, 2005. **41**(6): p. 1211-1219.

7. Kragh-Hansen, U., et al., *Detergents as probes of hydrophobic binding cavities in serum albumin and other water-soluble proteins*. Biophysical Journal, 2001. **80**(6): p. 2898-2911.
8. Sudlow, G., et al., *The characterization of two specific drug binding sites on human serum albumin*. Molecular Pharmacology, 1975. **11**(6): p. 824-832.
9. Peters Jr, T., *All about albumin: biochemistry, genetics, and medical applications*. 1995: Academic Press.
10. Fanali, G., et al., *Human serum albumin: from bench to bedside*. Molecular Aspects of Medicine, 2012. **33**(3): p. 209-290.
11. Sudlow, G., et al., *Further characterization of specific drug binding sites on human serum albumin*. Molecular Pharmacology, 1976. **12**(6): p. 1052-1061.
12. Ghuman, J., et al., *Structural basis of the drug-binding specificity of human serum albumin*. Journal of Molecular Biology, 2005. **353**(1): p. 38-52.
13. Bhattacharya, A.A., et al., *Binding of the general anesthetics propofol and halothane to human serum albumin: high resolution crystal structures*. Journal of Biological Chemistry, 2000. **275**(49): p. 38731-38738.
14. Wang, C., et al., *Skin autofluorescence is associated with endothelial dysfunction in uremic subjects on hemodialysis*. PloS One, 2016. **11**(1): p. e0147771.
15. Gajjala, P.R., et al., *Emerging role of post-translational modifications in chronic kidney disease and cardiovascular disease*. Nephrology Dialysis Transplantation, 2015. **30**(11): p. 1814-1824.
16. Rueth, M., et al., *Guanidinylation of albumin decreased binding capacity of hydrophobic metabolites*. Acta Physiologica, 2015. **215**(1): p. 13-23.

17. Badar, A., et al., *Carbamylation of human serum albumin generates high-molecular weight aggregates: fine characterization by multi-spectroscopic methods and electron microscopy*. International Journal of Biological Macromolecules, 2020. **164**: p. 2380-2388.
18. Martinez, A.W., et al., *Removal of P-cresol sulfate by hemodialysis*. Journal of the American Society of Nephrology, 2005. **16**(11): p. 3430-3436.
19. Pham, N.M., et al., *Removal of the protein-bound solutes indican and p-cresol sulfate by peritoneal dialysis*. Clinical Journal of the American Society of Nephrology, 2008. **3**(1): p. 85-90.
20. Rocchetti, M.T., et al., *Efficacy of Divinylbenzenic Resin in Removing Indoxyl Sulfate and P-cresol Sulfate in Hemodialysis Patients: Results from an In Vitro Study and an In Vivo Pilot Trial (xuanro4-Nature 3.2)*. Toxins, 2020. **12**(3): p. 170.
21. Patel, K.P., et al., *The production of p-cresol sulfate and indoxyl sulfate in vegetarians versus omnivores*. Clinical Journal of the American Society of Nephrology, 2012. **7**(6): p. 982-988.
22. Devine, E., et al., *Binding affinity and capacity for the uremic toxin indoxyl sulfate*. Toxins, 2014. **6**(2): p. 416-429.
23. Bergé-Lefranc, D., et al., *Binding of p-cresylsulfate and p-cresol to human serum albumin studied by microcalorimetry*. The Journal of Physical Chemistry B, 2010. **114**(4): p. 1661-1665.
24. Frazier, R.A., et al., *Isothermal titration calorimetry study of epicatechin binding to serum albumin*. Journal of Pharmaceutical Biomedical Analysis, 2006. **41**(5): p. 1602-1605.

25. Nakamura, S., et al., *A new multi-binding model for isothermal titration calorimetry analysis of the interaction between adenosine 5'-triphosphate and magnesium ion*. *Thermochimica Acta*, 2013. **563**: p. 82-89.
26. Dehkordi, M.N., et al., *Comprehensive study on the binding of iron Schiff base complex with DNA and determining the binding mode*. *Journal of Fluorescence*, 2013. **23**(4): p. 813-821.
27. Ràfols, C., et al., *Molecular interactions between warfarin and human (HSA) or bovine (BSA) serum albumin evaluated by isothermal titration calorimetry (ITC), fluorescence spectrometry (FS) and frontal analysis capillary electrophoresis (FA/CE)*. *Journal of Pharmaceutical Biomedical Analysis*, 2018. **150**: p. 452-459.
28. Honoré, B., et al., *Albumin binding of anti-inflammatory drugs. Utility of a site-oriented versus a stoichiometric analysis*. *Molecular Pharmacology*, 1984. **25**(1): p. 137-150.
29. Hage, D.S., et al., *Characterization of the protein binding of chiral drugs by high-performance affinity chromatography interactions of R- and S-ibuprofen with human serum albumin*. *Journal of Chromatography A*, 1995. **693**(1): p. 23-32.
30. Fatima, S., et al., *Hydrophobic interaction between domain I of albumin and B chain of detemir may support myristate-dependent detemir-albumin binding*. *Applied Biochemistry Biotechnology*, 2017. **182**(1): p. 82-96.
31. Zhang, G., et al., *Polyoxometalate binding to human serum albumin: a thermodynamic and spectroscopic approach*. *The Journal of Physical Chemistry B*, 2007. **111**(38): p. 11253-11259.
32. Demers, J., et al., *Binding mechanism of an SH3 domain studied by NMR and ITC*. *Journal of the American Chemical Society*, 2009. **131**(12): p. 4355-4367.

33. Jourde-Chiche, N., et al. *PROGRESS IN UREMIC TOXIN RESEARCH: Protein-Bound Toxins—Update 2009*. in *Seminars in dialysis*. 2009. Wiley Online Library.
34. Madero, M., et al., *Removal of protein-bound uremic toxins during hemodialysis using a binding competitor*. *Clinical Journal of the American Society of Nephrology*, 2019. **14**(3): p. 394-402.
35. Li, J., et al., *Response regulators CheB and CheY exhibit competitive binding to the kinase CheA*. *Biochemistry*, 1995. **34**(45): p. 14626-14636.
36. Zhang, G., et al., *Study of the interaction between icariin and human serum albumin by fluorescence spectroscopy*. *Journal of Molecular Structure*, 2008. **881**(1-3): p. 132-138.
37. Melamed, M.L., et al., *Retained organic solutes, patient characteristics and all-cause and cardiovascular mortality in hemodialysis: results from the retained organic solutes and clinical outcomes (ROSCO) investigators*. *BMC Nephrology*, 2013. **14**(1): p. 1-10.
38. Lakowicz, J.R., *Principles of Fluorescence Spectroscopy 3rd ed*. New York City. 2011, USA: Springer Science.
39. Tang, J., et al., *Binding analysis of glycyrrhetic acid to human serum albumin: Fluorescence spectroscopy, FTIR, and molecular modeling*. *Bioorganic Medicinal Chemistry*, 2006. **14**(9): p. 3210-3217.
40. Samari, F., et al., *Affinity of two novel five-coordinated anticancer Pt (II) complexes to human and bovine serum albumins: a spectroscopic approach*. *Inorganic Chemistry*, 2012. **51**(6): p. 3454-3464.
41. Lakowicz, J.R., *Protein fluorescence*, in *Principles of fluorescence spectroscopy*. 1983, Springer. p. 341-381.
42. Vivian, J.T., et al., *Mechanisms of tryptophan fluorescence shifts in proteins*. *Biophysical Journal*, 2001. **80**(5): p. 2093-2109.

43. Zhang, G., et al., *Probing the binding of the flavonoid diosmetin to human serum albumin by multispectroscopic techniques*. Journal of Agricultural Food Chemistry, 2012. **60**(10): p. 2721-2729.
44. Bakar, K.A., et al., *A critical view on the analysis of fluorescence quenching data for determining ligand–protein binding affinity*. Spectrochimica Acta Part A: Molecular Biomolecular Spectroscopy, 2019. **223**: p. 117337.
45. Sakai, T., et al., *Interaction mechanism between indoxyl sulfate, a typical uremic toxin bound to site II, and ligands bound to site I of human serum albumin*. Pharmaceutical Research, 2001. **18**(4): p. 520-524.
46. Sakai, T., et al., *Characterization of binding site of uremic toxins on human serum albumin*. Biological Pharmaceutical Bulletin, 1995. **18**(12): p. 1755-1761.
47. Watanabe, H., et al., *Interaction between two sulfate-conjugated uremic toxins, p-cresyl sulfate and indoxyl sulfate, during binding with human serum albumin*. Drug Metabolism Disposition, 2012. **40**(7): p. 1423-1428.
48. Viaene, L., et al., *Albumin is the main plasma binding protein for indoxyl sulfate and p-cresyl sulfate*. Biopharmaceutics Drug Disposition, 2013. **34**(3): p. 165-175.

Chapter 3

1. Lv, J., et al., *Prevalence and disease burden of chronic kidney disease*. Renal Fibrosis: Mechanisms Therapies, 2019: p. 3-15.
2. Klefter, R., et al., *Savings in dialysis treatment?* Artificial organs, 2002. **26**(1): p. 49-54.
3. Ma, Y., et al., *Adsorption-based strategies for removing uremic toxins from blood*. Microporous Mesoporous Materials, 2021. **319**: p. 111035.

4. Pavlenko, D., et al., *Carbon adsorbents with dual porosity for efficient removal of uremic toxins and cytokines from human plasma*. Scientific Reports, 2017. **7**(1): p. 1-7.
5. Jong, J.A., et al., *A Ninhydrin-Type Urea Sorbent for the Development of a Wearable Artificial Kidney*. Macromolecular Bioscience, 2020. **20**(3): p. 1900396.
6. Keçili, R., et al., *The use of magnetic nanoparticles in sample preparation devices and tools*, in *Handbook of Nanomaterials in Analytical Chemistry*. 2020, Elsevier. p. 75-95.
7. Kainz, Q.M., et al., *Polymer-and dendrimer-coated magnetic nanoparticles as versatile supports for catalysts, scavengers, and reagents*. Accounts of Chemical Research, 2014. **47**(2): p. 667-677.
8. Wang, X., et al., *A molecularly imprinted polymer-coated nanocomposite of magnetic nanoparticles for estrone recognition*. Talanta, 2009. **78**(2): p. 327-332.
9. Urbina, M.C., et al., *Investigation of magnetic nanoparticle-polymer composites for multiple-controlled drug delivery*. The Journal of Physical Chemistry C, 2008. **112**(30): p. 11102-11108.
10. Sarnak, M.J., *Cardiovascular complications in chronic kidney disease*. American Journal of Kidney Diseases, 2003. **41**: p. 11-17.
11. Kraut, J.A., et al., *Adverse effects of the metabolic acidosis of chronic kidney disease*. Advances in Chronic Kidney Disease, 2017. **24**(5): p. 289-297.
12. Patel, S.S., et al., *Serum creatinine as a marker of muscle mass in chronic kidney disease: results of a cross-sectional study and review of literature*. Journal of Cachexia, Sarcopenia Muscle, 2013. **4**(1): p. 19-29.
13. Namekawa, K., et al., *Fabrication of zeolite-polymer composite nanofibers for removal of uremic toxins from kidney failure patients*. Biomaterials Science, 2014. **2**(5): p. 674-679.

14. Yen, S., et al., *Carbon nanotube/conducting polymer hybrid nanofibers as novel organic bioelectronic interfaces for efficient removal of protein-bound uremic toxins*. ACS Applied Materials & Interfaces, 2019. **11**(47): p. 43843-43856.
15. Varan, C., et al., *Preparation and characterization of cyclodextrin nanosponges for organic toxic molecule removal*. International Journal of Pharmaceutics, 2020. **585**: p. 119485.
16. Li, J., et al., *Multi-sites polycyclodextrin adsorbents for removal of protein-bound uremic toxins combining with hemodialysis*. Carbohydrate Polymers, 2020. **247**: p. 116665.
17. Tsoi, T., et al., *Urinary polyamines: a pilot study on their roles as prostate cancer detection biomarkers*. PLoS One, 2016. **11**(9): p. e0162217.
18. Kopple, J.D., et al., *Risks of chronic metabolic acidosis in patients with chronic kidney disease*. Kidney International, 2005. **67**: p. S21-S27.
19. Schlenoff, J.B., *Zwitteration: coating surfaces with zwitterionic functionality to reduce nonspecific adsorption*. Langmuir, 2014. **30**(32): p. 9625-9636.
20. Ueda, T., et al., *Preparation of 2-methacryloyloxyethyl phosphorylcholine copolymers with alkyl methacrylates and their blood compatibility*. Polymer Journal, 1992. **24**(11): p. 1259-1269.
21. Ishihara, K., *Revolutionary advances in 2-methacryloyloxyethyl phosphorylcholine polymers as biomaterials*. Journal of Biomedical Materials Research Part A, 2019. **107**(5): p. 933-943.
22. Konno, T., et al., *Enhanced solubility of paclitaxel using water-soluble and biocompatible 2-methacryloyloxyethyl phosphorylcholine polymers*. Journal of Biomedical Materials Research Part A, 2003. **65**(2): p. 209-214.

23. Ishihara, K., et al., *Inhibition of fibroblast cell adhesion on substrate by coating with 2-methacryloyloxyethyl phosphorylcholine polymers*. Journal of Biomaterials Science, Polymer Edition, 1999. **10**(10): p. 1047-1061.
24. Ishihara, K., et al., *Preparation of phospholipid polymers and their properties as polymer hydrogel membranes*. Polymer Journal, 1990. **22**(5): p. 355-360.
25. Ishihara, K., et al., *Reduced thrombogenicity of polymers having phospholipid polar groups*. Journal of Biomedical Materials Research, 1990. **24**(8): p. 1069-1077.
26. Campbell, E.J., et al., *Biocompatible surfaces using methacryloylphosphorylcholine laurylmethacrylate copolymer*. ASAIO Journal, 1994. **40**(3): p. M853-7.
27. Hedges, A., *Cyclodextrins: properties and applications*, in *Starch*. 2009, Elsevier. p. 833-851.
28. Liu, J., et al., *Structure design and performance study on filtration-adsorption bifunctional blood purification membrane*. Journal of Membrane Science, 2021. **636**: p. 119535.
29. Vanholder, R., et al., *Review on uremic toxins: classification, concentration, interindividual variability*. Kidney International, 2003. **63**: p. 1934-1943.
30. Itoh, Y., et al., *Protein-bound uremic toxins in hemodialysis patients measured by liquid chromatography/tandem mass spectrometry and their effects on endothelial ROS production*. Analytical Bioanalytical Chemistry, 2012. **403**(7): p. 1841-1850.
31. Toshimitsu, N., et al., *A gas chromatographic-mass spectrometric assay for nine hydroxyphenolic acids in uremic serum*. Clinica Chimica Acta, 1979. **96**(3): p. 247-254.
32. Duranton, F., et al., *Normal and pathologic concentrations of uremic toxins*. Journal of the American Society of Nephrology, 2012. **23**(7): p. 1258-1270.

33. Wolfson, M., et al., *Amino acid losses during hemodialysis with infusion of amino acids and glucose*. *Kidney International*, 1982. **21**(3): p. 500-506.
34. Schools, A., et al., *Biochemical and neurophysiological parameters in hemodialyzed patients with chronic renal failure*. *Clinica Chimica Acta*, 1989. **185**(1): p. 91-107.
35. Landon, J., et al., *Blood pyruvate concentration measured by a specific method in control subjects*. *Journal of Clinical Pathology*, 1962. **15**(6): p. 579-584.
36. Saito, K., et al., *Mechanism of increases in l-kynurenine quinolinic acid in renal insufficiency*. *American Journal of Physiology-Renal Physiology*, 2000. **279**: p. F565-F572.
37. Bain, M.A., et al., *Accumulation of trimethylamine and trimethylamine-N-oxide in end-stage renal disease patients undergoing haemodialysis*. *Nephrology Dialysis Transplantation*, 2006. **21**(5): p. 1300-1304.
38. Taki, K., et al., *Indoxyl sulfate and atherosclerotic risk factors in hemodialysis patients*. *American Journal of Nephrology*, 2007. **27**(1): p. 30-35.
39. Vanholder, R.C., et al., *Assessment of urea and other uremic markers for quantification of dialysis efficacy*. *Clinical Chemistry*, 1992. **38**(8): p. 1429-1436.
40. Toshimitsu, N., et al., *RNA metabolism in uremic patients: accumulation of modified ribonucleosides in uremic serum*. *Kidney International*, 1998. **53**: p. 1801-1806.
41. Dong, H., et al., *Recyclable antibacterial magnetic nanoparticles grafted with quaternized poly (2-(dimethylamino) ethyl methacrylate) brushes*. *Biomacromolecules*, 2011. **12**(4): p. 1305-1311.
42. Zhang, L., et al., *A high-performing plasma metabolite panel for early-stage lung cancer detection*. *Cancers*, 2020. **12**(3): p. 622.

43. Tan, J., et al., *Facile preparation of hybrid vesicles loaded with silica nanoparticles via aqueous photoinitiated polymerization-induced self-assembly*. RSC Advances, 2017. **7**(37): p. 23114-23121.
44. Shown, I., et al. *Synthesis of Cyclodextrin and Sugar-Based Oligomers for the Efavirenz Drug Delivery*. in *Macromolecular symposia*. 2010. Wiley Online Library.
45. Sun, X., et al., *Facile graft of poly (2-methacryloyloxyethyl phosphorylcholine) onto Fe₃O₄ nanoparticles by ATRP: Synthesis, properties, and biocompatibility*. Journal of Biomedical Materials Research Part A, 2013. **101**(2): p. 607-612.
46. Santos, E.C., et al., *Guanidine-functionalized Fe₃O₄ magnetic nanoparticles as basic recyclable catalysts for biodiesel production*. RSC Advances, 2015. **5**(59): p. 48031-48038.
47. Han, G., et al., *Advanced anti-fouling membranes for osmotic power generation from wastewater via pressure retarded osmosis (PRO)*. Environmental Science Technology, 2018. **52**(11): p. 6686-6694.
48. Burujeny, S.B., et al., *Bactericidal dental nanocomposites containing 1, 2, 3-triazolium-functionalized POSS additive prepared through thiol-ene click polymerization*. Dental Materials, 2017. **33**(1): p. 119-131.
49. Mahmoud, W.E., et al., *A facile method to syntheses monodisperse gamma-Fe₂O₃ nanocubes with high magnetic anisotropy density*. Superlattices Microstructures, 2014. **68**: p. 1-5.

Chapter 4

1. Klefter, R., et al., *Savings in dialysis treatment?* Artificial Organs, 2002. **26**(1): p. 49-54.

2. Pavlenko, D., et al., *Carbon adsorbents with dual porosity for efficient removal of uremic toxins and cytokines from human plasma*. Scientific Reports, 2017. **7**(1): p. 1-7.
3. Lv, J., et al., *Prevalence and disease burden of chronic kidney disease*. Renal Fibrosis: Mechanisms Therapies, 2019: p. 3-15.
4. Ma, Y., et al., *Adsorption-based strategies for removing uremic toxins from blood*. Microporous Mesoporous Materials, 2021. **319**: p. 111035.
5. Bellringer, M., et al., *Beta-Cyclodextrin: 52-week toxicity studies in the rat and dog*. Food Chemical Toxicology, 1995. **33**(5): p. 367-376.
6. Zhou, Y., et al., *Enhanced removal of bisphenol A by cyclodextrin in photocatalytic systems: degradation intermediates and toxicity evaluation*. Chinese Chemical Letters, 2020. **31**(10): p. 2623-2626.
7. Yu, Q., et al., *Anti-fouling bioactive surfaces*. Acta Biomaterialia, 2011. **7**(4): p. 1550-1557.
8. Zhang, H., et al., *Anti-fouling coatings of poly (dimethylsiloxane) devices for biological and biomedical applications*. Journal of Medical Biological Engineering, 2015. **35**(2): p. 143-155.
9. Bhakta, S.A., et al., *Protein adsorption onto nanomaterials for the development of biosensors and analytical devices: A review*. Analytica Chimica Acta, 2015. **872**: p. 7-25.
10. Silva-Bermudez, P., et al., *An overview of protein adsorption on metal oxide coatings for biomedical implants*. Surface Coatings Technology, 2013. **233**: p. 147-158.
11. Pinholt, C., et al., *The importance of interfaces in protein drug delivery-why is protein adsorption of interest in pharmaceutical formulations?* Expert Opinion on Drug Delivery, 2011. **8**(7): p. 949-964.

12. Chen, S., et al., *Surface hydration: Principles and applications toward low-fouling/nonfouling biomaterials*. *Polymer*, 2010. **51**(23): p. 5283-5293.
13. Mohanty, J., et al., *Cyclodextrins in Anti-Biofouling Applications*, in *Supramolecular Chemistry in Corrosion and Biofouling Protection*. 2021, CRC Press. p. 335-346.
14. Liu, Y., et al., *Molecular simulations and understanding of antifouling zwitterionic polymer brushes*. *Journal of Materials Chemistry B*, 2020. **8**(17): p. 3814-3828.
15. He, M., et al., *Zwitterionic materials for antifouling membrane surface construction*. *Acta Biomaterialia*, 2016. **40**: p. 142-152.
16. Burns, N.L., et al., *Influence of surface charge on protein adsorption at an amphoteric surface: effects of varying acid to base ratio*. *Journal of Colloid Interface Science*, 1996. **178**(1): p. 116-122.
17. Phillips, S., et al., *Acrylamide and iodide fluorescence quenching as a structural probe of tryptophan microenvironment in bovine lens crystallins*. *Current Eye Research*, 1986. **5**(8): p. 611-620.
18. Krebs, H.A., *Chemical composition of blood plasma and serum*. *Pharmaceutical Research*, 1950. **19**(1): p. 409-430.
19. Sperling, C., et al., *Blood coagulation on biomaterials requires the combination of distinct activation processes*. *Biomaterials*, 2009. **30**(27): p. 4447-4456.
20. Fischer, M., et al., *Synergistic effect of hydrophobic and anionic surface groups triggers blood coagulation in vitro*. *Journal of Materials Science: Materials in Medicine*, 2010. **21**: p. 931-937.
21. Le, H.T., et al., *Synthesis, cytotoxicity, and phase-solubility study of cyclodextrin click clusters*. *Journal of Pharmaceutical Sciences*, 2014. **103**(10): p. 3183-3189.

22. Diget, J.S., et al., *Direct synthesis of well-defined zwitterionic cyclodextrin polymers via atom transfer radical polymerization*. European Polymer Journal, 2019. **116**: p. 84-90.
23. Goszczyński, T.M., et al., *Synthesis of beta-cyclodextrin-lysozyme conjugates and their physicochemical and biochemical properties*. Journal of Inclusion Phenomena Macroscopic Chemistry, 2017. **87**: p. 341-348.
24. Dong, H., et al., *Recyclable antibacterial magnetic nanoparticles grafted with quaternized poly (2-(dimethylamino) ethyl methacrylate) brushes*. Biomacromolecules, 2011. **12**(4): p. 1305-1311.
25. Yallapu, M.M., et al., *Multi-functional magnetic nanoparticles for magnetic resonance imaging and cancer therapy*. Biomaterials, 2011. **32**(7): p. 1890-1905.
26. Beaven, G.H., et al., *A spectroscopic study of the haemin-human-serum-albumin system*. European Journal of Biochemistry, 1974. **41**(3): p. 539-546.
27. Chipman, D.M., et al., *The binding of oligosaccharides containing n-acetylglucosamine and n-acetylmuramic acid to lysozyme: the specificity of binding subsites*. Journal of Biological Chemistry, 1967. **242**(19): p. 4388-4394.
28. Bahniuk, M.S., et al., *Human plasma protein adsorption to elastinlike polypeptide nanoparticles*. Biointerphases, 2020. **15**(2): p. 021007.
29. Bahniuk, M.S., et al., *Bioactive glass 45S5 powders: effect of synthesis route and resultant surface chemistry and crystallinity on protein adsorption from human plasma*. Biointerphases, 2012. **7**(1): p. 41.
30. Han, V., et al., *A comparative study of common techniques used to measure haemolysis in stored red cell concentrates*. Vox Sanguinis, 2010. **98**(2): p. 116-123.

31. Mahmoud, W.E., et al., *A facile method to syntheses monodisperse gamma-Fe₂O₃ nanocubes with high magnetic anisotropy density*. Superlattices Microstructures, 2014. **68**: p. 1-5.
32. Tombuloglu, H., et al., *Fate and impact of maghemite (γ -Fe₂O₃) and magnetite (Fe₃O₄) nanoparticles in barley (*Hordeum vulgare L.*)*. Environmental Science Pollution Research, 2022. **29**(3): p. 4710-4721.
33. Al-Harbi, L., et al., *Functionalized iron oxide nanoparticles: synthesis through ultrasonic-assisted co-precipitation and performance as hyperthermic agents for biomedical applications*. Heliyon, 2022. **8**(6): p. e09654.
34. Kmita, A., et al., *One-step synthesis of long term stable superparamagnetic colloid of zinc ferrite nanorods in water*. Materials, 2019. **12**(7): p. 1048.
35. Rösner, H.I., et al., *The human alpha-lactalbumin molten globule: comparison of structural preferences at pH 2 and pH 7*. Journal of Molecular Biology, 2009. **394**(2): p. 351-362.
36. Cadenas, E., et al., *Thiol redox transitions in cell signaling, part A: chemistry and biochemistry of low molecular weight and protein thiols*. 2010: Academic Press.
37. Steudle, A., et al., *Modelling of lysozyme binding to a cation exchange surface at atomic detail: the role of flexibility*. Biophysical Journal, 2011. **100**(12): p. 3016-3024.
38. Jain, T.K., et al., *Magnetic resonance imaging of multifunctional pluronic stabilized iron-oxide nanoparticles in tumor-bearing mice*. Biomaterials, 2009. **30**(35): p. 6748-6756.
39. Dobrovolskaia, M.A., et al., *Interaction of colloidal gold nanoparticles with human blood: effects on particle size and analysis of plasma protein binding profiles*. Nanomedicine: Nanotechnology, Biology and Medicine, 2009. **5**(2): p. 106-117.

40. Konno, T., et al., *Preparation of nanoparticles composed with bioinspired 2-methacryloyloxyethyl phosphorylcholine polymer*. *Biomaterials*, 2001. **22**(13): p. 1883-1889.
41. Ishihara, K., et al., *Hemocompatibility of human whole blood on polymers with a phospholipid polar group and its mechanism*. *Journal of Biomedical Materials Research*, 1992. **26**(12): p. 1543-1552.
42. Yang, J.J., et al., *How does biological sex affect the physiological response to nanomaterials?* *Nano Today*, 2021. **41**: p. 101292.
43. Davie, E.W., et al., *The coagulation cascade: initiation, maintenance, and regulation*. *Biochemistry*, 1991. **30**(43): p. 10363-10370.
44. Kratz, F., *Albumin as a drug carrier: design of prodrugs, drug conjugates and nanoparticles*. *Journal of Controlled Release*, 2008. **132**(3): p. 171-183.
45. Kowalczyńska, H.M., et al., *Albumin adsorption on unmodified and sulfonated polystyrene surfaces, in relation to cell–substratum adhesion*. *Colloids and Surfaces B: Biointerfaces*, 2011. **84**(2): p. 536-544.
46. Dabare, P.R.L., et al., *Surface nanotopography mediated albumin adsorption, unfolding and modulation of early innate immune responses*. *Materials Today Advances*, 2021. **12**: p. 100187.
47. Lin, W., et al., *Hemocompatibility of polyacrylonitrile dialysis membrane immobilized with chitosan and heparin conjugate*. *Biomaterials*, 2004. **25**(10): p. 1947-1957.
48. Henry, M., et al., *Conformation change of albumin adsorbed on polycarbonate membranes as revealed by ToF-SIMS*. *Langmuir*, 2003. **19**(15): p. 6271-6276.

49. Van Dulm, P., et al., *The adsorption of human plasma albumin on solid surfaces, with special attention to the kinetic aspects*. Journal of Colloid and Interface Science, 1983. **91**(1): p. 248-255.
50. Victor, S.P., et al., *Development and evaluation of cyclodextrin complexed hydroxyapatite nanoparticles for preferential albumin adsorption*. Colloids and Surfaces B: Biointerfaces, 2011. **85**(2): p. 221-228.
51. Walport, M.J., *Advances in immunology: complement (first of two parts)*. New England Journal of Medicine, 2001. **344**(14): p. 1058-1066.
52. Andersson, J., et al., *Binding of C3 fragments on top of adsorbed plasma proteins during complement activation on a model biomaterial surface*. Biomaterials, 2005. **26**(13): p. 1477-1485.
53. Melchior, P., et al., *Complement activation by dialysis membranes and its association with secondary membrane formation and surface charge*. Artificial Organs, 2021. **45**(7): p. 770-778.
54. Vidarsson, G., et al., *IgG subclasses and allotypes: from structure to effector functions*. Frontiers in Immunology, 2014. **5**: p. 520.
55. Harrison, P.M., et al., *The ferritins: molecular properties, iron storage function and cellular regulation*. Biochimica et Biophysica Acta (BBA)-Bioenergetics, 1996. **1275**(3): p. 161-203.
56. Ogun, A.S., et al., *Biochemistry, transferrin*, in *StatPearls [Internet]*. 2022, StatPearls Publishing.
57. Stafford, J.L., et al., *Transferrin and the innate immune response of fish: identification of a novel mechanism of macrophage activation*. Developmental & Comparative Immunology, 2003. **27**(6-7): p. 539-554.

58. Bale, M.D., et al., *Identification of vitronectin as a major plasma protein adsorbed on polymer surfaces of different copolymer composition*. *Blood*, 1989.
59. Berclaz, P., et al., *Rare Childhood Lung Disorders: α 1-Antitrypsin Deficiency, Pulmonary Alveolar Proteinosis, and Pulmonary Alveolar Microlithiasis*, in *Kendig's Disorders of the Respiratory Tract in Children*. 2006, Elsevier. p. 747-761.
60. Chidambaranathan-Reghupaty, S., et al., *Hepatocellular carcinoma (HCC): Epidemiology, etiology and molecular classification*. *Advances in Cancer Research*, 2021. **149**: p. 1-61.
61. Charbgoon, F., et al., *Gold nanoparticle should understand protein corona for being a clinical nanomaterial*. *Journal of Controlled Release*, 2018. **272**: p. 39-53.
62. Papa, E., et al., *Investigation of the influence of protein corona composition on gold nanoparticle bioactivity using machine learning approaches*. *SAR and QSAR in Environmental Research*, 2016. **27**(7): p. 521–538.
63. Samir, D., et al., *Cell cooperation and role of the P2X7 receptor in pulmonary inflammation induced by nanoparticles*. *Nanotoxicology*, 2012. **7**(8): p. 1302–1314.
64. Liu, R., et al., *Prediction of nanoparticles-cell association based on corona proteins and physicochemical properties*. *Nanoscale*, 2015. **7**(21): p. 9664-9675.
65. Armstrong, P.B., et al., *α 2-macroglobulin: an evolutionarily conserved arm of the innate immune system*. *Developmental & Comparative Immunology*, 1999. **23**(4-5): p. 375-390.
66. Vandooren, J., et al., *Alpha-2-macroglobulin in inflammation, immunity and infections*. *Frontiers in Immunology*, 2021. **12**: p. 803244.
67. Levy, J.H., et al., *Fibrinogen as a therapeutic target for bleeding: a review of critical levels and replacement therapy*. *Transfusion*, 2014. **54**(5): p. 1389-1405.

68. Lowe, G.D., et al., *Plasma fibrinogen*. *Annals of Clinical Biochemistry*, 2004. **41**(6): p. 430-440.
69. Nava-Ortiz, C.A., et al., *Cyclodextrin-functionalized biomaterials loaded with miconazole prevent Candida albicans biofilm formation in vitro*. *Acta Biomaterialia*, 2010. **6**(4): p. 1398-1404.
70. Austen, D., *Clinical Biochemistry of Blood Coagulation*, in *Scientific Foundations of Biochemistry in Clinical Practice*. 1994, Elsevier. p. 495-513.
71. Ashikaga, H., et al., *Blood Coagulation and Atherothrombosis*, in *Molecular Basis of Cardiovascular Disease (Second Edition)*. 2004, W.B. Saunders: Philadelphia. p. 498-518.
72. Wu, Y., *Contact pathway of coagulation and inflammation*. *Thrombosis Journal*, 2015. **13**(1): p. 1-9.
73. Ortega, V.A., et al., *Polymer-coated nanoparticle protein corona formation potentiates phagocytosis of bacteria by innate immune cells and inhibits coagulation in human plasma*. *Biointerphases*, 2020. **15**(5): p. 051003.
74. Ivanov, I., et al., *Protease activity in single-chain prekallikrein*. *Blood, The Journal of the American Society of Hematology*, 2020. **135**(8): p. 558-567.
75. Veloso, D., et al., *Western blot analyses of prekallikrein and its activation products in human plasma*. *Thrombosis and Haemostasis*, 1991. **65**(04): p. 382-388.
76. To, W.S., et al., *Plasma and cellular fibronectin: distinct and independent functions during tissue repair*. *Fibrogenesis & Tissue Repair*, 2011. **4**: p. 1-17.
77. Rogers, H.J., et al., *Hemostasis and thrombosis*, in *Hematopathology*. 2018, Elsevier. p. 57-105.

78. Woodhouse, K., et al., *Adsorption of plasminogen from plasma to lysine-derivatized polyurethane surfaces*. *Biomaterials*, 1992. **13**(15): p. 1103-1108.
79. Quandt, J., et al., *Interactive Hemocompatible Nanocoating to Prevent Surface - Induced Coagulation in Medical Devices*. *Advanced Materials Interfaces*, 2022. **9**(33): p. 2201055.
80. Nalezinková, M., *In vitro hemocompatibility testing of medical devices*. *Thrombosis Research*, 2020. **195**: p. 146-150.
81. Lippi, G., *Systematic assessment of the hemolysis index: pros and cons*. *Advances in Clinical Chemistry*, 2015. **71**: p. 157-170.
82. Thomas, M., et al., *High molecular weight kininogen adsorption on hemodialysis membranes: influence of pH and relationship with contact phase activation of blood plasma. Influence of pre-treatment with poly (ethyleneimine)*. *The International Journal of Artificial Organs*, 2000. **23**(1): p. 20-26.
83. Renaux, J., et al., *Activation of the kallikrein-kinin system in hemodialysis: role of membrane electronegativity, blood dilution, and pH*. *Kidney International*, 1999. **55**(3): p. 1097-1103.
84. Dobrovolskaia, M.A., et al., *Nanoparticle size and surface charge determine effects of PAMAM dendrimers on human platelets in vitro*. *Molecular Pharmaceutics*, 2012. **9**(3): p. 382-393.
85. Koziara, J., et al., *Blood compatibility of cetyl alcohol/polysorbate-based nanoparticles*. *Pharmaceutical Research*, 2005. **22**: p. 1821-1828.

Chapter 5

1. Burns, N.L., et al., *Influence of surface charge on protein adsorption at an amphoteric surface: effects of varying acid to base ratio*. Journal of Colloid Interface Science, 1996. **178**(1): p. 116-122.
2. Lim, Y.J., et al., *Uremic toxins in the progression of chronic kidney disease and cardiovascular disease: mechanisms and therapeutic targets*. Toxins, 2021. **13**(2): p. 142.
3. Sekine, T., et al., *The multispecific organic anion transporter (OAT) family*. European Journal of Physiology, 2000. **440**: p. 337-350.
4. Sekine, T., et al., *Molecular physiology of renal organic anion transporters*. American Journal of Physiology-Renal Physiology, 2006.
5. Lowenstein, J., et al., *Uremic toxins in organ crosstalk*. Frontiers in Medicine, 2021. **8**: p. 592602.
6. Kraut, J.A., et al., *Metabolic acidosis of CKD: an update*. American Journal of Kidney Diseases, 2016. **67**(2): p. 307-317.
7. Kim, H.J., *Metabolic acidosis in chronic kidney disease: pathogenesis, clinical consequences, and treatment*. Electrolytes Blood Pressure: E, 2021. **19**(2): p. 29.
8. Franz, S., et al., *Immune responses to implants-a review of the implications for the design of immunomodulatory biomaterials*. Biomaterials, 2011. **32**(28): p. 6692-6709.
9. Dahlbäck, B., *Blood coagulation*. The Lancet, 2000. **355**(9215): p. 1627-1632.
10. Smith, G.S., et al., *Clinical pathology in non-clinical toxicology testing*, in *Haschek and Rousseaux's Handbook of Toxicologic Pathology*. 2013, Elsevier. p. 565-594.

11. Zhang, M., et al., *Effectively Decontaminating Protein-Bound Uremic Toxins in Human Serum Albumin Using Cationic Metal-Organic Frameworks*. ACS Applied Materials Interfaces, 2022.
12. Ishihara, K., *Revolutionary advances in 2-methacryloyloxyethyl phosphorylcholine polymers as biomaterials*. Journal of Biomedical Materials Research Part A, 2019. **107**(5): p. 933-943.
13. Shigeta, M., et al., *Suppression of fibroblast and bacterial adhesion by MPC coating on acrylic intraocular lenses*. Journal of Cataract Refractive Surgery, 2006. **32**(5): p. 859-866.
14. Campbell, E.J., et al., *Biocompatible surfaces using methacryloylphosphorylcholine laurylmethacrylate copolymer*. ASAIO Journal, 1994. **40**(3): p. M853-7.
15. Ishihara, K., et al., *Photoinduced graft polymerization of 2-methacryloyloxyethyl phosphorylcholine on polyethylene membrane surface for obtaining blood cell adhesion resistance*. Colloids Surfaces B: Biointerfaces, 2000. **18**(3-4): p. 325-335.
16. Fu, Y., et al., *Effect of cyclodextrins on the structure and functions of blood components in vitro*. Journal of Bioactive Compatible Polymers, 2015. **30**(5): p. 541-554.
17. Li, J., et al., *Multi-sites polycyclodextrin adsorbents for removal of protein-bound uremic toxins combining with hemodialysis*. Carbohydrate Polymers, 2020. **247**: p. 116665.
18. Ghoshal, K., et al., *Overview of platelet physiology: its hemostatic and nonhemostatic role in disease pathogenesis*. The Scientific World Journal, 2014. **2014**.
19. Garraud, O., et al., *Platelets and cytokines: how and why?* Transfusion Clinique et Biologique, 2012. **19**(3): p. 104-108.
20. Thomas, M.R., et al., *The role of platelets in inflammation*. Thrombosis Haemostasis, 2015. **114**(09): p. 449-458.

21. Vanholder, R., et al., *European Uremic Toxin Work Group*. *Kidney International*, 2003. **63**: p. 1934-1943.
22. Itoh, Y., et al., *Protein-bound uremic toxins in hemodialysis patients measured by liquid chromatography/tandem mass spectrometry and their effects on endothelial ROS production*. *Journal of Biomedical Materials Research Part A*, 2012. **403**(7): p. 1841-1850.
23. Duranton, F., et al., *Normal and pathologic concentrations of uremic toxins*. *Journal of the American Society of Nephrology*, 2012. **23**(7): p. 1258-1270.
24. Wolfson, M., et al., *Amino acid losses during hemodialysis with infusion of amino acids and glucose*. *Kidney International*, 1982. **21**(3): p. 500-506.
25. Schools, A., et al., *Biochemical and neurophysiological parameters in hemodialyzed patients with chronic renal failure*. *Clinica Chimica Acta*, 1989. **185**(1): p. 91-107.
26. Landon, J., et al., *Blood pyruvate concentration measured by a specific method in control subjects*. *Journal of Clinical Pathology*, 1962. **15**(6): p. 579-584.
27. Bain, M.A., et al., *Accumulation of trimethylamine and trimethylamine-N-oxide in end-stage renal disease patients undergoing haemodialysis*. *Nephrology Dialysis Transplantation*, 2006. **21**(5): p. 1300-1304.
28. Taki, K., et al., *Indoxyl sulfate and atherosclerotic risk factors in hemodialysis patients*. *American Journal of Nephrology*, 2007. **27**(1): p. 30-35.
29. Daniewska-Michalska, D., et al., *Efficiency of hemodialysis of pyrimidine compounds in patients with chronic renal failure*. *Nephron*, 1993. **64**(2): p. 193-197.
30. Toshimitsu, N., et al., *RNA metabolism in uremic patients: accumulation of modified ribonucleosides in uremic serum*. *Kidney International*, 1998. **53**: p. 1801-1806.

31. Deltombe, O., et al., *Exploring binding characteristics and the related competition of different protein-bound uremic toxins*. *Biochimie*, 2017. **139**: p. 20-26.
32. Zaidi, N., et al., *A biophysical insight into structural and functional state of human serum albumin in uremia mimic milieu*. *International Journal of Biological Macromolecules*, 2019. **131**: p. 697-705.
33. Karbowska, M., et al., *The uremic toxin indoxyl sulfate accelerates thrombotic response after vascular injury in animal models*. *Toxins*, 2017. **9**(7): p. 229.
34. Viaene, L., et al., *Albumin is the main plasma binding protein for indoxyl sulfate and p - cresyl sulfate*. *Biopharmaceutics & Drug Disposition*, 2013. **34**(3): p. 165-175.
35. Mahmoud, W.E., et al., *A facile method to syntheses monodisperse gamma-Fe₂O₃ nanocubes with high magnetic anisotropy density*. *Superlattices Microstructures*, 2014. **68**: p. 1-5.
36. Li, S., et al., *Indoxyl and p-cresol sulfate binding with human serum albumin*. *Colloids and Surfaces A: Physicochemical and Engineering Aspects*, 2022. **635**: p. 128042.
37. Gessner, A., et al., *Influence of surface charge density on protein adsorption on polymeric nanoparticles: analysis by two-dimensional electrophoresis*. *European Journal of Pharmaceutics and Biopharmaceutics*, 2002. **54**(2): p. 165-170.
38. Kratz, F., *Albumin as a drug carrier: design of prodrugs, drug conjugates and nanoparticles*. *Journal of Controlled Release*, 2008. **132**(3): p. 171-183.
39. Kowalczyńska, H.M., et al., *Albumin adsorption on unmodified and sulfonated polystyrene surfaces, in relation to cell–substratum adhesion*. *Colloids and Surfaces B: Biointerfaces*, 2011. **84**(2): p. 536-544.

40. Dabare, P.R.L., et al., *Surface nanotopography mediated albumin adsorption, unfolding and modulation of early innate immune responses*. *Materials Today Advances*, 2021. **12**: p. 100187.
41. Zaidi, N., et al., *A comprehensive insight into binding of hippuric acid to human serum albumin: a study to uncover its impaired elimination through hemodialysis*. *PloS One*, 2013. **8**(8): p. e71422.
42. Kuten Pella, O., et al., *Albumin as a Biomaterial and Therapeutic Agent in Regenerative Medicine*. *International Journal of Molecular Sciences*, 2022. **23**(18): p. 10557.
43. Lin, W., et al., *Hemocompatibility of polyacrylonitrile dialysis membrane immobilized with chitosan and heparin conjugate*. *Biomaterials*, 2004. **25**(10): p. 1947-1957.
44. Ogun, A.S., et al., *Biochemistry, transferrin*, in *StatPearls [Internet]*. 2022, StatPearls Publishing.
45. Stafford, J.L., et al., *Transferrin and the innate immune response of fish: identification of a novel mechanism of macrophage activation*. *Developmental & Comparative Immunology*, 2003. **27**(6-7): p. 539-554.
46. Moghimi, S.M., et al., *Material properties in complement activation*. *Advanced Drug Delivery Reviews*, 2011. **63**(12): p. 1000-1007.
47. Toda, M., et al., *Complement activation on surfaces carrying amino groups*. *Biomaterials*, 2008. **29**(4): p. 407-417.
48. Vidarsson, G., et al., *IgG subclasses and allotypes: from structure to effector functions*. *Frontiers in Immunology*, 2014. **5**: p. 520.
49. Bahniuk, M.S., et al., *Human plasma protein adsorption to elastinlike polypeptide nanoparticles*. *Biointerphases*, 2020. **15**(2): p. 021007.

50. Harrison, P.M., et al., *The ferritins: molecular properties, iron storage function and cellular regulation*. Biochimica et Biophysica Acta (BBA)-Bioenergetics, 1996. **1275**(3): p. 161-203.
51. Sano, K., et al., *Changes in glycosylation of vitronectin modulate multimerization and collagen binding during liver regeneration*. Glycobiology, 2007. **17**(7): p. 784-794.
52. Berclaz, P., et al., *Rare Childhood Lung Disorders: α 1-Antitrypsin Deficiency, Pulmonary Alveolar Proteinosis, and Pulmonary Alveolar Microlithiasis*, in *Kendig's Disorders of the Respiratory Tract in Children*. 2006, Elsevier. p. 747-761.
53. Chidambaranathan-Reghupaty, S., et al., *Hepatocellular carcinoma (HCC): Epidemiology, etiology and molecular classification*. Advances in Cancer Research, 2021. **149**: p. 1-61.
54. Bahniuk, M.S., et al., *Bioactive glass 45S5 powders: effect of synthesis route and resultant surface chemistry and crystallinity on protein adsorption from human plasma*. Biointerphases, 2012. **7**(1): p. 41.
55. Armstrong, P.B., et al., *α 2-macroglobulin: an evolutionarily conserved arm of the innate immune system*. Developmental & Comparative Immunology, 1999. **23**(4-5): p. 375-390.
56. Vandooren, J., et al., *Alpha-2-macroglobulin in inflammation, immunity and infections*. Frontiers in Immunology, 2021. **12**: p. 803244.
57. Levy, J.H., et al., *Fibrinogen as a therapeutic target for bleeding: a review of critical levels and replacement therapy*. Transfusion, 2014. **54**(5): p. 1389-1405.
58. Lowe, G.D., et al., *Plasma fibrinogen*. Annals of Clinical Biochemistry, 2004. **41**(6): p. 430-440.

59. Sreedhara, R., et al., *Uremic patients have decreased shear-induced platelet aggregation mediated by decreased availability of glycoprotein IIb-IIIa receptors*. American Journal of Kidney Diseases, 1996. **27**(3): p. 355-364.
60. Kozek-Langenecker, S.A., et al., *Fibrinogen fragments and platelet dysfunction in uremia*. Kidney International, 1999. **56**(1): p. 299-305.
61. Ocak, G., et al., *Chronic kidney disease and bleeding risk in patients at high cardiovascular risk: a cohort study*. Journal of Thrombosis and Haemostasis, 2018. **16**(1): p. 65-73.
62. Kaplan, B., et al., *Search for peptidic "middle molecules" in uremic sera: isolation and chemical identification of fibrinogen fragments*. Journal of Chromatography B, 2003. **796**(1): p. 141-153.
63. Austen, D., *Clinical Biochemistry of Blood Coagulation*, in *Scientific Foundations of Biochemistry in Clinical Practice*. 1994, Elsevier. p. 495-513.
64. Ashikaga, H., et al., *Blood Coagulation and Atherothrombosis*, in *Molecular Basis of Cardiovascular Disease (Second Edition)*. 2004, W.B. Saunders: Philadelphia. p. 498-518.
65. Wu, Y., *Contact pathway of coagulation and inflammation*. Thrombosis Journal, 2015. **13**(1): p. 1-9.
66. Ortega, V.A., et al., *Polymer-coated nanoparticle protein corona formation potentiates phagocytosis of bacteria by innate immune cells and inhibits coagulation in human plasma*. Biointerphases, 2020. **15**(5): p. 051003.
67. Ivanov, I., et al., *Protease activity in single-chain prekallikrein*. Blood, The Journal of the American Society of Hematology, 2020. **135**(8): p. 558-567.

68. Veloso, D., et al., *Western blot analyses of prekallikrein and its activation products in human plasma*. *Thrombosis and Haemostasis*, 1991. **65**(04): p. 382-388.
69. Yun, Y., et al., *Initial hemocompatibility studies of titanium and zirconium alloys: Prekallikrein activation, fibrinogen adsorption, and their correlation with surface electrochemical properties*. *Journal of Biomedical Materials Research*, 1996. **32**(1): p. 77-85.
70. To, W.S., et al., *Plasma and cellular fibronectin: distinct and independent functions during tissue repair*. *Fibrogenesis & Tissue Repair*, 2011. **4**: p. 1-17.
71. Gierula, M., et al., *Anticoagulant protein S—New insights on interactions and functions*. *Journal of Thrombosis and Haemostasis*, 2020. **18**(11): p. 2801-2811.
72. Quandt, J., et al., *Interactive Hemocompatible Nanocoating to Prevent Surface - Induced Coagulation in Medical Devices*. *Advanced Materials Interfaces*, 2022. **9**(33): p. 2201055.
73. Woodhouse, K., et al., *Adsorption of plasminogen from plasma to lysine-derivatized polyurethane surfaces*. *Biomaterials*, 1992. **13**(15): p. 1103-1108.
74. Thomas, M., et al., *High molecular weight kininogen adsorption on hemodialysis membranes: influence of pH and relationship with contact phase activation of blood plasma. Influence of pre-treatment with poly (ethyleneimine)*. *The International Journal of Artificial Organs*, 2000. **23**(1): p. 20-26.
75. Renaux, J., et al., *Activation of the kallikrein-kinin system in hemodialysis: role of membrane electronegativity, blood dilution, and pH*. *Kidney International*, 1999. **55**(3): p. 1097-1103.

Appendix A

A Detailed Protocol of Making Metabolite Solution

1. Metabolite solution preparation

1.1 Materials

3-Deoxyglucosone (Sigma Aldrich, St. Louis, Missouri, USA)

4-Ethylphenyl sulfate (Sigma Aldrich, St. Louis, Missouri, USA)

Argininic acid (Sigma Aldrich, St. Louis, Missouri, USA)

Asymmetric dimethylarginine (Sigma Aldrich, St. Louis, Missouri, USA)

Creatinine, Dimethyl glycine (Sigma Aldrich, St. Louis, Missouri, USA)

Guanidinopropionic acid (Sigma Aldrich, St. Louis, Missouri, USA)

Hippuric acid (Sigma Aldrich, St. Louis, Missouri, USA)

Homocysteine (Sigma Aldrich, St. Louis, Missouri, USA)

Hypoxanthine (Sigma Aldrich, St. Louis, Missouri, USA)

Indole acetic acid (Sigma Aldrich, St. Louis, Missouri, USA)

Indoxyl glucuronide (Sigma Aldrich, St. Louis, Missouri, USA)

Indoxyl sulfate (Sigma Aldrich, St. Louis, Missouri, USA)

Kynurenine (Sigma Aldrich, St. Louis, Missouri, USA)

Methyl histidine (Sigma Aldrich, St. Louis, Missouri, USA)

Orotic acid (Sigma Aldrich, St. Louis, Missouri, USA)

p-Cresol sulfate (Sigma Aldrich, St. Louis, Missouri, USA)

Phenylacetic acid (Sigma Aldrich, St. Louis, Missouri, USA)

Phenylalanine (Sigma Aldrich, St. Louis, Missouri, USA)

p-Hydroxyhippuric acid (Sigma Aldrich, St. Louis, Missouri, USA)

p-Hydroxyl phenylacetic acid (Sigma Aldrich, St. Louis, Missouri, USA)

Putrescine (Sigma Aldrich, St. Louis, Missouri, USA)

Pyruvic acid (Sigma Aldrich, St. Louis, Missouri, USA)

Quinolinic acid (Sigma Aldrich, St. Louis, Missouri, USA)

Spermidine (Sigma Aldrich, St. Louis, Missouri, USA)

Spermine (Sigma Aldrich, St. Louis, Missouri, USA)

Trimethylamine N-oxide (Sigma Aldrich, St. Louis, Missouri, USA)

Uric acid (Sigma Aldrich, St. Louis, Missouri, USA)

Uridine (Sigma Aldrich, St. Louis, Missouri, USA)

Xanthine (Sigma Aldrich, St. Louis, Missouri, USA)

Xanthosine (Sigma Aldrich, St. Louis, Missouri, USA)

l-Tyrosine (Sigma Aldrich, St. Louis, Missouri, USA)

l-Asparagine (Sigma Aldrich, St. Louis, Missouri, USA)

PBS tablet (Fisher Scientific, Hampton, New Hampshire, USA)

1.2 Procedure of preparing metabolite solution for non-plasma included experiment

1. PBS buffer preparation

Two PBS tablets are dissolved in 400 mL DI water and stored in a 500 mL bottle with lid.

2. Supplies preparation

Rinse and dry 84 5 mL microcentrifuge tubes and put them in the rack for use. Cut 84 aluminum films at the size of 4 cm × 4 cm.

3. Stock solution preparation

The stock solution and amount taken to make 250 mL metabolite solution is listed in **Table A1**. In the column of stock solution, volume represents the added DI water volume. This is for the convenience of future metabolite solution maker.

Table A.1 The metabolite solution formula includes the toxins, stock solution concentration, and volume/amount taken from the stock solution in order to make 250 mL metabolite solution.

Toxin	Stock solution concentration	Volume/amount taken
3-deoxyglucosone	1.02 mg/3mL	1 mL
4-ethylphenyl sulfate	0.1 mg/2mL	1 mL
Argininic acid	0.3 mg/2mL	0.1 mL
Asymmetric dimethylarginine	1.2 mg/ 1.56mL	0.1 mL
Creatinine	61.93 mg/2.27mL	1 mL
Dimethyl glycine	0.78 mg/6.6mL	1 mL
Guanidinopropionic acid	1.15 mg/2mL	0.1 mL
Hippuric acid	57.59 mg/20mL	16.46 mL
Homocysteine	3.24 mg/2mL	1 mL
Hypoxanthine	0.8 mg/2mL	1 mL
Indole acetic acid	0.96 mg/2.36mL	1 mL
Indoxyl glucuronide	1 mg/2mL	1 mL
Indoxyl sulfate	21.2 mg/2mL	1 mL
Kynurenine	0.48 mg/2.66mL	1 mL
Methylhistidine	0.2 mg/6mL	1 mL
Orotic acid	0.77 mg/4mL	1 mL

p-Cresol sulfate	8.36 mg/2mL	1 mL
Phenylalanine	3.7 mg/2mL	1 mL
p-Hydroxyhippuric acid	1.7 mg/2mL	1 mL
p-Hydroxyphenylacetic acid	1.35 mg/2.7mL	1 mL
Putrescine	0.38 mg/2mL	0.001 mL
Pyruvic acid	4680 mg	2.34 g
Quinolinic acid	0.47 mg/2.8mL	0.1 mL
Spermidine	16.9 mg/1mL	0.00114 mL
Spermine	0.98 mg/2.72mL	0.001 mL
Trimethylamine N-oxide	3 mg/2mL	1 mL
Uric acid (add last)	16.6 mg original powder	0.017 mg
uridine	3.92 mg/2mL	1 mL
Xanthine	0.6 mg/2mL	1 mL
Xanthosine	19.32 mg/mL	1 mL
l-Tyrosine	21.74 mg/2mL	1 mL
l-Asparagine	3.15 mg/2.2mL	1 mL

Attention:

- a. Hippuric acid stock solution is recommended to dissolve overnight before mixing with the bulk solution.
- b. Uric acid is recommended to add to the bulk solution **last** as it might cause precipitation.
- c. Pyruvic acid is weighed through the following steps:
 - i. Assemble a needle on a 5mL syringe, suck pyruvic acid to the maximum of the syringe, then inject them back into the original bottle. (This step is performed for the purpose of offsetting the residue weight in the needle after pyruvic acid is injected into the bulk solution.)
 - ii. Put the setup (keep the needle lid-free) in a 50 mL beaker.
 - iii. Position the setup on the scale and close the door.
 - iv. Tare and weight needed amount.

- v. Inject the pyruvic acid into the bulk solution without any further retaking and reinjecting of the air. (This ensured that the weight left in the needle is the same weight as it is in step i.)
- vi. Clean the scale. Put a lid back on the needle and dispose it properly.

1.2.1 Metabolite solution preparation

- a. A 500 mL bottle (with lid) and the pipette tips are DI water rinsed and heat dried (do not heat dry the lid). Add the stock solution to the bottle with pipettes. This step will introduce ~20 mL liquid in the bottle.
- b. Add 50 mL PBS solution to the bulk solution followed by adding the uric acid powder.
- c. Transfer the liquids to a 500 mL measuring cylinder, then rinse the 500 mL bottle 5 times with 10 mL water for each rinse. Combine the eluted solution with the bulk solution in measuring cylinder. Bring the volume to 200 mL.
- d. Pour the solution from measuring cylinder into the 500 mL bottle.
- e. Rinse the measuring cylinder with **PBS**, 5 times 10 mL each. Combine the eluted solution with the bulk solution in bottle. After performing this step, 250 mL metabolite solution is placed in the bottle. At this point, the solution should be transparent with no color. Please note some precipitation might occur. (The volume indicator on the bottle is not accurate, therefore the solution transfer between bottle and measuring cylinder is necessary.)
- f. Rinse and dry a stirrer in optimal size. Add it to the bottle. Place the bottle on the magnetic stir plate (Ensure the heat is turned off if a magnetic hotplate stir is used)
- g. Initiate the pH meter and calibrate it using the standard solution set.

- h. Rinse the pH meter with DI water and remove the water on the tip and body with Kimwipe **gently**.
- i. Test the pH value of the bulk solution. It should be acidic.
- j. Use a stone grinder to grind 2 NaOH beads into powder.
- k. Put the pH meter aside. Take the minimum amount of NaOH powder as you can to add into the solution while stirring. Remeasure the pH value of the bulk solution to estimate how much NaOH powder is to be added next.
- l. Repeat step k. until pH is brought to 7.4. The color of the solution should be **mild yellow** compared to the color after performing 4.r.
- m. Use a strong magnet to remove the stirrer.

1.2.2 Aliquot the stock solution

- a. Add 3 mL of metabolite solution to each tube.
- b. Close the lid and label the tube with data, volume, solution name, and owner name.
- c. Put the tubes on rack to -80 °C refrigerator.

1.2.3 Lyophilization

- a. Initiate the lyophilization machine properly.
- b. Upon use, take a glass drying flask as the container to transfer the metabolite solution tubes from the -80 °C refrigerator.
- c. Open the lid of each tube and put the prepared aluminum film on each tube. Punch ~15 holes on the aluminum film for the evacuation of solvent. Squeeze the edge of the tubes to ensure the appropriate attachment of aluminum film to the tube.
- d. Combined up to 5 tubes together by piling their lids and wrapping them with a rubber band.

- e. Place the octopus-like set back into the glass drying flask, then refrigerate it at -80 for another 30 minutes. The operations in c and d will lead to the melting of the frozen solution. The liquid will further result in the bubble forming during lyophilization, which will contact the aluminum film and leads to a condensation of metabolite powder on the aluminum that influences the accuracy of the powder weight.
- f. Take the glass drying flask out and load it on the lyophilization machine.
- g. Leave it overnight. The estimated time consumption depends on the number of tubes loaded.
- h. Unload the glass drying flask. Remove the aluminum lids carefully and close the tube lid.
- i. Store the extras in the -80 °C.

1.3 Experiment

Add 3 mL DI water to resume the original concentration.

1.4 Procedure of preparing metabolite solution for plasma included experiment

1.4.1 Supplies preparation

Rinse and dry 84 5 mL microcentrifuge tubes and put them in the rack for use. Cut 84 aluminum films at the size of 4 cm × 4 cm.

1.4.2 Stock solution preparation

The stock solution and the amount taken to make 250 mL metabolite solution is listed in **Table A2**. In the column of stock solution, volume represents the added DI water volume. This is for the convenience of future metabolite solution makers.

Table A.2 The metabolite solution formula includes the toxins, stock solution concentration and volume/amount taken from the stock solution in order to make 250 mL metabolite solution for plasma included experiment.

Toxin	Stock solution concentration	Volume/amount taken
3-deoxyglucosone	1.02 mg/3 mL	0.82 mL
4-ethylphenyl sulfate	0.1 mg/2 mL	0.80 mL
Argininic acid	0.3 mg/2 mL	0.07 mL
Asymmetric dimethylarginine	1.2 mg/ 1.56 mL	0.08 mL
Creatinine	61.93 mg/2.27 mL	0.91 mL
Dimethyl glycine	0.78 mg/6.6 mL	0.34 mL
Guanidinopropionic acid	1.15 mg/2 mL	0.10 mL
Hippuric acid	57.59 mg/20 mL	16.39 mL
Homocysteine	3.24 mg/2 mL	0.83 mL
Hypoxanthine	0.8 mg/2 mL	0.25 mL
Indole acetic acid	0.96 mg/2.36 mL	0.75 mL
Indoxyl glucuronide	1 mg/2 mL	0.50 mL
Indoxyl sulfate	21.2 mg/2 mL	0.99 mL
Kynurenine	0.48 mg/2.66 mL	0.00 mL
Methylhistidine	0.2 mg/6 mL	0.00 mL
Orotic acid	0.77 mg/4 mL	0.00 mL
p-Cresol sulfate	8.36 mg/2 mL	1.00 mL
Phenylalanine	3.7 mg/2 mL	0.26 mL
p-Hydroxyhippuric acid	1.7 mg/2 mL	0.44 mL
p-Hydroxyphenylacetic acid	1.35 mg/2.7 mL	0.00 mL
Putrescine	0.38 mg/2 mL	0.00 mL
Pyruvic acid	4680 mg	1.11 mg
Quinolinic acid	0.47 mg/2.8 mL	0.00 mL
Spermidine	16.9 mg/1 mL	0.00 mL
Spermine	0.98 mg/2.72 mL	0.00 mL
Trimethylamine N-oxide	3 mg/2 mL	0.62 mL
Uric acid (add last)	16.6 mg of the original powder	8.50 mg
uridine	3.92 mg/2 mL	0.85 mL
Xanthine	0.6 mg/2 mL	0.00 mL
Xanthosine	19.32 mg/mL	0.35 mL
l-Tyrosine	21.74 mg/2 mL	0.70 mL
l-Asparagine	3.15 mg/2.2 mL	0.51 mL

1.4.3 Metabolite solution preparation

- a. A 500 mL bottle (with lid) and the pipette tips are DI water rinsed and heat dried (do not heat dry the lid). Add the stock solution to the bottle with pipettes. This step will result in ~20 mL liquid in the bottle.
- b. Add 50 mL **DI water** to the bulk solution followed by adding the uric acid powder.
- c. Transfer the liquids to a 500 mL measuring cylinder, then rinse the 500 mL bottle 5 times with 10 mL water for each rinse. Combine the eluted solution with the bulk solution in measuring cylinder. Bring the volume to 200 mL.
- d. Pour the solution from measuring cylinder into the 500 mL bottle.
- e. Rinse the measuring cylinder with **DI water**, 5 times 10 mL each. Combine the eluted solution with the bulk solution in bottle. This will result in 250 mL metabolite solution in the bottle. At this point, the solution should be transparent with no color. Please note some precipitation might occur. (The volume indicator on the bottle is not accurate, therefore the solution transfer between bottle and measuring cylinder is necessary.)
- f. Rinse and dry a stirrer in optimal size. Add it to the bottle. Place the bottle on the magnetic stir plate (Ensure the heat is turned off if a magnetic hotplate stir is used).
- g. Initiate the pH meter and calibrate it using the standard solution set.
- h. Rinse the pH meter with DI water and remove the water on the tip and body with Kimwipe **gently**.
- i. Test the pH value of the bulk solution. It should be acidic.
- j. Use a stone grinder to grind 2 NaOH beads into powder.
- k. Put the pH meter aside. Take the minimum amount of NaOH powder as you can to add into the solution while stirring. Remeasure the pH value of the bulk solution to estimate how much NaOH powder is to be added next.

- l. Repeat step 13 until pH is brought to 7.4.
- m. Use a strong magnet to remove the stirrer.

1.4.4 Aliquot the stock solution

- a. Add 3 mL of metabolite solution to each tube.
- b. Close the lid and label the tube with data, volume, solution name, and owner name.
- c. Put the tubes on a rack in -80 °C refrigerator.

1.4.5 Lyophilization

- a. Initiate the lyophilization machine properly.
- b. Upon use, take a glass drying flask as the container to transfer the metabolite solution tubes from -80-degree refrigerator.
- c. Open the lid of each tube and put the prepared aluminum film on each tube. Punch ~15 holes on the aluminum film for the evacuation of solvent. Squeeze the edge of the tubes to ensure the appropriate attachment of aluminum film to the tube.
- d. Combined up to 5 tubes together by piling their lids and wrapping them with rubber band.
- e. Place the octopus-like set back to glass drying flask, then refrigerate it in -80 for another 30 minutes. The operations in c and d will lead to the melting of frozen solution. The liquid will further result in the bubble forming during lyophilization, which will contact the aluminum film and lead to a condensation of metabolite powder on the aluminum that influences the accuracy of the powder weight.
- f. Take the glass drying flask out and load it on the lyophilization machine.
- g. Leave it overnight. The estimated time consumption depends on the number of tubes loaded. The product is **purple-ish red**.
- h. Unload the glass drying flask. Remove the aluminum lids carefully and close the tube lid.

- i. Store the extras in the $-80\text{ }^{\circ}\text{C}$.

1.4.6 Experiment

Add 3 mL platelet-poor plasma to resume the original concentration.

Appendix B

A Detailed Protocol of Fluorescence Spectroscopy

Experiment

1. Materials

KH_2PO_4 (Fisher Scientific, Hampton, New Hampshire, USA)

NaCl (Fisher Scientific, Hampton, New Hampshire, USA)

KCl (Fisher Scientific, Hampton, New Hampshire, USA)

Na_2HPO_4 (Fisher Scientific, Hampton, New Hampshire, USA)

Human serum albumin (Sigma Aldrich, St. Louis, Missouri, USA)

p-Cresol sulfate potassium salt (MuseChem, Fairfield, New Jersey, USA)

Indoxyl sulfate potassium salt (Sigma Aldrich, St. Louis, Missouri, USA)

2. Procedure to conduct fluorescence experiments

2.1 Sample preparation

- a. Prepare the 1X PBS solution use the following concentration for each component: NaCl : 137 mM, KCl : 2.7 mM, Na_2HPO_4 : 10 mM, KH_2PO_4 : 1.8 mM.
- b. Weight demanded amount of the p-cresol sulfate potassium salt (PCS) and indoxyl sulfate potassium salt (IS) and dissolved them in the according volume of the PBS buffer.
- c. Weight demanded amount of human serum albumin (HSA) and dissolved them in the according volume of the PBS buffer. HSA solution is recommended to made fresh prior to experiment, although the residue can be used within one week if stored at 4 degree.

2.2 Experiment

- a. Preheat the fluorescence spectrometer to a designated temperature.
- b. Set up the excitation and emission wavelength as indicated in Chapter 1 for HSA (Tryptophan in this case).

- c. Prepare a 96 well plate with black walls and transparent bottom.
- d. Inject the HSA solution into each well. Inject an according volume of PCS/IS/PBS solution into designated well following the experiment plan. Upon injection, **immerse** the pipette tips under the surface and **gently** push out the solution. Mix the PCS/IS/PBS well with the HSA solution by repeating the injecting and sucking (5 times). All movement need to be gentle as any sudden movement will cause long lasting bubble.
- e. Initiate measurement

Attention: If the experiment is to be performed under designated temperature, then the plate and solutions **must** be preheated to the corresponding temperature.

2.3 Data analysis

Fluorescence spectrometry can provide more than just quenching data; it can also be used to calculate binding constants. In this thesis, Stern-Volmer equation was used to determine whether the quenching mechanism was dynamic or static:

$$F^0/F = 1 + K_{SV}[Q] \quad (\text{Equation B1})$$

where F^0 is the fluorescence intensity in the absence of PCS/IS, F is in the presence of PCS/IS, K_{SV} is the Stern–Volmer quenching constant, and $[Q]$ is the concentration of PCS/IS. This data can be represented by plotting $[Q]$ against F^0/F as. In this way, the K_{SV} is yielded to determine the quenching mechanism.

The binding parameters were calculated following the equation:

$$\log \frac{F^0-F}{F} = n \log K_a - n \log \frac{1}{[Q] - \frac{(F^0-F)[P]}{F^0}} \quad (\text{Equation B2})$$

Where K_a is the association constant and n is the average number of binding sites. $[P]$ represents protein concentration. We can obtain the interception value and conclude the value of K_a and n by plotting $\log(1/([Q] - (F^0 - F)[P]/F^0))$ against $\log((F^0 - F)/F)$.

Appendix C

A Detailed Protocol of Isothermal Titration Calorimetry

Experiment

1. Materials

KH_2PO_4 (Fisher Scientific, Hampton, New Hampshire, USA)

NaCl (Fisher Scientific, Hampton, New Hampshire, USA)

KCl (Fisher Scientific, Hampton, New Hampshire, USA)

Na_2HPO_4 (Fisher Scientific, Hampton, New Hampshire, USA)

Human serum albumin (Sigma Aldrich, St. Louis, Missouri, USA)

p-Cresol sulfate potassium salt (MuseChem, Fairfield, New Jersey, USA)

Indoxyl sulfate potassium salt (Sigma Aldrich, St. Louis, Missouri, USA)

2. Procedure to conduct experiment on isothermal titration calorimetry

The 1X PBS stock solution is made following these concentrations: NaCl : 137 mM, KCl : 2.7 mM, Na_2HPO_4 : 10 mM, KH_2PO_4 : 1.8 mM. The PBS solution used for HSA/PCS/IS solution preparation in the experiment must be degassed for 10 minutes before making solution. Follow these steps to prepare the calorimeter:

- a. Turn on the ITC switch and initiate the software. The machine will perform a home reset automatically.
- b. Twist and disassemble the buret and fill the reference cell with DI water using a long needle syringe. Remove the steel tube insertion with tweezers and fill the water until the surface is visible. Then, re-insert the insertion and remove any excess water using Kimwipes or suction tool. This process should be done once a month. The reference cell should not be left dry at anytime.
- c. Click 'monitor' tab in the software to observe the current balancing pattern.
- d. Empty the sample cell by gently sucking out any previously present liquid with a needle and refill it with $\sim 300\mu\text{l}$ of degassed water at **RT**. Avoid pressing the syringe to its end,

- as this would leave air inside the cell. Prior to refill the sample cell with DI water, ensure that no air bubbles occur in the syringe.
- e. Assemble the buret by gently pressing it downwards and turning it. A successfully assembled buret should be fixed.
 - f. Leave the machine undisturbed for ~ 1 hr. The balancing of the calorimeter can be monitored by observing the fluctuation records on the screen. When the fluctuation is within the range of 0.02 on the Y axis, balance is reached. A longer time span may apply depends on the solution temperature.
 - g. Empty the sample cell by gently sucking out DI water used for balancing with a needle and refill it with ~ 300 μ l of HSA solution at **RT**. Repeat step e and f.
 - h. Fill the syringe (the one with a volume of 50 uL).
 - i. Suck the PCS/IS solution to the maximum amount. This will give you a syringe half-filled with air bubble and half-filled solution.
 - ii. Flip the syringe (needle up) then pull out the plunger. Let gravity bring the liquid surface to the bottom of the syringe.
 - iii. Plug the plunger back in quickly. After this step, the white rubber on the plunger should be in contact with solution in the syringe.
 - iv. Flip the syringe (needle down) and repeat the suction to desired level. After this step, no bubble should present in the syringe. Otherwise repeat step h.
 - i. Disassemble the buret from the body. Screw on the syringe (50 uL capacity) by holding the rounded steal panel on the syringe.
 - j. Place the buret setup in the correct position (Ideally centered, the syringe is aimed to fit in the sample cell.)
 - k. Close the buret by gently pushing the buret downwards and twist-lock.

- l. Wait until the calorimeter is balanced again. This step is approximately taking 1 hr.
- m. Select an appropriate stirring rate (150 rpm is used in this case), set up a proper titration scheme by choosing injection numbers. Click stirring, set the start delay to 1800s. Click 'start experiment'.
- n. The blank experiments are performed by injection PCS/IS to PBS.

Attention: Any air bubble or suspected air gap will lead to the failure of the experiment!

3. Data analysis

A software named NanoAnalyze can be downloaded from the TA instrument website and is used for the analysis of the ITC data. The analysis follows the steps below:

- a. Open the data sets to be analyzed, which are the experiment and blank.
- b. Fill in the concentration data with the right **unit** in the experimental data set.
- c. Drag and drop the blank file to the yellow square named blank.
- d. Under the modeling tab, select the independent binding fitting model.
- e. Start fitting.
- f. Upon finishing fitting, the thermal dynamic data will present automatically.

Appendix D

A Detailed Protocol of Circular Dichroism Experiment

1. Materials

$\text{NaH}_2\text{PO}_4 \cdot \text{H}_2\text{O}$ (Fisher Scientific, Hampton, New Hampshire, USA)

Na_2HPO_4 (Fisher Scientific, Hampton, New Hampshire, USA)

Human serum albumin (Sigma Aldrich, St. Louis, Missouri, USA)

p-Cresol sulfate potassium salt (MuseChem, Fairfield, New Jersey, USA)

Indoxyl sulfate potassium salt (Sigma Aldrich, St. Louis, Missouri, USA)

Citric acid liquid (Made Unknown)

2. Procedure to conduct fluorescence experiments

The concentration used of making 0.1 M PB stock solution is Na_2HPO_4 for 75 mM and 25 mM for $\text{NaH}_2\text{PO}_4 \cdot \text{H}_2\text{O}$.

2.1 Sample preparation

- a. Make designated PCS/IS solution and HSA/Lysozyme/ α -Lactalbumin solution with PB buffer.
- b. Mix the toxins with proteins prior to the experiment and keep the mixture at the designated temperature.

2.2 Experiment

- a. Wash the glass cuvette with citric acid and rinse it off **thoroughly**, or the protein will be denatured.
- b. Inject the protein-toxin mixture solution into the cuvette without leaving any air gap in the cuvette.
- c. Fixed the cuvette in the sample cell and initiated the measuring.
- d. Repeat **a** to **c** until finish all the samples.

3. Data analysis

The analysis of circular dichroism data is performed using CDNN 2.0 software. After selecting the correct unit of the Y axis, the number of amino acids of each protein should be input. The data yield several options in different wavelengths. 190 nm to 260 nm was chosen for the experiment in this thesis.